

Universität  
Rostock



Traditio et Innovatio

# Enhancement of the Efficiency of Photocatalysts by Hierarchical Structuring with Ordered Mesoporous Silicates

Dissertation

zur

Erlangung des akademischen Grades

*doctorrerumnaturalium (Dr. rer. nat.)*

der Mathematisch-Naturwissenschaftlichen Fakultät

der Universität Rostock

vorgelegt von *Mishal Ibrahim*, geb. am 24.09.1977 in Mosul (Iraq)

Rostock, 27.04.2018

Die vorliegende Arbeit wurde in der Zeit von März 2014 bis September 2017 am Institut für Chemie der Universität Rostock am Lehrstuhl für Anorganische Chemie in der Arbeitsgruppe von Prof. Dr. Axel Schulz angefertigt.

1. Gutachter: Prof. Dr. Axel Schulz
2. Gutachter:

## **ERKLÄRUNG**

Ich versichere hiermit an Eides statt, dass ich die vorliegende Arbeit selbstständig angefertigt und ohne fremde Hilfe verfasst habe. Dazu habe ich keine außer den von mir angegebenen Hilfsmitteln und Quellen verwendet und die den benutzten Werken inhaltlich und wörtlich entnommenen Stellen habe ich als solche kenntlich gemacht.

Rostock, 27.04.2018

.....

MishalWalid Ibrahim

## **Acknowledgements**

First of all, I would like to gratefully and sincerely thank Prof.Dr. Axel Schulz (Department of Inorganic Chemistry, Institute of Chemistry, University of Rostock) who provided me the opportunity to join his research group. I would also like to express my deepest and sincere gratitude to my Co-supervisor Dr. Hendrik Kosslick for the continuous help and support in my PhD studies and research, for his patience and motivation. Beside my supervisor, I would also like to thank Dr. Muhammad Farooq Ibad for sharing his experience and assistance in PXRD, Raman, N<sub>2</sub> adsorption/desorption and UV/Vis measurements. I would also like to say special thanks to Dr. Norbert Steinfeldt for SAXS and UV/Vis diffuse reflectance measurements, Dr. Christine Fischer for ESI-TOF-MS analysis; (Leibniz-Institute for Catalysis, LIKAT), MSc. Sören Arlt for TG-DSC analysis, Mrs .Petra Duncker for TOC measurements (University of Rostock, as well as Dr. sc. Marcus Frank and Dr. Armin Springer for SEM, TEM and EDX investigations. Also I thank to all my PhD friends in Rostock and my colleagues in AK Schulz group for their encouragement, friendship and support during my work in the laboratory. Last, but not the least I would like to thank my dear family whom deserves a sincere appreciation for all what they have done for me. They have provided me with endless support over the last years. I have to thank the most important persons in my life my father and my mother. They have always been an inspiration to me. Their support during past years is highly appreciable. I owe sincere and heartiest gratitude to my children and my wife who tolerated my busy hours, supporting and trusting in my ability to reach the goal. It is also worth mentioning brothers and sisters for supporting me spiritually throughout my PhD study and for their efforts to provide me the most suitable environment for my work. Again, sincere thanks to all my teachers, colleagues, friends and family who have given me love and support throughout my life.

And finally, I would definitely make use of this opportunity to thank the Iraqi Ministry of Higher Education for granting me a scholarship over three and a half years.

## Zusammenfassung

Die Erhöhung der Effizienz von Photokatalysatoren mittels hierarchischer Strukturierung mit geordneten mesoporösen silikatischen Materialien wurde untersucht. Dazu wurden geordnete mesoporöse Silikate mit unterschiedlicher spezifischer Oberfläche, Porengröße, Porenvolumen und Porendimension hydrothermal synthetisiert: MCM-41, MCM-48, KIT-6, SBA-12, SBA-15, SBA-16 und FDU-12. Die Präparation der hierarchisch strukturierten Photokatalysatoren erfolgte mechano-chemisch durch Mischung und Mahlung mit der katalytischen Komponente  $\text{AgVO}_3/\text{g-C}_3\text{N}_4$  und anschließender thermischer Nachbehandlung.  $\text{AgVO}_3/\text{g-C}_3\text{N}_4$  wurde ebenfalls mechano-chemisch aus den Einzelkomponenten präpariert. Die erhaltenen komplexen  $\text{AgVO}_3/\text{g-C}_3\text{N}_4/\text{Meso-Materialien}$  wurden hinsichtlich ihrer Struktur, Porosität und Morphologie mittels XRD, FTIR, SEM, TEM, SAXS und Stickstoff-Ad- und Desorption charakterisiert. Die Dispersität des Katalysators wurde zusätzlich mittels Elementspezifisches Mapping (EDX) vermessen. Die katalytische Aktivität wurde mittels photokatalytischen Abbaus von Ibuprofen unter anwendungsnahen Bedingungen wie niedriger Schadstoffkonzentration, niedriger Bestrahlungsintensität mit UV/Vis und sichtbarem Licht (Tageslicht bzw. Raumlicht) sowie niedrigem Katalysator-zu-Schadstoff-Verhältnis untersucht und mit der von Titandioxid und Zinkoxid-basierten Katalysatoren verglichen. Der Gehalt der mesoporösen Komponente wurde variiert. Die oxidative Öffnung des aromatischen Ringes wurde UV/Vis spektroskopisch verfolgt. Die Mineralisation wurde mittels TOC-Messung bestimmt. Die beteiligten photokatalytisch aktiven Spezies wie Elektronenlöcher, OH- und Hydroperoxid-Radikale bzw. Superoxid-Radikal-Anionen wurden mittels Zusatzes von „Scavenger-Molekülen“ untersucht. Die Untersuchungen zeigen, dass die hierarchische Strukturierung zu einer deutlichen Steigerung der Effizienz der Photokatalysatoren und damit zu einer erheblichen Materialeinsparung (Ag) führt. Außerdem ist die Abtrennung des Katalysators von der Reaktionslösung verbessert. Die mikroskopischen Untersuchungen zeigen, dass die Effizienzsteigerung auf eine erhöhte Dispersität der katalytischen Komponente beruht. Diese ist teilweise schalenförmig auf dem Träger angeordnet. Dadurch erhöht sich der Anteil der zugänglichen Oberfläche an der bzw. in deren Nähe die Photokatalyse abläuft. Der Stofftransport zum Katalysator ist verbessert. Die Katalysatoren zeichnen sich durch eine geringe Bildung von Nebenprodukten aus und sind aktiv mit sichtbarem Licht. Mittels der hochaufgelösten SEM-Untersuchungen konnte erstmals festgestellt werden, dass es sich bei den mesoporösen Silikaten um Mesokristalle handelt, die aus kleineren sub-mikrometer- und nanometer-großen agglomerierten Partikeln bestehen (kein Vollmaterial).

## Summary

The enhancement of the efficiency of photocatalysts by hierarchical structuring with ordered mesoporous materials was investigated. For this, mesoporous materials of different pore structure and porosity were hydrothermally synthesized: MCM-4, MCM-48, KIT-6, SBA-12, SBA-15, SBA-16 and FDU-12.  $\beta$ -AgVO<sub>3</sub>/mpg-C<sub>3</sub>N<sub>4</sub> Core Shell catalysts and composites were used as photocatalytic component. For comparison ZnO and TiO<sub>2</sub>/mesoporous silica composites were involved. The hierarchical structured photocatalysts were prepared mechano-chemical by mixing and milling of the single components solvent free. The materials were characterized according to the structure, textural properties, chemical composition and the dispersion of the catalytic components using XRD, SEM, TEM, SAXS, EDX, FTIR, and N<sub>2</sub> adsorption/desorption. The photocatalytic activity of the materials was tested in the degradation of ibuprofen under reliable conditions (as low pollutant concentration, low catalyst/IBPratio of 4, low intensity sun and room light equivalent irradiation). Reaction by-products were studied by ESI-TOF-MS and the contribution of different reactive oxidation species (ROS) such as hydroxyl radicals ( $\bullet$ OH), superoxide radical anions ( $\bullet$ O<sub>2</sub><sup>-</sup>) and holes (h<sup>+</sup>) was investigated by using scavenger experiments. As a result, highly active Core Shell and composite catalysts were obtained with superior UV/Vis and visible light activity. The efficiency of the photocatalysts could be markedly enhanced by hierarchical structuring with ordered mesoporous materials. The reason is an improved dispersion of the catalytic component on the mesoporous material allowing better access of hazardous contaminants to the catalyst and the enhanced mass transfer to and from the catalyst surface. The porosity of mesoporous materials had minor impact on the efficiency enhancement.

## Content

List of Abbreviations.....	X
1. Goals and Objectives .....	1
1.1. Goals.....	1
1.2. Objectives .....	1
1.3. Approach .....	2
2. Introduction.....	3
2.1. General.....	3
2.2. State-of-The-Art .....	5
2.3. Theoretical Background .....	7
2.3.1 Solid State Semiconductor .....	7
2.3.2 General Mechanism of the Photocatalytic Process: .....	8
2.3.3 General Course of the Photocatalytic Degradation .....	11
2.4. Description of used Photocatalytic Materials and Mesoporous Supports .....	12
2.4.1 Polymeric Graphitic Carbon Nitrides ( $g\text{-C}_3\text{N}_4$ ) .....	12
2.4.2 Silver Vanadate ( $\beta\text{-AgVO}_3$ ) .....	14
2.5. Porous Materials .....	14
2.5.1 Mesoporous Materials .....	17
2.5.2 1D Mesoporous Silica: MCM-41 .....	18
2.5.3 2D Mesoporous Silica: SBA-15 .....	19
2.5.4 3D Mesoporous Silica: SBA-12 .....	19
2.5.5 3D Mesoporous Silica: KIT-6 .....	20
2.5.6 3D Mesoporous Silica: MCM-48 .....	21
2.5.7 3D Mesoporous Silica: SBA-16 and FDU-12 .....	21
2.6. Composite Materials.....	22
2.6.1 Supported Photocatalysts .....	23
2.6.2 Photocatalyst Composite Mixtures.....	23
2.6.3 Core Shell Catalysts .....	24

2.6.4	Hierarchical Nanoscale Photocatalyst.....	24
3.	Results and Discussion .....	25
3.1	Materials .....	25
3.1.1	Silver Vanadate, Mesoporous Graphitic Carbon Nitride and $\beta$ -AgVO <sub>3</sub> /mpg-C <sub>3</sub> N <sub>4</sub> Composites /Core Shell Catalysts.....	25
3.1.2	Mesoporous Ordered Silica Mesoporous Structures.....	27
3.1.3	Advanced Complex Inorganic Nanomaterials .....	48
3.2	Photocatalysis .....	52
3.2.1	Photocatalytic Performance of Mechano-Chemical Prepared $\beta$ -AgVO <sub>3</sub> /mpg-C <sub>3</sub> N <sub>4</sub> Core Shell Composites.....	52
3.2.2	Photocatalytic Performance of Hierarchical Structured, Core Shell, 25-30% $\beta$ -AgVO <sub>3</sub> /mpg-C <sub>3</sub> N <sub>4</sub> Catalyst Supported on Ordered Mesoporous Silica.....	57
3.2.3	Photocatalytic Performance of Mechano-Chemical Prepared 25 % $\beta$ -AgVO <sub>3</sub> /mpg-C <sub>3</sub> N <sub>4</sub> /Mesoporous Silica Composite (Advanced Complex Inorganic Nanomaterials) .....	69
3.2.4	Further Examples with Variation of the Compositions of CAT-25 / Silica with FDU-12-S, FDU-12-L, MCM-41-S, MCM-41L, SBA-12, SBA-15, SBA-16, MCM-48-S and MCM-48-L.....	71
3.3	Reactive Oxidative Species .....	77
4.	Conclusion .....	79
5.	Appendixes .....	82
5.1	<i>Materials</i> .....	82
5.2	Synthesis of Photocatalysts .....	82
5.2.1	Preparation of the Advanced Complex Inorganic Nanomaterials (ACIN) $\beta$ -AgVO <sub>3</sub> /mpg-C <sub>3</sub> N <sub>4</sub> /SiO <sub>2</sub> Composite.....	83
5.2.2	Preparation of Mesoporous Silica Materials.....	84
5.3	Characterization.....	87
5.4	Photocatalytic Testing and Analysis.....	89
6	Titanium dioxide (TiO <sub>2</sub> ) .....	89

6.1	Experimental: TiO <sub>2</sub> /SBA-12.....	90
6.2	Photocatalytic Activity of Titania P-25 / Mesoporous Silica Composite.....	94
7	Zinc oxide (ZnO) .....	101
7.1	Experimental: Composite-Type Inorganic Nanomaterials: 20% ZnO/SBA-12 .....	101
7.2	ZnO/SiO <sub>2</sub> Composite Photocatalytic Activity.....	106
8	References.....	122

## List of Abbreviations

<b>1D</b>	One-dimensional	<b>2D</b>	Two-dimensional
<b>ACIN</b>	Advanced complex inorganic material	<b>nm</b>	Nanometer
<b>AOPs</b>	Advanced oxidation processes	<b>m/z</b>	Mass to charge ratio
<b>BET</b>	Brunauer–Emmett–Teller	<b>O<sub>2</sub><sup>-•</sup></b>	Superoxide radical
<b>BJH</b>	Barrett-Joyner-Halenda	<b>•OH</b>	Hydroxyl radical
<b>BQ</b>	Benzoquinone	<b>•OOH</b>	Hydro peroxy radical
<b>t-BuOH</b>	Tertiarybutanol	<b>P-123</b>	Pluronic123
<b>ccp</b>	Cubicclosepacked	<b>PEG</b>	Poly(ethyleneglycol)
<b>C</b>	Concentration	<b>PEO</b>	Polyethylene oxide
<b>°C</b>	Degree Celsius	<b>ppm</b>	Parts per million
<b>ca.</b>	Circa	<b>PPO</b>	Polypropyleneoxide
<b>CB</b>	Conduction band	<b>p/p<sub>0</sub></b>	Relative pressure
<b>CTMABr</b>	Cetyltrimethylammoniumbromide	<b>Ref.</b>	Reference
<b>DSC</b>	Differential scanning calorimetric	<b>ROS</b>	Reactive oxygen species
<b>DRS</b>	Diffuse reflectancespectroscopy	<b>SAXS</b>	Small Angle X-ray Scattering
<b>e<sub>CB</sub><sup>-</sup></b>	Conduction band electron	<b>SBA</b>	University of California Santa Barbara
<b>EDTA</b>	Ethylenediaminetetraaceticacid	<b>SEM</b>	Scanning electron microscopy
<b>E<sub>g</sub></b>	Band gapenergy	<b>TEM</b>	Transmission electron microscopy
<b>e.g.</b>	“Exempli gratia”, fore xample	<b>TEOS</b>	Tetraethylorthosilicate
<b>ESI</b>	Electro spray ionization	<b>TG</b>	Thermo gravimetric
<b>F-127</b>	Pluronic-127, poly(ethyleneoxide) poly(propyleneoxide)poly(ethyleneoxide) (EO106PO70EO106)	<b>TMB</b>	Trimethylbenzene
<b>FDU</b>	Fudan University (Shanghai, China), type of mesoporous molecular sieve	<b>TOF-MS</b>	Time-of-flight mass spectrometry
<b>hcp</b>	Hexagonal close packed	<b>TOC</b>	Total organic carbon
<b>h/hr</b>	Hour	<b>UV</b>	Ultraviolet
<b>h<sup>+</sup></b>	Valence band holes	<b>UV-Vis</b>	Ultraviolet–visible
<b>IBP</b>	Ibuprofen	<b>V</b>	Volume
<b>IUPAC</b>	International Union of Pure and Applied Chemistry	<b>VB</b>	Valence band
<b>KIT</b>	Korea Advance Institute of Science and Technology, type of mesoporous molecular sieve	<b>V<sub>p</sub></b>	Pore volume
<b>MCM</b>	Mobile Composition of Matter, Ordered mesoporous molecular sieve	<b>vs.</b>	Versus
<b>mpg-C<sub>3</sub>N<sub>4</sub></b>	Mesoporous polymeric graphitic carbon nitride	<b>Wt%</b>	Weight percent
<b>NLDFT</b>	Non-local density functional theory	<b>SSA</b>	Specific surface area

# 1. Goals and Objectives

## 1.1.Goals

- 1- Removal of low concentrated organic and pharmaceutical pollutants from contaminated water by solid state semiconductor photocatalyst for drinking water supply,
- 2- Improvement of photocatalytic performance of ZnO, TiO<sub>2</sub> and  $\beta$ -AgVO<sub>3</sub>/mpg-C<sub>3</sub>N<sub>4</sub> Core Shell catalyst by hierarchical structuring with mesoporous silica to improved accessibility and mass transfer,
- 3- Preparation of composite and of complex advanced inorganic composite nanomaterial (ACIN) photocatalysts by mechano-chemical solvent free synthesis, and
- 4- Testing under reliable (practical) conditions as low pollutant concentration , low catalyst to substrate ratio (use of low catalyst amount), sun light equivalent radiation power instead of higher power UV light irradiation, use of low intense visible light (room light lamps).

## 1.2.Objectives

This study focuses on preparation and characterization of the supported visible light active photocatalysts, and their detailed investigation of UV/Vis photocatalytic performance. The main objectives are:

- Synthesis and characterization of mesoporous silica with tuned porosity for supports,
- Development of visible light active photocatalytic materials based on mesoporous carbon nitrides and silver vanadate,
- Development of supported photocatalysts based on mesoporous supports and photocatalysts such as Zinc Oxide, Titania and visible light active  $\beta$ -AgVO<sub>3</sub>/mpg-C<sub>3</sub>N<sub>4</sub>, and testing of the supported catalyst for possible photocatalytic potential, such as ( $\beta$ -AgVO<sub>3</sub>/mpg-C<sub>3</sub>N<sub>4</sub>)/mesoporous silica,
- Detailed investigation of the photocatalytic abatement and degradation of pharmaceutical organics such as ibuprofen, at low concentration and low irradiation power and detecting the formation of intermediates,
- The contribution of active species valence band holes (h<sup>+</sup>), hydroxyl (<sup>•</sup>OH) and superoxide (O<sub>2</sub><sup>•-</sup>)/hydroperoxyl (<sup>•</sup>OOH) radicals) to the photocatalytic degradation of contaminants has been studied by the addition of the scavengers EDTA (h<sup>+</sup>), *t*-BuOH (<sup>•</sup>OH), and 1,4-BQ (O<sub>2</sub><sup>•-</sup> or <sup>•</sup>OOH), and

- Comparison of the photocatalytic performance of  $\beta$ -AgVO<sub>3</sub>/mpg-C<sub>3</sub>N<sub>4</sub>) composites and of complex  $\beta$ -AgVO<sub>3</sub>/mpg-C<sub>3</sub>N<sub>4</sub>/mesoporous silica photocatalysts with that of ZnO and titania as well as ZnO and titania /mesoporous silica composite photocatalysts.

### 1.3.Approach

- Catalyst preparation, characterization and photocatalytic testing,
- Synthesis of mesoporous graphitic carbon nitride with the help of soft templates thermal polymerization at 600°C,
- Physical mixing and milling of beta silver vanadate and mesoporous graphitic carbon nitride resulting with different percentage of AgVO<sub>3</sub>/mpg-C<sub>3</sub>N<sub>4</sub> composite visible light active photocatalysts,
- Preparation of mesoporous silica with tuned porosity from small pores to large pores with 1D, 2D and 3D pores system, such as SBA-12, SBA- 16, FDU-12, KIT-6, MCM-41, and MCM-48,
- Physically mixing, milling and thermally treating of photocatalysts with mesoporous silica in different percentage ratios tuning for best photocatalytic activity, such as
  - ZnO/mesoporous silica materials
  - TiO<sub>2</sub>/mesoporous silica materials
  - (AgVO<sub>3</sub>/mpg-C<sub>3</sub>N<sub>4</sub>)/mesoporous silica materials
- Detailed study of the photocatalytic performance of each composite photocatalyst in photocatalytic degradation of Ibuprofen (IBP), under practical and reliable conditions (low concentration of substrate and low ratio of catalyst to substrate) with sunlight equivalent UV/Vis radiation.

## 2. Introduction

### 2.1. General

The remediation of hazardous organic contaminants from polluted drinking water is highly required to reduce indirect or direct health problems. <sup>[1]</sup> Among various pollutants, organic compounds like pharmaceuticals, dyes containing aromatic hydrocarbons (aromatic rings) have impacted seriously on natural ecosystems and public health. <sup>[2,3]</sup> These hazardous compounds often contain aromatic hydrocarbon units and may have a severe impact on human's and aquatic systems in the environment. Recent investigations have shown that among others numbers of biological compounds are not eliminated in wastewater treatment and also not biodegraded in the environment. <sup>[4]</sup> Many pollutants are present in very low concentrations within the lower ppt-ppb-ng/L scale. A couple of active compounds such as antibiotics and contraceptives have extremely high biological potency even at low concentration down to the ng/day doses. They are enriched in the body and unpredictable cross effects with other hazardous low concentrated contaminations can occur. Therefore, even concentrations, which are low as 1 ng/L, can be dangerous. <sup>[5]</sup>

Mainly physical, chemical, and biological treatments are used for the removal of organic pollutants from water for drinking water production. <sup>[4,6]</sup> In the chemical treatment oxidizing chemicals as chlorine or ozone are used for the elimination of organics and colors. Due to the high costs, there are limitations for the use of these AOPs <sup>[7,8]</sup> Contrary to chemical methods in biological treatment of organic pollutants enzymes are used to degrade organic pollutants. Due to high poisonous nature and resistivity of pollutants to microbes make this procedure less active for full abatement of pollutants. <sup>[7,8]</sup> Physical treatments including conventional processes such as reverse osmosis, adsorption on activated charcoal or flocculation are unable to degrade eliminate or degrade completely but are only transferring the pollutants to secondary form which may be more dangerous than preliminary pollutants. In general with applications of these processes *ca.* 95% of these contaminants remain in the water. Pure ground water resources are limited. Reliable processes to recycle water for household, industrial and agricultural use are highly required. There is a strong need for new advanced drinking water treatment technologies based on innovative research for economic, environmentally friendly and effective water mineralization technologies to produce harmless clean water.

Beside these methods advanced oxidation processes (AOPs) are of potential for the remediation of organic pollutants. <sup>[9]</sup> Highly oxidative species are produced and utilized for

the degradation of organics. Hydroxyl radicals ( $\bullet\text{OH}$ ), super oxides ( $\bullet\text{O}_2$ ) and other species are formed and used by heterogeneous photocatalysis.<sup>[10]</sup> This process allows full mineralization of organics to  $\text{CO}_2$  and water. Low-cost materials such as  $\text{TiO}_2$  and  $\text{ZnO}$  are UV light active photocatalysts.<sup>[9]</sup>

Due to the availability of sufficient sun light and growing demand for sustainable renewable energy sources, sunlight-driven systems such as photocatalysis, photodegradation, photovoltaics etc, have been extensively studied and still under development.<sup>[5,11]</sup> Photocatalysis with solid semiconductors is considered to be an attractive and sustainable technology with high utilization potential for the degradation of water pollutants. It needs no additional chemicals, and the non-hazardous photocatalysts can be separated and re-used. Photocatalysis has been explored rapidly after the report of Fujishima and Honda for water splitting under UV radiations.<sup>[12]</sup> For the remediation of hazardous materials from polluted water, photocatalysis with semiconductors has been investigated with much attention.<sup>[5]</sup> Photocatalysis is non-selective which can decompose a broad range of organic moieties such as alkenes, phenolic compounds, aromatics, organic acids and amines and also inorganic compounds. Especially cyanide or nitrite can be degraded. Suitable possible applications are in low concentration range.

Semiconducting metal oxides such as specially  $\text{ZnO}$  and  $\text{TiO}_2$  are potential photocatalysts for the remediation of drinking water from organic pollutants. They are available, not poisonous, environmental benign and not soluble in water and stable ( $\text{ZnO}$  is less stable). But still low efficiency due to the low quantum efficiency and small spectral range of light sensitivity i.e., in UV range. Other systems like  $\text{CdS}$ ,  $\text{ZnS}$ ,  $\text{SnO}_2$ ,  $\text{Fe}_2\text{O}_3$ ,  $\text{BiPO}_4$ ,  $\text{BiWO}_3$  and  $\text{WO}_3$  in part hazardous, less stable or show much lower activity. Carbon nitride is new visible active photocatalytic material for water remediation, but its photocatalytic activity is still not sufficient even the activity might be larger than that of tungsten containing materials. This challenge requires the improvement of available photocatalysts and the development and searching for new photocatalytic materials.<sup>[13]</sup> Therefore this study focuses  $\text{CN}$ ,  $\text{TiO}_2$ ,  $\text{ZnO}$ , Supporting in mesoporous silica involving benign available and stable,  $\text{ZnO}$  less stable because other system poisonous. Therefore this study focuses on development of visible light activity photocatalytic materials. Specifically this work aims to prepare hierarchical structured  $\beta\text{-AgVO}_3/\text{mpg-C}_3\text{N}_4$  Core Shell photocatalytic structures by solvent-free mechano-chemical method and to compare it with commercial  $\text{TiO}_2$ ,  $\text{ZnO}$  photocatalysts which catalytic performance was also improved by supporting on mesoporous materials.

The study is not only concentrated to binary system but is extended to the ternary system  $\beta$ -AgVO<sub>3</sub>/mpg-C<sub>3</sub>N<sub>4</sub>/SiO<sub>2</sub> composite nanoparticles, with large specific surface area, which are synthesized by the application of a solid state mechano-chemical mixing of  $\beta$ -AgVO<sub>3</sub>/mpg-C<sub>3</sub>N<sub>4</sub> or ZnO and TiO<sub>2</sub> with mesoporous silica. It will be shown that mesoporous silica supports markedly enhance the dispersion and, therefore, accessibility of the catalytic component. The photocatalytic activity of the synthesized nanoparticles was evaluated in the photodegradation of Ibuprofen (as a model for pollutants in wastewater). Attention has focused on the decomposition and mineralization of IBP at low concentration at low catalyst to substrate ratio of 4, with room light active visible irradiations or low UV irradiations. The contribution of active species and formation of by-products, the formation of intermediates during the photocatalytic treatment was thoroughly studied. Obtained Core Shell and composite materials were characterized by XRD, SEM, TEM, SAXS, EDX, UV/Vis/DRS, and BET analysis.

## 2.2.State-of-The-Art

**Water Treatment:** The problem of emerging hazardous pollutants in water is very dangerous even they occur in very low concentrations. The development of new technologies for the removal of these contaminations is a new challenge. Pharmaceuticals often appear in lower (lower ppm to ppb) concentrations and were detected even in ground and drinking water.<sup>[14]</sup> Conventional water treatment systems are not able to remove these contaminants sufficiently by applying biological treatment and adsorption on active carbon.<sup>[4, 6-8]</sup> There is a lack of knowledge about treatment of such low concentrations and the behaviour of small concentrated solutions regarding adsorption and mineralization.<sup>[5]</sup> Some methods for oxidative decomposition of organic compounds like pharmaceutical are available such as ozonation, chlorination, oxidation with H<sub>2</sub>O<sub>2</sub>. However, they require often chemicals, soluble homogeneous catalysts and they are less eco-friendly. New advanced oxidation processes (AOP) are required to address this problem.<sup>[9-15]</sup>

Advanced oxidation processes (AOPs) with the use of high oxidation potential species such as, hydroxyl radicals ( $\bullet$ OH), superoxide ( $\bullet$ O<sub>2</sub>) and other species allows full mineralization of organics to CO<sub>2</sub> and water.<sup>[16]</sup> Low-cost materials such as TiO<sub>2</sub> and ZnO are active photocatalysts with relative high chemical stability. However, the titania and zinc oxide photocatalysts suffer from efficiency due to low quantum yield, charge separation and limited use of the spectral range of the sunlight which is limited to the UV part. New available carbon

nitride based photocatalysts show visible light response but suffer from photocatalytic activity.

**Materials:** The visible light response of titania could be improved by doping with metals (e.g. Ni, Co, Ga, Ta, Cr, V, Mn, Fe, Mo, W, Ru, Pt, and non-metals (e.g. B, C, N, S, O, P, F)).<sup>[5,1718]</sup> But for practical application still further improvement is required.

Several other materials for example BiOCl, AgVO<sub>3</sub>, TaON, Ta<sub>3</sub>N<sub>5</sub>,<sup>[19]</sup> CaBi<sub>6</sub>O<sub>10</sub>,<sup>[20]</sup> Sr<sub>0.25</sub>Bi<sub>0.75</sub>O<sub>1.36</sub>,<sup>[21]</sup> Ag<sub>3</sub>PO<sub>4</sub>,<sup>[22]</sup> BiVO<sub>4</sub>,<sup>[23]</sup> or polymeric carbon nitride C<sub>3</sub>N<sub>4</sub> are shown to be visible light active photocatalysts for the degradation of organic pollutants. But still these photocatalysts suffer from rapid recombination of photo-generated electron-hole pairs resulting in low photocatalytic activity. Because of the unique electronic structure, the g-C<sub>3</sub>N<sub>4</sub> could act as a candidate for coupling with various functional materials to enhance the performance. A couple of composite catalysts based on the g-C<sub>3</sub>N<sub>4</sub>/single metal oxide (metal sulfide) heterojunction, the g-C<sub>3</sub>N<sub>4</sub>/halide hetero junction, g-C<sub>3</sub>N<sub>4</sub>/composite oxide, g-C<sub>3</sub>N<sub>4</sub>/noble metal hetero structures, the g-C<sub>3</sub>N<sub>4</sub> based metal-free hetero junction and the g-C<sub>3</sub>N<sub>4</sub> based complex system have been prepared and investigated in order to further increase the activity of the mesoporous graphitic nitrides mpg-C<sub>3</sub>N<sub>4</sub>. Core Shell Ag / C<sub>3</sub>N<sub>4</sub>,<sup>[24]</sup> binary C<sub>3</sub>N<sub>4</sub> / Ag<sub>3</sub>VO<sub>4</sub>,<sup>[25]</sup> Ag<sub>3</sub>PO<sub>4</sub>/C<sub>3</sub>N<sub>4</sub>,<sup>[26]</sup> AgX / C<sub>3</sub>N<sub>4</sub>,<sup>[27]</sup> SmVO<sub>4</sub> / C<sub>3</sub>N<sub>4</sub>,<sup>[28]</sup> t-LaVO<sub>4</sub> / C<sub>3</sub>N<sub>4</sub>, m-LaVO<sub>4</sub> / C<sub>3</sub>N<sub>4</sub>,<sup>[29]</sup> and ternary systems such as Ag/Ag<sub>3</sub>PO<sub>4</sub>/g-C<sub>3</sub>N<sub>4</sub>,<sup>[30]</sup> Ag / AgVO<sub>3</sub> / C<sub>3</sub>N<sub>4</sub>,<sup>[31]</sup> g-C<sub>3</sub>N<sub>4</sub> / Ag / TiO<sub>2</sub>,<sup>[32]</sup> with low carbon nitride loading. However improvements achieved with carbon nitride composites are still not sufficient for visible light application. These materials contain large amounts of expensive noble metals and resulted with low atomic efficiency and complicated preparation methods.

Different types of silica containing composite materials are reported which are prepared by sol-gel, impregnation or co-precipitation methods such as ZnO-SiO<sub>2</sub>, TiO<sub>2</sub>-SiO<sub>2</sub>, CrO<sub>3</sub>/TiO<sub>2</sub>-SiO<sub>2</sub>, V<sub>2</sub>O<sub>5</sub>/TiO<sub>2</sub>-SiO<sub>2</sub>, Rh/TiO<sub>2</sub>-SiO<sub>2</sub>, Ni/TiO<sub>2</sub>-SiO<sub>2</sub>.<sup>[33]</sup> Most of them are nonporous. Impregnated mesoporous silica often show low activity.<sup>[34]</sup> Ordered mesoporous silica carbon nitrate composites with a variety of different mesoporous silica structures were not reported to our knowledge. Mostly such materials are used as heterogeneous catalysts in different types of organic synthetic reactions.<sup>[35]</sup> Some reports have shown increased photocatalytic efficiency of these supported catalysts compared to the single photocatalysts.<sup>[36]</sup> However these materials are embedded in non-active silica which hinders irradiations to active photocatalytic sites. Great efforts are devoted to improve the charge separation (electron-hole pairs).<sup>[14]</sup> Metallic or non-metallic doping and supporting metal nanoparticles are used to

reduce recombination.<sup>[16,37]</sup> Metallic nanoparticles have lower Fermi energy than that of the semiconductors, resulting in electron capturing via Schottky-contact.

**Reaction conditions:** Most of these studies are focussed on the easier decolourization of dyes such as methyl orange, methyl blue and rhodamine B while much less attention has focused on the decomposition and mineralization of recalcitrant materials such as pharmaceuticals in low concentrations. Often huge amount of catalysts are used to decompose small amounts of pollutants (catalyst to substrate mass ratio *ca.* 100). Further there is a lack of practical and reliable conditions for photocatalytic testing. Mostly huge catalyst to substrate ratio is used. And the power of irradiations is mostly higher above 300 watt lamps. So a quick reaction is needed to understand completely the photocatalysis in low concentration, low catalyst to substrate ratio and low irradiation power. Supporting catalysis is one of the phenomena to improve the dispersion of the active photocatalysts sites. Supporting catalysts will prove to be easily recovered and purification. Recycling of the materials will be easy, economical and environmentally friendly, resulting in saving energy and materials. Supporting catalysts will improve the transferring of active species to the surface of photocatalysts which results in reducing charge recombination and improved photocatalysis. Supporting photocatalysts will help in increasing the efficiency with respect to single ingredients. Composite formation has shown an important strategy to reduce the charge carrier combination of active semiconductors. The photo excited electrons are transferred from semiconductors to 2D carbon containing materials.<sup>[38]</sup>

## 2.3. Theoretical Background

### 2.3.1 Solid State Semiconductor

The transfer of electrons from an electron donor (reductant) to an electron acceptor (oxidant) is known as oxidation. In oxidation processes using oxidants used species may be radicals, having high reactive unpaired electron which can initiate oxidation reactions. The strength of an oxidant is related its oxidation potential. Some well-known oxidants are hydroxyl radicals ( $\bullet\text{OH}$ , 2.70 eV), ozone ( $\text{O}_3$ , 2.07 eV), fluorine (F, 2.85 eV), and chlorine (Cl, 1.49 eV).<sup>[39]</sup>

Advanced oxidation processes for the degradation of organic pollutants in water often use species such as ozone ( $\text{O}_3$ ),  $\text{O}_3/\text{H}_2\text{O}_2$ , UV,  $\text{O}_3/\text{UV}$ ,  $\text{UV}/\text{H}_2\text{O}_2$ , and  $\text{O}_3/\text{UV}/\text{H}_2\text{O}_2$ .<sup>[40]</sup> In case of photocatalysis so called reactive oxidative species (ROS) as hydroxyl radicals ( $\text{OH}\bullet$ ), hydroperoxyl radicals ( $\bullet\text{OOH}$ ) and Super oxide (oxygen radical anions) ( $\text{O}_2^{\bullet-}$ ) are involved in the oxidation process, which are formed in situ by the photocatalyst. Photocatalysis differ

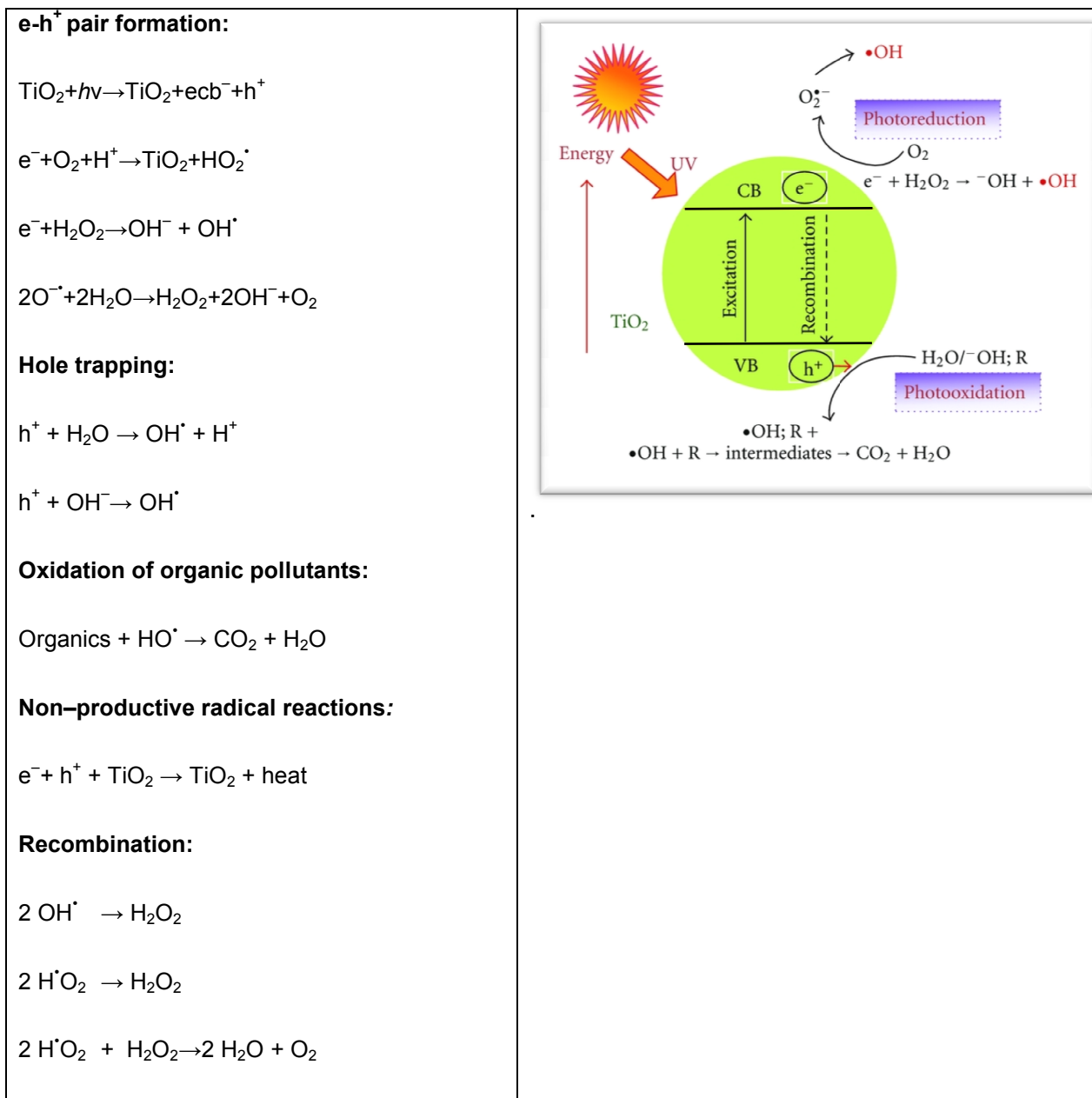
from other AOPs by the use of semiconductors and light energy instead of external expensive oxidants such as  $\text{H}_2\text{O}_2$  and  $\text{O}_3$  (Esplugas et al., 2002). The effectiveness of the AOPs is related to the formation of a high number of hydroxyl radicals and highly active electron holes  $\text{h}^+$ . Total mineralization of organic compounds is achieved by complete oxidation to carbon dioxide and water at the end of treatment. <sup>[41]</sup>

According to Herrmann, <sup>[42]</sup> the photocatalytic degradation of pollutants proceeds in 5 steps:

- 1– Mass transfer of reactants (contaminants) to the catalyst surface,
- 2– Adsorption of the reactants on the catalyst surface,
- 3– Photochemical reaction on the surface,
- 4– Desorption of the reaction products from the surface,
- 5– Mass transfer of the photocatalytic oxidation products from the catalyst surface into the fluid.

### **2.3.2 General Mechanism of the Photocatalytic Process:**

The electronic band structure of semiconductor materials consists of two bands. Highest occupied energy band denoted as valence band (VB) consists of electrons available while lowest unoccupied band are denoted as conduction band (CB). The energy difference between the VB and the CB is called band gap energy ( $E_g$ ) of the semiconductor. The excitation of a VB electron to the conduction band leads to the formation of holes in valence band and accumulation of electrons occurs in the conduction band. The whole process proceeds in three steps: i) photo excitation of charge carriers (electrons), (ii) charge carrier separation (formation of electron hole pairs ( $\text{e}^- - \text{h}^+$ ) and its diffusion/migration to the photocatalyst surface; and (iii) the reaction of electrons and holes with adsorbed electron acceptors and donors. <sup>[20,43]</sup> Thereby, ROS are formed and organic molecules are oxidized or reduced. General reaction mechanisms are formulated as below in scheme 1.



**Scheme 1:** Photocatalytic reaction mechanism.<sup>[16]</sup>

Formed CB electrons and VB holes react with adsorbed organic species, water or dissolved oxygen in contact to the surface of the particle, resulting in the formation hydroxyl radical (•OH), hydro peroxy or superoxide radicals, hydrogen peroxide, organic oxidation products and others.<sup>[44]</sup>To achieve photocatalytic degradation of organic compounds by oxidation, the valence band (VB) and conduction band (CB) edge positions of semiconductors should be located in such a way that the redox potential of reacting molecule, e.g. water, oxygen or other organic molecules are located within the band gap of the VB and CB of the semiconductor (Fig. 1).<sup>[16]</sup>In other words to oxidize an organic substrate, its redox potential must be negative than the redox level of the photo generated hole, in result reducing the h<sup>+</sup> and itself converting to organic cat ion. If the consecutive reactions of organic cat ion are

faster than electron accepting, substrate proceeds to product formations. Mean while if water adsorbs or reduces the hole, it changes in  $\text{HO}^\bullet$  and or  $\text{OH}^-$  ions followed by oxidation of organic moieties. The electron is taken up by an oxidizing agent, normally the adsorbed oxygen. The charge separation efficiency, i.e. the formation of lasting  $e^- - h^+$  pairs, can be diminished by recombination of photo generated charge carriers and results in release of energy in form of heat or luminescence. Either excited electrons  $e^-$  jump back into VB holes ( $h^+$ ) directly or are trapped in crystal defect sites.<sup>[45]</sup>

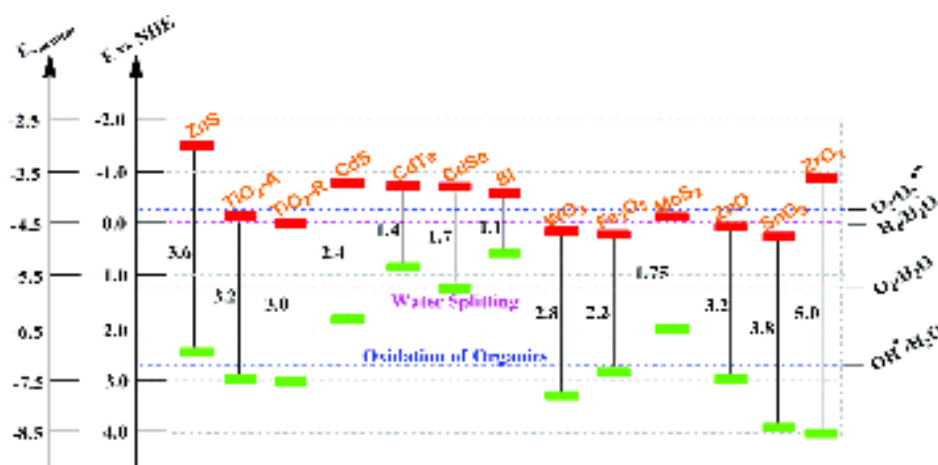
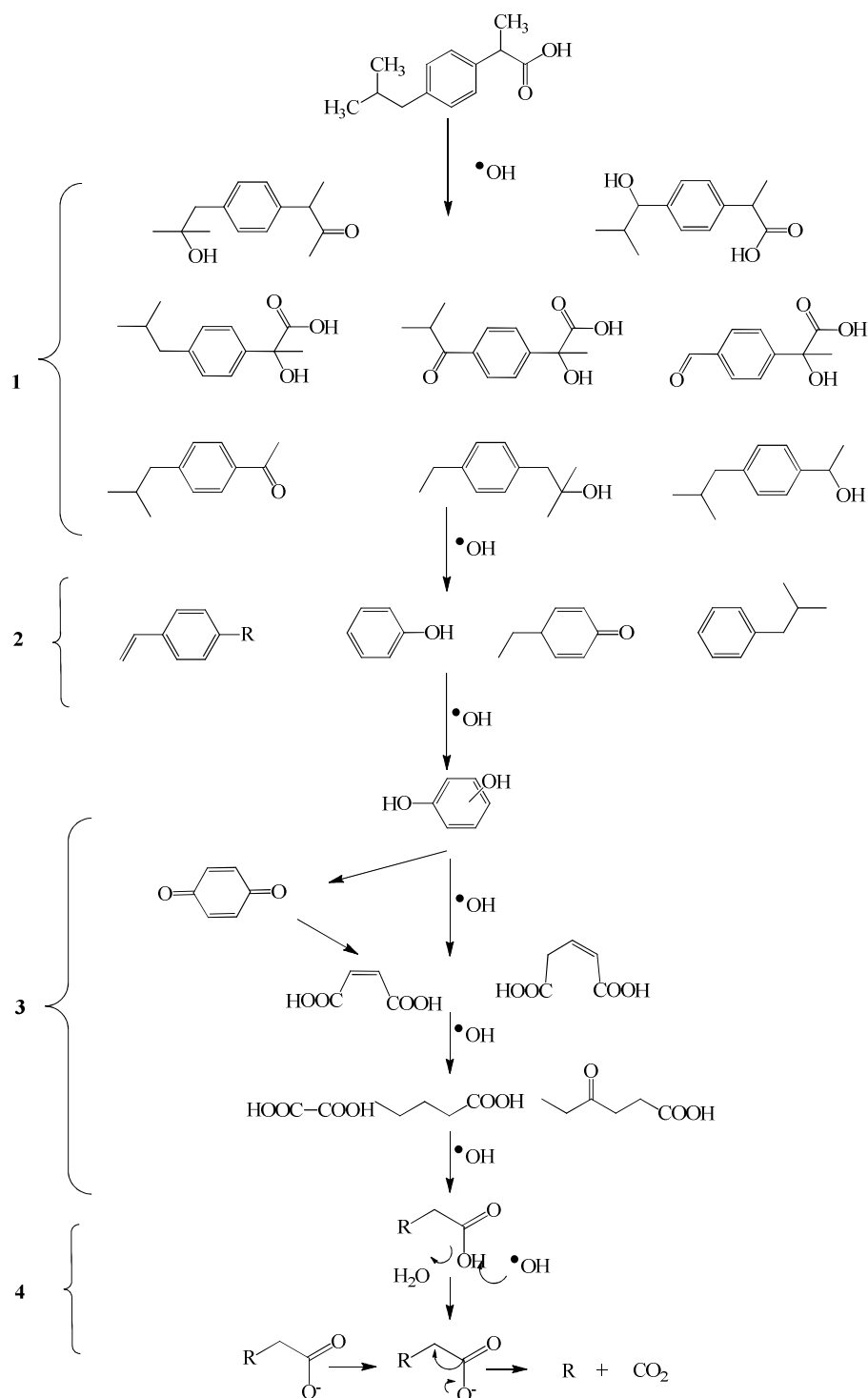


**Figure 1:** Band gaps and band edge positions of some semiconductor photocatalysts on a potential scale (V) versus the normal hydrogen electrode (NHE) at pH= 0.<sup>[46]</sup>

### 2.3.3 General Course of the Photocatalytic Degradation



**Scheme 2 :** Formation of (1) side chain products and (2) deep oxidation products, (3) aromatic ring opening of phenol and (4) decarboxylation as intermediate during the photocatalytic degradation of ibuprofen.<sup>[47,38e]</sup>

Usually, the photocatalytic degradation of organic pollutants proceeds in three main steps, the formation of different side chain products via hydroxylation (partial oxidation) and/or demethylation, the hydroxylation of the phenyl group and the following aromatic ring

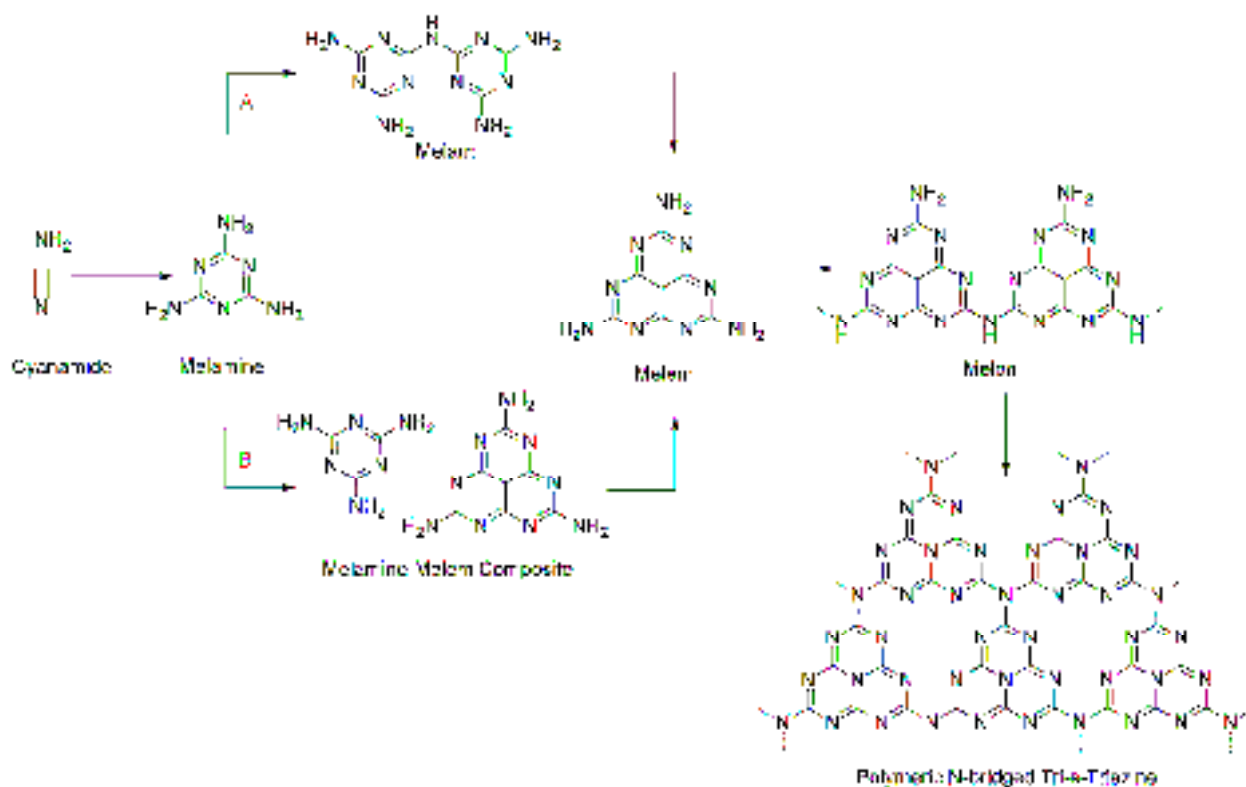
opening, and the oxidative decarboxylation of intermediate carboxylic acids which ends up in the total mineralization to carbon dioxide (Kolbe-reaction) and water.<sup>[30-31]</sup> Systematically an example of ibuprofen as a modal pollutant consisting of single phenyl ring is discussed below in Scheme 2.

## **2.4. Description of used Photocatalytic Materials and Mesoporous Supports**

Here i will review the own prepared materials corresponding of this thesis, *i.e.* photocatalysts, mesoporous materials and composite photocatalysts. In addition, the standpoint (view point) of this work will be described.

### **2.4.1 Polymeric Graphitic Carbon Nitrides ( $g-C_3N_4$ )**

Polymeric graphitic carbon nitride is an inorganic polymer consisting of a network of C and N atoms and is generally denoted as ( $g-C_3N_4$ ).  $g-C_3N_4$  is a potential material for the remediation of hazardous organic pollutants. Due to its band gap (2.69 eV) in the visible-light range, chemical stability, high thermal, electrical conductivity, and synthesis from less expensive available starting materials it a promising photocatalyst.<sup>[48]</sup> But its use is limited due to the fast recombination rate of its photo generated electron- hole pairs.<sup>[9,10]</sup> Therefore, the first generation of carbon nitrides are subjected to modification with different techniques, out of which chemical functionalization with different functionalities such as aldehydes, ketones and acids are mentionable. Designing suitable porosity, texture with soft and hard template has improved the photocatalytic activity to greater extent. Doping and coupling  $g-C_3N_4$  with metals, etc., is another approach developed so far for enhancing photocatalytic capacity.<sup>[35, 41]</sup>



**Scheme 3** : Reaction Pathway for synthesis of carbon nitride C<sub>3</sub>N<sub>4</sub>.<sup>[50]</sup>

Structurally, graphitic carbon nitrides are related to 2D sheets-like graphenes, containing alternating carbon-nitrogen atoms with sp<sup>2</sup> hybridization. Sheets are stacked together with  $\pi$ -conjugation. Precursors such as cyanamide, dicyanamide, urea, melamine and different types of C to N ration containing molecules are used for the synthesis of carbon nitrides.<sup>[49]</sup> In brief precursor materials undergo condensation and rapid transform to a melamine (Scheme. 3), which transforms to melem under heating. Two pathways are predicted to happen to reach thermal polymerization. Via Path A, melamine dimerizes to melam, with release of a single ammonia molecule.<sup>[36]</sup> While via path B, melamine forms melamine-melem composites at 350-400°C. Both the intermediates further condensate the melem. On further heating above 600°C, melem polymerize for the formation of melon, which quickly further thermally polymerize to polymeric N-bridged tri-s-triazine.<sup>[50]</sup> Usually, soft templates such as surfactants and block polymers are used for the synthesis of mesoporous g-C<sub>3</sub>N<sub>4</sub>.<sup>[51]</sup> Programmed thermal treatment removes the soft templates materials, while subjecting controlled mesoporosity in resultant polymeric species.<sup>[52]</sup> Hard templates produce high surface area and porosity but are more difficult to remove.<sup>[53]</sup> Soft templates can be easy removed and are suitable for the synthesis of microporous g-C<sub>3</sub>N<sub>4</sub> materials.

### 2.4.2 Silver Vanadate ( $\beta$ -AgVO<sub>3</sub>)

AgVO<sub>3</sub> with band energy of about 1.9 eV is a visible-light active photocatalytic material but its activity is not sufficient due to fast recombination and low capacity of  $e^-h^+$  pair separation (the intrinsic optical properties of ternary metal-oxide photocatalysts with low band gap energies, they are able to absorb a wide range of visible light. In addition, the mobility of photo-generated charges was also improved, attributed to the incorporation of various elements in ternary metal oxides, thus preventing electron-hole recombination via charge-separation mechanisms).<sup>[54]</sup>



**Figure 2:** Solid state structure of  $\alpha$ -AgVO<sub>3</sub> and  $\beta$ -AgVO<sub>3</sub>.<sup>[55]</sup>

Typically silver vanadate with formula of AgVO<sub>3</sub> has three crystallographic forms,  $\alpha$ -AgVO<sub>3</sub>,  $\beta$ -AgVO<sub>3</sub> and  $\gamma$ -AgVO<sub>3</sub> shown in Figure 2.<sup>[56]</sup> Alpha form is dynamic and metastable and converts into stable beta form even at temperature near to 200°C, while gamma form requires high thermal treatment. Out of different phases of silver vanadates, beta form is a highly studied in photocatalysis. Beta silver vanadates consists of a 3D network of [V<sub>4</sub>O<sub>12</sub>]<sub>n</sub> double chains, which are linked together with AgO<sub>6</sub> octahedral with interconnected Ag<sub>2</sub>O<sub>5</sub> and Ag<sub>3</sub>O<sub>5</sub> square pyramids (Fig. 2). It is synthesized by precipitation from salt solutions. Silver vanadates (Ag<sub>3</sub>VO<sub>4</sub>, Ag<sub>4</sub>V<sub>2</sub>O<sub>7</sub>,  $\alpha$ -AgVO<sub>3</sub>, and  $\beta$ -AgVO<sub>3</sub>,) were used for the investigation of photocatalytic evolution of O<sub>2</sub>.<sup>[44d,57]</sup> Due to the availability of more positive valence band than the O<sub>2</sub>/H<sub>2</sub>O potential level (1.23 V vs. SHE, pH=0), silver vanadate has oxidizing potential.

## 2.5. Porous Materials

Porosity as variable pores, pore arrangement, pore diameters, pore volume and particle sizes have an important influence and allow to tune material properties regarding application in the

field of sensors, electrochemistry, catalysis, gas storage etc. and allow Materials with variable pores, pores arrangement, pores diameters, pores volume and particle sizes This has have strongly encouraged the synthesis, characterization and applications of porous materials. Modification of the pores materials surface with inorganic and organic functionalities leads to new and developed applications.

**Definition and Classification of Porous Materials:** Porous materials either natural or synthetic have isolated or interconnected porosity. Usually porosity is emerged in the process of crystallization or by following treatments. Pores can be cylindrical, ink-bottled, slit shaped or more zigzag disordered. Depending on the pore size, porous materials are classified according to IUPAC nomenclature as micro porous, mesoporous and macro porous.<sup>[58]</sup>

- Microporous materials have pore diameter below 2 nm.
- Mesoporous materials have pore diameter between 2 and 50 nm.
- Macroporous materials have pore diameters above 50 nm.

Porosity is more defined as ratios of pore and void volumes compared to the total volume of solid materials. Therefore, porous materials are additional classified by its adsorption stuffs, the adsorption and desorption isotherms of test molecules like nitrogen of Ar. and others, They allow to extract relations between porosity and sorption and are classified into six types typically observed with materials containing different sized pores as shown in (Fig. 3):

Type I	Micro porous materials,
Type II, III, VI	Non porous or macro porous materials,
Type IV, V	Mesoporous materials.

Shape and hysteresis loops in the isotherms define the nature of the materials with respect to its pore size distribution, geometry and connectivity. According to IUPAC hysteresis are classified into 4 types denoted with H's as shown in (Fig. 4). H1 type is associated with cylindrical pores whereby H2 types are associated with bottle neck type materials. H3 types are normally slit shaped pores or aggregates with plate-like particles. H4 is also associated with narrow slit pores with limited adsorption.

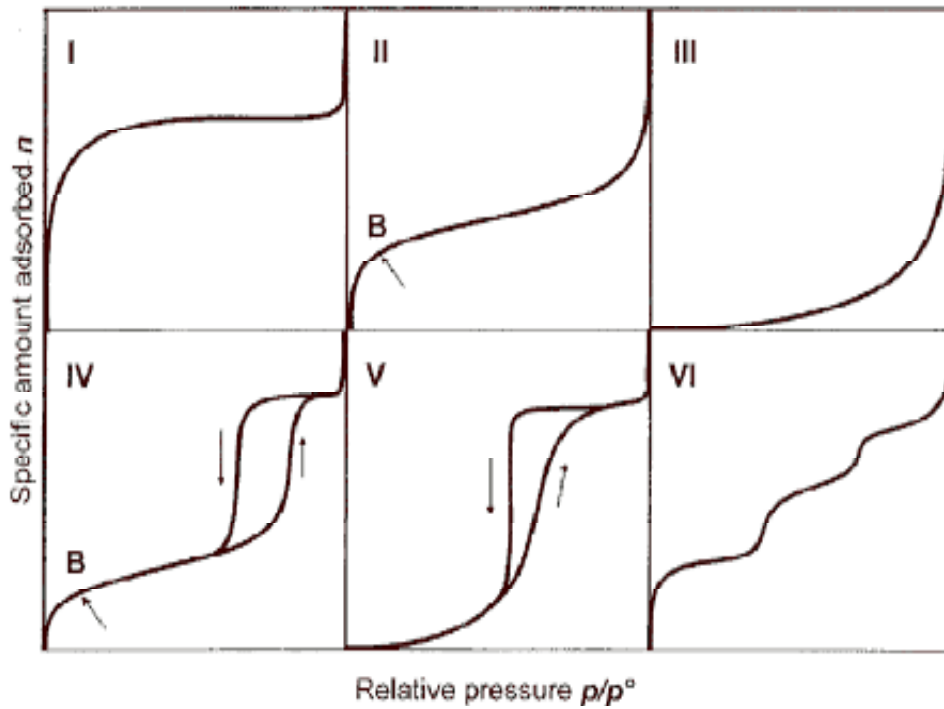


**Figure 3:** Types of adsorption isotherms according to IUPAC classification. <sup>[44,59]</sup>

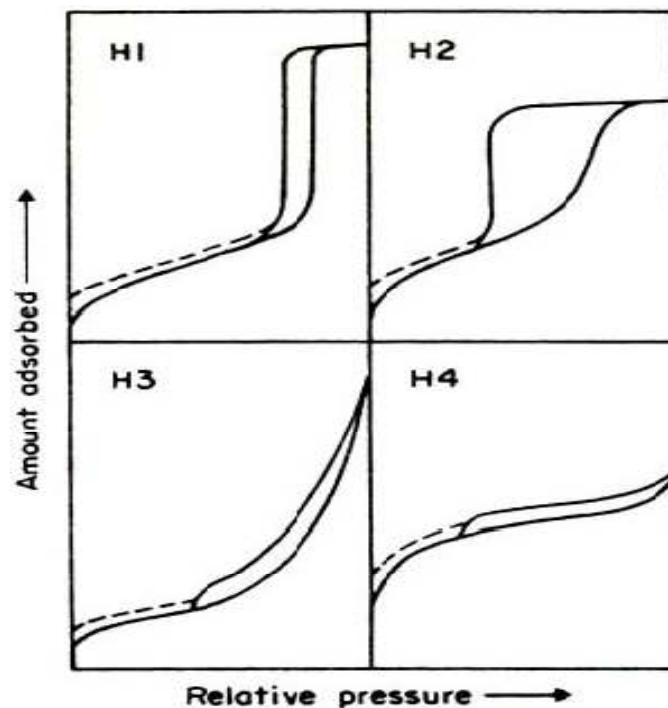


**Figure 4:** The four main types of hysteresis loops according to IUPAC classification. <sup>[60]</sup>

Mostly pores materials may be crystalline, paracrystalline or amorphous. Amorphous materials do not possess long-range order in the bulk material e.g., silica gel or alumina gel.

While zeolites are crystalline containing a well-defined pore system as a part of the crystal structure with narrow pore size distribution. Mesoporous silica can be disordered in the bulk but contain an ordered pore system embedded in the amorphous bulk. Due to the periodicity of ordered and uniform sized and shaped pores, ordered porous materials show low angle XRD reflections. These ordered materials possess narrow to broad pore size distribution, high specific surface areas and volumes, and tunable porosity. Its molecular pore sizes have potential adsorption and desorption capacity for active compounds.

### 2.5.1 Mesoporous Materials

Mesoporous materials have pore diameter between 2 and 50 nm. Before 1990 mesoporous materials were amorphous with broad distribution of pores sizes. Early in 1990 Kresge et al. announced the new family of molecular sieves. Its exceptional properties like high specific surface areas promote adsorption, separation, catalysis, and energy storage.

Strategically synthesis of ordered porous materials with high surface area, are developed with surfactant-directed synthetic procedures (Fig. 5).<sup>[61]</sup> In process of preparation ordered porous structures are directed by the assemblies of molecules due to the energetic of solutions, e.g., micelles formation. Ordered materials structurally can be altered with the help of these auxiliaries chemicals, reaction parameters, which results in families of either 1D, 2D (cylindrical pores), or 3D (interconnected cage type pores) ordered mesoporous materials. M41S family is a common example of such tunable system.

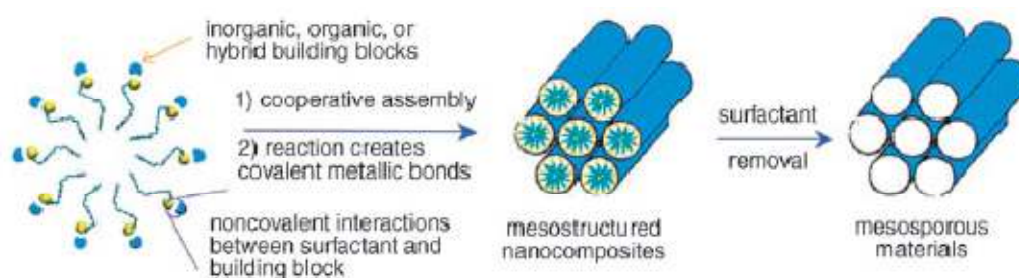


**Figure 5:** Formation pathway of hexagonal structured mesoporous silica MCM-41.<sup>[62]</sup>

Extensive research with the mentioned discovery of surfactant to surface-directed assembling of building inorganic blocks has opened new area of specific architecture and organized materials. Non covalent interactions drive this specific organization and assembling the spatial orientations of inorganic materials. Simultaneously condensation via covalent bonds among the building blocks and inorganic blocks results in mesostructured materials. Various methods are used to remove the surfactants e.g., thermal treatment, calcination, washing and acidic etching etc. These procedures have resulted in various shapes, size and pores of

mesoporous materials with hexagonal, lamellar, cubic, and other mesostructured as shown in (Fig. 6).

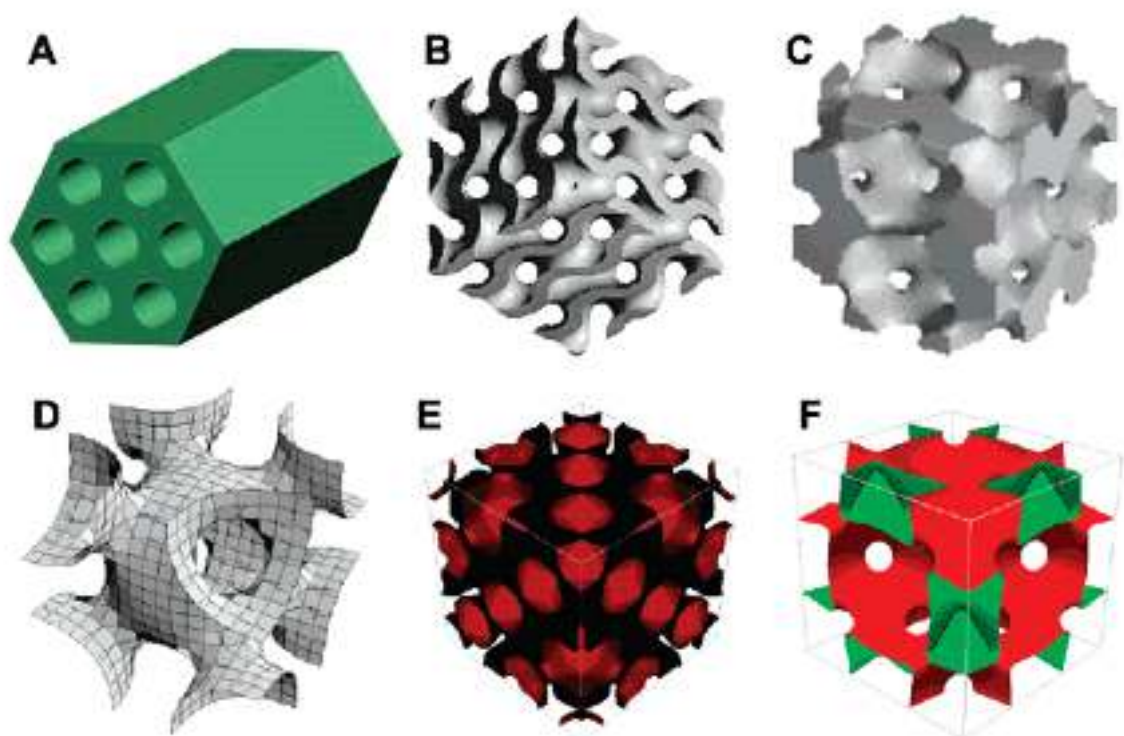


**Figure 6:** Pore models of mesostructures with different symmetries of (A) Hexagonal, (SBA-15), (B) 3D gyroidal cubic pores structured, (MCM-48), (C) Cubic, (SBA-1 and 6), (D) Cubic, 3D cage-like structure of pores, (SBA-16), (E) Cubic, (FDU-2) (F) Centered cubic closed-packing (fcc) mesostructure, (KIT-5).<sup>[63]</sup>

**Materials with Hexagonal Phases:** Normally hexagonal silica are found in 1D structures consisting of close packed cylindrical pored tubes, (e.g., MCM-41), but 2D structured SBA-15 is also reported with cylindrical pores with uniform pore diameter. MCM-41 and SBA-15 are mostly studied and representative ones and are used in this research topic.

### 2.5.2 1D Mesoporous Silica: MCM-41

MCM-41 is mesoporous silica with uniform structure and shape composed by isolated parallel channels disposed in a hexagonal packing and extendable over micrometer length scale. Pore apertures are accessible and tunable with diameter of 1.5 nm - 6.5 nm with different alkyl chain templates and additives. Micro porous MCM-41 of 1.2 nm pore size and a specific surface area of 1000 m<sup>2</sup>/g, were synthesized with C<sub>6</sub>H<sub>13</sub>N (CH<sub>3</sub>)<sub>3</sub>Br as template. Different models out of which classical molecular dynamic (CMD) simulations confirms the cylinder-like pore channels, matching the experimental XRD pattern completely. Some reports have prediction of hexagonal prism-like pore channels.<sup>[64]</sup> Powder x-rays diffractions, confirms the

quasi-regular arrangement of mesopores with strong diffraction at  $2\theta$  of about  $2^\circ$  followed by weak diffraction peaks at 2-3. At higher angles, diffractions are indexed to (100), (110), (200), and (210) planes of hexagonal symmetry. [65]

### 2.5.3 2D Mesoporous Silica: SBA-15

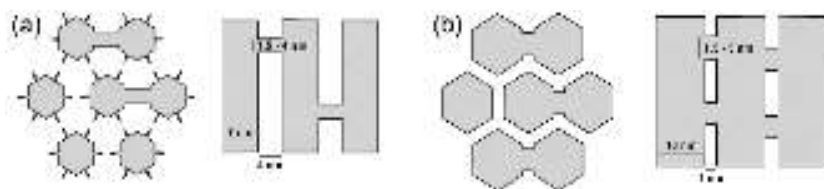


**Figure 7:** A schematic representation of SBA-15, synthesized at 80 °C (a) and 140 °C (b), respectively. [66]

Mesoporous silica sieve SBA-15 has 2D uniform hexagonal pores showing narrow pore size distribution as shown in (Fig. 7). The pore sizes are tunable within diameter range of 5-15nm. The synthesis of SBA-15 is sensitive to the temperature and wall thickness can be tailored in the range from 2.5 to 6.4nm, which gives the material a higher hydrothermal and mechanical stability compared to MCM-41. [67] As temperature increases the mesopore size increases with decrease in pore wall thickness and the amount of small micro pores (and ultra micro pores) within the pore walls. At higher temperature (100°C) 2D inter-connected pores can be produced, which results in irregular micro pores and mesopores interconnecting main hexagonal channels. The interconnected 2D uniform pores system results in the high internal surface area of typically 400–900 m<sup>2</sup>/g.

SBA-15 shows XRD pattern having a main single diffraction peak with two to three weak diffractions, proves 2D hexagonal phase system. Shifting to lower angle of the diffraction patterns confirms the larger cell parameters than MCM-41. [68]

### 2.5.4 3D Mesoporous Silica: SBA-12

SBA-12 has a partially hexagonal close packing and partially cubic structure as shown in (Fig.8). XRD peaks are usually merged together and are undistinguishable such as for (1 0 0) and (1 0 1) diffractions. TEM images confirm the presence of inter grown hcp and ccp meso structures. Also at SBA-12 structure containing large portion of cubic phase, with the cell

parameters of 8.2 nm, where each cage is connected via a small window to 12 other cages, was reported.<sup>[69]</sup> NLDFT calculations predict a diameter of ~6.1nm of spherical cages, with a wall thickness of ~1.3 nm. SBA-12 is known as more stronger and thermal stable than SBA-2 due to thick walls.<sup>[70]</sup> N<sub>2</sub> sorption study shows type-IV adsorption isotherm, with well-ordered mesopores structure.

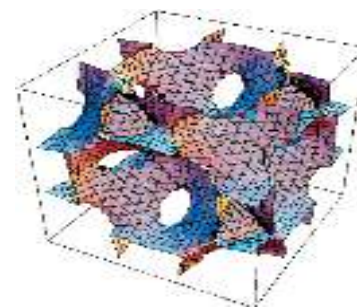


**Figure 8:** 3D structure of SBA-12.<sup>[70]</sup>

### 2.5.5 3D Mesoporous Silica: KIT-6

KIT-6 is an ordered mesoporous material with large pores, which was synthesized for first time at Korea Institute of Science and Technology. It has a similar structure as MCM-48 (Fig.9). shows similar structure of KIT-6 as MCM-48 but with the similar pore wall thickness and dimension as SBA-15.<sup>[71]</sup> KIT-6 is structured with a pair of bi-continuous interwoven cylindrical pores, of changeable diameter of 4 to 12 nm via hydrothermal synthesis temperature (25-35°C). The pores are interconnected by micro pores or small mesopores within a disordered way. It results in efficient adsorption properties. KIT-6 with its interpenetrating branched channels provides an open pore structure with fluent flow and diffusion of guest species, without pore blockage. KIT-6 shows a nitrogen adsorption isotherm of type IV which is similar to MCM-48. The micro pores of materials can be visualized using this material as hard template for nanocasting, e.g. the preparation of mesoporous carbons.

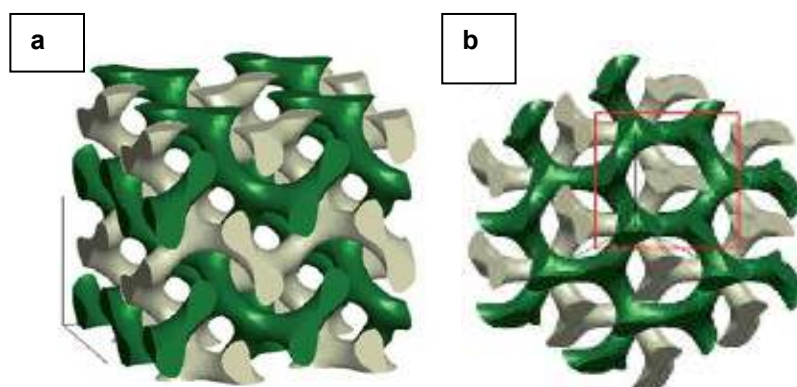


**Figure 9:** KIT-6 with interpenetrating mesoporous channels in the template (a) [111] projection of the mesostructure (b).<sup>[72]</sup>

### **2.5.6 3D Mesoporous Silica: MCM-48**

Figure.6B shows MCM-48 consists of two independent interwoven bicontinuous pore systems. The pore system is periodically arranged with large specific surface area, pore size distributions and high thermal stability. The pores are interconnected system of cylindrical pores, and the wall surface follows exactly the periodic minimal surface of gyroid. The wall separates two interpenetrating and non interconnecting channel systems with different chiralities.

MCM-48 and KIT-6 are 3D gyroid structured cubic pores materials. [73] Eight stronger XRD diffraction patterns are reported. Peaks are indexed to cubic mesostructure of the MCM-48. Cubic structure is simulated from TEM images and electron crystallography method. Results confirm the similarity of TEM images from different direction to simulated ones. [74]

### **2.5.7 3D Mesoporous Silica: SBA-16 and FDU-12**

SBA-16 comprises a well-structured 3D, body-centered cubic, is discussed as stacked sphere-like cages. [75] XRD of SBA-16 studies show 3 identifiable diffraction peaks at 2 theta 1-1.4°. Main peak below 1° is assigned (1 1 0), while other 2 small peaks are identified as (2 0 0) and (2 1 1) respectively. [76] These are followed by several weak peaks in range of 1.4°-2.4°. N<sub>2</sub> sorption analysis shows isotherm of type IV, with H2 type hysteresis loop, which confirms cage-like pores materials. NLDFT calculations diameters of the cage as ~8.5 nm, and pore wall thickness of ~5.9nm. Electron crystallography studies propose the interconnected mesopores are arranged one to eight, of spherical body-centered nanocages with cubic arrangement, wherein each spheres connected to eight neighboring spheres(Fig.10a). Which confirms the pore entrance from one mesopore to another smaller than the primary mesopore size. This makes hard to obtain the pore entrance size correctly.

In contrast FDU-12 has a face-centered cubic structure with same pores system of interconnectivity. [77] In FDU-12 each spherical nanocage is coordinated with 12 neighboring cages (Fig10b) which is more in number than SBA-16. Normally similar templates such as pluronic F127 series are used which results in similar pore sizes. In case of FDU- 12, it is easy to increase pore size up to 27 nm with hydrothermal treatment at 15 °C. Size of entrance pore joining two cavities can be adjusted from 4-9 nm in diameter, with aging temperature from 100 to 140 °C.

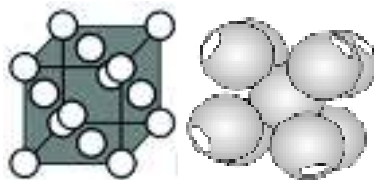


**Figure 10:** 3D structure of FDU-12 (left) and SBA-16 (right).<sup>[78]</sup>

## 2.6. Composite Materials

Catalysts are an important class of materials which accelerate the chemical reaction and improve the reaction selectivity regarding to the wished product. Beside chemical processes catalysts are used for environmental remediation from chemical pollution. Composites or supported catalysts are formed with two or more components. They show improved properties compared to bulk catalysts by saving of active compounds or improved catalytic performance (activity, selectivity):

Mixed or supported catalysts may result with benefits such as

- Saving material, e.g.  $\text{AgVO}_3$  by simple supporting
- Improved dispersion of catalytic active components
- Stabilizing the microstructure or active components e.g. Ag nanocluster
- Improved access and flux of molecule (transport) adsorption/desorption and diffusion of molecules
- Combining different functions (e.g. dual- acidity and redox properties)
- Enhancing the mechanical and thermal stability

These catalytic materials can be prepared by physical mixing, sol-gel synthesis, co-precipitation, and others. (Fig.11) shows important types of supported or composite catalysts as:

1. Supported Catalysts
2. Composite (Mixture of two or more components)
3. Core Shell
4. Hierarchical porous composites, which have combined pore systems containing micro pores, mesopores and macro pores combined together and/different catalytic (nano)components (ACIN- advanced inorganic nanomaterials)

### 2.6.1 Supported Photocatalysts

Supported catalysts are normally anchored or affixed on a solid material with high surface area. Catalysis reactions take place on surface atoms of catalyst. Normally used supported materials range from semiconductors to Metal oxide and micro porous or mesoporous materials such as alumina, silica, zeolite, carbon, polymers, different types of clays etc. Supports may or may not take part in chemical reactions. Either it functions as stabilizing agent for the active sites, or provides uniform dispersion or adjusting acid base sites. Most attention is given to increase the life time of the active catalyst and stop repining and poisoning of the catalyst. A large number of preparation methods are developed for creating supported catalysts such as impregnation, ion exchange, adsorption, grafting, anchoring, deposition or co-precipitation, chemical vapor deposition, and physically spreading. Mostly metals/metal oxides, vanadates are reported with increased activity while supported on supporting materials. Supporting catalysts ranges from nanoclusters to micron sized. Typical schemes of supported, mixed (composite), Core Shell and hierarchical structured catalysts are shown (Fig. 11).

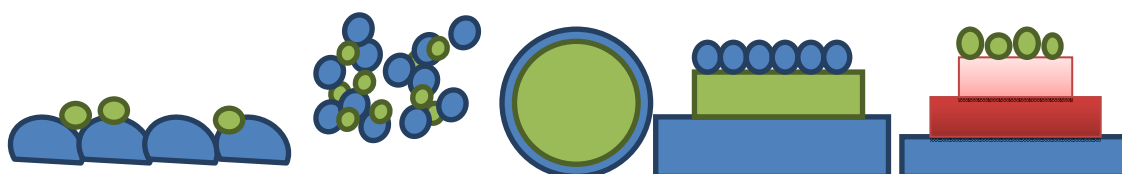


**Figure 11:** Supported Catalyst composite mixture, Core-Shell, hierarchical structured photocatalysts green defines the active component; blue defines nonporous or porous support, while other colors show in part contribution to the photocatalytic process.

### 2.6.2 Photocatalyst Composite Mixtures

Mixed catalysts are physical mixture of solid material mostly mixed metal oxides, vandates etc. Mixed catalysts are particularly reported for sowing intrinsic bi-functional properties. Mixed photocatalysts play an important role in degradation of pollutants through a charge transfer mechanism decreasing the recombination of photo generated electron–holes (e.g., a  $\text{WO}_3\text{--ZnO}$  in 1:9 weight percentage mixtures). These materials are nearly homogenous dispersed and strongly stick onto each other during physical mixing. Photocatalytic reactions take place on surface of mixed photocatalysts. Normally used supports range from different semiconductors to metal oxides and micro porous or mesoporous materials such as alumina, silica, zeolite, carbon, polymers, different types of clays etc.

### **2.6.3 Core Shell Catalysts**

Core Shell catalysts are prepared for increasing the activity or decreasing leaching and other aggressive effects or making safe the catalyst to coat them with active or non-active catalysts. Most of the reactions and catalysts are reported with coating with inactive materials has boosted the catalytic cycle. For example copper nanoparticles are known for the formation of methanol from CO, CO<sub>2</sub> and H<sub>2</sub>, but with coating of inactive zinc oxide catalytic activity is highly boosted.<sup>[79]</sup>

### **2.6.4 Hierarchical Nanoscale Photocatalyst**

Hierarchical structured photocatalysts are a combination of materials of distinguished structure and porosity in a defined order to improve specific properties. The simplest example of hierarchical photocatalysts is the arrangement of different sized and scaled materials or the combination of materials with different pores. Hierarchical structured photocatalysts provide strength and toughness, or unusual optical properties by reducing charge recombination and improve of visible light activity. These materials are obtained by mechano-chemical preparation followed by thermal treatment (annealing).

### 3. Results and Discussion

#### 3.1 Materials

##### 3.1.1 Silver Vanadate, Mesoporous Graphitic Carbon Nitride and $\beta$ -AgVO<sub>3</sub>/mpg-C<sub>3</sub>N<sub>4</sub> Composites /Core Shell Catalysts

**Nitrogen Adsorption:**-The textural properties of the mesoporous graphitic carbon nitride (mpg-C<sub>3</sub>N<sub>4</sub>), silver vanadate ( $\beta$ -AgVO<sub>3</sub>) and the composite samples were investigated by nitrogen adsorption-desorption measurements (Fig. 12). The silver vanadate shows an adsorption isotherm typically observed for nonporous materials. It shows a low uptake, which slightly increases with relative pressure and no textural porosity which would give rise to a markedly up take at high relative pressure. It is not porous. In contrast, mpg-C<sub>3</sub>N<sub>4</sub> is mesoporous showing an additional N<sub>2</sub> uptake at high relative pressure of  $p/p_0 > 0.8$ . The BET Surface area calculated from isotherm amounts to *ca.* 44.5 m<sup>2</sup>/g (BET).

The nitrogen sorption measurements of  $\beta$ -AgVO<sub>3</sub>/mpg-C<sub>3</sub>N<sub>4</sub> composites show that the specific surface areas and pore volumes of composites are only slightly changed with low silver Vanadate loading up to *ca.* 20-30%. The mesoporosity is maintained even with the Core Shell sample.

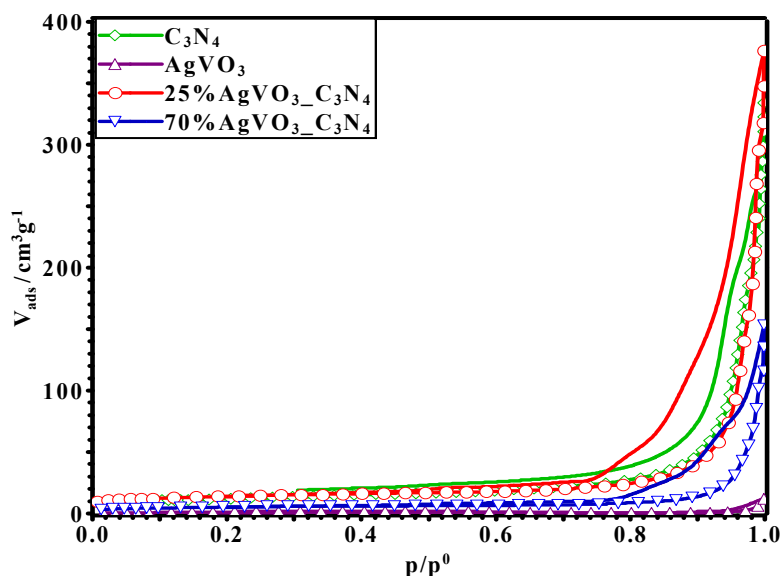


**Figure 12:** Nitrogen adsorption (assigned lines) and desorption (plain lines) isotherms of prepared  $\beta$ -AgVO<sub>3</sub>, mpg-C<sub>3</sub>N<sub>4</sub>, and the corresponding  $\beta$ -AgVO<sub>3</sub>/mpg-C<sub>3</sub>N<sub>4</sub> composite and “Core-Shell” material.

With further increase of the silver vanadate loading, the specific surface area decreases down to *ca.* 19 m<sup>2</sup>/g, with 70%  $\beta$ -AgVO<sub>3</sub>/mpg-C<sub>3</sub>N<sub>4</sub> composite. The cumulative specific pore volume of the  $\beta$ -AgVO<sub>3</sub>/mpg-C<sub>3</sub>N<sub>4</sub> composites decreases from 0.58 to 0.24 cm<sup>3</sup>/g with growing silver vanadate content from 20 to 70% respectively.

***$\beta$ -Silver Vanadate*** :-The TEM images of the prepared  $\beta$ -AgVO<sub>3</sub> are shown in Figure.13 a-b. They show that the silver vanadate consists of rods with diameters of 20 nm to 60 nm, with lengths in the micron range ( $\geq 1 \mu\text{m}$ ). These rods are mostly stacked together or agglomerated.

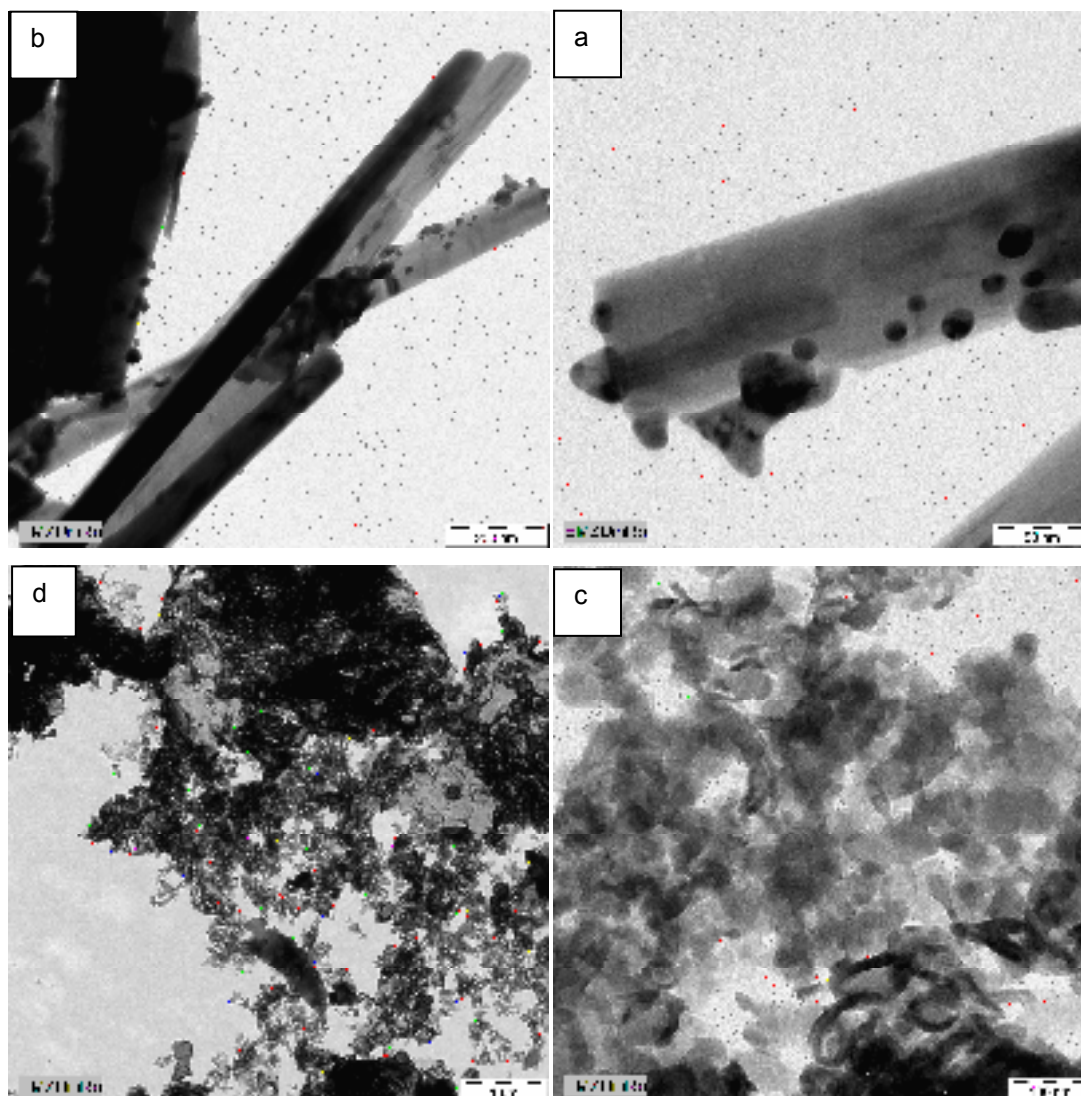


**Figure 13:** TEM images of  $\beta$ -AgVO<sub>3</sub> (a,b) and  $\text{mpg-C}_3\text{N}_4$  after calcination at 500°C (c,d).

***Mesoporous Polymeric Graphitic Carbon Nitride (mpg-C<sub>3</sub>N<sub>4</sub>)***:-The TEM images show that the synthesized  $\text{mpg-C}_3\text{N}_4$  sample consist of strongly agglomerated or inter grown nanoparticles of *ca.* 50-100 nm size (Fig. 13.c and d). Carbon nitride nanoparticles form interwoven sheets of 60 to 100 nm sizes which are also interwoven sometimes like nano-worms.

***$\beta$ -AgVO<sub>3</sub>/mpg-C<sub>3</sub>N<sub>4</sub> Composites and Core Shell Catalysts***:-The appearance of a composite particle depends strongly on the carbon nitride content. Interestingly, with the 20-30%  $\beta$ -

AgVO<sub>3</sub>/ mpg-C<sub>3</sub>N<sub>4</sub> materials complete covering of the body of the β-AgVO<sub>3</sub>nanorods by carbon nitride is observed. A “Core-Shell” catalyst is formed. Figures 14a-b show β-AgVO<sub>3</sub>/mpg-C<sub>3</sub>N<sub>4</sub> catalyst particles consisting of a ca.125 nm thick aggregated silver vanadate nanorods completely surrounded by small mpg-C<sub>3</sub>N<sub>4</sub> nanoparticles or in part by mpg-C<sub>3</sub>N<sub>4</sub> layers of ca.7-12 nm thickness (carbon nitride shell).

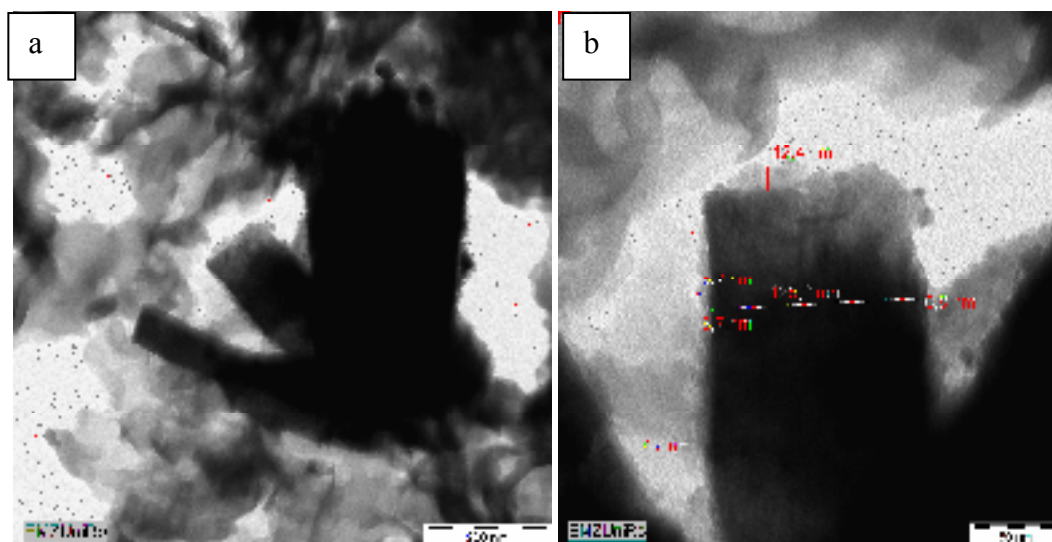


**Figure 14:** TEM images of 20% β-AgVO<sub>3</sub>/mpg-C<sub>3</sub>N<sub>4</sub> (a-b).

### 3.1.2 Mesoporous Ordered Silica Mesoststructures

**MCM-41:-** In Figure15a, the nitrogen adsorption isotherm of MCM-41-S shows small pores. Typically adsorption starts at very low pressure, which confirms the presence of some amount of micro pores. Type IV isotherm with a narrow steps of capillary condensation with no hysteresis loop indicates high pore size uniformity.

Uniform and gradual uptake in the region of 0.2 to 0.35 correlated to the pore size distribution indicates high quality small mesoporous material (Fig.15b). The isotherm is consistent with the presence of cylindrical pores. BJH calculations confirm the uniformity and narrow size distribution of mesopores with a pore size maximum ca. 2.6 nm. Above p/p<sub>0</sub> of 0.9 a sudden increase in volume of adsorbed nitrogen indicates the presence of large mesopores due to inter particle pores. The BET surface area is 1034 m<sup>2</sup>/g. While very little amount of micro pores are found below 1 nm in diameter at low relative pressure p/p<sub>0</sub> near to zero. A total cumulative volume of 1.10cm<sup>3</sup>/g is calculated at 0.95 p/p<sub>0</sub>. Cumulative volumes of mesopores and micro pores are calculated with t-plot of 1.02cm<sup>3</sup>/g and 0.08cm<sup>3</sup>/g respectively.

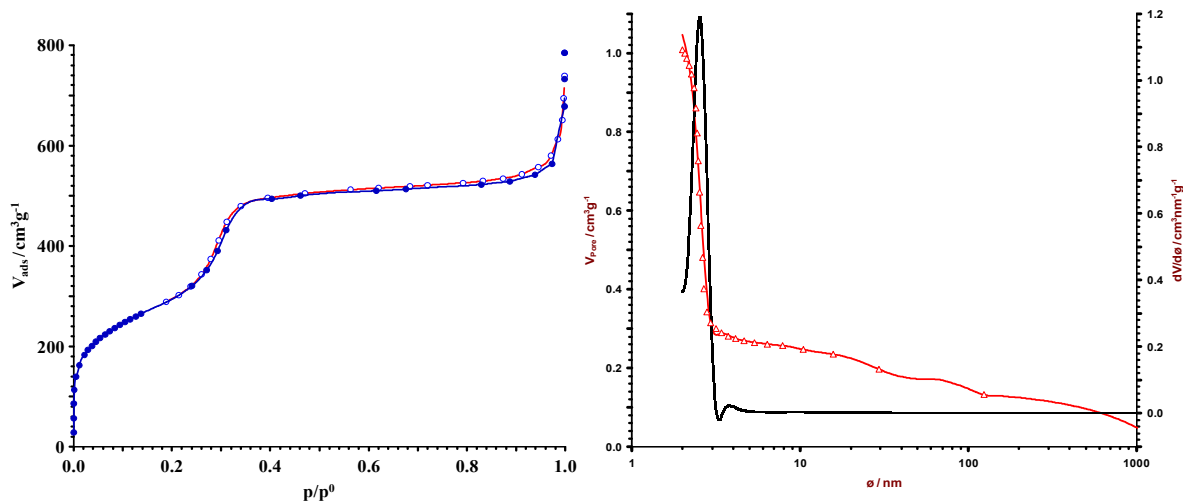


**Figure 15:** N<sub>2</sub> adsorption-desorption isotherm curve (a) and pore size distributions (b) of the MCM-41-S.

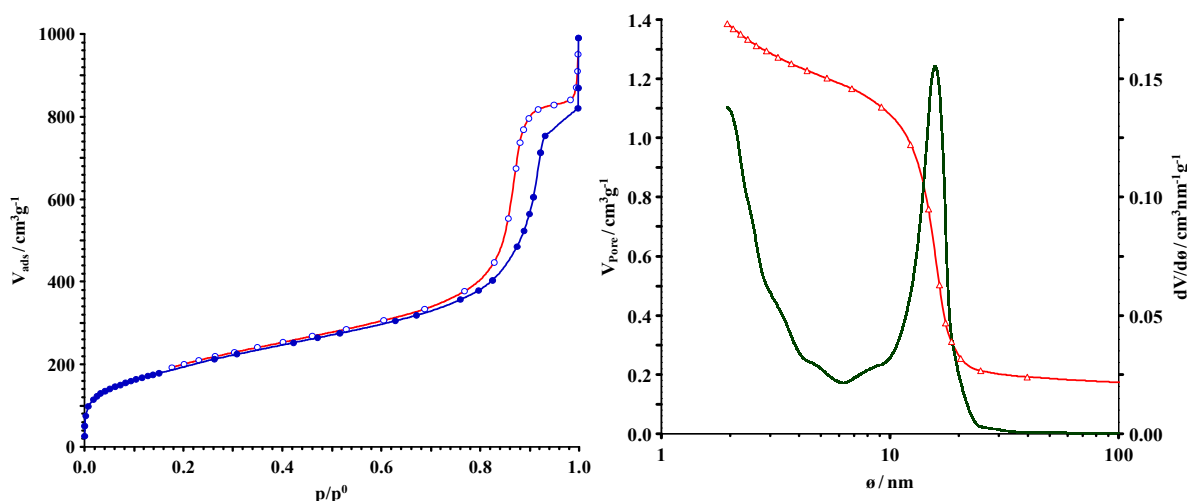


**Figure 16:** N<sub>2</sub> adsorption-desorption isotherm curve (a) and pore size distributions (b) of the MCM-41-L.

The nitrogen adsorption isotherm of large pore MCM-41-L shows a uniform and gradual uptake which represents broad distribution of mesopore sizes. The adsorption/desorption isotherm is of type IV and shows a hysteresis loop of H2 type at  $p/p_0 \sim 0.85$  observed. This finding confirms existing of well-defined tubular pores with comparatively uniform pore sizes and connectivity (Fig.16a). The nitrogen uptake at  $0.995 p/p_0$  indicates the presence of large inter particle pores. The diameter of mesoporous calculated with the BJH method is  $\sim 15$  nm (Fig.16b). Also very small amounts of micro pores with diameters below 1 nm are present as indicated by the low uptake at very low relative pressure  $p/p_0$  near to zero. A total cumulative volume of  $1.79 \text{ cm}^3/\text{g}$  is calculated at  $0.95 p/p_0$  with negligible amount of micro pores  $0.02 \text{ cm}^3/\text{g}$ . BET surface area of  $719 \text{ m}^2/\text{g}$  is calculated.

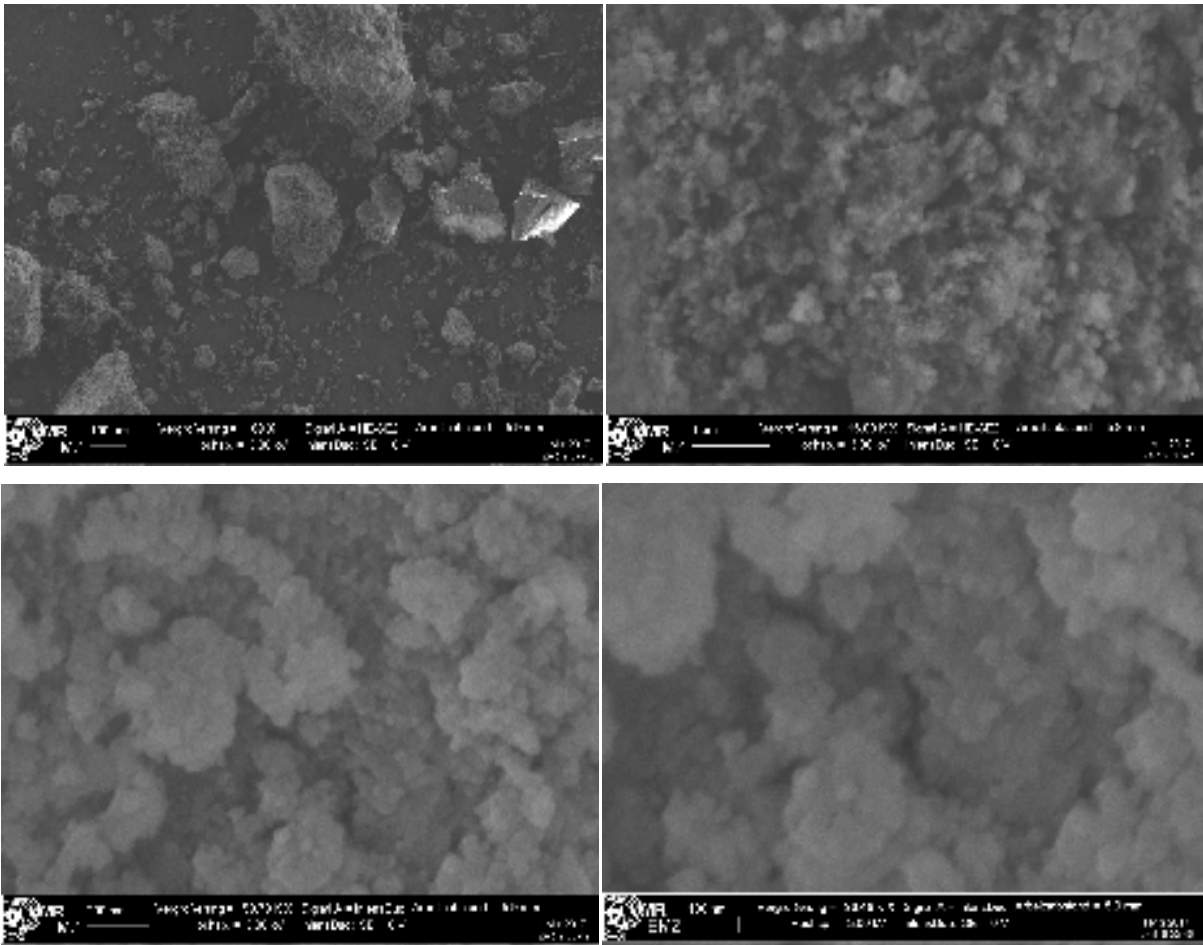
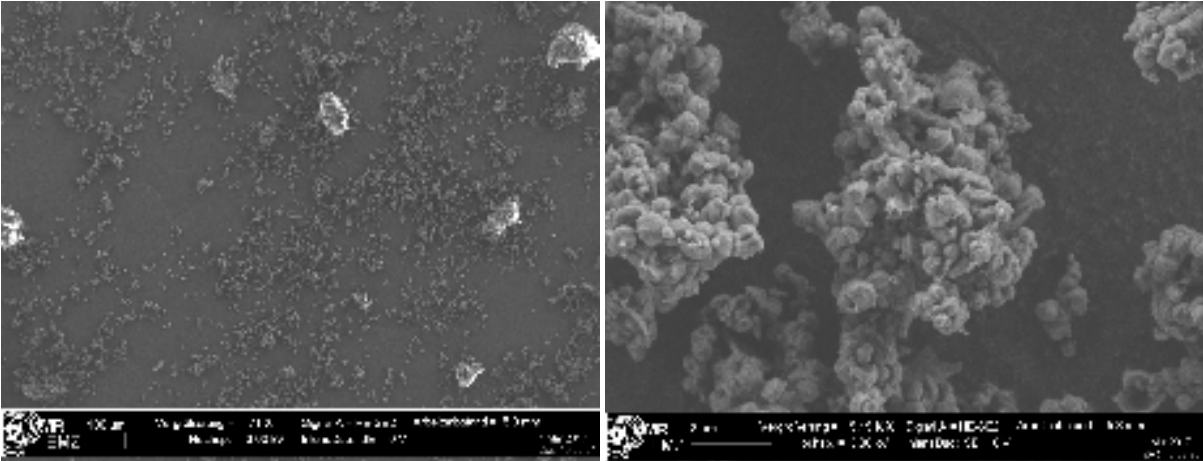
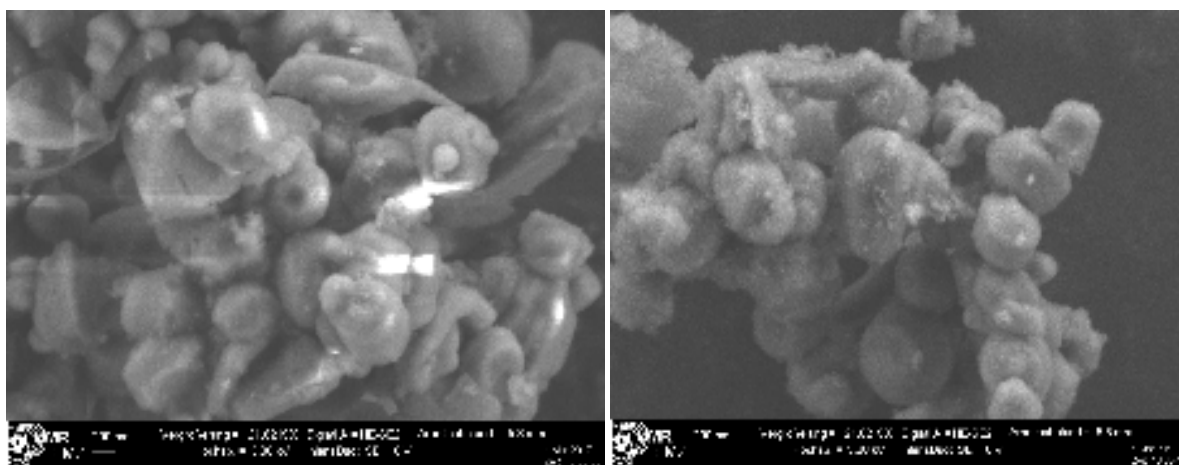


Figure 17: SEM images showing the morphology of MCM-41-L (Large porous).





**Figure 18:** SEM images showing the morphology of MCM-41-S (small porous).

Above findings are confirmed by SEM images showing bulk particles (Fig. 17). The surface of bulk particles is highly rough. High resolution shows that bulk particles are composed of small nanoparticles as shown in (Fig. 18). SEM images of MCM 41-S with small pores shows big particles composed of well-defined spherical balls of nanoparticles in range of 200 to 300 nm (Fig.18). These spherical nanoparticles are loosely aggregated together with the formation of over micron sized particles.

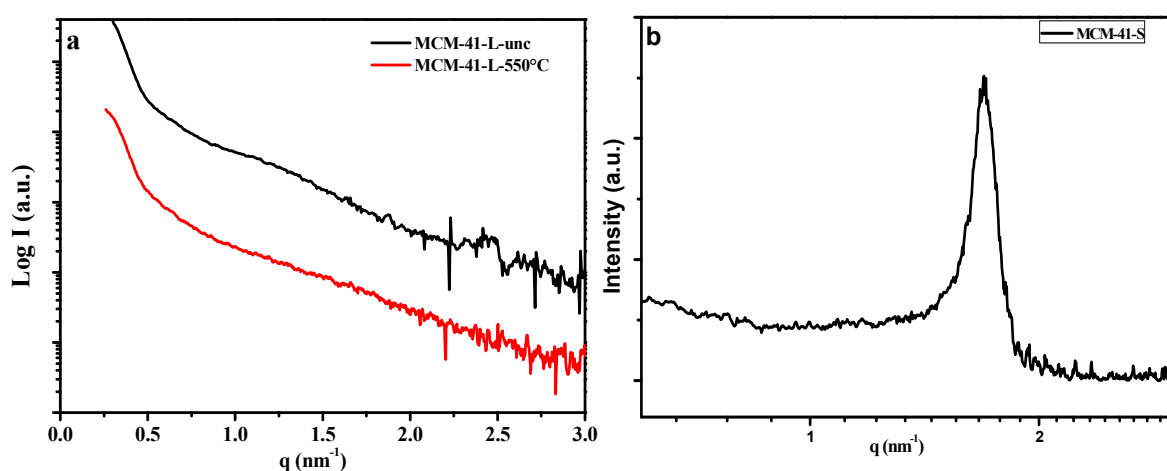


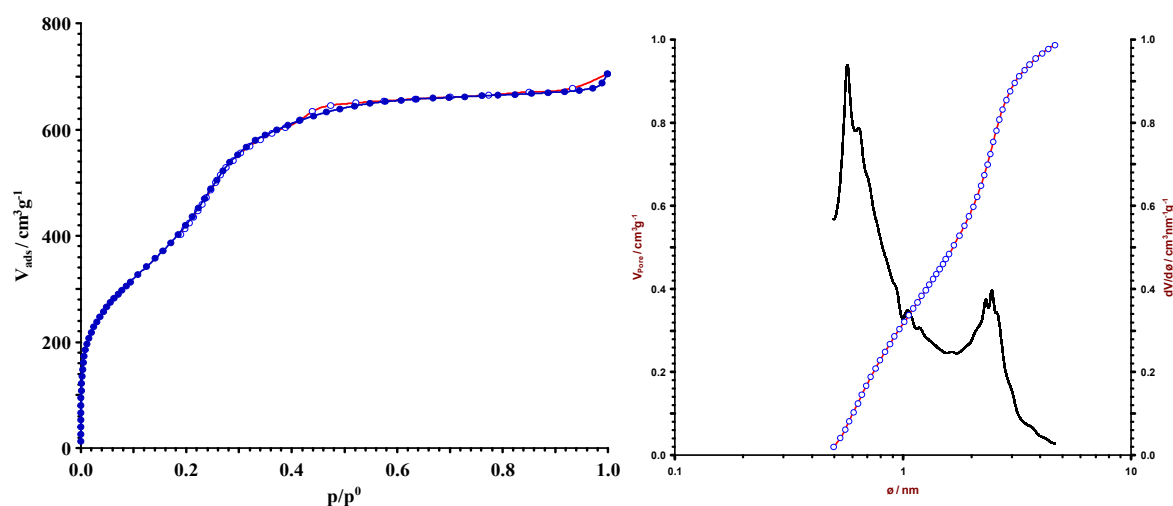
**Figure 19:** SAXS patterns of MCM-41-L (large pore), as-synthesized and calcined at 550°C (a), and MCM-41-S (small pore) (b).

Small-angle XRD (SAXS) pattern of small and large porous MCM-41-S and MCM-41-L, respectively, are shown in (Fig. 19). MCM-41-S shows an intense narrow peak at  $q=1.69 \text{ nm}^{-1}$  which corresponds to (1 0 0) reflection. The pore system is ordered as previously reported for hexagonal structures (Fig. 19b).<sup>[80]</sup> The d-spacing was calculated as 3.71 nm which is roughly in line with N<sub>2</sub>-sorption studies with pore sizes of ~2.6 nm. The difference of the d-spacing and pore size corresponds to a size of the pore wall of ~1.0 nm. Other small reflections of (1 1

0) and (2 0 0) planes are too weak to be noticed. The SAXS pattern of MCM-L show a continuous increase of the scattering intensity with decreasing q-value, especially beyond  $q=0.5$  and a weak broad peak for the as-synthesized indicating the presence of large disordered pores.

**MCM-48:**-The nitrogen adsorption isotherm of MCM-48 is almost similar to that of MCM 41-S with small pores. Two of MCM-48 samples were prepared with different reaction time, 10 hours and 11 days and are discussed as bellow.

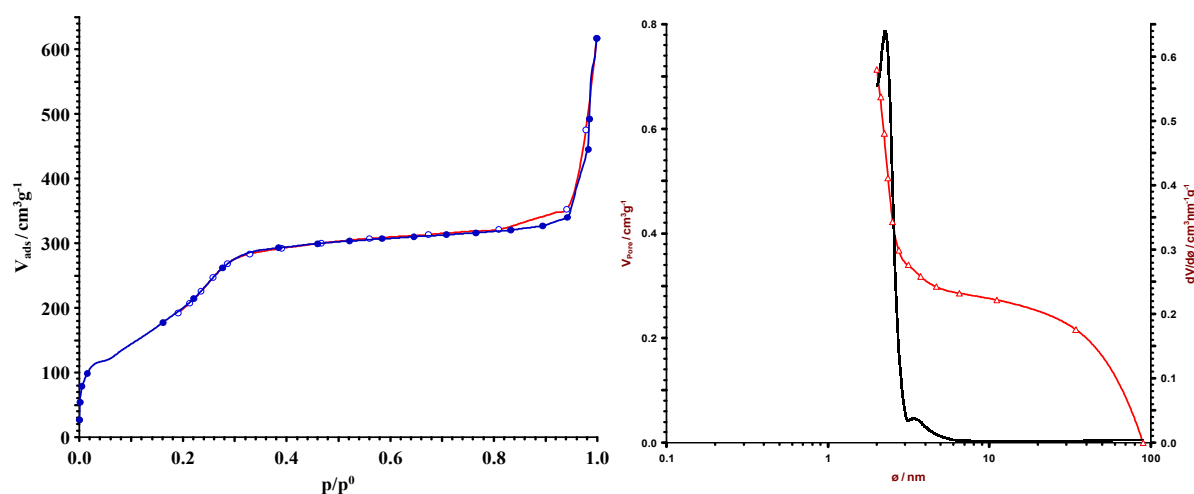
**MCM-48-S:** MCM-48-S (prepared in 10 hours of reaction time) isotherm has high uptake at low pressure referring to the micro pore region (Fig. 20a). A sudden large uptake of  $\sim 400\text{cm}^3/\text{g}$  nitrogen with a shoulder at a relative pressure of  $\sim 0.2$  is noted. Further rapid increase in uptake of  $\sim 700\text{cm}^3/\text{g}$  up to relative pressure of 0.5 is followed. At relatively high pressure isotherm remains uniform showing low uptake above  $p/p_0 \sim 0.55$ . The BET surface area of  $\sim 1800\text{cm}^2/\text{g}$  is calculated. The calculated cumulative volume amounts to  $1.10\text{cm}^3/\text{g}$  giving mesopores of diameter 2.45nm. Clearly huge amounts of micro pores are also noted with a size of  $\sim 1$  nm diameter (Fig. 20b). The cumulative micro pore volume calculated with t-plot is  $0.2\text{cm}^3/\text{g}$ .



**Figure 20:** N<sub>2</sub> adsorption-desorption isotherms (a) pore size distributions (b) of the MCM-48-S (obtained after 10h hydrothermal treatment and calcined).

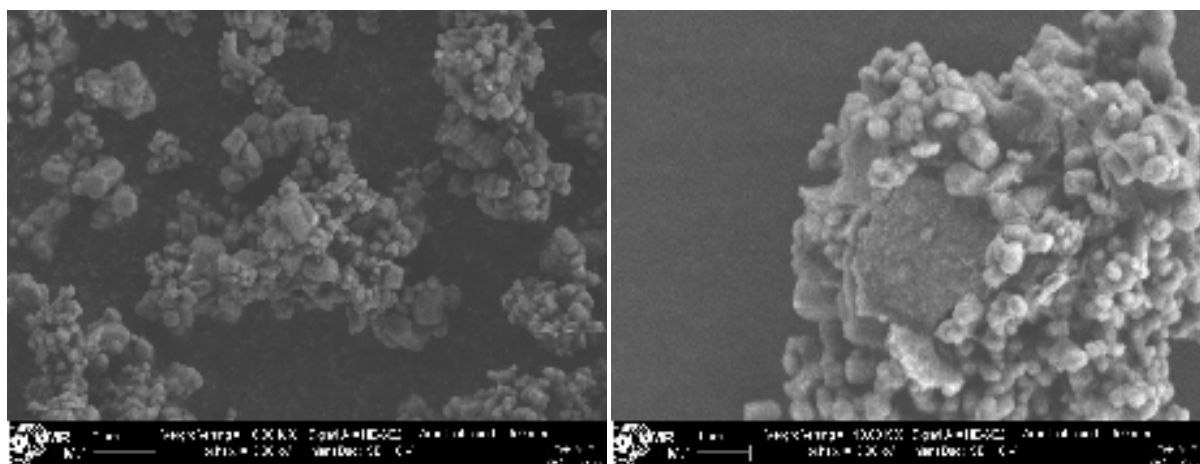
**MCM 48-L:** MCM-48 prepared in 11 days shows a type IV isotherm (Fig. 21a). Adsorption starts at relatively low pressure which confirms the presence of micro pores. Adsorption proceeds fast up to  $p/p_0 \sim 0.3$  due to the filling of the mesopores. Some multilayer formation occurs to higher  $p/p_0 \sim 0.8$  (additional low uptake). Above  $p/p_0 = 0.9$  a sudden increase of

nitrogen uptake indicates the presence of large meso- and macro pores due to inter particle pores.



**Figure 21:**  $\text{N}_2$  adsorption-desorption isotherms (a) and pore size distributions (b) of the MCM-48-L (obtained after 11 days of hydrothermal treatment and calcined).

Gradual uptake of nitrogen up to  $p/p_0 \sim 0.35$  indicates a broad size distribution of small mesopores, with a size maximum at  $\sim 2.40 \text{ nm}$  (Fig. 21b). The BET surface area calculated from isotherm is  $1100 \text{ m}^2/\text{g}$ . Small amounts of micro pores are also present is indicated by the nitrogen uptake at  $p/p_0$  close to zero. The micro pore volume is *ca.*  $0.16 \text{ cm}^3/\text{g}$ . Total cumulative volume of  $0.96 \text{ cm}^3/\text{g}$  is calculated from t-plot. MCM-48-S consists of large particles with well-defined shape, which might consists of small nano crystallites resulting with formation of super-structured mesocrystals which are loosely aggregated together (Fig. 22).



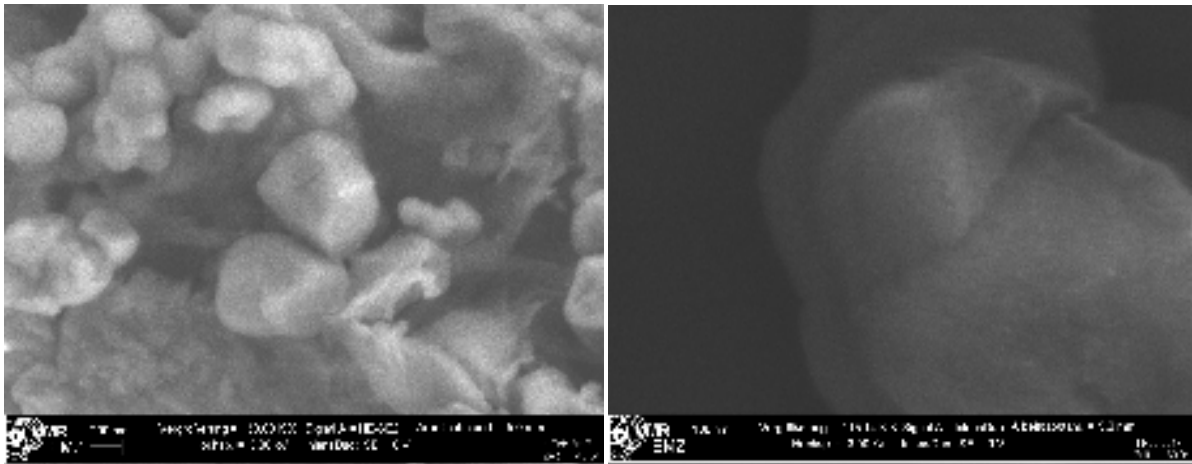


**Figure 22:** SEM images showing the morphology of MCM-48-S.

Morphology studied with SEM, for MCM-48-L shows images consist of large micron sized aggregated particles developed from small nanoparticles. Aggregated nanoparticles shows sufficient amount of secondary pores created in uniform fashion (Fig.23).

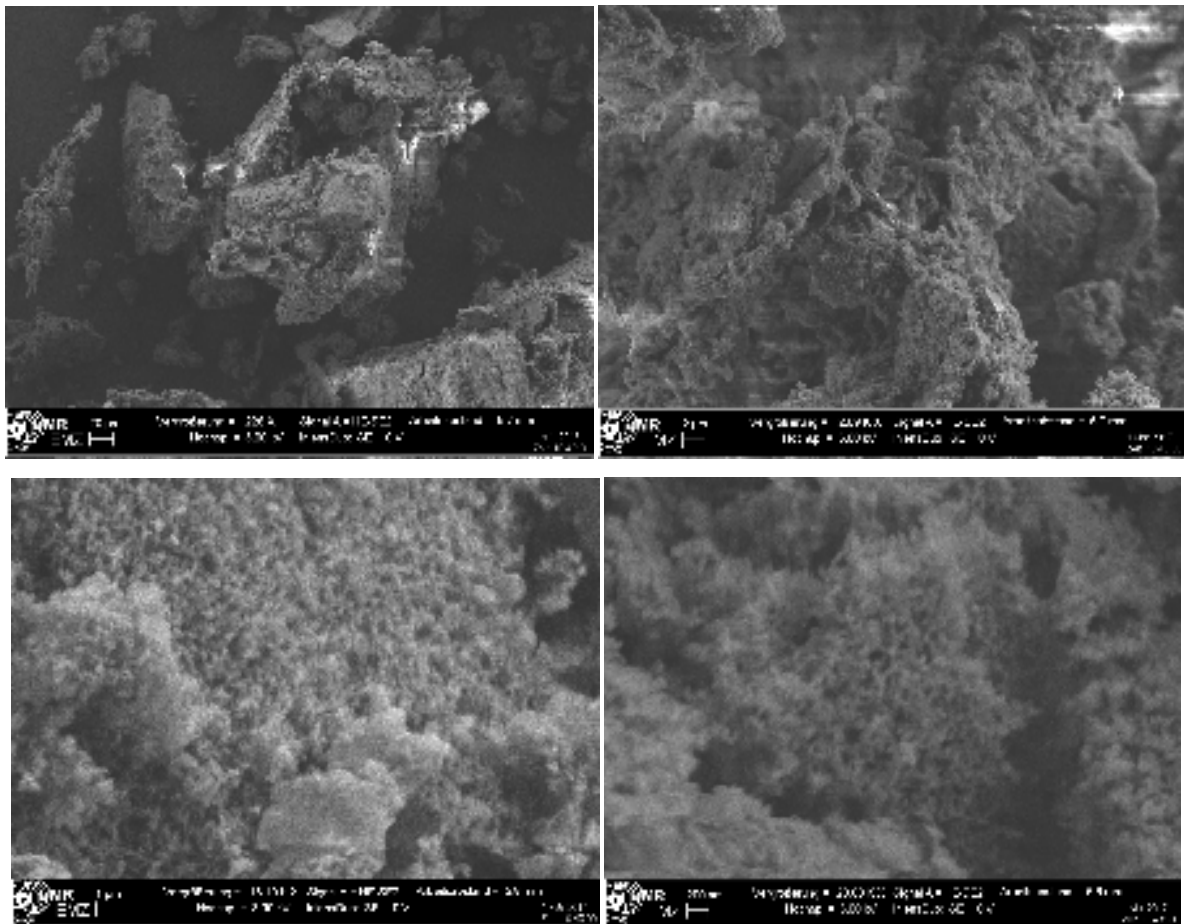


**Figure 23:** SEM images showing the morphology of MCM-48-L.

Crystallization degree highly depends on reaction temperature and duration.<sup>[81]</sup> SAXS pattern

of MCM-48-L and S are shown in (Fig.24). SAXS pattern is broadened and unresolved which is due to the small sized nanomaterials and amorphous walls of pores silica. MCM-48-L prepared at 11 days shows a broad peak with  $q$  position 1.78, while the MCM-48-S prepared in 10 hours shows sharp but less intense scattering pattern with shifting of scattering angle to high value of 1.94 (Fig.24). This indicates the small unit cell caused by the condensation of the silanol groups, indexed to (2 1 1). The d-spacing was

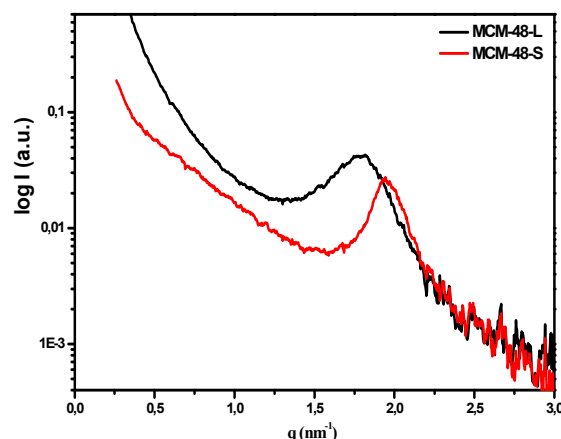


**Figure 24:** SAXS patterns of MCM-48-L and MCM-48-S.

calculated as 3.22 nm and 3.52 nm for MCM-48 -S and L respectively. MCM-48- L has big unit cell than MCM-48-S this proves the parallel effect of reaction time on unit cell volume

**KIT-6:** The nitrogen adsorption isotherm of KIT-6 is according to the earlier reports (Fig.25a).<sup>[80]</sup> Typically adsorption starts at relatively low pressure, which confirms the presence of minute amount of micropores. A type IV isotherm with narrow hysteresis loop is observed, which shows the capillary condensation step at  $p/p_0$  between 0.7 and 0.8. The steep adsorption step indicates the presence of unique sized pores.

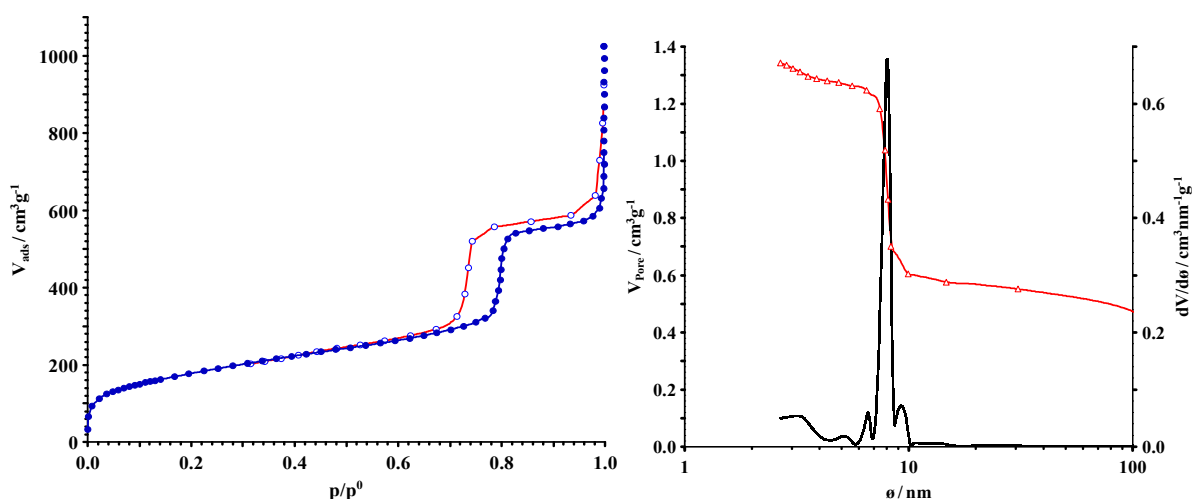


**Figure 25:** N<sub>2</sub> adsorption-desorption isotherm curve (a) and pore size distributions (b) of the KIT-6.

The BJH calculations show uniform and narrow distribution of mesopores with a size maximum at ~7.8 nm (Fig. 25b). Above a relative pressure of  $p/p_0$  of 0.95 a sudden increase in volume of adsorbed nitrogen indicates the presence of inter particle macro pores resulting

from agglomeration of particles. The BET surface area is *ca.*645 m<sup>2</sup>/g calculated. A H2 type of hysteresis loop typically found with ink-bottle pores is noticed which confirms the presence of uniform channel-like pores network with pores of narrow mouths. The total cumulative volume amounts to *ca.*2.20 cm<sup>3</sup>/g. The cumulative micro pore volume is *ca.*0.01cm<sup>3</sup>/g with mean diameter of ~ 0.84 nm, which might indicate that some mesopores are interconnected by micro pores.

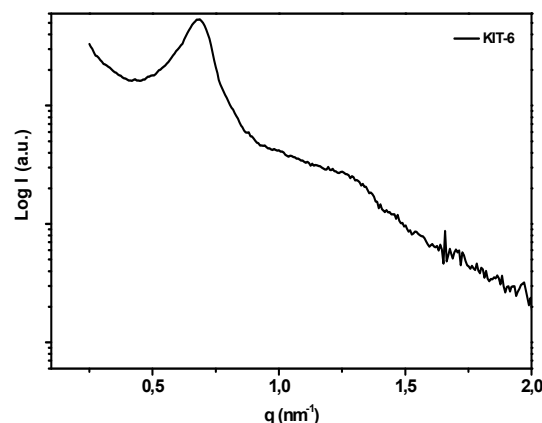


**Figure 26:** SAXS patterns of KIT-6.

The SAXS pattern of KIT-6 shows an intense narrow peak at  $q = 0.68 \text{ nm}^{-1}$  which is assigned to (2 1 1) lattice plane reflection and a small hump at  $q = 1.28 \text{ nm}^{-1}$  belonging to the (3 2 2) plane. The peak of the (2 2 0) plane at  $q \sim 0.75$  is not resolved. The calculated d-spacing of 9.2 nm of the (2 1 1) plane and 5 nm of the (2 2 0) plane confirm the presence of large pores and a large unit cell volume. These findings are in line with earlier reports which showed that KIT-6 represents a well resolved structure and, conclusively, a well ordered mesoporous silica with bi-continuous cubic, with body centered cubic symmetry (Fig. 26).<sup>[82]</sup>

Scanning electron microscopy (SEM) was used for studying the morphology and size of KIT-6 particle (Fig. 27). At low magnification the KIT-6 particles look like bulky dumbbells of 20-200  $\mu\text{m}$  size. Interestingly, high magnification SEM images show that the KIT-6 particles represent a superstructure (mesocrystal) where nanoparticles are interwoven with each other to build up large, apparent bulky, particles. The surface of these materials appears relatively rough and disordered. The presence of secondary inter particle macro pores is evidenced with N<sub>2</sub> adsorption/desorption isotherm. Hence, SEM images and nitrogen adsorption/desorption measurements show that KIT-6, synthesized here, contains a hierarchical pores system of combined micro, meso, and macro pores.

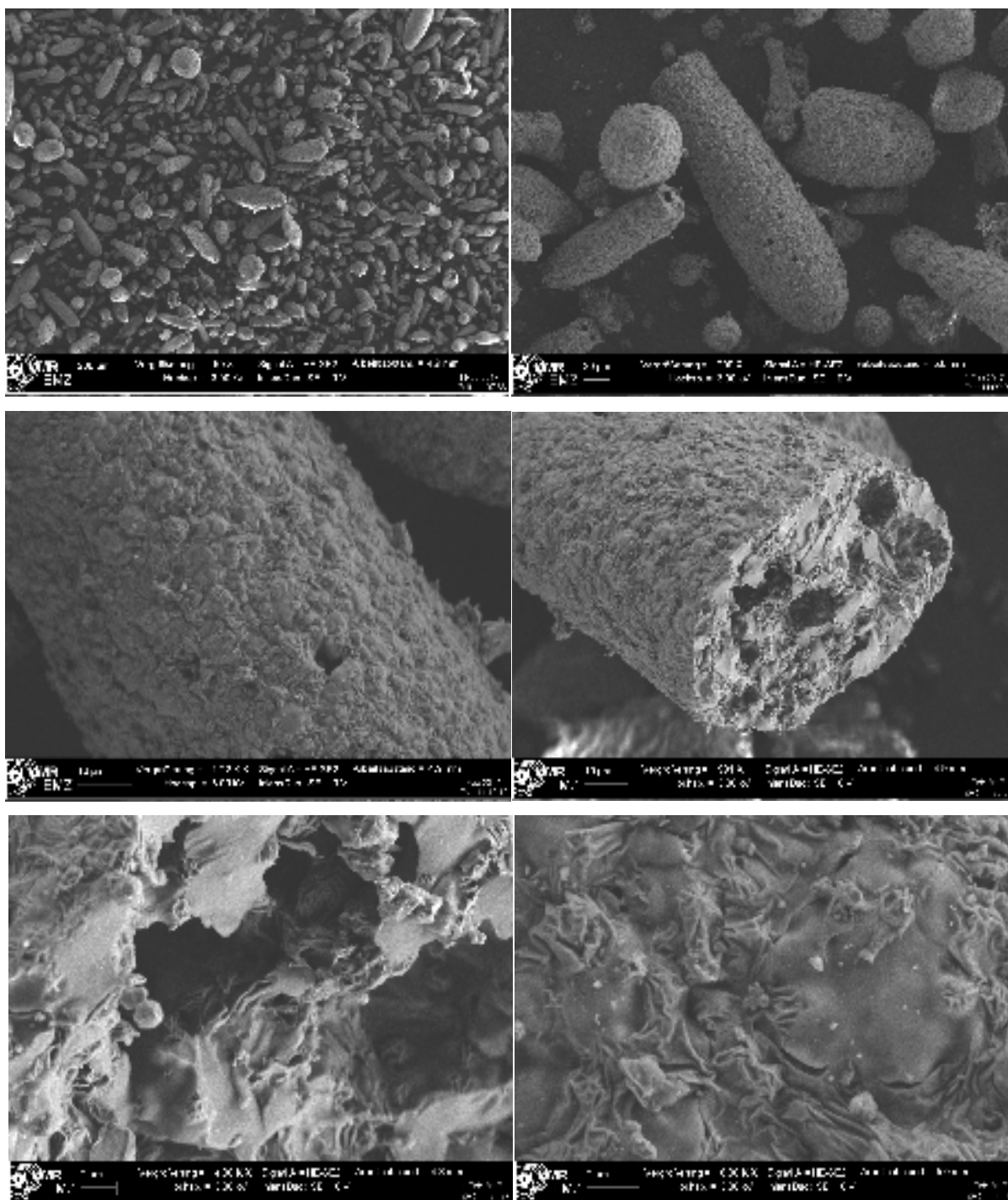


**Figure 27:** SEM images showing the morphology of KIT-6.

**SBA-15:** SBA-15 ordered hexagonal mesoporous silica material containing large pores, which pore structure is related to MCM-41. (Fig. 28) shows nitrogen adsorption/desorption isotherm of own prepared SBA-15. The type IV isotherm shows a large increase at very low pressure confirming the presence of a large amount of micro pores, followed by addition of nitrogen up-take step near  $p/p_0 = 0.3$ . The Isotherm shows narrow steps of capillary condensation with pore size uniformity but shows no visible hysteresis loop. Almost half amount of  $N_2$  is

adsorbed within relative pressure of 0.3. A gradual uptake is observed with increasing relative pressure up to  $p/p_0=0.94$ . The BJH calculation show uniform and narrow distribution of mesopores with pore size maximum at  $\sim 2.5$  nm (Fig. 28b). Above  $p/p_0$  of 0.9 little increase in volume of adsorbed nitrogen indicates the presence of large inter particle mesopores/macro pores. BET surface area calculated from isotherm is  $978\text{m}^2/\text{g}$ , with cumulative volume of  $0.88\text{cm}^3/\text{g}$ . While very small amount of micro pores are present at relative  $p/p_0$  near to zero with micro porous volume of  $0.1\text{cm}^3/\text{g}$ .

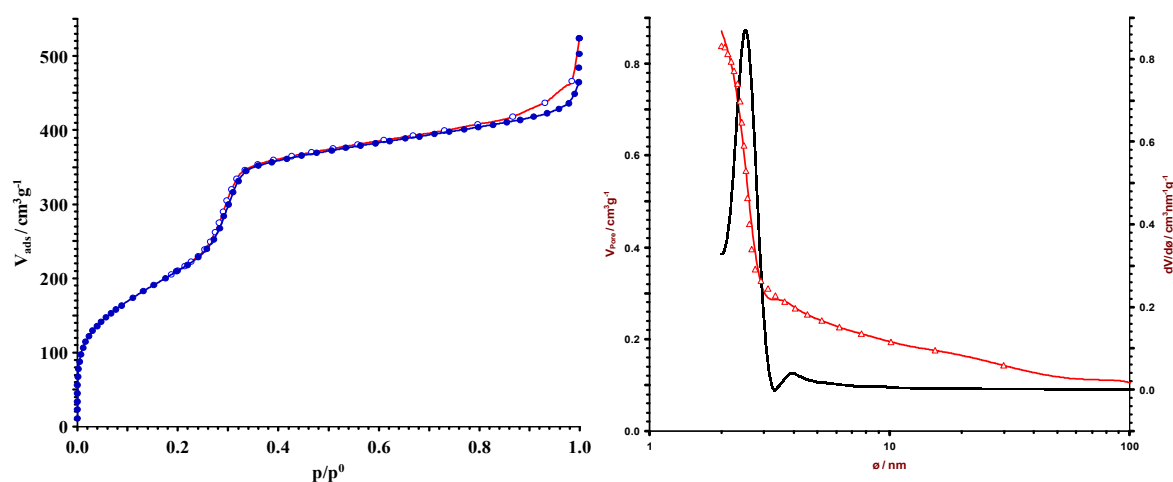


**Figure 28:**  $\text{N}_2$  adsorption-desorption isotherm and pore size distribution of the SBA-15.

SAXS pattern of the calcined SBA-15 shows a narrow intense peak at  $q = 0.76\text{nm}^{-1}$  together with broad second reflection at  $q = 1.5\text{nm}^{-1}$  (Fig. 29). The intense reflection is assigned to the (1 0 0) plane and the small reflection at  $1.50\text{nm}^{-1}$  is assigned to (2 0 0) plane of a hexagonal structure. Both well resolved reflections confirm the formation of a hexagonal ordered mesoporous material.

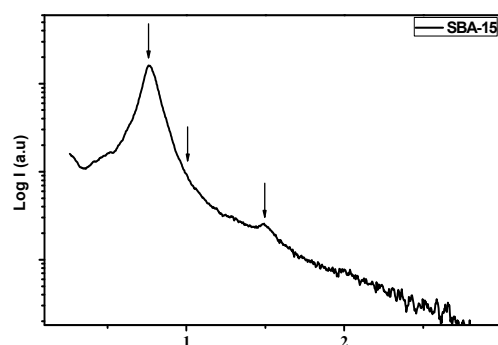


**Figure 29:** SAXS patterns of the SBA-15.

[83] The d-spacing of the peaks are 8.24 and 4.32, respectively. These results confirm the high order in this mesoporous silica. Spherical morphologies of micron sized particles are noted with scanning electron microscopy (SEM) for SBA-15, which are interwoven and aggregated together for the formation of micron sized particles. High resolution SEM shows, the structures are composed of agglomerated small nanosized particle (*ca.* 30nm size). Hence, the prepared SBA-15 is a mesocrystal (Fig. 30, bottom right).

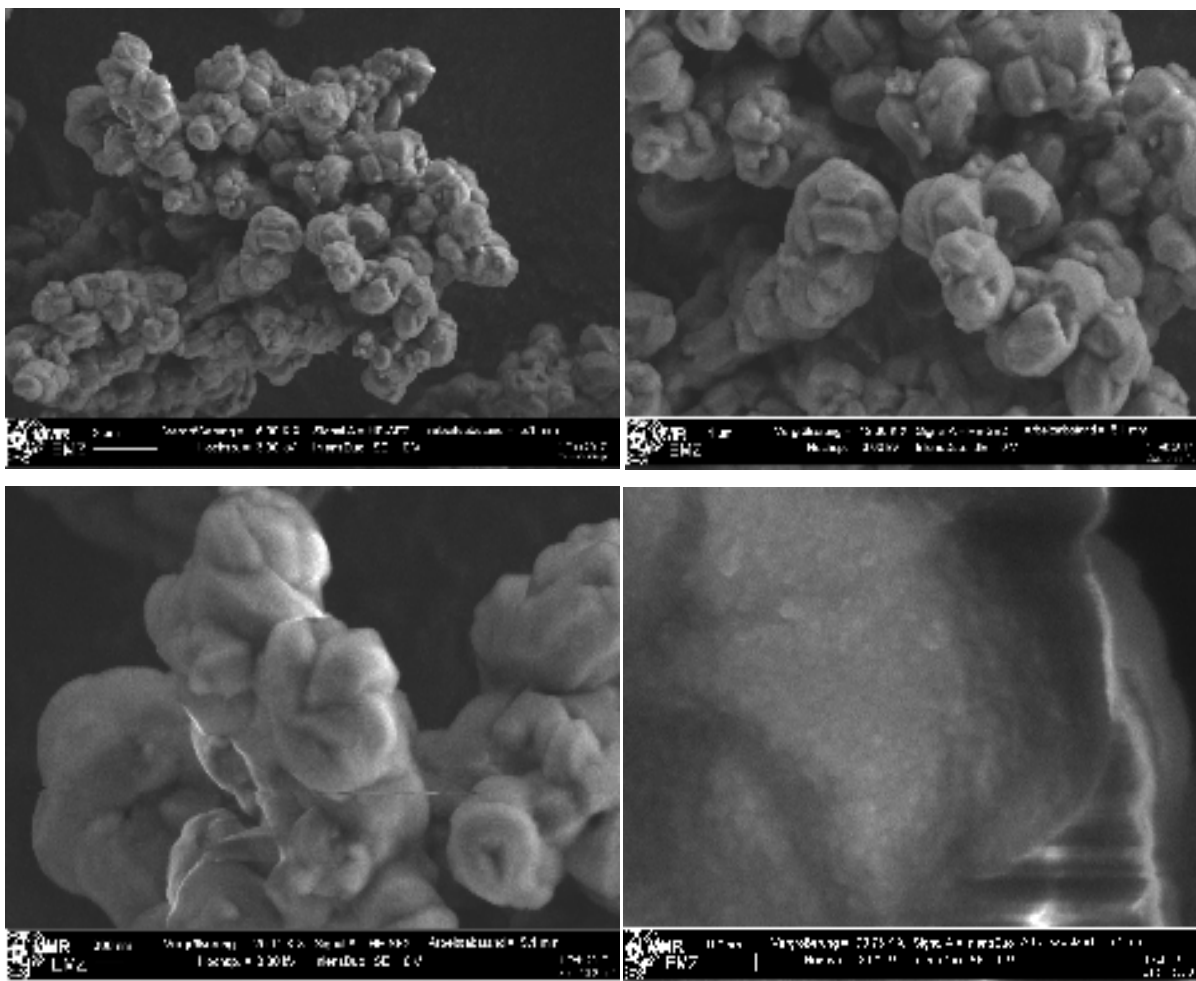


**Figure 30:** SEM images showing the morphology of SBA-15.

**SBA-16:** The Nitrogen adsorption isotherm of SBA-16 shows a steep increase of the isotherm at very low relative pressure due to adsorption in micro pores. It is followed by a gradual but large increase up to a relative pressure of *ca.*  $p/p_0 = 0.4$ , and a small adsorption step between  $p/p_0$  0.5 to 0.6 due to filling of small and larger mesopores (Fig.31 a). The reversible adsorption isotherm is of type IV and shows a H2 type hysteresis loop at  $p/p_0 \sim 0.5$ , which is consistent with the pore structure of SBA-16. The SSA is *ca.*  $414 \text{ m}^2/\text{g}$ , The BJH mesopore diameter is  $\sim 3.47 \text{ nm}$  (determined from desorption branch). A total cumulative volume of  $0.389 \text{ cm}^3/\text{g}$  is found. These findings agree with the known porosity of SBA-16. SBA-16 contains thick walls of  $\sim 6 \text{ nm}$  diameter. The adjacent cages are connected by micro pores or small mesopores, which are formed during the escape of the decomposed surfactant molecules during the calcinations process. <sup>[84]</sup>

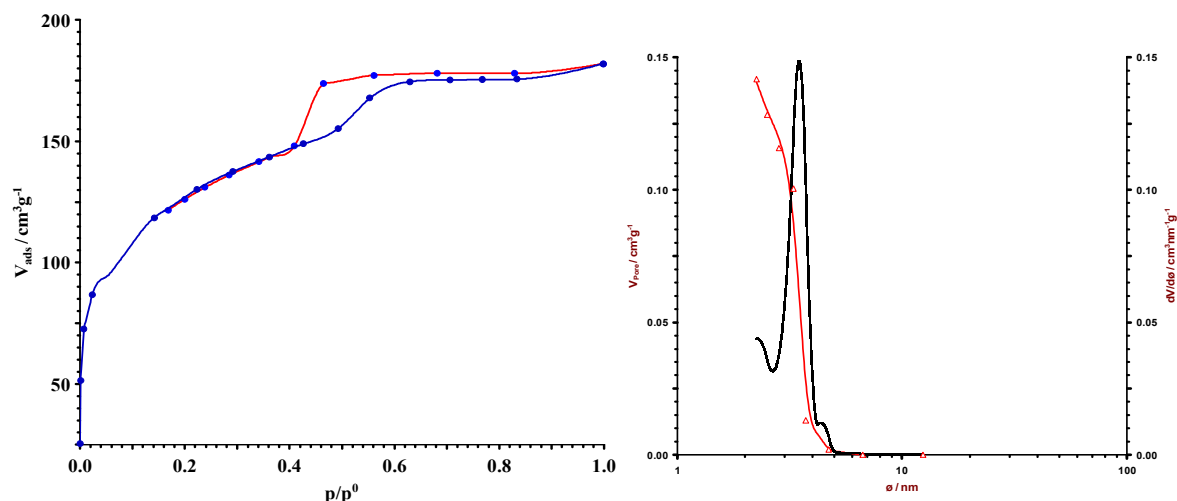


**Figure 31:** N<sub>2</sub> adsorption-desorption isotherm curve (a) and pore size distributions (b) of the SBA-16.

The SAXS pattern of SBA-16 shows a main diffraction peak at  $q=0.64 \text{ nm}^{-1}$ , and two further scattering diffraction peaks at  $q=0.89$  and  $1.07 \text{ nm}^{-1}$ . These peaks correspond to a body centered cubic meso structure, while other weak peaks are not visible (Fig. 32). The calculated d-spacing are  $\sim 9.8, 7.06$  and  $5.87 \text{ nm}^{-1}$ , correspondingly.

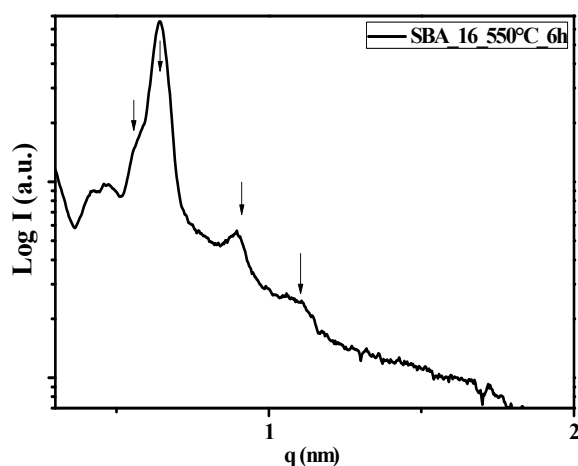


**Figure 32:** SAXS patterns of the SBA-16.

These findings are in line with reported literature data. They show that SBA-16 contains stacked spherical cages, according to body-centered cubic symmetry. The well resolved SAXS pattern shows that the synthesized material is a highly ordered mesoporous structure. The micrographs of SBA-16 obtained from SEM shows agglomerated micron-sized particles consists in part of ink bottle shaped spheres.<sup>[85]</sup> The *ca.* 10  $\mu\text{m}$  sized particles form agglomerates containing large macro pores, which can be considered as hollow from inside (Fig 33). These particles again consist of strongly agglomerated nanoparticles of *ca.* 20-40 nm diameter. Hence, the prepared SBA-16 represents also a mesocrystal or a so-called superstructure.

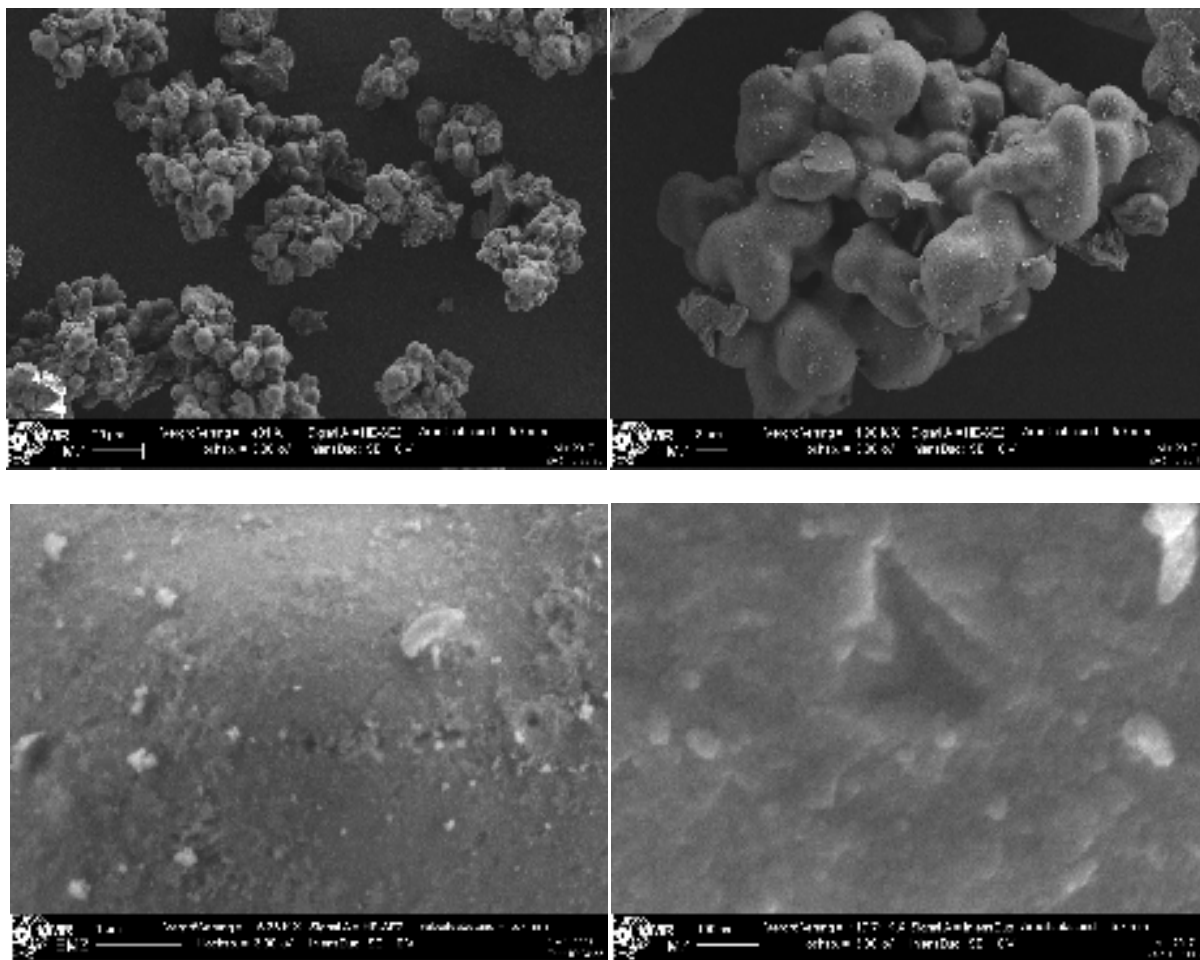


**Figure 33:** SEM images showing the morphology of SBA-16. The big bulky-like particles are composed of agglomerated small nanoparticle (bottom right).

**SBA-12:** SBA-12 is a hexagonal mesoporous material. The nitrogen adsorption isotherm of SBA-12 confirms presence of micro pores by nitrogen up-take at very low relative pressure (Fig 34). A gradual continuous increase of the isotherm is observed up to  $p/p_0$  ca. 0.3. This uptake is assigned to multilayer adsorption of nitrogen and finally complete filling of small mesopores. Until a relative pressure of ca. 0.95 the adsorption remains nearly unchanged. Due to large inter particle mesopores an additional step increase of the adsorption isotherm is observed above a relative pressure of 0.95. A hysteresis loop of H4 type is observed at  $p/p_0 \sim 0.5$ , which is assigned to slit-like pores of ca. 5.5 nm size. The BET surface is ca. 513 m<sup>2</sup>/g. The pore size distribution indicates narrow small mesopores with a pore size maximum at  $\sim 3.81$  nm.

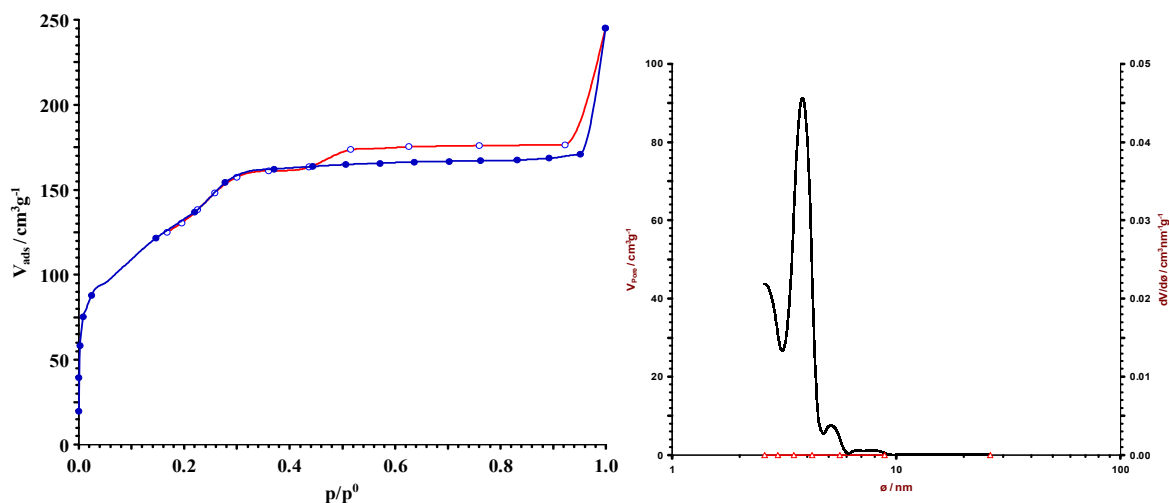


**Figure 34:** N<sub>2</sub> adsorption-desorption isotherm curve (a) and pore size distributions (b) of the SBA-12 calcined.

SBA-12 is known for having *hcp* or *ccp* structure. In the SAXS pattern of the prepared SBA-12 appears an intense scattering peak at  $q = 1.36 \text{ nm}^{-1}$  (Fig.35). This peak is assigned to (0 0 2) plane. Although no well resolved patterns for diffractions (1 0 0) and (1 0 1) diffractions are visible, can be due to the poor mesoporosity or increased cubic phase ratio. On calculating the average distance

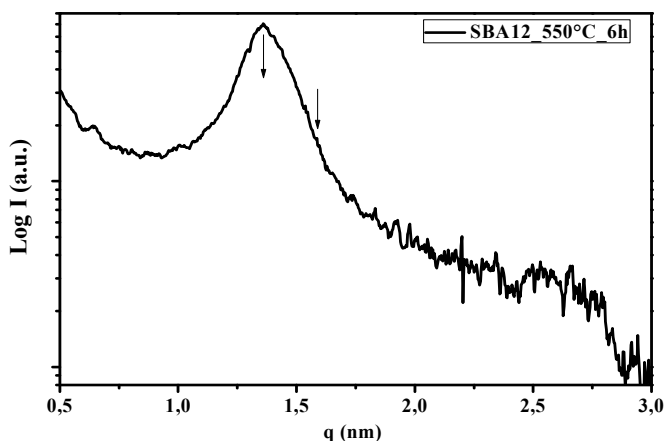


**Figure 35:** SAXS patterns of the calcined SBA-12.

between particles using formula  $2\pi/q$  is SBA-12 is known for having *hcp* or *ccp* structure. In the SAXS pattern of the prepared SBA-12 appears an intense scattering peak at  $q = 1.36 \text{ nm}^{-1}$  (Fig.35). This peak is assigned to (0 0 2) plane. Although no well resolved patterns for diffractions (1 0 0) and (1 0 1) diffractions are visible, can be due to the poor mesoporosity or increased cubic phase ratio. On calculating the average distance between particles using formula  $2\pi/q$  is 4.62 nm.<sup>[86]</sup>

The SEM micrographs of SBA-12 show irregular shaped rugged particles of *ca.* 10- 50 $\mu\text{m}$  size (Fig.36). The particle surface is strongly fissured and porous. The higher magnification image show micron-sized primary particles consist of secondary spherical agglomerated large nanoparticles of *ca.* 50-200 nm size (Fig. 36, bottom right).

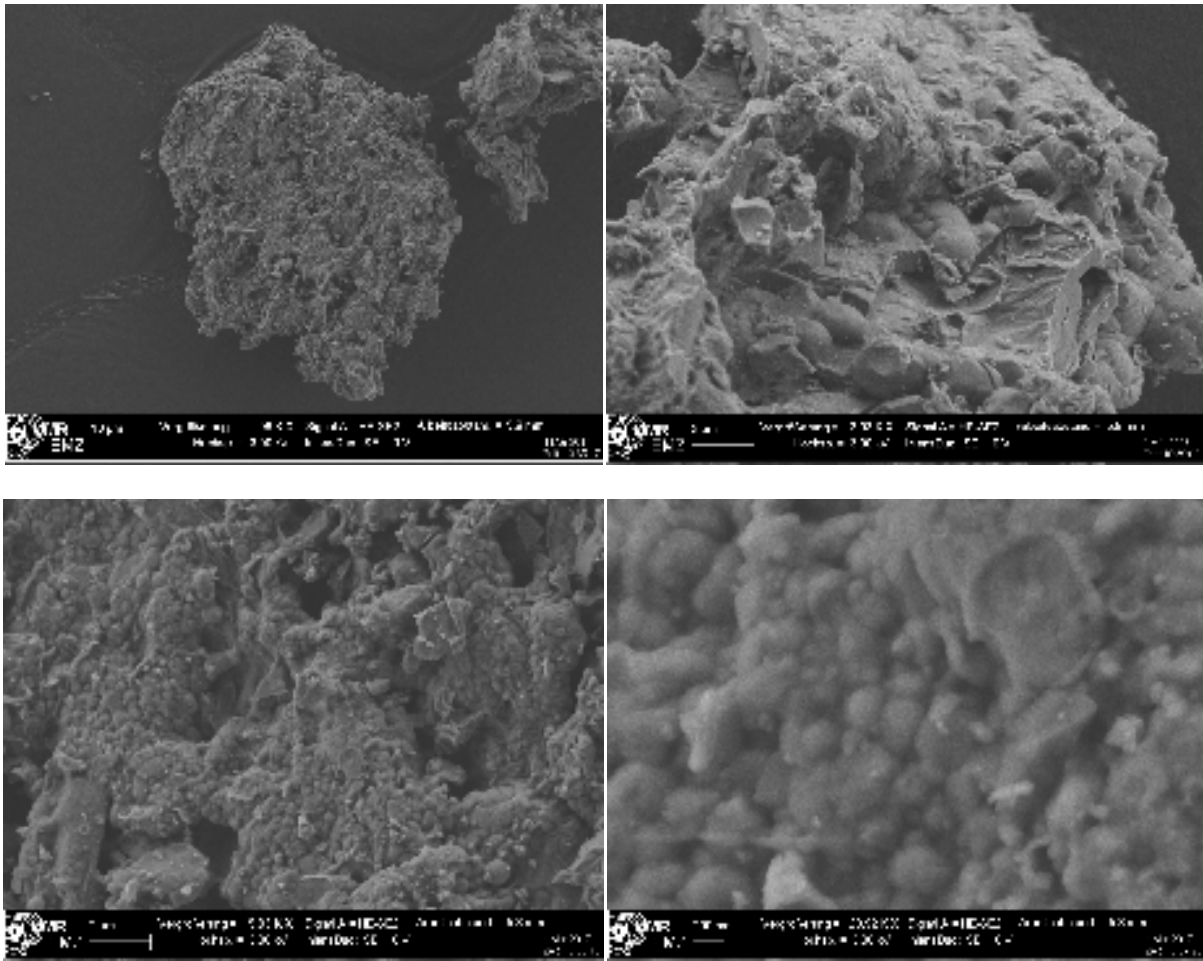


**Figure 36:** SEM images showing the morphology of SBA-12. Primary SBA-12 particle (top) consist of agglomerated submicron-sized particles (bottom).

Inspection with TEM shows the walls of these spheres can be considered to be made of the regular array arising might from the (1 0 0) which contains relatively large region for the cubic phase. TEM shows the large nanoparticles consist of tertiary agglomerated small nanoparticles (20-50nm size) which show in part the regular array of the channels (Fig. 37). This is also in line with the study of Terasaki and coworkers, who reported high-quality TEM images and concluded the functionalized SBA-12 having a pure face-centered cubic structure in which via small windows each sphere-like cage is connected to 12 other adjacent cages.<sup>[87]</sup> TEM confirms the regular array arising might from the (1 0 0) which contains relatively large region for the cubic phase.

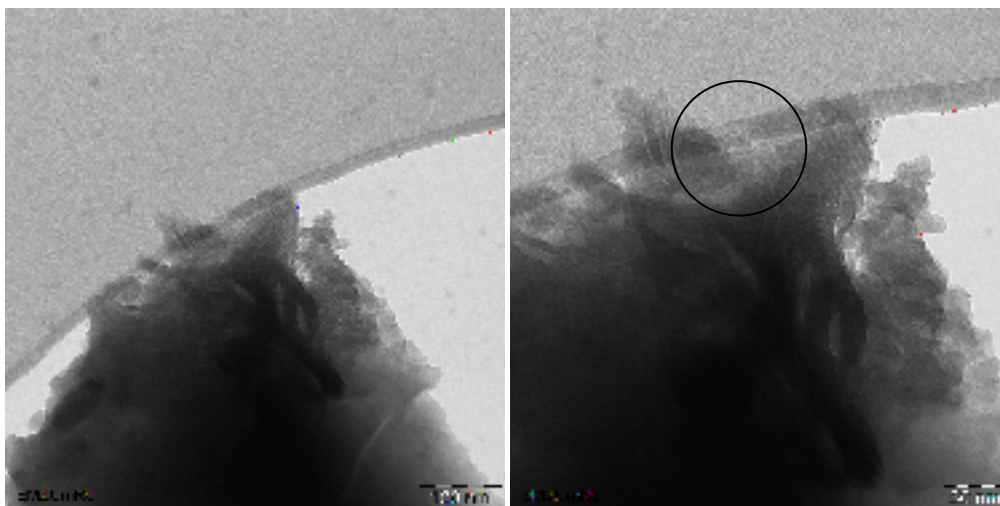


**Figure 37:** TEM images of the secondary agglomerated sub- $\mu\text{m}$ -sized nanoparticles forming the spherical  $\mu\text{m}$ -sized primary particles of SBA-12.

**FDU-12:-** Two types of FDU-12 samples were prepared with different reaction temperature at  $100^\circ\text{C}$  (FDU-S) and  $120^\circ\text{C}$  (FDU-L) and are discussed as bellow.

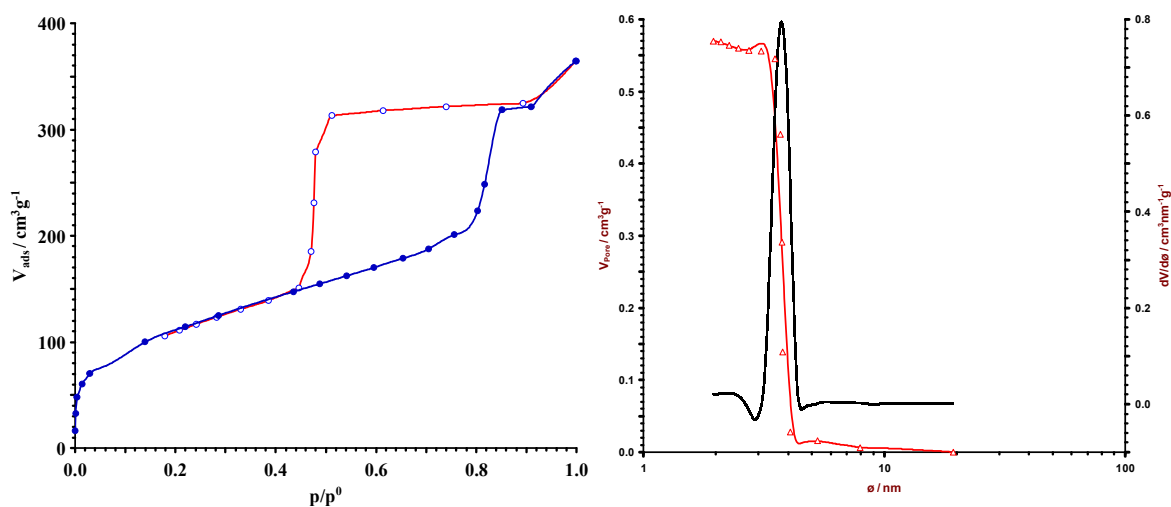


**Figure 38:**  $\text{N}_2$  ad-desorption isotherm curve and pore size distributions of the FDU-12-S.

Nitrogen adsorption isotherms of FDU-12-S and FDU-12-L show a steep increase of the isotherm at very low relative pressure due to adsorption in micropores. Isotherms of FDU-S show a gradual increase up to a relative pressure of *ca.*  $p/p_0 = 0.8$ , and a small adsorption step between  $p/p_0$  0.4 to 0.8 likely due to gradual pores filling of mesopores (Fig.38a). The reversible adsorption isotherms are of type IV and show a H2 type hysteresis loop at  $p/p_0 \sim 0.8$ , which starts at *ca.*  $p/p_0 = 0.4$  in  $\text{N}_2$  sorption isotherms of FDU-12s indicates large mesopores which vary with temperature (Fig.38 -39). With increasing synthesis temperature, window sizes of FDU-12-L is increased as shown in isotherms of samples treated at  $100^\circ\text{C}$  and  $120^\circ\text{C}$ ,

hysteresis loop transforms from H1 to H2 types, with maxima at  $\sim 4$  and  $5$  nm. Also at high temperature ( $120^\circ\text{C}$ ) hierarchical pores system with pore sizes from  $2$  to  $8$  nm is noted. The surface area decreases with increasing temperature from  $400$  to  $321\text{m}^2/\text{g}$  with increase of cumulative volume from  $0.56$  to  $0.85\text{cm}^3/\text{g}$ .

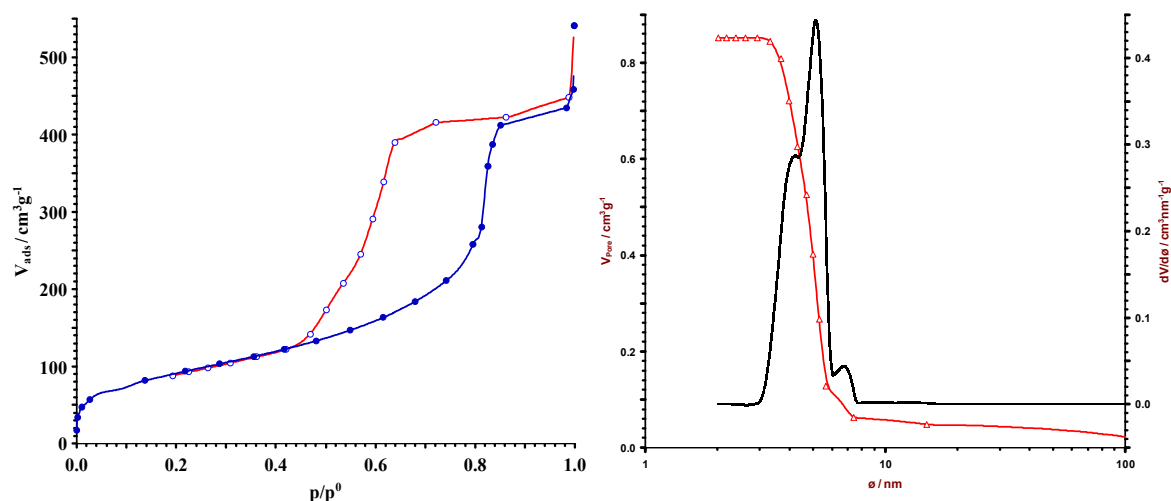


**Figure 39:**  $\text{N}_2$  adsorption-desorption isotherm curve and pore size distributions of the FDU-12-L.

From (Fig. 40), SAXS patterns of FDU-12, prepared at different temperatures shows well resolved scattering peaks and spacing distance. The peaks are shifted to lower  $q$  value with for sample treated at higher temperature. The FDU-12-S prepared at  $100^\circ\text{C}$  shows scattering maxima ( $q$ ) at  $\sim 0.39\text{nm}^{-1}$  which is assigned to (111) lattice plane. The peak maximum is shifted to  $\sim 0.40\text{nm}^{-1}$  when the preparation temperature of sample was increased to  $120^\circ\text{C}$ .  $q$  Scattering of (2 2 0) lattice plane is hidden inside the (1 1 1) lattice plane. Peak at  $q \sim 0.72\text{-}0.74\text{nm}^{-1}$  is assigned to (3 1 1) plane and  $0.95\text{-}0.97$  are assigned to (3 3 1) lattice planes. According to previous reports these can be indexed to face-centered cubic mesostructure according to reports before.<sup>[88]</sup>

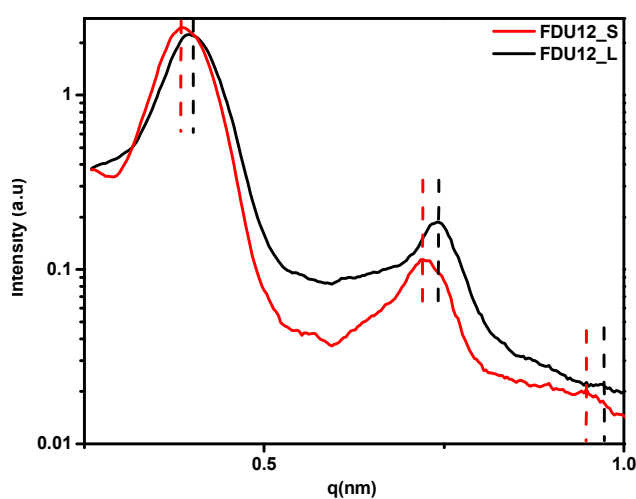


**Figure 40:** Small angle XRD patterns of the calcined FDU-S and FDU-12-L.

With scanning electron microscopy (SEM) for FDU-12-S spherical morphologies of micron sized particles are noted, which are composed of edged blocks, formed of spherical nanoparticles (Fig. 41). These spherical particles have relatively uniform sizes less than  $50$

nm. While FDU-12-L show well-defined crystalline materials of near hexagonal shaped particles (Fig. 42). These materials in high resolution show to consist of well-organized arrays of nanoparticles compacted together in correct order for the formation of mesocrystals. It is known to be difficult of direct measuring the pore sizes with TEM images. In case of FDU-12-L isolated hollow spheres can be easily find out at the fringe regions (Fig. 43). Based on TEM images and with N<sub>2</sub> isotherm reliable cage diameters can be deduced from the thin edges of the particle in Figure of about 8nm.<sup>[89]</sup> TEM images suggest that the FDU-12 is a uniform, well defined cubic mesostructure with highly ordered lattice array over large domains. Hence synthesized FDU-12 mesostructures are hierarchical structured and represent primary mesocrystals or so-called superstructures build up sub-micrometer-sized secondary and nanometer sized tertiary particles.

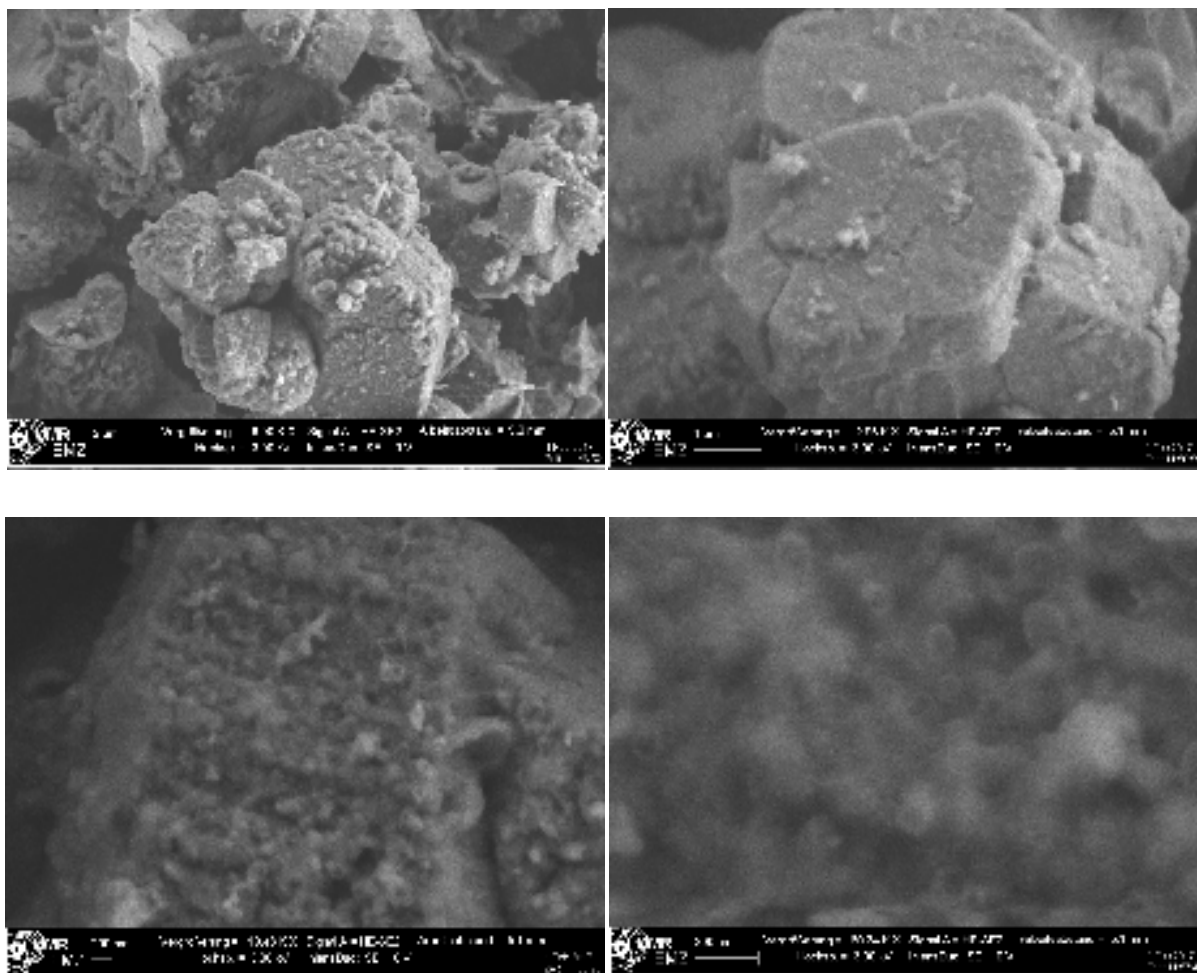


**Figure41:** SEM images showing the morphology of FDU-12-S.

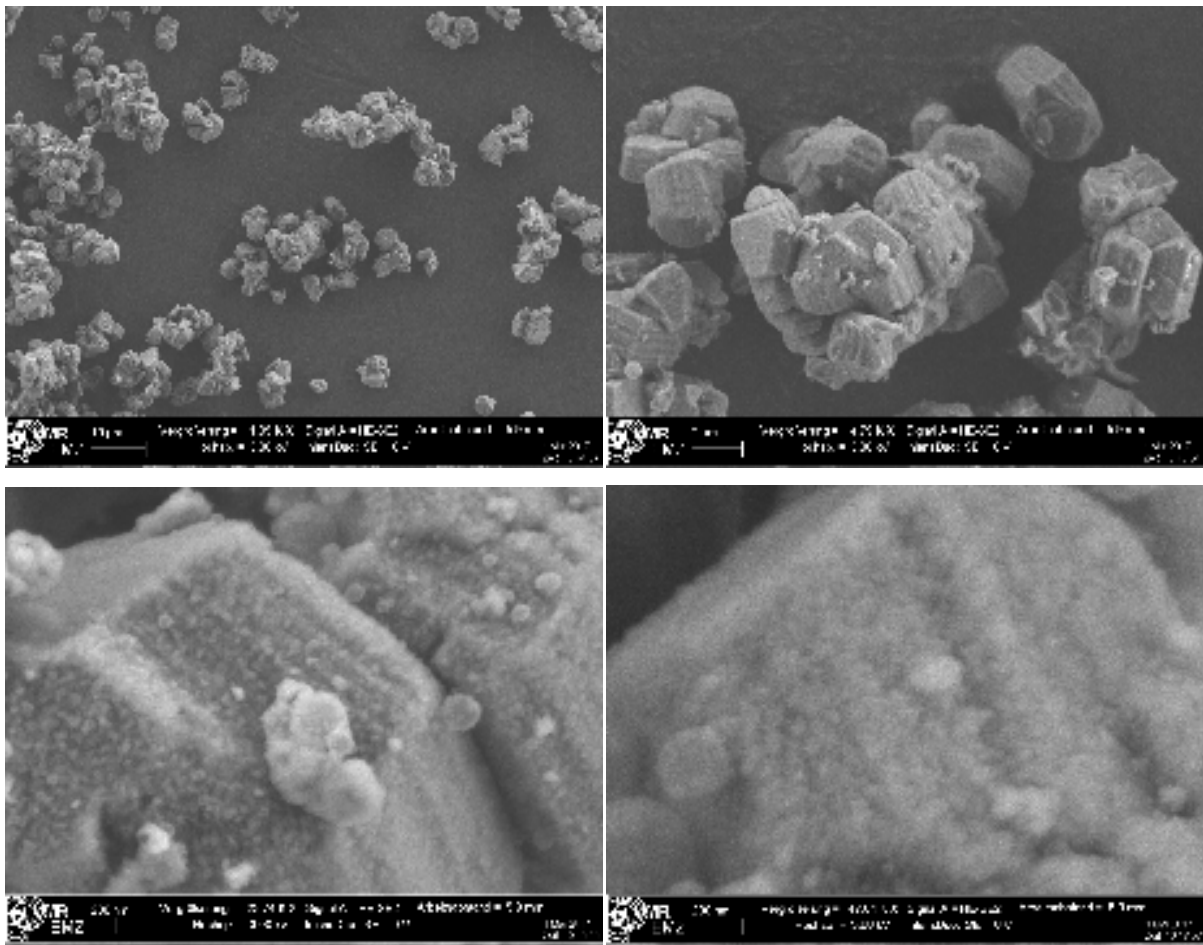
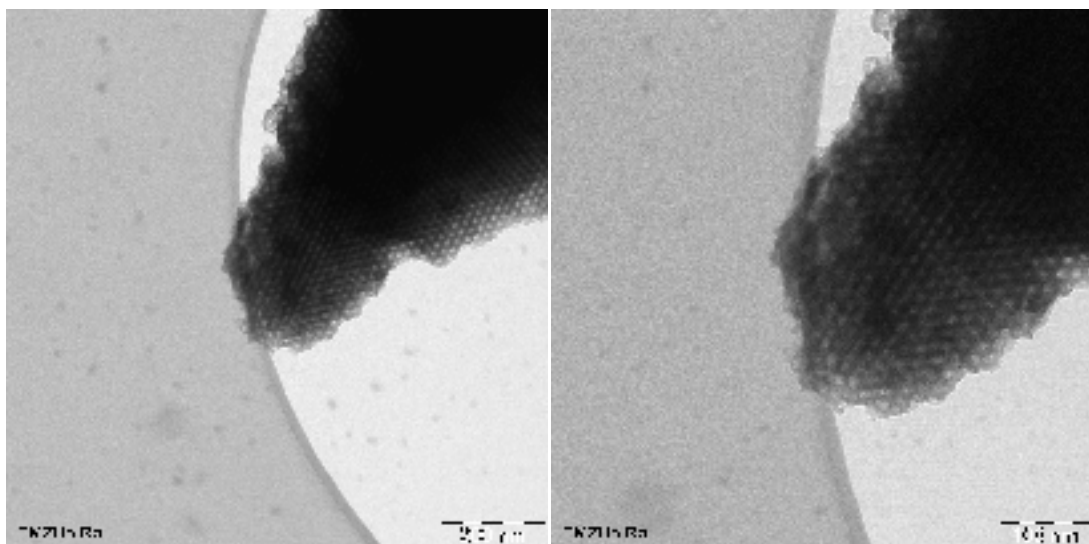
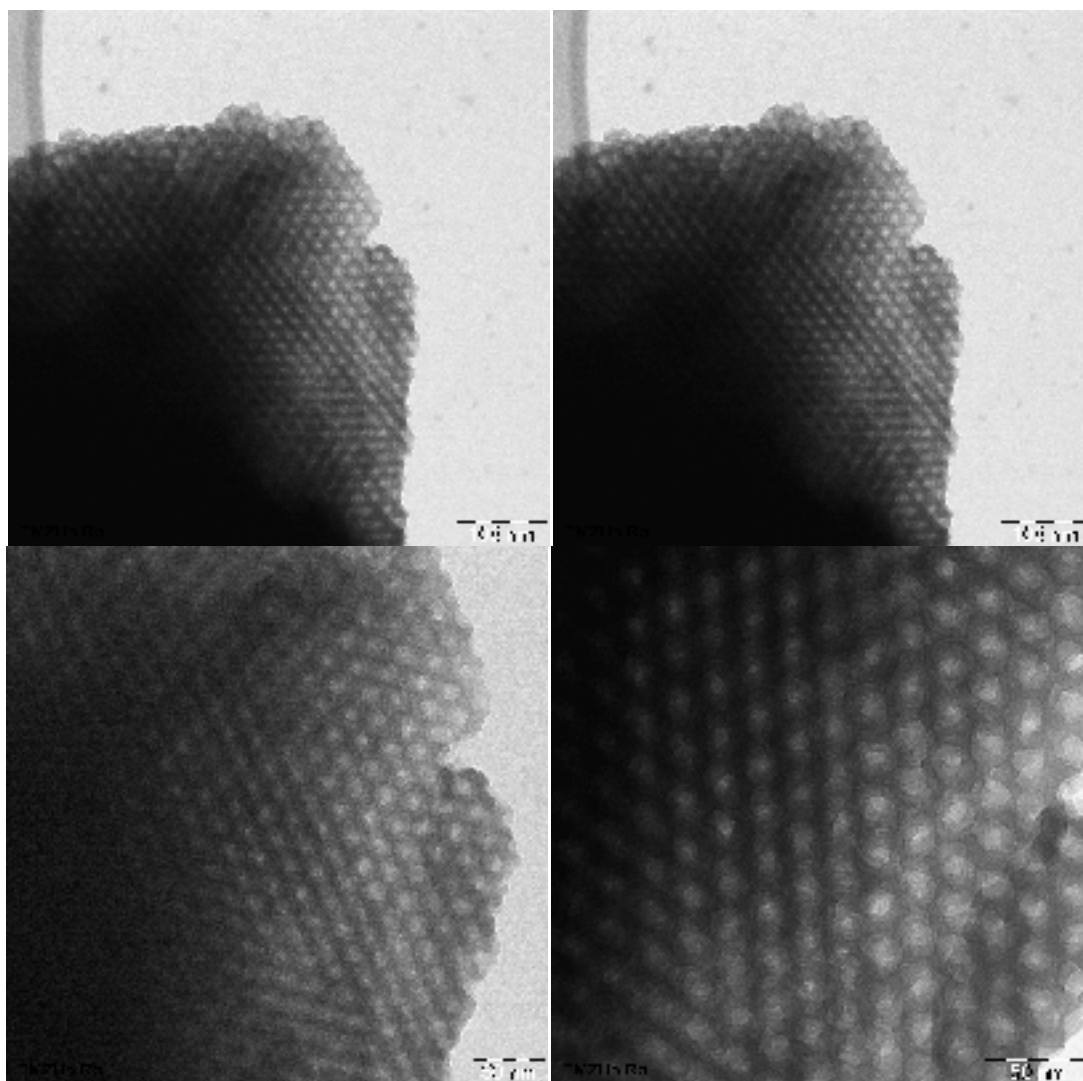


Figure 42: SEM images showing the morphology of FDU-12-L.





**Figure 43:** TEM images showing the uniform sized and ordered arranged mesopores of FDU-12-L.

**Table 1:** Summary of the Prepared Silica; Used templates, BET Surface area ( $\text{m}^2/\text{g}$ ), Average Pore Diameter BJH (nm), Desorption Cumulative Volume of Pores BJH ( $V_p$ ) ( $\text{cm}^3/\text{g}$ ).

No.	Sample	Template	Pore dimension	BET Surface area( $\text{m}^2/\text{g}$ )	$D_{\text{BJH}}$ (nm)	BJH ( $V_p$ ) ( $\text{cm}^3/\text{g}$ )
1	MCM-41-L	$\text{C}_{19}\text{H}_{42}\text{BrN}$	1D	719	13	1.79
2	MCM-41-S	$\text{C}_{19}\text{H}_{42}\text{BrN}$	3D	1034	2.62	1.10
3	MCM-48-S	$\text{C}_{19}\text{H}_{42}\text{BrN}$	3D	1800	2.45	1.10
4	MCM-48-L	$\text{C}_{19}\text{H}_{42}\text{BrN}$	3D	1100	2.40	0.96
5	KIT-6	Pluronic (P123)	3D	645	7.8	2.20
6	SBA-15	Pluronic (P123)	2D	978	2.5	0.88
7	SBA-16	Pluronic (F127)	3D	414	3.47	0.389
8	SBA-12	( $\text{C}_{18}\text{EO}_{10}$ )	3D	513	3.81	0.18
9	FDU-12(120)L	Pluronic (F127)	3D	321	5.12	0.85
10	FDU-12(100)S	Pluronic (F127)	3D	400	3.84	0.56

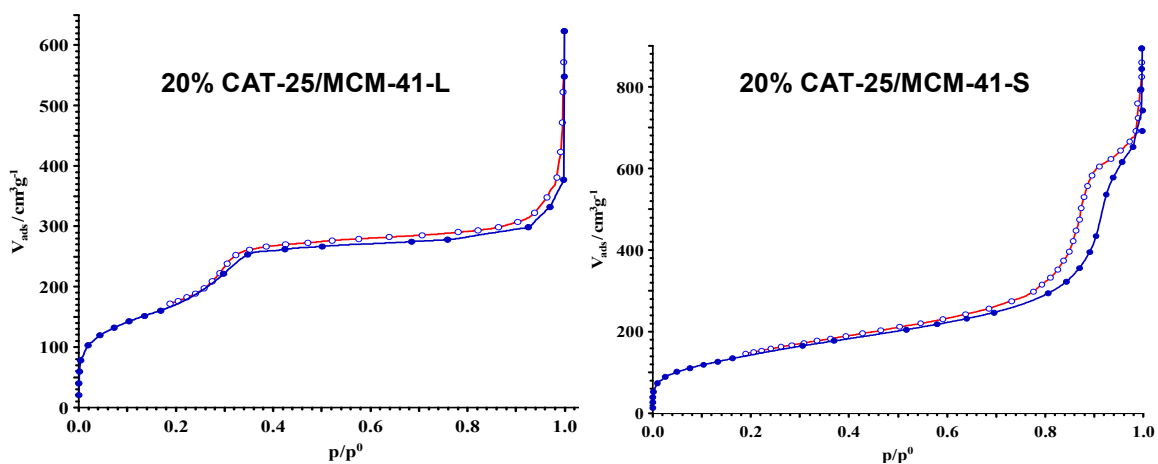
Ordered mesoporous silica-based materials containing pore systems of different dimensionality and pore size were prepared.

The specific surface areas are *ca.* 300-1800 m<sup>2</sup>/g and specific pore volumes *ca.* 0.2 -2.2cm<sup>3</sup>/g. High resolution SEM and TEM images that the bulky primary particles are composed of hierarchical secondary sub-micrometer sized secondary particles. And the latter are composed of agglomerated small nanoparticle of *ca.* 20-50 nm size.

### **3.1.3 Advanced Complex Inorganic Nanomaterials**

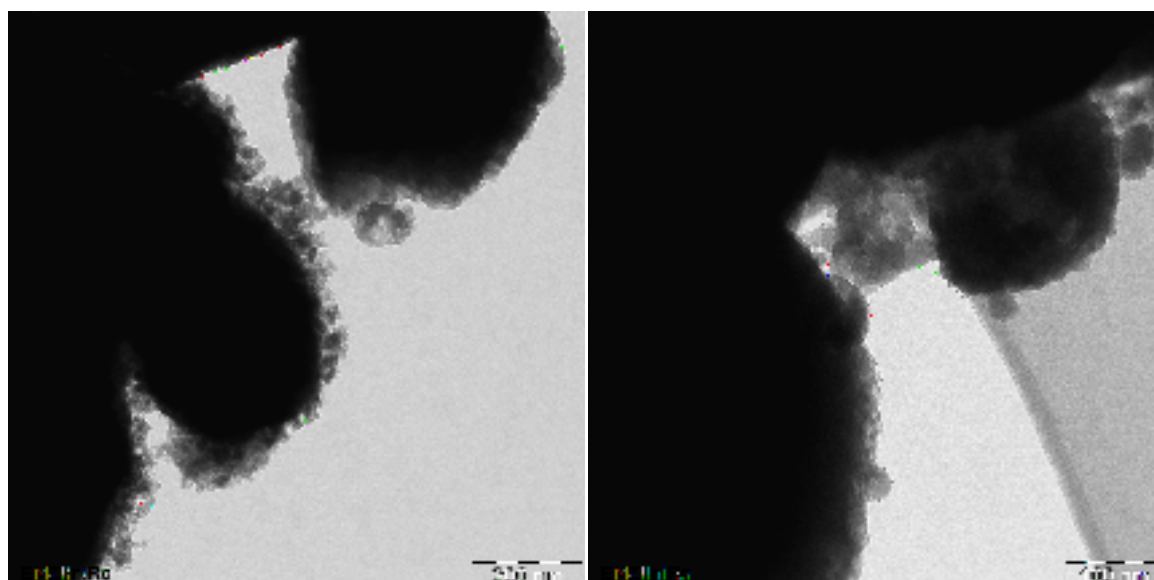
Advanced complex inorganic nanoparticles were obtained with mechanically mixing different percent of  $\beta$ -AgVO<sub>3</sub>/mpg-C<sub>3</sub>N<sub>4</sub> Core Shell /Composite catalyst with mesoporous silica such as KIT-6, MCM41, MCM48, SBA-n where n= 12, 15, 16 and FDU-12. Two selected examples containing 20% and 30% of highly active catalysts, CAT-25 and CAT-30, were mixed and mechano-chemical treated by milling with different mesoporous molecular sieves and are discussed here in detail.

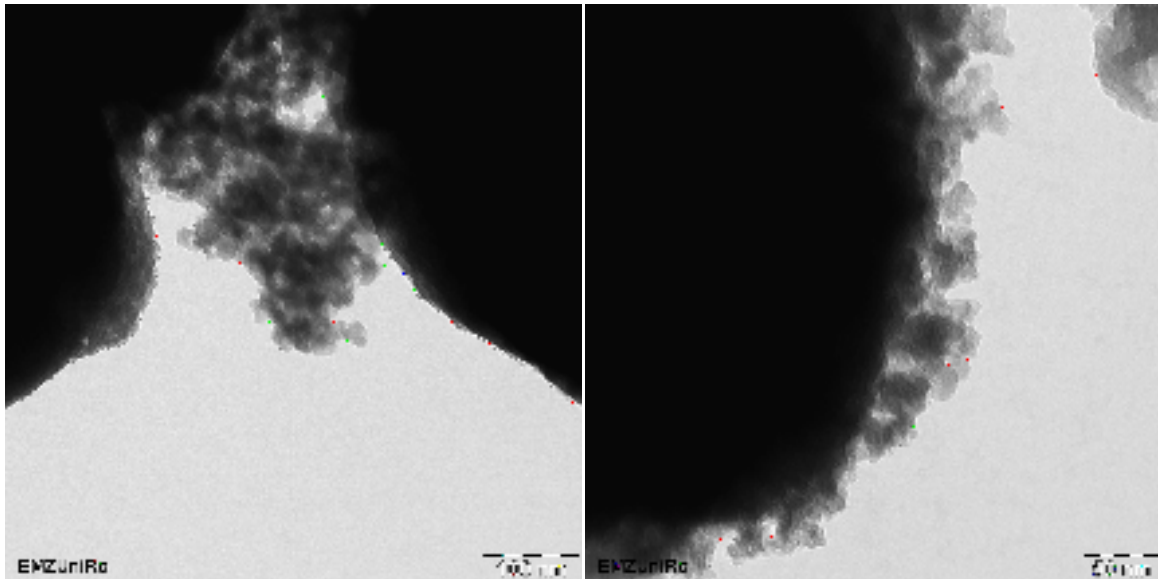
**20% CAT-25/MCM-41-S:-** The nitrogen isotherm of the 20% (25% $\beta$ -(AgVO<sub>3</sub>/ mpg-C<sub>3</sub>N<sub>4</sub>)/MCM-41-L assigned as 20%CAT-25/MCM-41-S, behaves similar as of the pure silica with similar hysteresis loop and uptake (Fig 44).They differ only in the increased N<sub>2</sub> uptake in the region above 0.95 which is referred to the aggregates of carbon nitride particles. Compared to the pure molecular sieve, the total surface area decreases to 526m<sup>2</sup>/g, with reduced cumulated pore volume and pore diameter of 15-16 nm. The isotherm shape of 20% CAT-25/MCM-41-S (with small porous system) is similar as MCM-41-S, the pore volume is decreased to 1.46 cm<sup>3</sup>/g, and reduced surface area to 618m<sup>2</sup>/g. The cumulative pore volume is 0.83cm<sup>3</sup>/g, and the maximum pore diameter is 2 nm according to BJH analysis. But the sample contains also hierarchical pores with diameter 28.2 nm due to hierarchical structure of the bulk.



**Figure 44:** N<sub>2</sub> adsorption-desorption isotherm curve of the 20% CAT-25/MCM-41-L and 20% CAT-25/MCM-41-S.

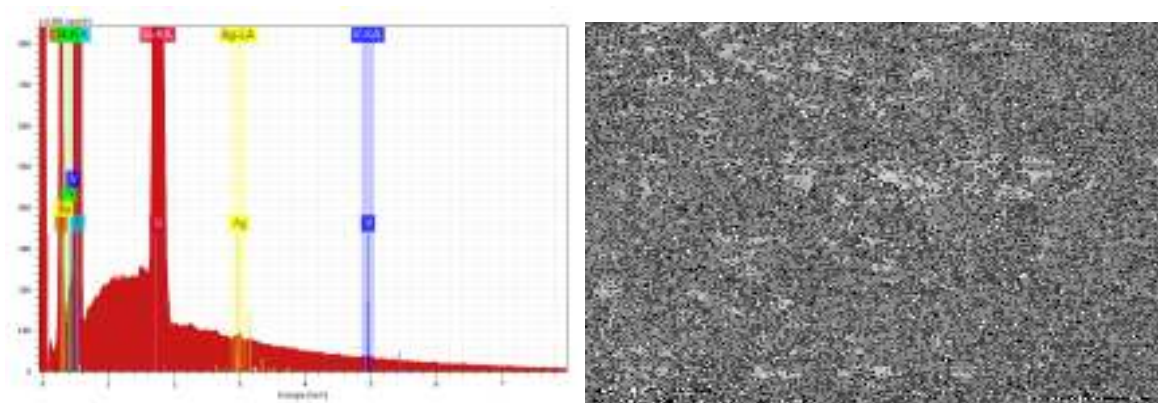
Interesting TEM images are observed with advanced complex inorganic materials where MCM-41-S is covered by the  $\beta$ -AgVO<sub>3</sub>/mpg-C<sub>3</sub>N<sub>4</sub> Core Shell/Composite catalyst with formation of porous cover on the upper surface of MCM (Fig. 45). The thickness of this surface layer is 10-30 nm. Still aggregates of carbon nitride can also be found nearby silica particles. Carbon nitride nanosheets range from 20 to 50 nm. Although silver vanadate rods cannot be spotted out, this is in low concentration and might be embedded inside the carbon nitride and silica.

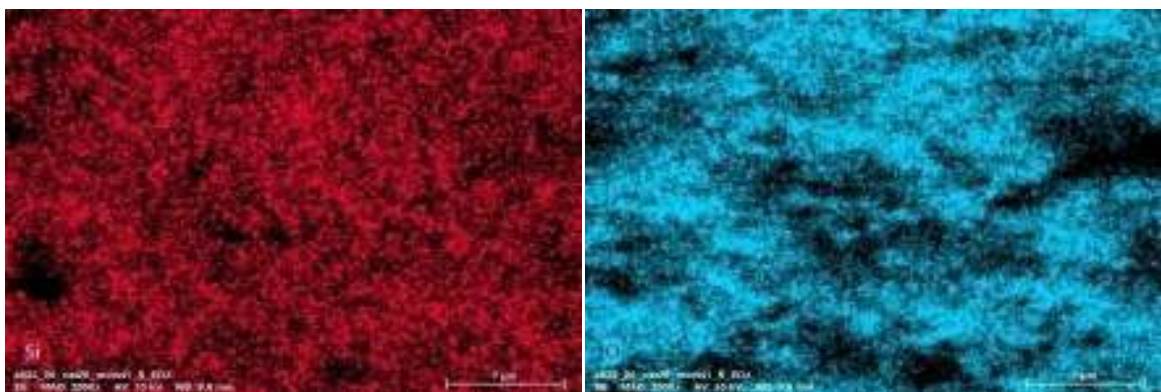
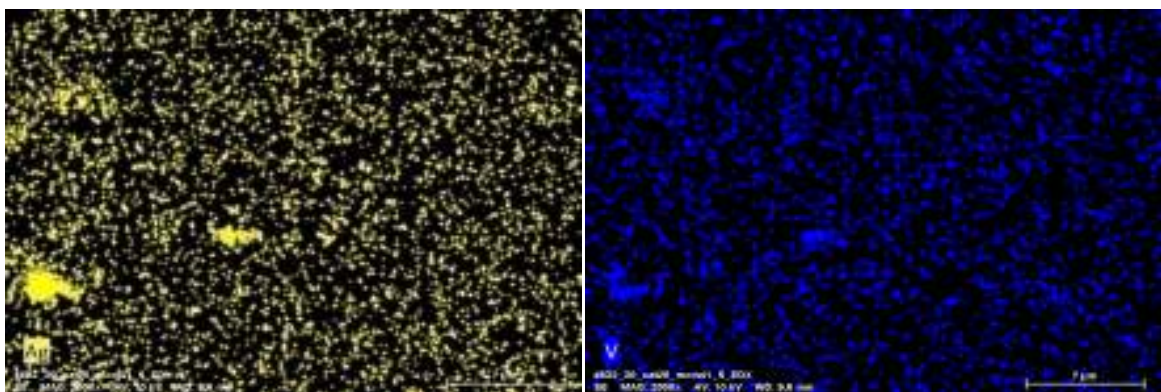
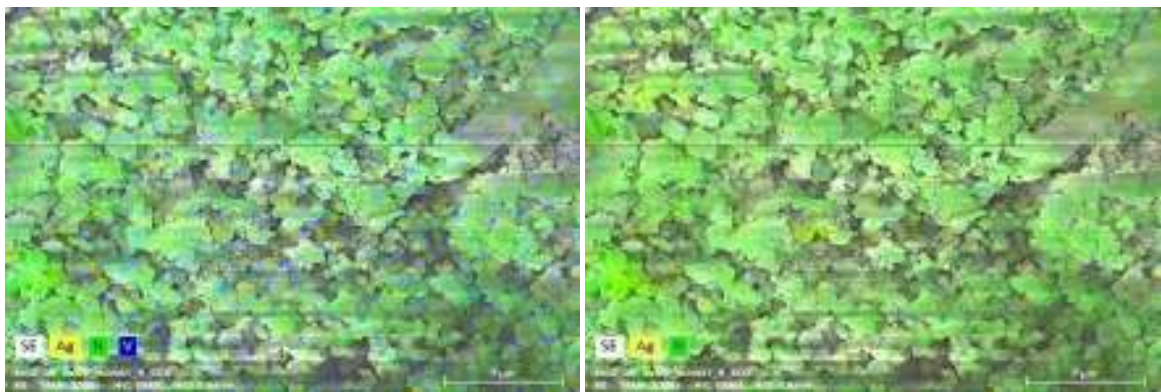
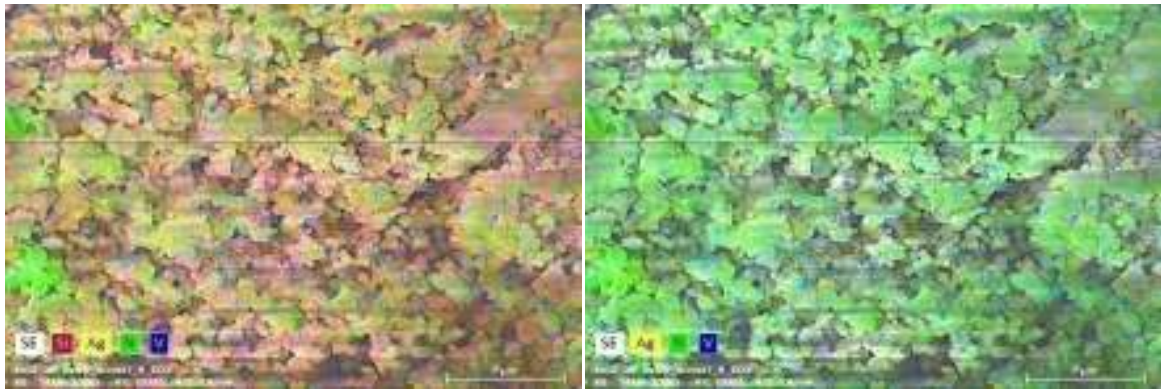




**Figure 45:** TEM images showing the morphology of 20% CAT-25/MCM-41-S.

The elemental analysis of the prepared SilverVanadate/Carbon Nitride/Silica ternary system called as CAT-25/Silica was studied with Energy dispersive x-ray spectra (EDX). The EDX spectra reveal the elements Ag, V, O, Si, C, and N in the material without any other significant impurities as shown in Fig.46. Elemental mapping shows high dispersion of the catalyst and uniform distribution of all elements within sample, which not only supports the Core Shell catalyst, but also the observation of equal distribution of Core Shell photocatalyst above the silica.





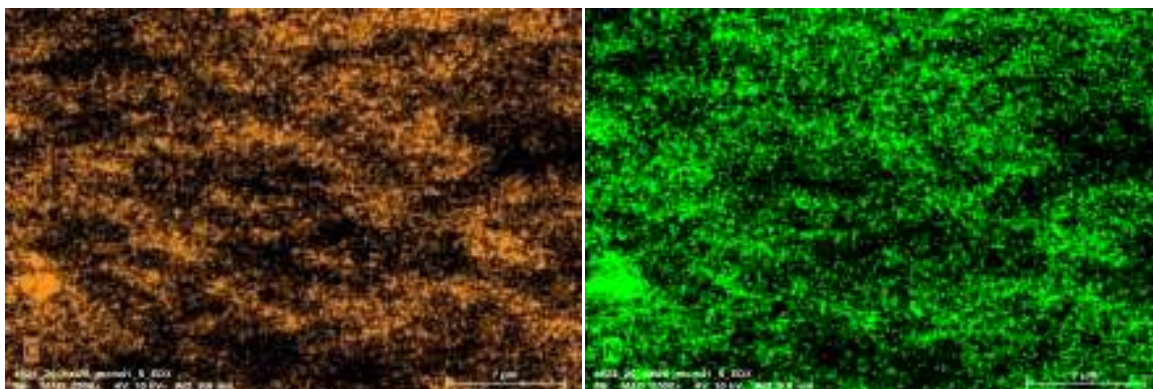


**Figure 46:** EDX spectrum, and elemental mapping showing the uniform distribution of the 20% CAT-25/MCM-41-S. Elements Ag (yellow circle), V (blue circle), O (light blue circle), Si (red circle), N (green circle), C (orange circle).

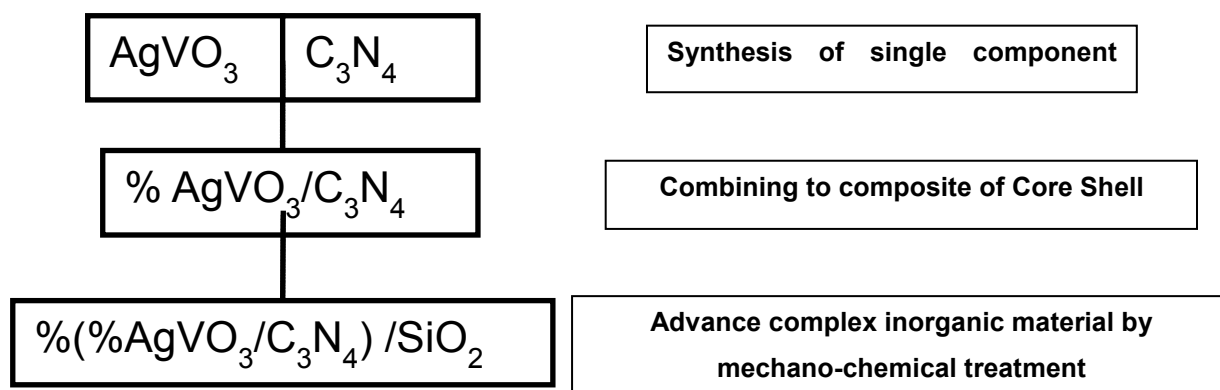
The high dispersion of the catalytic component, which is combined (supported) with the mesoporous materials, which are also hierarchical regarding the porosity and the bulk composition, should ensure superior dispersion and accessibility of catalytic active sites as well as exhibit enhance mass transfer properties.

## 3.2 Photocatalysis

### 3.2.1 Photocatalytic Performance of Mechano-Chemical Prepared $\beta$ -AgVO<sub>3</sub>/mpg-C<sub>3</sub>N<sub>4</sub> Core Shell Composites

In order to prepare and optimize an effective Core Shell catalyst by simple mechano-chemical treatment, the mpg-C<sub>3</sub>N<sub>4</sub> to  $\beta$ -AgVO<sub>3</sub> ratio was systematically varied. The obtained catalysts were characterized (see above) and photocatalytically tested. Finally, the activity was compared with that of the titania and ZnO photocatalyst.

As a result, an advanced complex inorganic nanomaterial (ACIN) type catalyst was obtained by additional combining the obtained Core Shell catalysts with different types mesoporous silica.



**Scheme 4:** Scheme of the development /preparation of an advanced complex inorganic photocatalytic nanomaterial: from single catalytic component to composites/Core Shell s to catalytic ACINs.

In the present work,  $\beta\text{-AgVO}_3/\text{mpg-C}_3\text{N}_4$  Core Shell composites and complex supported  $\beta\text{-AgVO}_3/\text{mpg-C}_3\text{N}_4/\text{SiO}_2$ , were developed and compared to titania, zinc oxide and as well as supported  $\text{TiO}_2\text{-SiO}_2$ ,  $\text{ZnO-SiO}_2$ , nano-sized photocatalysts. The composite and silica supported catalysts show large specific surface areas and were synthesized by a solvent-free mechano-chemical treatment, i.e. by simply milling the photocatalysts (metal oxides/vanadates, carbon nitrides) and the supports. The photocatalytic activity of the synthesized nanoparticles was evaluated by the photocatalytic degradation of ibuprofen (IBP) as a model pollutant under UV/Vis irradiation.

Figure.48 shows typical UV/Vis spectra of Ibuprofen solutions after photocatalytic treatment over  $\beta\text{-AgVO}_3/\text{mpg-C}_3\text{N}_4$  Core Shell photocatalyst with UV/Vis and visible light. The absorbance decreases during the course of photocatalytic treatment time, under UV and visible irradiations indicating IBP degradation. Typically after specific intervals of time, ~4 mL of the ibuprofen solution was separated and the intensity change of UV/Vis absorption bands of IBP were measured (Fig. 47a-b). The spectra show a decrease of the aromatic ring absorbance at 193.5 and 222nm, due to the degradation or cleavage (opening) of the aromatic ring. At the same time, a new broad absorbance appears at *ca.* 260 nm. Its intensity increases at onset of reaction faster and decreases again with prolonged photocatalytic treatment. This band is assigned to the formation of reaction intermediates; likely hydroxylated IBP molecules (compare Scheme 1 Mechanism 1)

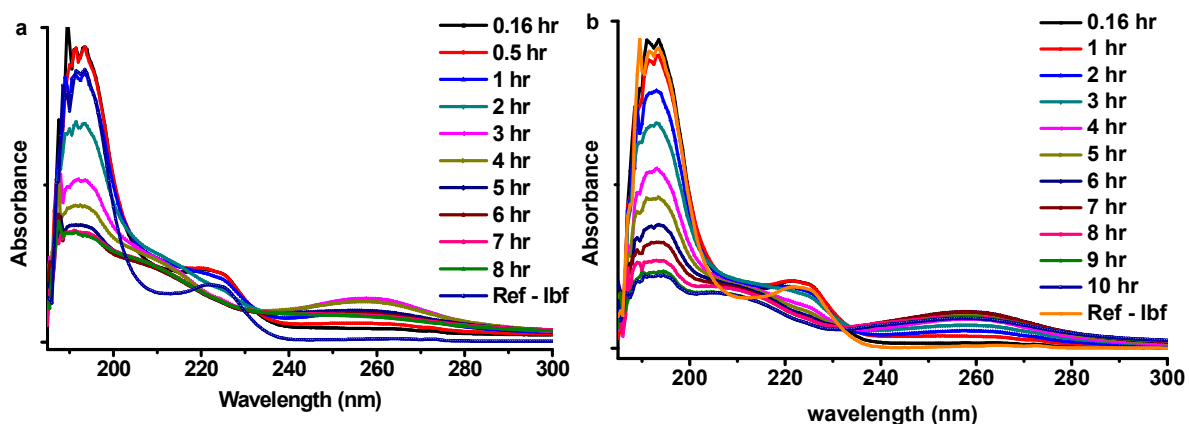


**Figure 47:** UV/Vis spectra of photocatalytic treated Aqueous IBP solution in dependence of time, over  $\beta$ -AgVO<sub>3</sub>/mpg-C<sub>3</sub>N<sub>4</sub> Core Shell photocatalyst using a) UV/Vis, b) Visible light; (10 mg/L catalyst, 250 mL of 10 ppm IBP. Solution, Irradiation: 60W UV/Vis light or 16.

### *Variation of the $\beta$ -AgVO<sub>3</sub>/mpg-C<sub>3</sub>N<sub>4</sub> composition*

Briefly a quick and simple procedure for the preparation of different composed  $\beta$ -AgVO<sub>3</sub>/mpg-C<sub>3</sub>N<sub>4</sub> Core Shell catalysts was developed, which showed excellent visible room light activity. In a simple mechano-chemical way we have physically combined and mixed proper amounts of ingredients and milled the mixtures for *ca.* 15 minutes thoroughly. The resultant materials were thermally treated at 300°C for 3 hours. This treatment increases the contact of both ingredients and forces the polymeric carbon nitrides to wrap around the silver vanadate rods. We have intensively studied different possible loading ratios between 0 and 1. It was found that 20-30% loading of  $\beta$ -AgVO<sub>3</sub> nanorods with mesoporous graphitic carbon nitride results in the formation of a Core Shell type catalyst. Besides, some free ingredients ( $\beta$ -AgVO<sub>3</sub>, mpg-C<sub>3</sub>N<sub>4</sub>) were present. These catalysts show highest activity compared to similar composed non-Core Shell composites. The photocatalytic activity was  $\sim$ 20 times higher compared to the starting graphitic carbon nitride. Silver vanadate nanorods show only formation of minute amount of unknown intermediates under same conditions. The mineralization (determined from TOC-total organic carbon content of the reaction solution) confirms the 80% removal within 8 hours of treatment over catalysts. It is found that degradation and mineralization of the ibuprofen proceeds parallel, not like most studied TiO<sub>2</sub> photocatalysts, where the mineralization is markedly lower than the degradation determined by UV/Vis spectrometry. (Fig. 48) shows the abatement of Ibuprofen solution over different loaded  $\beta$ -AgVO<sub>3</sub>/mpg-C<sub>3</sub>N<sub>4</sub> photocatalysts under UV/Vis and visible light irradiation with a catalyst to substrate ratio of 4.

The different silver vanadate loaded  $\beta$ -AgVO<sub>3</sub>/mpg-C<sub>3</sub>N<sub>4</sub> composites are named according to the percentage of loading as follow: 20% $\beta$ - AgVO<sub>3</sub>/mpg-C<sub>3</sub>N<sub>4</sub> = CAT-20; 30%  $\beta$ -AgVO<sub>3</sub>/mpg-C<sub>3</sub>N<sub>4</sub> = CAT-30, and so on.

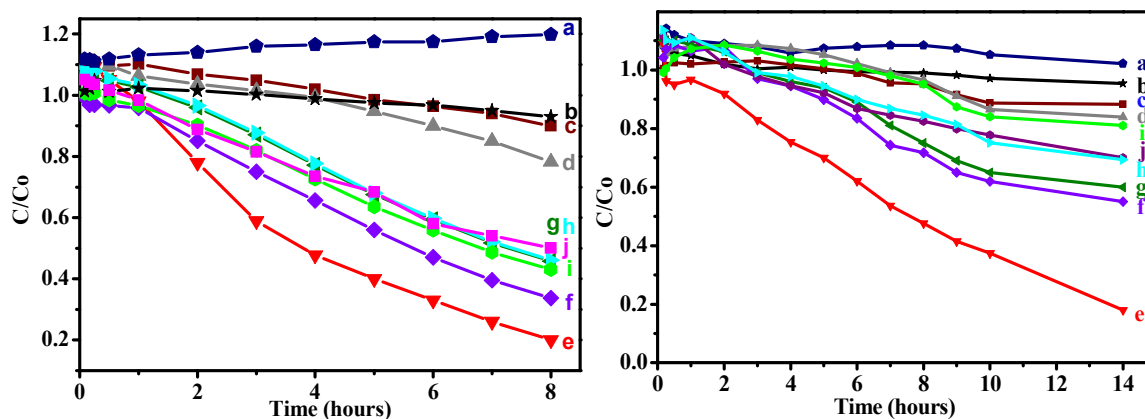


**Figure 48:** Relative abatement of IBP during the course of photocatalytic treatment under UV/Vis (left) and visible light (right) irradiation over a)  $\beta$ -AgVO<sub>3</sub>, b) mpg-C<sub>3</sub>N<sub>4</sub>, and  $\beta$ -AgVO<sub>3</sub>/mpg-C<sub>3</sub>N<sub>4</sub> composites containing c) 5% d) 10% e) 20% f) 30% g) 40% h) 50% i) 70% of silver vanadate and 20%  $\beta$ -AgVO<sub>3</sub>/mpg-C<sub>3</sub>N<sub>4</sub> (j) prepared with co-precipitation.

#### ***Irradiation with UV/Vis irradiation:***

The relative abatement of Ibuprofen vs. photocatalytic treatment time over different 5-70%  $\beta$ -AgVO<sub>3</sub>/mpg-C<sub>3</sub>N<sub>4</sub> Core Shell composites and the starting components  $\beta$ -AgVO<sub>3</sub> and mpg-C<sub>3</sub>N<sub>4</sub> are shown (Fig. 48left). Interestingly, an apparent increase in the abatement is observed in the first 30 min. of photocatalytic treatment, which is not observed in the dark. Obviously, it is due to the formation of reaction intermediates, partial oxidation products or radicals, which show a higher extinction coefficient than the starting IBP solution. Thereafter, a gradually decrease is observed due to the degradation of the IBP and intermediates. About 5% abatement of IBP is achieved after 8h with the mpg-C<sub>3</sub>N<sub>4</sub> alone. The addition of  $\beta$ -AgVO<sub>3</sub> (composites) leads to an improvement of the degradation to 10 and 22% with 5 and 10-%  $\beta$ -AgVO<sub>3</sub> loading, respectively. Surprisingly, a boosting of the activity is observed with the 20%  $\beta$ -AgVO<sub>3</sub>/mpg-C<sub>3</sub>N<sub>4</sub> catalysts. Ca. 80% abatement is achieved after 8h. However, further enhancement of the  $\beta$ -AgVO<sub>3</sub> content to 70% leads again to a decrease of the degradation to ca. 55%. It is concluded that the exceptional high activity of the 20%  $\beta$ -AgVO<sub>3</sub>/mpg-C<sub>3</sub>N<sub>4</sub> composite catalyst is related to the “Core Shell” nature of this material, where the mpg-C<sub>3</sub>N<sub>4</sub> is forming a thin (7 – 10nm) shell around the  $\beta$ -AgVO<sub>3</sub>nanorods. As evidenced by TEM, at higher loading  $\beta$ -AgVO<sub>3</sub>/mpg-C<sub>3</sub>N<sub>4</sub>composites were obtained showing lower activity (Fig. 48).The pure  $\beta$ -AgVO<sub>3</sub> shows only low activity with the formation of some partial oxidation

products leading to an increase in the absorption band at *ca.* 193.5 nm with UV/Visible spectroscopy. Interestingly, the mechano-chemical prepared Core Shell catalyst showed markedly higher activity (80%) than a similar composed catalyst obtained by co-precipitation (50%) confirming the high potential of the solvent-free and simple mechano-chemical preparation method.

#### ***Irradiation with visible room light:***

The degradation behaviour of the  $\beta$ -AgVO<sub>3</sub>/mpg-C<sub>3</sub>N<sub>4</sub> composite catalysts under room light visible irradiation is similar to the results obtained under UV/Vis solarium light irradiation (Fig. 49right). The photocatalytic degradation of the IBP proceeds 2 times slower. But it has to be taken in to account that the visible light irradiation power is also markedly lower. Again the catalyst (20%  $\beta$ -AgVO<sub>3</sub>/mpg-C<sub>3</sub>N<sub>4</sub>) showed superior activity. About 80% of ibuprofen degradation was achieved after 13-14 h. Again, formation of reaction intermediates was observed in UV/Vis spectra of the reaction solution at the beginning of the treatment giving rise to an absorbance at *ca.* 260 nm. The other composites showed a distinctly lower activity with up to *ca.* 30% of degradation of IBP over 30, 50 and 70%  $\beta$ -AgVO<sub>3</sub>/mpg-C<sub>3</sub>N<sub>4</sub> composites. Hence, the difference in the photocatalytic degradation activity between the core-shell and composite catalyst as well as co-precipitated catalyst is much more pronounced under room light conditions than under UV irradiation. 20%  $\beta$ -AgVO<sub>3</sub>/mpg-C<sub>3</sub>N<sub>4</sub> prepared with co-precipitation showed *ca.* 30% of degradation.

Both, irradiation with sunlight UV as well as room light, cause similar changes in the UV /Vis spectra of the irradiated solution indicating that there is no difference in the degradation mechanism between the two light sources. A *ca.*20 times increase of photocatalytic activity was noted with the Core Shell catalyst compared to the single mpg-C<sub>3</sub>N<sub>4</sub>, while the increase is a markedly lower with the composites (*ca.*9 times) or hybrid systems (co-precipitation). Compared to silver vanadate the activity in the degradation of ibuprofen is enhanced almost by 100 times under sunlight equivalent UV and visible light.

These findings form the basis for the improvement of the binary composite systems to ternary hierarchical structured systems by supporting mesoporous  $\beta$ -AgVO<sub>3</sub>/mpg-C<sub>3</sub>N<sub>4</sub> composites of different silver vanadate content on different structured ordered mesoporous silica materials. The developed Core Shell catalyst and other composites with mesoporous silica as a stationary support were mixed and mechano-chemical treated for the preparation of ternary systems. The use of other preparation methods as impregnation or supporting via sol-gel and

thermal hydrolysis resulted in lower active photocatalysts. While the mechano-chemical preparation method yielded catalysts with improved photocatalytic activity.

### ***3.2.2 Photocatalytic Performance of Hierarchical Structured, Core Shell, 25-30% $\beta$ -AgVO<sub>3</sub>/mpg-C<sub>3</sub>N<sub>4</sub> Catalyst Supported on Ordered Mesoporous Silica***

As shown in the scheme 4, this study was extended to the development of improved complex hierarchical  $\beta$ -AgVO<sub>3</sub>/mpg-C<sub>3</sub>N<sub>4</sub> composite catalysts loaded on selected ordered mesoporous materials MCM-41, KIT-6 and FDU-12. The hierarchical catalysts were prepared by mechano-chemical mixing with different ordered mesoporous silica as described in chapter 2. The 3 different structure types were selected in order to study the effect of porosity, architecture and sizes of pores provided by various silica structures. Additionally, the composition of the complex catalysts (silica content) was varied in order to optimize the photocatalytic performance. The obtained ternary systems show boosted photocatalytic activity which allows to reduce the used amount of photocatalysts (improved atom efficiency regarding noble silver) as shown below.

#### ***30% $\beta$ -AgVO<sub>3</sub>/mpg-C<sub>3</sub>N<sub>4</sub> (CAT- 30) Core Shell Catalyst Loaded on MCM-41***

For general representation single model examples based on highly active catalysts 30%  $\beta$ -AgVO<sub>3</sub>/mpg-C<sub>3</sub>N<sub>4</sub> (CAT- 30) and 25%  $\beta$ -AgVO<sub>3</sub>/mpg-C<sub>3</sub>N<sub>4</sub> (CAT-25) were photocatalytically investigated using UV /Vis and visible light (room light) irradiation. In the example below, a system was developed, where 30 %  $\beta$ -AgVO<sub>3</sub>/C<sub>3</sub>N<sub>4</sub> Core Shell photocatalyst (assigned as Cat-30) in variable amount was mixed with mesoporous silica such as MCM-41 as a support via mechano-chemical mixing, milling and calcinations to 300°C.

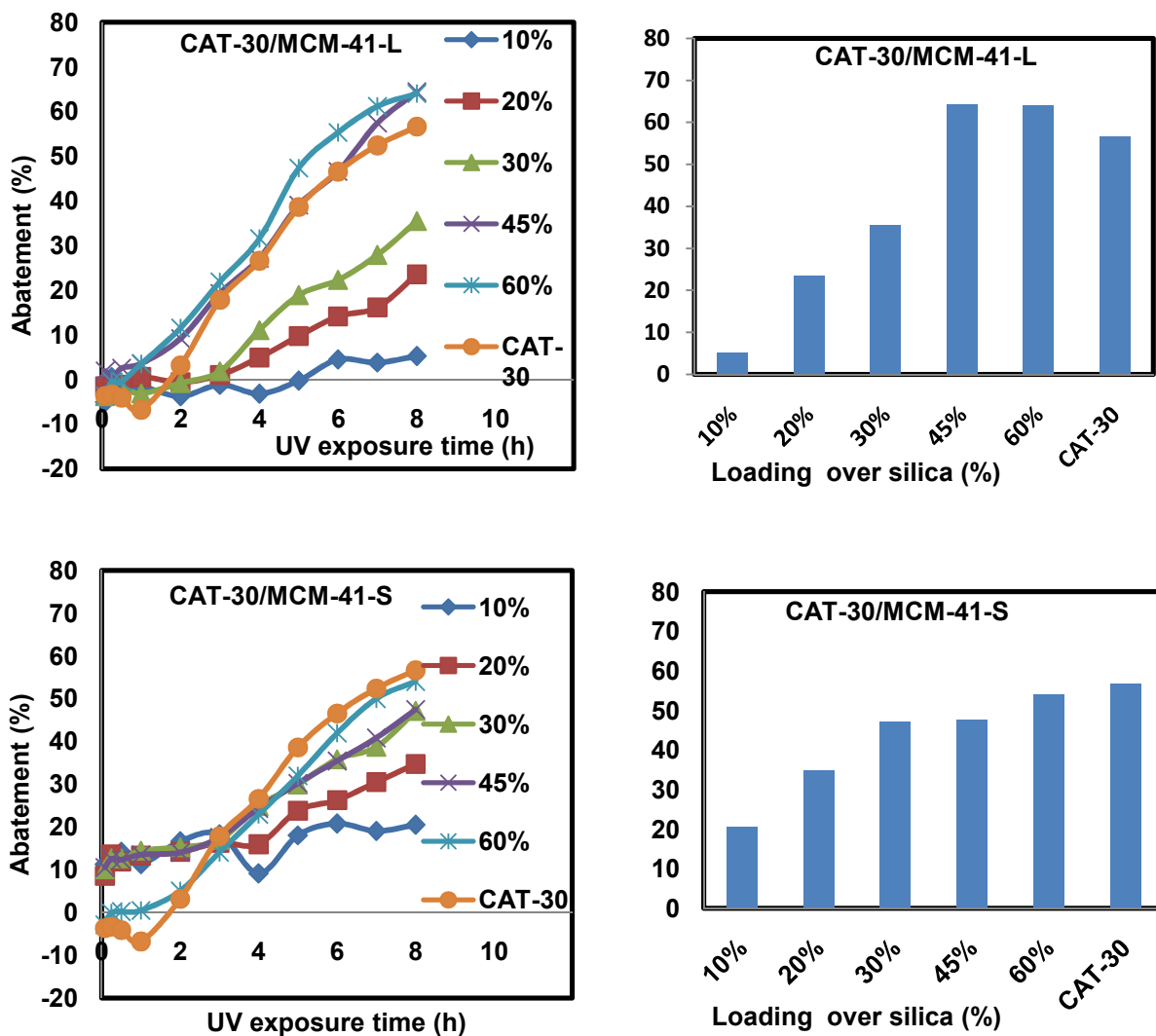


**Figure 49:** Relative abatement of IBP during the course of photocatalytic treatment under UV/Vis irradiation over a) % CAT-30/MCM-41-L (Left, up) and % CAT-30/MCM-41-S (left down). Final degradation of IBP after 8 hours of photocatalytic treatment over a) % CAT-30/MCM-41-L (right, up) and % CAT-30/MCM-41-S (right down).

Variable amount of CAT-30 was loaded on small and large pore mesoporous silica MCM-41, which resulted in a pronounced improvement of the photocatalytic degradation efficiency (Fig. 49). The CAT-30 content was varied from 10% to 60% loading in steps of 10%.

Large porous MCM-41 with low loading of CAT-30 such as 10, 20 and 30% show low photocatalytic activity of 5, 20 and 30% abatement 8 hours treatment under UV/Vis light, respectively. In contrast to large pore MCM-41, the small pore MCM-41 shows higher abatement. This is due to an enhanced adsorption of the pollutant in the smaller pores and further facilitated by the larger specific surface area. Already at the onset of treatment ca. 10% of IBP is abated by adsorption. The adsorption takes place in the silica component, because with CAT-30 and 60% CAT-30 loaded catalyst no adsorption is found with small pore MCM-41 sample (Fig. 36).

### Relative Atomic efficiency:

Because silver vanadate is the expensive active component catalyst, costs are determined by the amount of used silver vanadate. It is observed that the supporting of the silver vanadate/carbon nitride composite on mesoporous silica significantly enhances the efficiency of the catalyst based on the silver content.

The atomic efficiency was calculated according formula was developed as below:

$$\text{Relative atomic efficiency} = \frac{\text{Achieved deg With CAT}-X [\%]}{\text{Deg.by 100 \% pure Catalyst} [\%]} X * f ,$$

where X is the loading of the active composite component on the mesoporous silica support and the factor  $f = 100 / \% \text{ of CAT catalytic component}$ .

The relative changes in the efficiency achieved with the complex hierarchical catalyst compared to the pure loaded  $\beta\text{-AgVO}_3/\text{mpg-C}_3\text{N}_4$  composite component are shown in Figure 51. A remarkable  $\sim 2$  times increase in the specific abatement over the resultant ternary photocatalysts containing 20-30 % of  $\beta\text{-AgVO}_3/\text{mpg-C}_3\text{N}_4$  is noted for large porous MCM-41. While loading of MCM-41-L with 10% CAT-30, results in an atomic efficiency similar to that of the original CAT-30. While 2.5 times atomic ratio enhancement in activity was noted for 45% loading, this is followed by 2 times increase in activity for 65% loading. Overall it is concluded that with large porous silica (MCM-41-L) the photocatalytic activity is highly increased. The efficiency of ternary composite systems is always higher than that of a binary Core Shell catalyst. With the highest loading of 60% photocatalyst, the efficiency of the ternary system is 2 times higher than that of the original binary system. Small porous silica MCM-41-S loaded with CAT-30, behaves differently from large porous silica MCM-41-L.

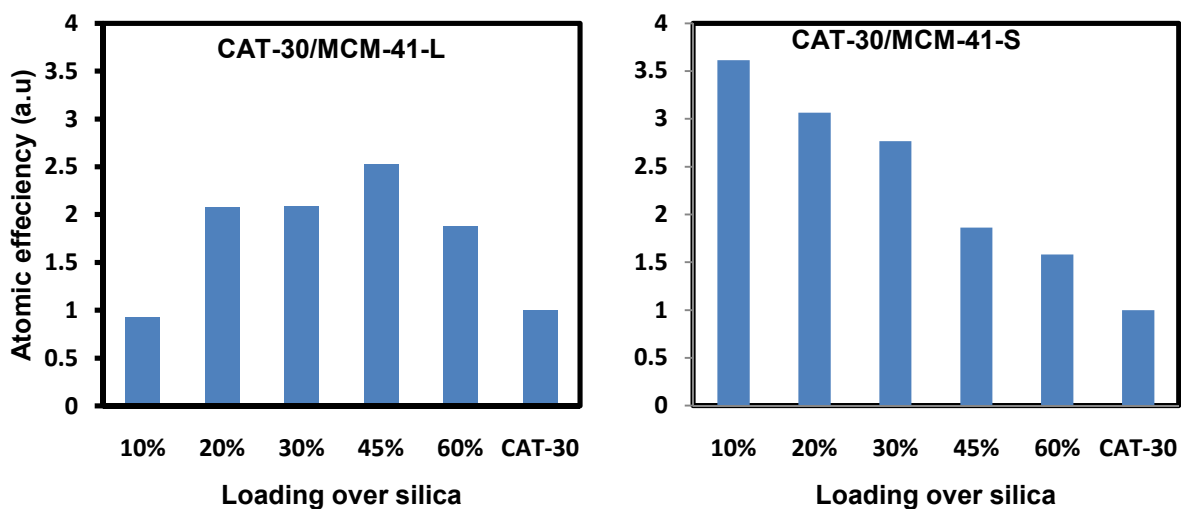


**Figure 50:** Calculated relative atomic efficiencies compared to the starting CAT-30 composite of (a) % CAT-30/MCM-41-L and (b) % CAT-30/MCM-41-S in the photocatalytic treatment of IBP after 8 hours, under UV/Vis irradiation.

#### ***Mineralization:***

During the course of photocatalytic treatment, solution aliquots were taken in order to determine the remaining carbon content (TOC). The TOC measurements of the photocatalytic solution confirm that the photocatalytic treatment over the 30% of Core Shell catalyst (CAT-30) leads not only to a 60% degradation/abatement but also to 60% mineralization, i.e. complete oxidation to  $\text{CO}_2$  and  $\text{H}_2\text{O}$ , of the organic pollutant ibuprofen (Fig. 51). The determined mineralization is in line with the degradation determined by UV/Vis spectroscopy. That means, the catalyst works “clean”. It is a green catalyst. The degraded organic pollutant is completely oxidized and nearly no intermediates or by-products remain in the photocatalytic treated solution. This is in contrast to  $\text{TiO}_2$  and  $\text{ZnO}$  catalysts where the pollutant is not completely oxidized.

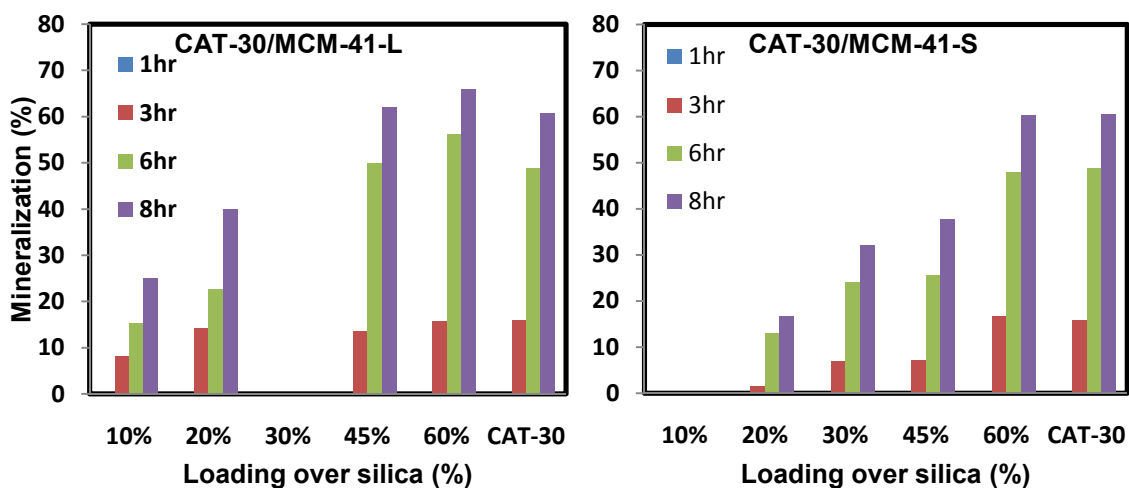


**Figure 51:** Mineralization of IBP over % CAT-30/MCM-41-L and % CAT-30/MCM-41-S composites after photocatalytic treatment (8 h) using UV/Vis irradiations.

In case of the ternary systems (ACIN catalyst) with different loadings of Core Shell photocatalyst (CAT-30) on mesoporous silica MCM-41, mineralization increases with growing active composite content. The mineralization achieved with small pore MCM-41 support with lower active composites are lower than with corresponding large pore MCM-41 catalysts. Obviously, this is due to adsorption and desorption of pollutants and reaction intermediates from small pore MCM-41, which interferes the mineralization. In this way, the adsorption can show a positive and also a negative effect of the photocatalytic abatement performance.

The mineralization of Ibuprofen over low loaded CAT-30/MCM-41-L (large porous) is much higher than degradation. For example, 10% loading results with 25% mineralization while degradation was recorded of ~ 6%. Similarly 20% loading resulted with 40% of mineralization which is almost ~1.7 times of degradation of 23%. Absolutely loading above 30%, such as 45% and 60% results of increased ~ 65% mineralization parallel to degradation. Similar to degradation, an induction period of up to 2 hours is observed in mineralization such as about negligible activity in 1 hour which is increased and remained up to 10-16% in 3 hours of photocatalytic treatments. While a fast rate of photocatalysis is noted in range of 3 to 8 hours in case of 45 and 60% loading.

**Core Shell 30%  $\beta$ -AgVO<sub>3</sub>/mpg-C<sub>3</sub>N<sub>4</sub>/ Loaded on KIT-6**

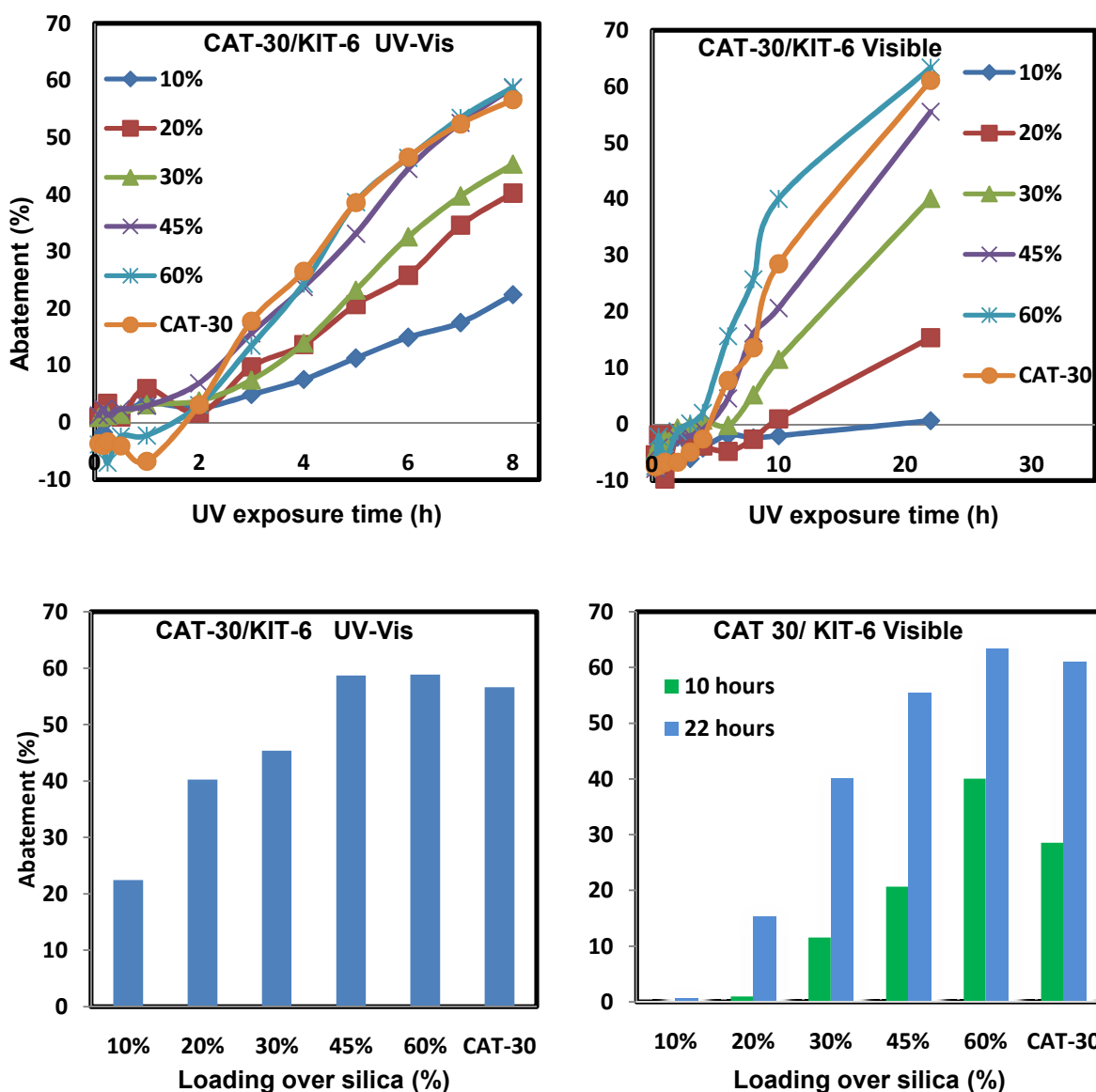


**Figure 52:** Photocatalytic degradation of IBP over CAT-30/KIT-6 (a) UV/Vis and (b) Visible light irradiation. With different percentage of catalyst loaded on mesoporous silica KIT-6 and final degradation of IBP over CAT-30/KIT-6 composite with different catalyst co content after 8h under UV/Vis (c), under visible light irradiation after 22 hours (d).

30% $\beta$ -AgVO<sub>3</sub>/mpg-C<sub>3</sub>N<sub>4</sub> Core Shell photocatalyst (CAT-30) was mechanical mixed with quasi 3-dimensional mesoporous silica KIT-6 as a support and, thereafter thermally treated at 300°C. With mesoporous silica KIT-6 loaded with 10% CAT-30 already ~ 22% abatement of ibuprofen is achieved after 8h of photocatalytic treatment under UV/Vis irradiation compared to only *ca.* 6% using large pore one-dimensional MCM-41-L support. The abatement thoroughly increases with reaction time (Fig. 52). With enhanced loading of the active component CAT-30 from 20 to 60%, the activity increases and reaches almost 60% of the value, which is observed with the active component alone after 8 hours treatment. These

results suggest an apparent increase in photocatalytic activity for silica supported hierarchical catalysts compared to the starting CAT-30 composite.

An example of visible light irradiations photocatalysis of 30% $\beta$ -AgVO<sub>3</sub>/mpg-C<sub>3</sub>N<sub>4</sub> Core Shell photocatalyst (CAT-30) was checked. Interesting results were found, where 4 hours prohibitions period was observed. 10% Loading of CAT-30 on KIT-6 showed no photoactivity while 20% loading degraded 15% of ibuprofen after 22 hours, while only 1% degradation was noted within 10 hours. 30% loading showed 40% degradation after 22 hours. 45 % loading shows good photocatalytic cativity which is similar to CAT-30 almost 60%. Best photocatalytic activity was noted with 60% loading of about 64% degradation.

Compared to UV/Vis light irradiation, photocatalysis under visible light irradiation starts with prohibition time and increases slowly within reaction time. These results suggest an apparent increase in visible light photocatalytic activity for silica supported hierarchical photocatalysts compared to the starting CAT-30 composite. Visible light photocatalysis is more than 2 times slower than UV/Vis irradiations.

#### **Relative atomic efficiency:**

The relative atomic efficiency calculated based on the abatement achieved after for 8 h of reaction are shown in Figure 53. Interestingly an efficiency increase of by a factor of ~4 is observed with the prepared complex hierarchical mesoporous silica loaded catalyst compared to the single active composites. In contrast to MCM-41 based complex catalysts, the efficiency increases also with low loadings of the active component and reaches a maximum value with the lowest loading of 10% only. Besides improved dispersion of the catalytic component on the silica support. This

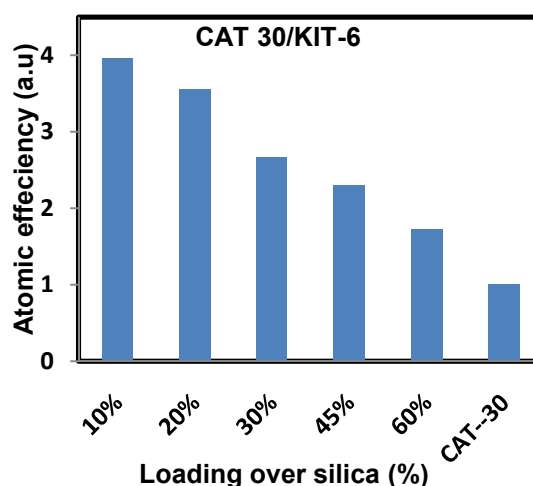


**Figure 53:** Calculated relative atomic efficiency of CAT-30/KIT-6 in the photocatalytic treatment of IBP after 8 hours, under UV/Vis irradiation.

finding can be explained by the large pore and quasi 3-dimensional pore system and high porosity of KIT- 6 (compare Table 1). It allows access to the catalyst component from all sides and facilitates mass transfer. MCM -41 contains only a one dimensional pore system.

The efficiency of the ternary composite system is always higher than that of the binary Core Shell catalyst. With the highest loading of 65% photocatalyst, the efficiency of the ternary system is still 2 times higher than that of the original binary system. The degradation is almost

similar to mineralization in case of 45% and 65% loading, which is almost identical to pure Core Shell photocatalysts.

**Mineralization:**

The TOC measurements of the photocatalytic treated solution confirm that the photocatalytic treatment over the 30% of Core Shell catalyst leads not only to degradation of the IBP, but also mineralization in parallel to the degradation (Fig. 54).

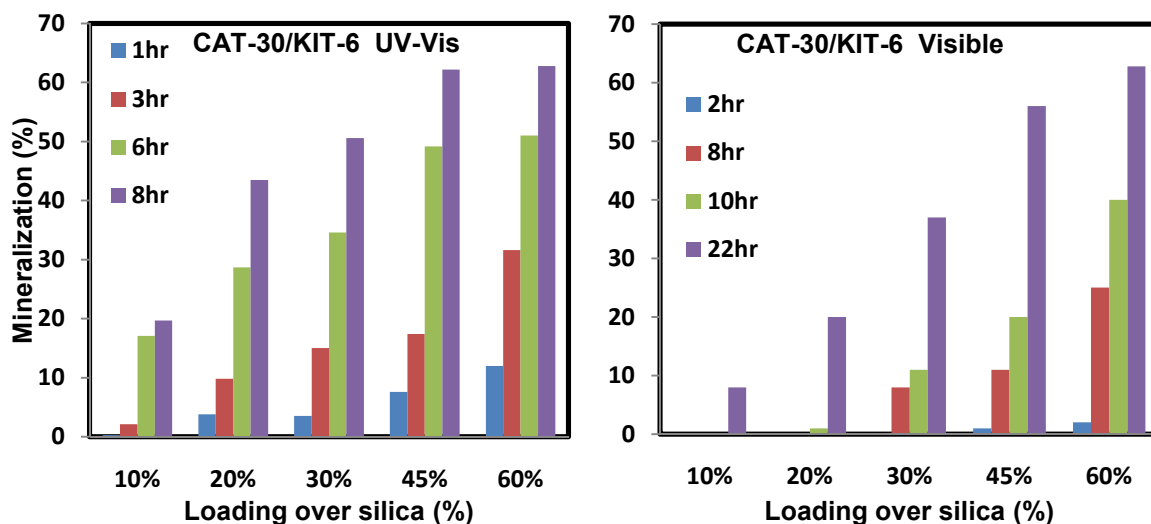


**Figure 54:** Mineralization of IBP over CAT-30/KIT-6 photocatalyst a) under UV/Vis b) under visible light irradiations (Cat. 10 mg/L, 250 mL of 10 ppm IBP).

As expected, mineralization increases with enhanced loading of the active component, the Core Shell catalyst on the KIT-6 support. The mineralization increases with prolonged treatment time within 8 hours. The determined degradation is in line with the UV/Vis spectroscopic results. With 10% loading almost 19% of the ibuprofen mineralization occurred within 8 hours. With increase of the loading to 20%, mineralization is almost doubled to 43%. With 45% loaded catalyst almost 63% of mineralization is achieved after within 8 hours of treatment. The CAT-30, KIT-6 supported hierarchical catalysts acts as “clean” or green catalyst. Formation of by-product is avoided.

Contrast to UV/Vis, mineralization of ibuprofen with visible light photocatalytic irradiations shows induction period of 2-3 hours until mineralization starts. Prohibition is highly clear with low loading which can be seen up to first 10 hours in 10 and 20% loading. With increase of time to 22 hours, mineralization can be noted. Above 30% loading prohibition of 2 hours are noted. While 8 hours photocatalysis shows mineralization. Mineralization increases with increasing loading of CAT-30 on KIT-6. Maximum amount of mineralization is noted with 45 to 65% loading. After 10 hours of photocatalysis rate of mineralization is high. Reaction rate shows that visible light photocatalysis is 2.5 times slower than UV/Vis irradiation. But it can

be donated to high energy of UV irradiations and strength of UV lamps. Core Shell 30%  $\beta$ -AgVO<sub>3</sub>/mpg-C<sub>3</sub>N<sub>4</sub> (CAT-30) Loaded on FDU-12

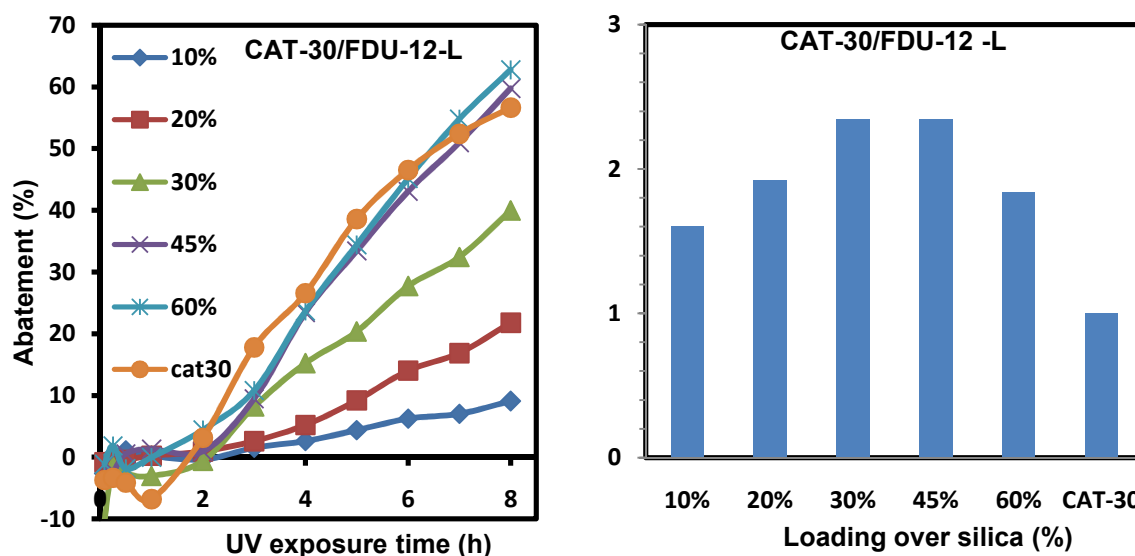


**Figure 55:** Photocatalytic degradation of IBP over % CAT-30/FDU-12-L with different photocatalyst loading (a).Final degradation of IBP over % CAT-30/FDU-12-L composite with different catalyst content after 8h (b).

Additionally, another example of a complex hierarchical supported  $\beta$ -AgVO<sub>3</sub>/mpg-C<sub>3</sub>N<sub>4</sub> (CAT-30) Core Shell composite catalyst supported on ordered large mesoporous FDU-12-L type silica was photocatalytic tested. The course of abatement of ibuprofen vs. photocatalytic treatment time over different 10-60% CAT-30/FDU-12-L composites was similar to that observed with the silica support KIT-6 (Fig.52).About 9% abatement of IBP is achieved after 8h with the 10% loading of CAT-30 on FDU-12-L. The increase of the CAT-30 composite loading on FDU-12-L to 20 and 30% leads to an enhancement of the photocatalytic degradation from 10 to 22 and 40%, respectively. The further increase of CAT-30 loading to 45 and 65% enhances the degradation of IBP to 63% after 8h, which is almost similar to the photocatalytic activity of CAT-30 without silica supports. These improvements (especially at lower CAT loading on silica) are somewhat lower than those found with KIT-6. With increase of the CAT-30 loading, the photocatalytic activity increases and the abatement of IBP reaches a maximum at 45% of CAT-30 loading on silica (Fig. 55).

### Relative Atomic Efficiency:

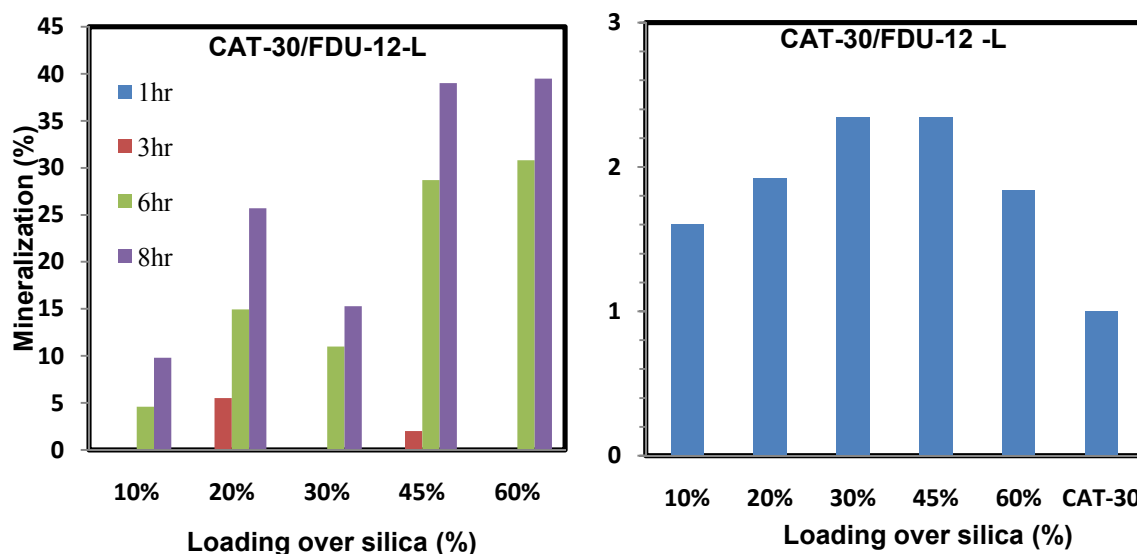


**Figure 56:** (a) Improvement of the atomic efficiency of % CAT-30/FDU-12-L composite independence of  $\beta$ -AgVO<sub>3</sub>/mpg-C<sub>3</sub>N<sub>4</sub> content after 8h photo catalytic treatment, (b) mineralization of IBP over CAT-30/FDU-12-L composite after photo catalytic treatment.

Figure 56 a shows the atomic efficiency of the silica loaded compiste compared to that of the pure 30%  $\beta$ -AgVO<sub>3</sub>/mpg-C<sub>3</sub>N<sub>4</sub>, composite. The silica loading increases the efficiency regarding the silver loading by a factor of 1.5 to 2.5, depending on composite content.compared to that of the pure on with 10% loading.

### Mineralization:

Due to the induction period only a slow abatement is observed in the first 1-2 hours of photo catalytic treatment. Almost no mineralization is observed in first 3 hours (Fig.56b) compared to KIT-6 loaded hierarchical catalysts (Fig. 55). The mineralization starts after 6h of treatment and reaches 45%. With higher composite catalyst loaded samples (45% and 60%), achieved mineralization is marked lower (35%) than with KIT-6 containing catalysts.

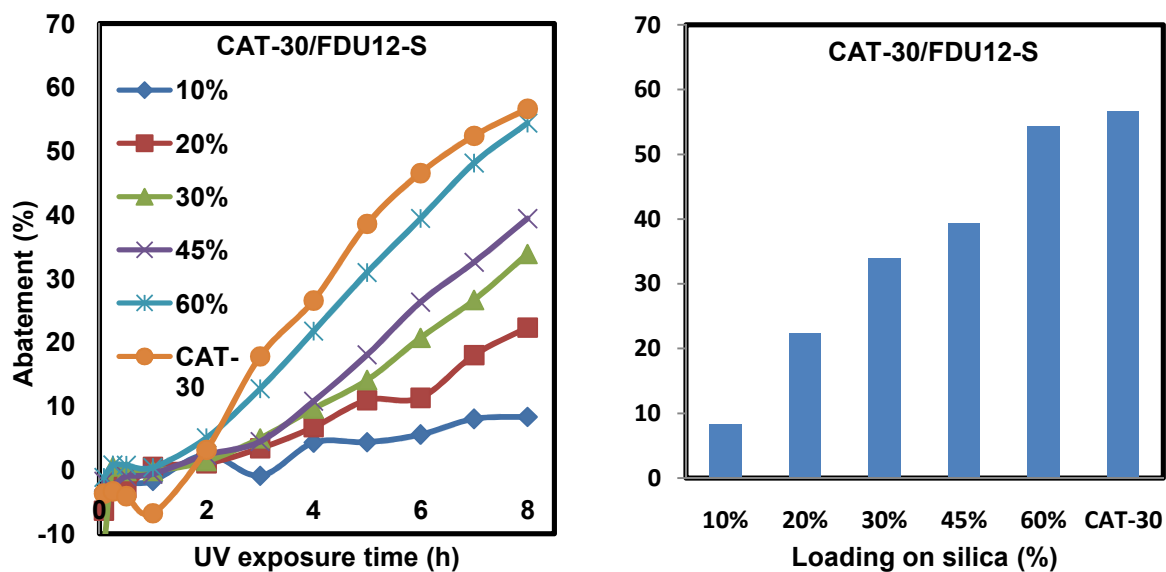


**Figure 57:** Photo catalytic degradation of IBP over CAT30/FDU-12-S with different catalyst content(a), Final degradation of IBP over % CAT-30/FDU-12-L composite with different catalyst content after 8h (b).

Attempts to improve the synthesis efficiency of FDU-12 by decreasing the synthesis temperature from 120°C to 100°C resulted in a decrease of the porosity. i.e. the pore diameter and specific pore volume decreased markedly from 5.12 nm and 0.85 cm<sup>3</sup>/g to 3.84 nm and 0.57 cm<sup>3</sup>/g (CAT-30/FDU12-S), respectively. Correspondingly, CAT-30 loaded on FDU-12-S shows in tendency a lower photo catalytic activity than FDU-12-L supported ones (Fig. 57). The enhancement of the atomic efficiency achieved after loading on the FDU-12 supports decreases from *ca.* 1.8-2.5 to 1.6-2 with the small pore FDU-12-S (Fig. 57a). Obviously mass transfer to the catalytic component is facilitated with large pore FDU-12-L leading to higher activity.

The amount of photo catalytic activity experienced with 10 and 20% loading is similar to previous FDU-12 and KIT-6, but with 30% loading activity is 33% which is lower than previous catalysts. With 45 and 60% loadings lower activity of 39 and 54% is recorded. From chapter 2 we know that FDU-12-S is with small pores of about 3.75 nm while FDU-12 at 120°C has hierarchical system with bottle shaped big pores of 5 to 7 nm, interconnected via small pores. Cumulative volume of the pores is higher. This concludes, with big pores and hierarchical system reflects good photo catalytic activity.

Atomic efficiency after 8 hours is shown in (Fig. 58a). Calculations shows that the resultant ternary photocatalysts shows efficiency higher ratio of 1.5 to 2. 20-30% loading results with 2 times higher ratio, while activity of 45 and 60% is calculated to ~ 1.5 and 1.7 times.

Mineralization of the 30% loaded CAT-30 on mesoporous silica FDU-12-S was ~2% in first 3 hours which is similar to the abatement results in the first 3 hours considering as induction period. But above 3 hours mineralization is achieved within 5, 6, and 8 hours, such as 10.4, 16, 28, and 28.6 respectively (Fig.58b). The final value of mineralization is close to the degradation determined by UV/Vis spectroscopy. Hence, CAT-30 on mesoporous silica FDU-12-S behaves as a clean catalyst.

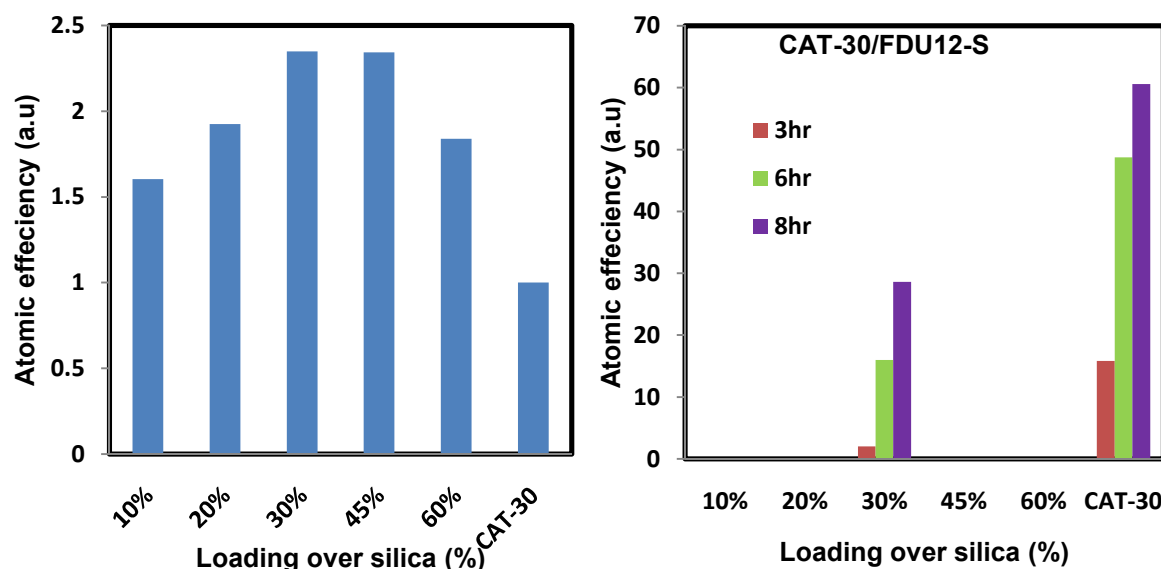


**Figure 58:** Atomic efficiency of IBP over % CAT-30/ FDU-12-S composite with different catalyst content after 8h (a).mineralization of IBP over 30% CAT-30/ FDU-12-S composite after photo catalytic treatment (b).

### Conclusions:

- Enhancement and improvement of photo catalytic activity by supporting 30% of  $\beta$ -AgVO<sub>3</sub>/mpg-C<sub>3</sub>N<sub>4</sub> on large mesopore of KIT-6, MCM-41-L and FDU-12-L. Moreover achieve efficient mineralization under UV/Vis exposure. On the other hand, efficiency decreased by half by visible light processing as well as mineralization.
- Improve mechano-chemical of solid state solvent free method by mixing and milling under ambient room temperature and thermal treatment.
- Improve efficiency due to high dispersion of catalyst particle in mesoporous support usually pore catalyst particle agglomerate suspension of solution reaction which reduce the accessibility.
- The scatter of photo catalytic activity for different mesoporous support at min and maximum of  $\pm 20\%$ .

- No clear relation between porosity of support and activity, possibility of interference with efficiency of mechano-chemical preparation which determine achieve of dispersion.
- The influence of dispersion is higher than the influence of porosity of the support.
- The problem of the reproducibility of the mechano-chemical preparation regarding achieve dispersion.

### 3.2.3 Photocatalytic Performance of Mechano-Chemical Prepared 25 % $\beta$ -AgVO<sub>3</sub>/mpg-C<sub>3</sub>N<sub>4</sub>/Mesoporous Silica Composite (Advanced Complex Inorganic Nano-materials)

It is already proved that AgVO<sub>3</sub>/C<sub>3</sub>N<sub>4</sub> Core Shell catalyst loaded with of 20 to 30% loading of  $\beta$ -AgVO<sub>3</sub> on 70-80% of mpg-C<sub>3</sub>N<sub>4</sub> graphitic carbon nitrides show excellent photocatalytic activity in the degradation of pollutants. For comparison, 25%  $\beta$ -AgVO<sub>3</sub>/mpg-C<sub>3</sub>N<sub>4</sub>Core Shell photocatalyst (assigned as CAT-25) was mixed with a couple of different mesoporous silica and mechanically treated and photo catalytic tested in order to investigate the impact of the silica porosity on the photocatalytic performance.

#### Variation of the CAT-25/KIT-6 Composition

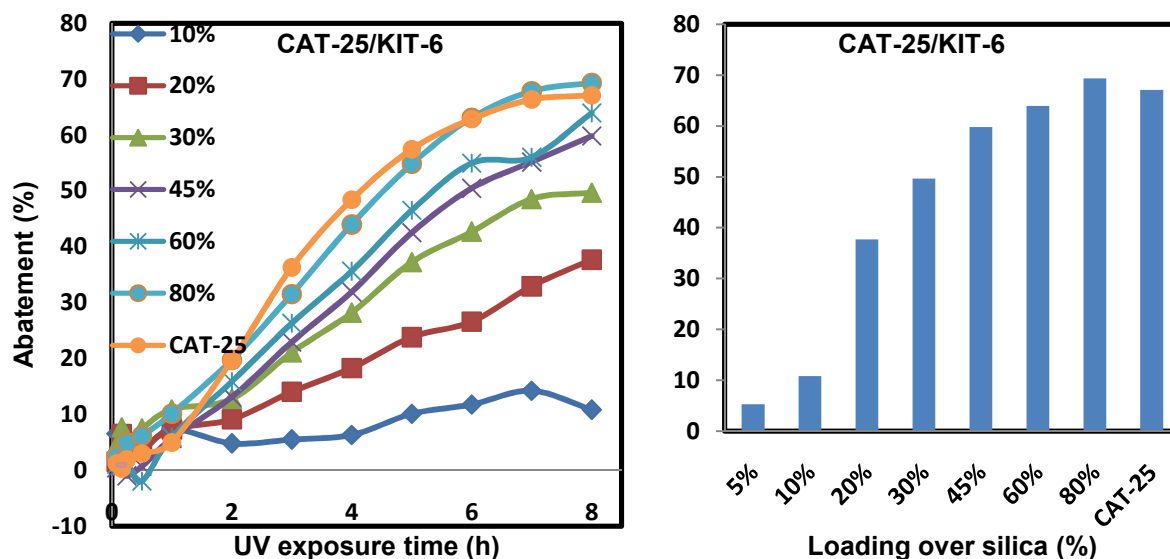


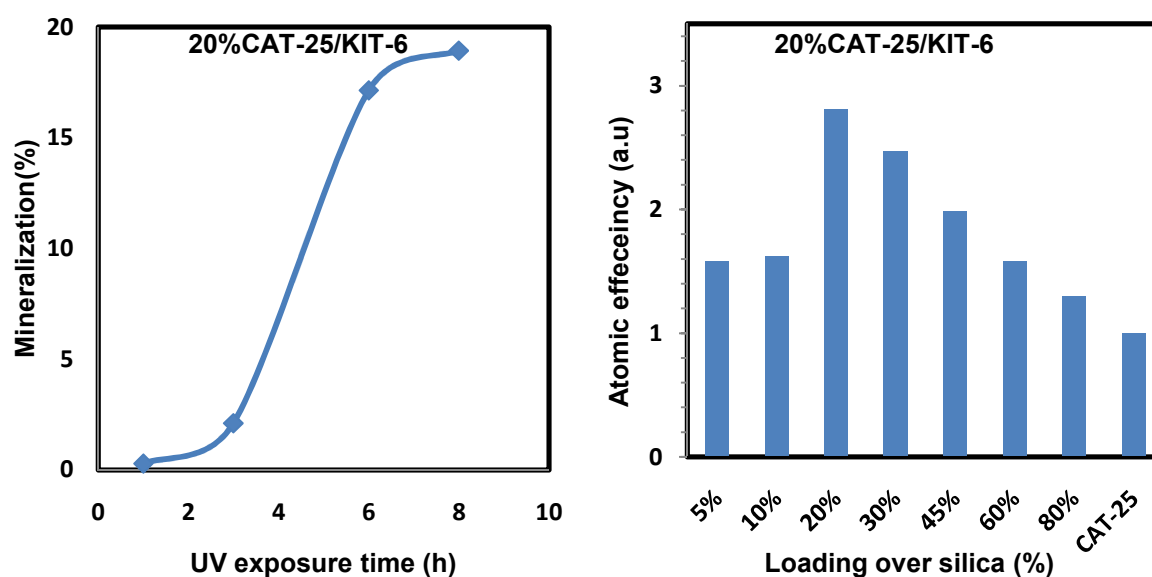
**Figure 59:** Photocatalytic degradation of IBP over % CAT-25/KIT-6 with different catalyst content (a). Final degradation of IBP over % CAT-25/KIT-6 composite with different catalyst content after 8h (b) Condition: 250 ml batch reactor, 10 ppm IBP solution, 10 mg catalyst loading, cat /IBP = 4, 60 W UV/Vis Solarium lamp irradiation.

An example of the CAT-25/KIT-6 with different loading percent is described in detail (Fig. 60). With low amount of loading of CAT-25 (95% silica and 5% of CAT-25,

i.e.  $\text{AgVO}_3$  is  $\sim 1.25\%$ ),  $\sim 5\%$  IBP degradation was achieved during 8h of photocatalytic treatment, which rises steadily with increasing catalyst loading to 60%. With 20% catalyst loading already 50% of activity of silica free catalyst (CAT-25) is reached. Highest activity is achieved with 80% loading.

### Mineralization and Atomic Efficiency:

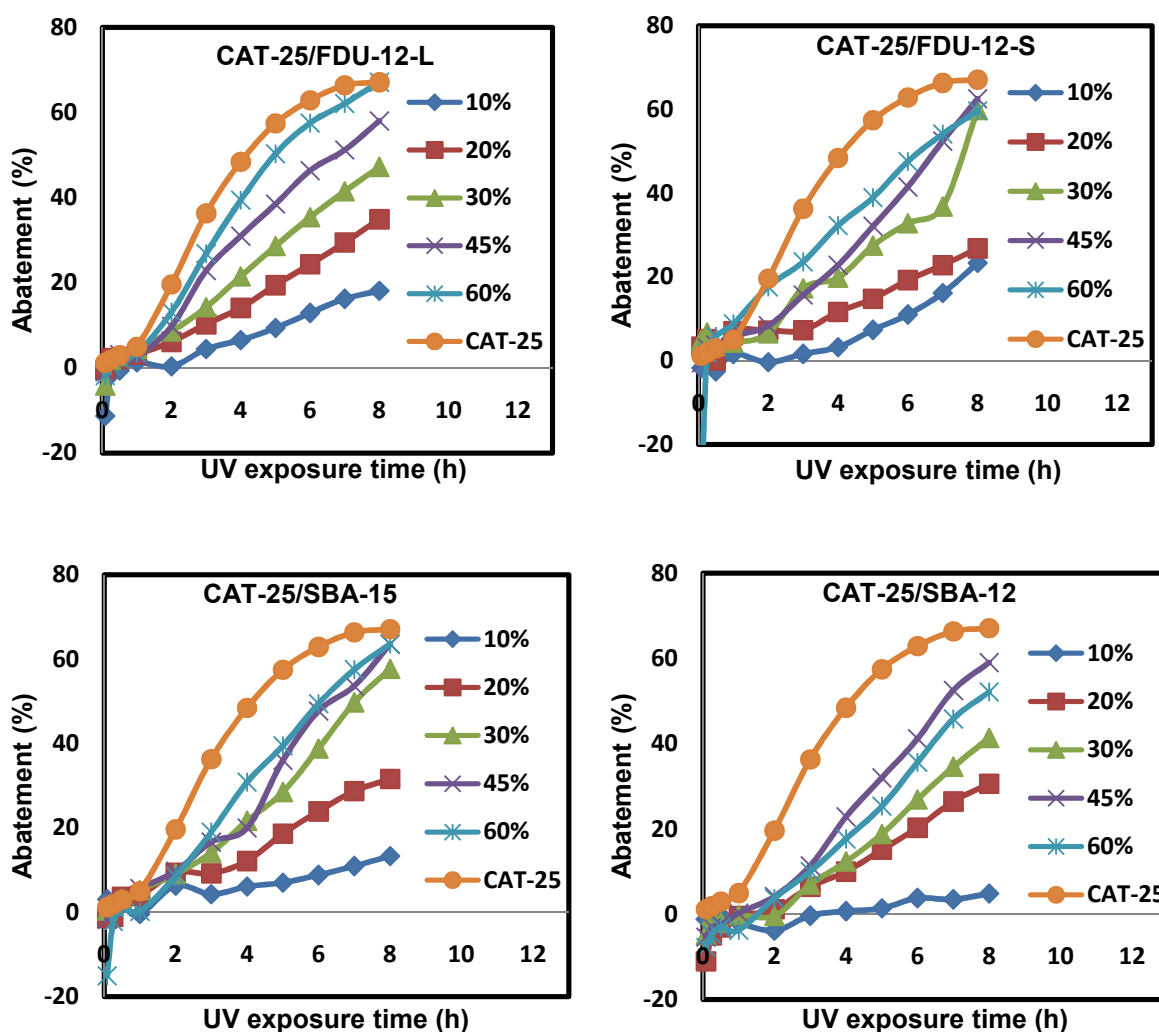
The mineralization is markedly lower. With 20% loading of Cat-25 on KIT-6 ca. 40% of degradation is achieved after 8h, whereas the mineralization reached only  $\sim 18.9\%$  (Fig. 60a). Indeed, an induction period of 2h with almost no mineralization is observed with this system. The calculated relative atomic efficiency increase achieved by catalyst loading on mesoporous KIT-6 (based on photocatalytic abatement after 8 hours) is about 2.8 times with 20% loading, followed by a gradual decrease of efficiency to 1.3 with 60% loading, i.e. the atomic efficiency is still higher compared to the CAT-25 Core Shell catalyst (Fig. 60b).



**Figure 60:** (a) mineralization of IBP over % CAT-25/KIT-6 composite after photocatalytic treatment. (b) Improvement of the atomic efficiency of % CAT-25/KIT-6 composite independence of  $\text{AgVO}_3/\text{C}_3\text{N}_4$  content after 8 hours of photocatalytic treatment.

### 3.2.4 Further Examples with Variation of the Compositions of CAT-25 / Silica with FDU-12-S, FDU-12-L, MCM-41-S, MCM-41L, SBA-12, SBA-15, SBA-16, MCM-48-S and MCM-48-L

The influence of the composite loading and the influence of the structure-type of the used ordered mesoporous silica on the photocatalytic abatement of IPB UV/Vis irradiation was studied and summarized in Figure 61. In one case the performance under visible light irradiation was tested with MCM-41-S as support (Fig. 61. bottom right). All studies were performed using the CAT-25 as catalytic component.



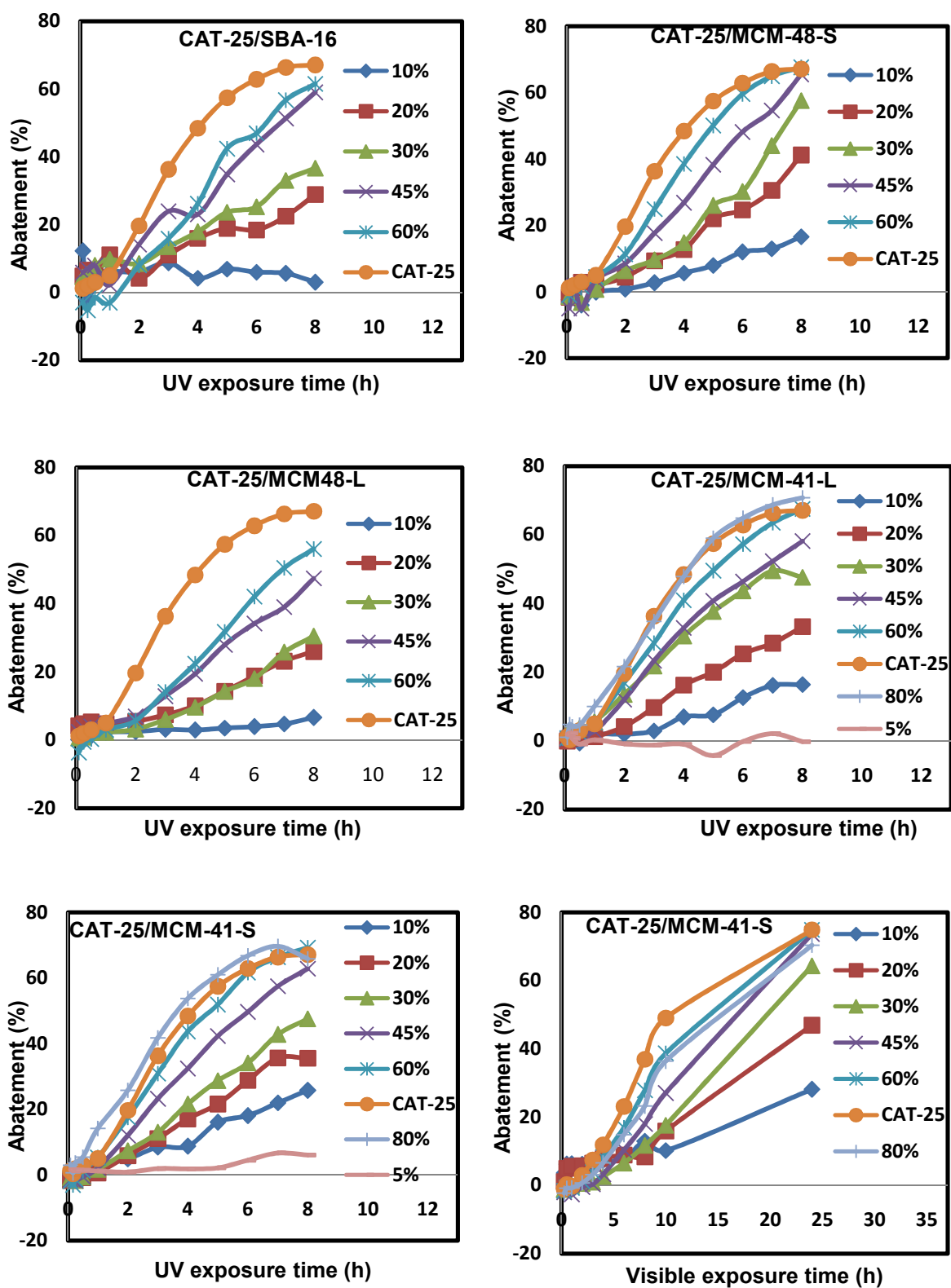


**Figure 61:** Influence of the type of mesoporous materials and of the catalyst CAT-25 content (25%  $\beta$ - $\text{AgVO}_3$ /mpg- $\text{C}_3\text{N}_4$ ) on the course of photocatalytic degradation of IBP over CAT-25/Mesoporous silica under UV/Vis and Visible light (bottom right): 250 ml batch reactor, 10 ppm IBP solution, 10 mg catalyst loading, Cat /IBP = 4, 60 W UV/Vis Solarium lamp irradiation or 16 W Visible LED room light (last).

The different used ordered mesoporous molecular sieve silica supports show general the same effect on the photocatalytic performance in the abatement of IBP with some exceptions only

(Fig. 61). Similar loadings result in similar degradations. An increase of the photocatalytic activity is found with increasing loading of Cat-25 on silica (FDU-12 (L and S), MCM-41(L and S), MCM-48 (L and S), SBA-15, SBA-12, and SBA-16. CAT-25 loaded on MCM-48-L showed lowest activity compared similar loaded other types of silica. Also catalysts loaded on SBA-12, -15, and -16) showed lower photocatalytic activity compared to others type of silica. Similar conversions (IBP degradation) can be achieved under visible light showing the superior visible light performance of CAT-25 and silica loaded CAT-25 photocatalysts. However, conversion proceeds slower and the required reaction time are 2-3 times longer. The loading on the mesoporous silica enhances also the atomic efficiency in a similar way. The summarize of the data after 8 hours of the photocatalytic abatement in bar graph shows that most of the supported catalysts on different silica behave similarly with little difference in the achieved final abatement (Fig. 62). In case of 20% loaded CAT-25, FDU-12 prepared at low temperature of 100°C and MCM-48-L prepared in the duration of 11 days shows lower activity of ~26% than the other silica of ~33-35%. Highest activity was noted with MCM-48-S which reaches~ 41% conversion almost more than half of the activity of the original catalyst CAT-25. With reference to Figure. 63 we can conclude that the complex composite catalysts containing MCM-48-S, MCM41-S and KIT-6 show high performance and SBA-15 in part shows best performance.

In case of 30% loaded CAT -25, very similar photocatalytic abatement was noted with KIT-6, MCM-41-L, MCM-41-S, and FDU-12-L have shown similar photocatalytic abatement of ~47-49%, while SBA-12 and SBA-16 supported catalysts shows abatements of ca. 36% and 41%. Lowest abatement is noted with MCM-48-L of 30% conversion. High photocatalytic abatement of about 57-60% is found with FDU-12-S, MCM-48-S and SBA-15 supported catalysts. This value is almost near to that of the original photocatalyst of CAT-25, which shows ~67% conversion under these conditions.

Loadings of 45 % and 60% of CAT-25 on silica behave almost similar with almost little difference in abatement. With 45% loading of CAT-25 abatement is nearly 58-60%, while in case of MCM-48-L activity is ~48 %. 65% loading shows increased activity above 63% which is almost similar to the activity of CAT-25. Except FDU-12-S, MCM-48-L and SBA-12, all other silica loaded CAT-25 shows similar behavior. This is almost in line with above 20 and 30 % loadings.

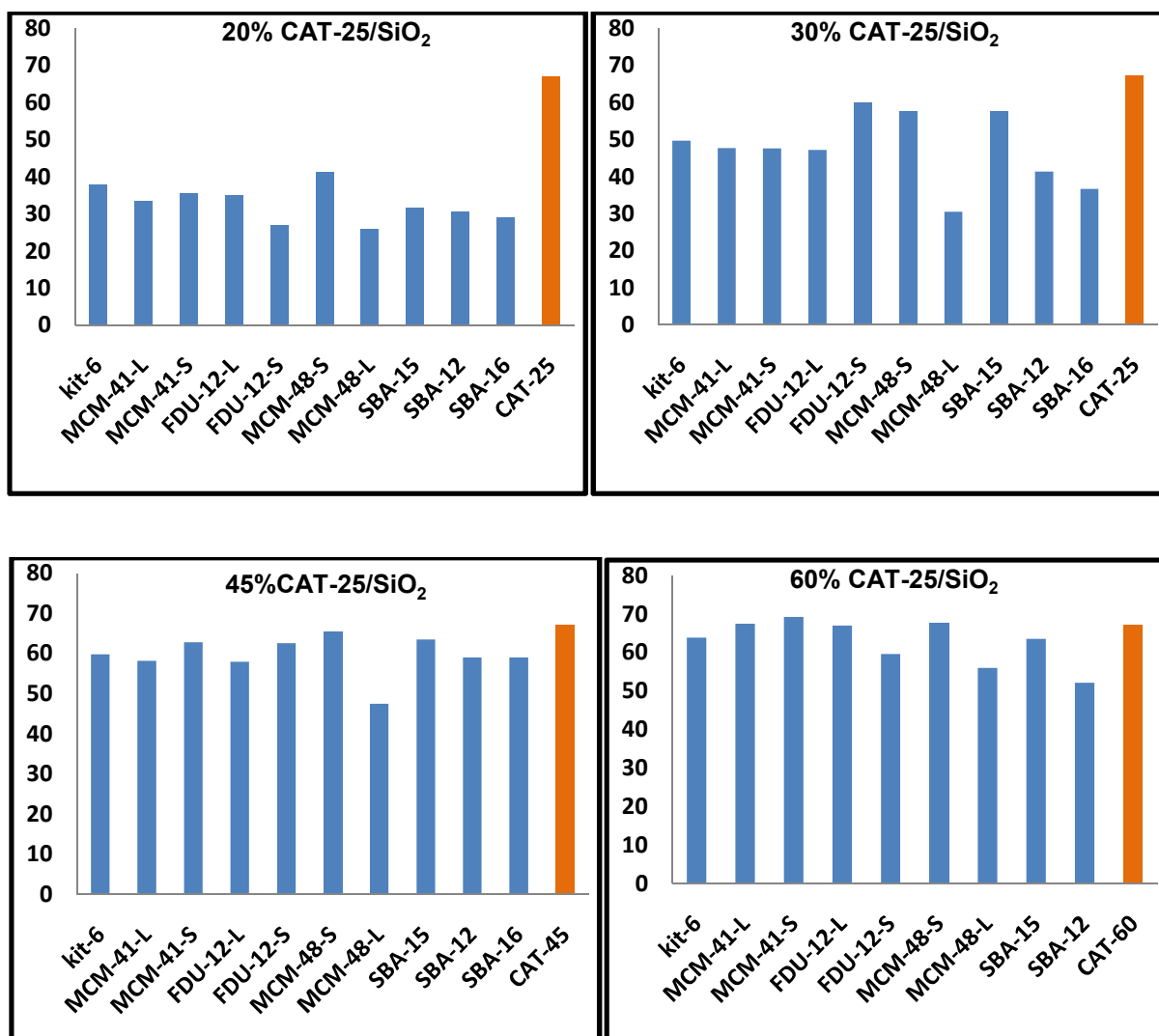


**Figure 62:** Photocatalytic degradation of IBP over 20%, 30%, 45% and 60% loading of CAT-25/Mesoporous silica (reaction volume: 250 mL reaction time: 8h, IBP concentration: 10 mg/L, catalyst loading 10 mg).

**In conclusion** from the selected MCM-48(S), KIT-6, FDU-12(S), MCM-41(S) and in part SBA-15 are good support for CAT-25 in photocatalysis and show high performance, while supporting on SBA-12 and SBA-16 shows less conversion. These differences might be due to the mechanical mixing (preparation method) with milling. The homogeneous mixing of equivalent amount of single components is easier to be achieved with 45% loading. On other side core-shell structure is better retained.

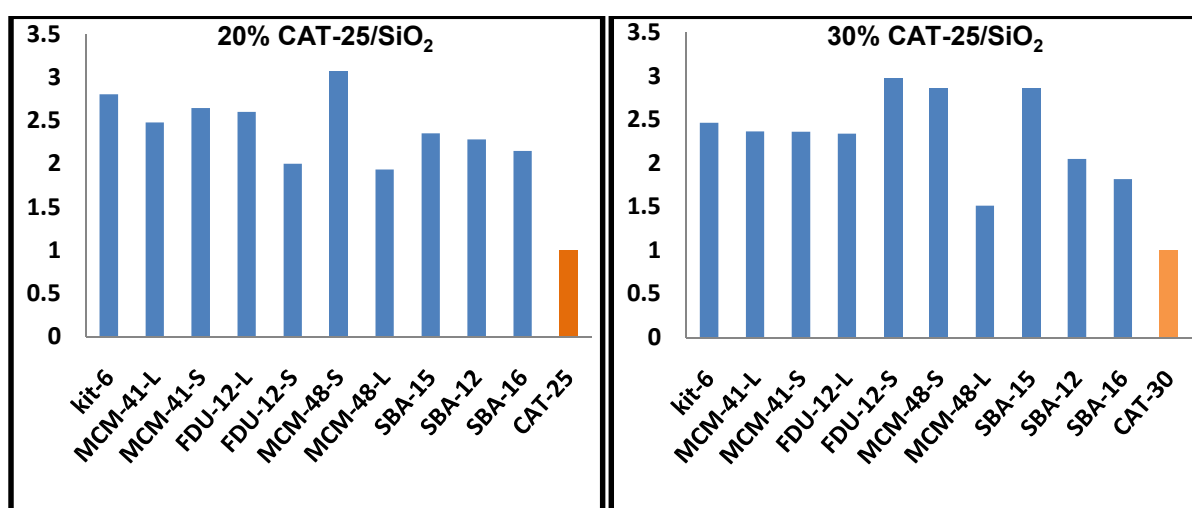
The preparation influences the performance of photocatalyst on interface of used Silica material therefore this make difficult to estimate the effect of the support. Over all the mesoporous material mentioned are efficient supports. A precise relation between the textural properties of mesoporous molecular sieves and the improvement of the photocatalytic efficiency was not observed. The conversion values scatter by using different mesoporous

silica. E. g, with 20% loading of CAT-25 on different silica an average conversion of *ca.*32.6  $\pm$ 7% is observed .On average with different loadings conversions the maximum values differ by *ca.*  $\pm$ 20%,MCM-41-S, MCM-41-L and FDU-L mesoporous catalyst supports with respect and mineralization. In this case mineralization is achieved with nearly complete mineralization. In other cases degradation is higher, but mineralization is distinctly lower.

### Atomic efficiency:

Based on the formula, described in Section 3.2.2, for calculating atomic efficiency based on  $\text{AgVO}_3$  content was performed for CAT-25 with different loading percent, after 8 hours of abatement time. (Fig. 63).With 20% loading of CAT-25 on silicas shows almost remarkable increase of  $\sim$  2.5 times while CAT-25 on FDU-12-S and MCM-48-L shows atomic efficiency of 2 times than the same amount of CAT-25. Similarly with 30% loading of CAT-25 on silicas same pattern is retained with the calculation of 2.5 times than original CAT-25. While noted huge amount of photocatalytic abatement with FDU-12-S, MCM-48-S and SBA-15 boosts the atomic efficiency up to 3 times. The lowest amount of abatement with MCM-48-L results with 1.5 times of CAT-25.

In tendency the boosting of efficiency decreases with increasing the catalyst loading of CAT-25 to 45%. Although abatement of 45% loaded on silica is near to the original CAT-25. But resultant atomic efficiency is reduced to almost  $\sim$ 2. The pattern and effect of different silica is similar as explained in section of abatement. The 65% loaded CAT-25 shows atomic efficiency of  $\sim$ 1.5 w.rt. CAT-25.



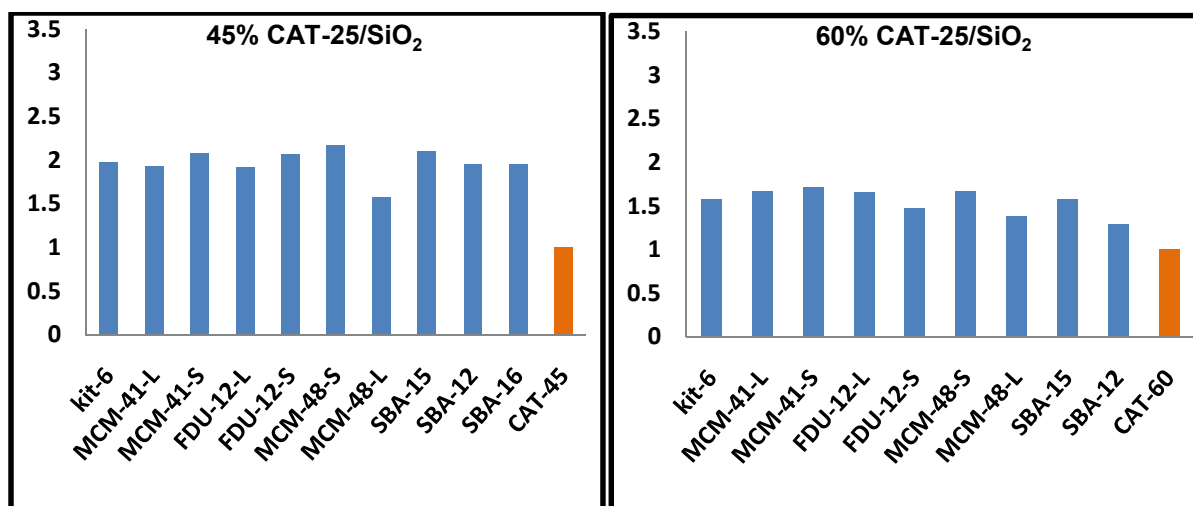


**Figure 63:** Improvement of the atomic efficiency of CAT-25/Silica composite independence of  $\text{AgVO}_3/\text{C}_3\text{N}_4$  content after 8h photocatalytic treatment (reaction volume: 250mL reaction time: 8h, IBP concentration: 10mg/L, catalyst loading 10 mg).

In conclusion, high relative atomic efficiency of average factor 2.4 is achieved with low loading of 20%. The highest optimum abatement of average 60.6 is achieved with high loading 45% but the relative increase of the atomic efficiency by a factor of 2 is lower.

**Mineralization:** TOC analysis and data measured for 30% loading of CAT-25 on different silica are shown in Figure 64.

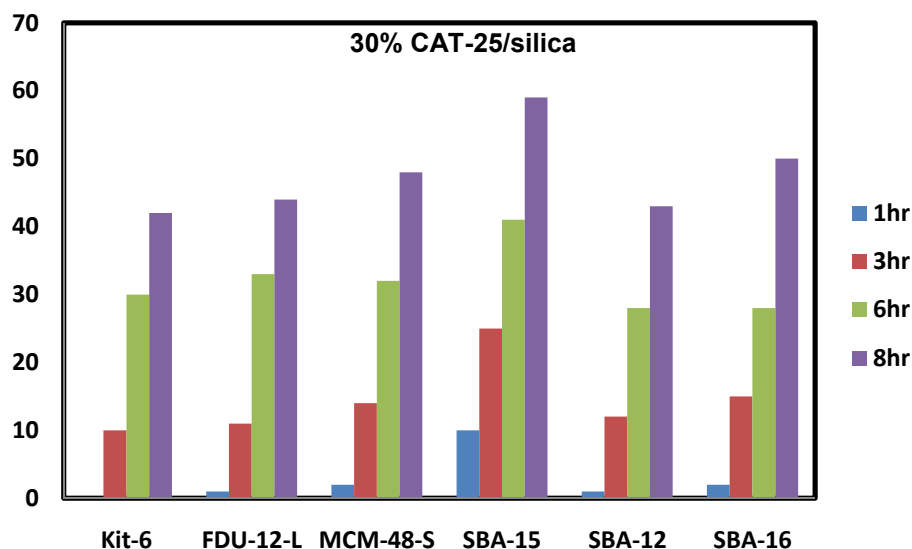


**Figure 64:** mineralization of IBP over 30% CAT-25/Silica composite after photocatalytic treatment with UV/Vis irradiation (reaction volume: 250 mL reaction time: 8h, IBP concentration: 10 mg/L, catalyst loading 10 mg).

KIT-6 loaded catalyst shows very low mineralization, while FDU-12, MCM-48, SBA-12 show almost ~45% mineralization, which is related to the high activity of these samples

(Fig. 61-62). Highest mineralization of 59% is noted with SBA-15. The Mineralization is almost related to the amount of abatement achieved. In conclusion, the TOC confirms the highest activity of CAT-25 with 30% loading on different silica. In conclusion, complex composite catalysts with silica supports act as clean catalysts as observed the starting  $\text{AgVO}_3/\text{C}_3\text{N}_4$  composites.

### 3.3 Reactive Oxidative Species

In the photocatalytic degradation reactive species such as hydroxyl radicals  $\cdot\text{OH}$ , super oxide radical anions ( $\text{O}_2^{\cdot-}$ ), hydroperoxyl radicals ( $\cdot\text{OOH}$ ), and conductive band electrons  $e^-$  and valance band holes ( $h^+$ ) are involved in the hydroxylation and oxidation steps. The photocatalytic behavior is influenced by the contribution of the different reactive oxidative species and can be tested using appropriate scavenger molecules. Generally EDTA (ethylenediaminetetraacetic acid) acts as a hole ( $h^+$ ) scavenger, t-BuOH acts as a  $\cdot\text{OH}$  radical scavenger and 1, 4-BQ (1, 4-Benzoquinone) acts as a  $\text{O}_2^{\cdot-}$  radical or hydroperoxyl  $\cdot\text{OOH}$  scavenger. [90]

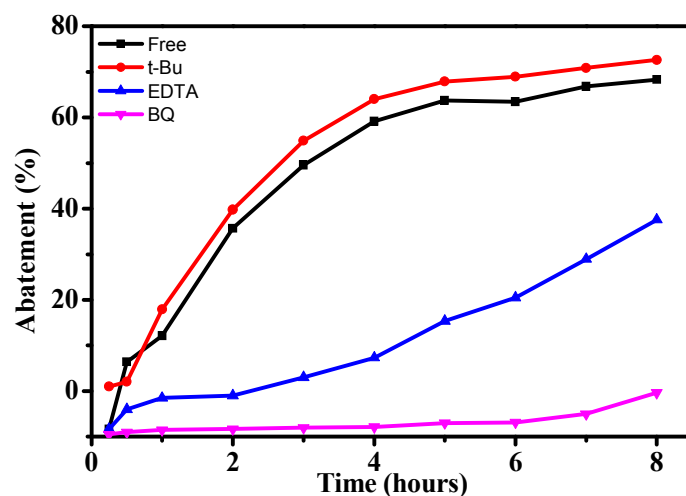


**Figure 65:** Impact of different scavengers on abatement of IBP over CAT-25 under UV/vis irradiation. Reaction conditions: room temperature, Co (IBP): 10 ppm, Vo (IBP): 250 mL, C (catalyst): 10 mg, scavengers: 1.46 mg EDTA, 0.1 mL t-BuOH, 2.704 mg 1,4-BQ.

In this study different types of catalysts and supports are studied as  $\beta\text{-AgVO}_3/\text{mpg-C}_3\text{N}_4$  composites and advanced complex  $\beta\text{-AgVO}_3/\text{mpg-C}_3\text{N}_4/\text{mesoporous silica}$  composites as well as  $\text{TiO}_2$  (P25) or ZnO catalysts for comparison. Therefore, it was of interest to study the influence of different ROS on the photocatalytic behavior. For this scavenger (4.6 mg of EDTA, 0.1 mL of t-BuOH, and 2.704 mg of 1,4-BQ) were added to the reaction solution

reaction solution (250 mL of aqueous reaction solution (250 mL aqueous solution containing 10 ppm IBP and 10mg catalyst).

Figure.66 shows the impact of different scavengers (EDTA, t-butanol and 1, 4-Benzoquinone), respectively, on the abatement of ibuprofen over CAT-25 under UV/Vis irradiation. Pronounced effect of the hole-scavengers was observed in the case of addition of EDTA which retarded the degradation of the ibuprofen. The addition of t-butanol shows almost no effect on the photocatalytic degradation. Nearly complete retardation is observed with the addition of benzoquinone (Fig. 65). This shows that both, holes and superoxide  $O_2^{\bullet-}$  or hydroperoxyl  $\bullet OOH$  radicals are the major active species in the photocatalytic decomposition of organics over  $25\% \beta\text{-AgVO}_3/\text{mpg-C}_3\text{N}_4$  Core Shell composites. A similar behaviour is observed with the advanced complex  $\text{AgVO}_3/\text{C}_3\text{N}_4$  / mesoporous silica composites -ACIN (Table 2).

**Table 2:** Relative decrease in order, effect of the addition scavengers on the photocatalytic abatement of IBP (%) over photocatalysts CAT-25 or 30/SiO<sub>2</sub>.with different silica supports after 8hours.

Photocatalyst	Abatement * %	[t-Bu] abatement %	[EDTA] abatement %
30%(CAT-25)/MCM-41-L	55	36	17
30% (CAT-25)/MCM-41-S	35	29	2
30% (CAT-25)/MCM48-S	49	48	19
45% (CAT-30)/FDU-12-S	47	48	28
60% (CAT-25)/SBA-16	65	64	20
60% (CAT-25)/KIT-6	75	70	30
60% (CAT-25)/MCM-41-L	74	76	41

\*Abatement achieved with the catalyst without addition of scavenger.

Table 2 shows the photocatalytic abatement achieved after 8h. The results confirm that addition of t-butanol as a  $\bullet OH$  radical scavenger has no effect on the abatement rate, except in case of 30 %(CAT-25)/MCM-41 either with large porous system or with small pores. Addition of EDTA leads to more pronounced effect with lowering the rate of abatement probably near to half with respect to the photocatalytic reaction without any scavenger (Free). While a strong effect of addition of 1, 4-benzoquinone leads to a markedly drop of the conversion which shows that superoxide radicals  $O_2^{\bullet-}$  or hydroperoxyl  $\bullet OOH$  radicals behaves as main active species for the abatement of ibuprofen in photocatalytic reaction. This finding shows that the photocatalytic behaviour is determined by the  $\text{AgVO}_3/\text{C}_3\text{N}_4$  Core Shell composites. Photocatalysts with

different loading of AgVO<sub>3</sub> on C<sub>3</sub>N<sub>4</sub> supported on mesoporous silica supports such as KIT-6, SBA or MCM - types behaves similar in mechanism of photocatalytic degradation, because they produce similar active species. The supporting silica has no impact on involved active species.

**Table 3:** Order of the influence of the addition of scavenger sensitive to holes, hydroxyl radicals and superoxide radical anions (or hydro peroxide radicals HOO•) on the abatement of ibuprofen over different photocatalysts (Scavenger reduce the abatement).

TiO <sub>2</sub> (P25)	Fr * < h <sup>+</sup> < •OH <<< O <sub>2</sub> <sup>•-</sup>
ZnO	Fr * < •OH << h <sup>+</sup> <<< O <sub>2</sub> <sup>•-</sup>
AgVO <sub>3</sub> /C <sub>3</sub> N <sub>4</sub>	Fr * ≈ •OH << h <sup>+</sup> <<< O <sub>2</sub> <sup>•-</sup>

\*Abatement prior addition of scavenger.

Photocatalysts supported on/SiO<sub>2</sub> behaves similar in all three systems TiO<sub>2</sub> (P25), ZnO, AgVO<sub>3</sub>/C<sub>3</sub>N<sub>4</sub> respectively, with respect to increase in photocatalytic efficiency, while different photocatalysts behaves differently in nature of the quantity of the produced active species in the presence of scavengers. The addition of both hole and •OH radical quenching agents shows little effect on the activity of TiO<sub>2</sub>-P25, but the added benzoquinone for quenching O<sub>2</sub><sup>•-</sup> shows high effect. In case of ZnO, the effect of added holes scavenger is higher than that of the hydroxyl radical scavenger. While the superoxide and hydroperoxide radical scavenger benzoquinone retards the photocatalytic abatement with all photocatalysts. β-AgVO<sub>3</sub>/mpg-C<sub>3</sub>N<sub>4</sub> behaves differently. Almost no effect was found by addition of t-butanol as hydroxyl radical scavenger. But, both hole and superoxide radical anion scavengers markedly decrease the abatement. Therefore, it is concluded that holes and super peroxide radical anions play a major role with β-AgVO<sub>3</sub>/mpg-C<sub>3</sub>N<sub>4</sub> composite photocatalysts. Under visible light (room light irradiation) the same ROS, holes and hydro peroxide radicals, are formed. Therefore, the mechanism of the abatement/degradation mechanism should be the same as with UV/Vis irradiation but the concentration of active species is lower with visible light.

#### 4. Conclusion

Strategy developed discussed in this thesis resulted with benefits in

- Novel Visible light active Core Shell and composite photocatalysts (β-AgVO<sub>3</sub>/mpg-C<sub>3</sub>N<sub>4</sub>) were developed based on mechano-chemical mixing, grinding and calcinations.

- A novel strategy was used by combining porous materials and  $\beta$ -AgVO<sub>3</sub>/mpg-C<sub>3</sub>N<sub>4</sub> composites with different silver content to form new complex hierarchical structured  $\beta$ -AgVO<sub>3</sub>/mpg-C<sub>3</sub>N<sub>4</sub>/mesoporous material composite catalysts.
- Different mesoporous materials such as MCM-41, MCM48, FDU-12, KIT-6, SBA - 12, 15, 16 etc., have been prepared and proved interesting supporting materials for photocatalysts, due to a combination of good accessibility, uniform pore size and high surface area.
- Mesocrystals are developed which are composed of macro, meso, and nanosized hierarchical particles (TEM, SEM).
- Mesoporosity, surface area and pore sizes plays small to no role in improvement of photocatalysis. Finally improvement is due to high dispersion and better accessibility of size, e.g., agglomeration of photocatalytic particles.
- Similarly photocatalysts Zinc Oxide and titania P25 were loaded over the mesoporous host through simple mechano-chemical process.
- Mechano-chemical preparation facilitates uniform dispersion of the photocatalysts in the mesoporous host to exhibit the emission at UV wavelength due to the quantum confinement of ZnO and TiO<sub>2</sub> which proved improved activity.
- Obtained photocatalytic materials have been tested in the degradation of recalcitrant, which resulted in enhanced photocatalytic activity with photodegradation almost 2-3 times faster.
- Activity of Core Shell catalyst is higher and to best of our knowledge is the best visible light active catalyst.
- TOC mineralization proved that photocatalysts based on AgVO<sub>3</sub>/C<sub>3</sub>N<sub>4</sub>/SiO<sub>2</sub>, shows not only improved activity in abatement (decomposition) but also with total mineralization of the pollutants, which proceeds simultaneously.
- While ZnO and TiO<sub>2</sub> system has not improved the TOC mineralization, e.g., Total mineralization of ZnO is 4 times lower than abatement.
- Supported photocatalysts are easier to recover from the reaction solution due to large size, which are beneficially reused with minute loss of activity up to 10%. (append. 2)
- Different photocatalysts behaves differently in nature of the active species in the presence of scavengers. Effect of scavengers increases in sequence as  $h^+ < \bullet OH$

$\lll\lll O_2^{\bullet-}$  in TiO<sub>2</sub>-P25. While in ZnO and AgVO<sub>3</sub>/C<sub>3</sub>N<sub>4</sub>Core Shell photocatalysts effect of scavengers are as  $\bullet OH \lll h^+ \lll\lll O_2^{\bullet-}$ .

- Photocatalysts/SiO<sub>2</sub> behaves similar to the individual photocatalysts in all three systems TiO<sub>2</sub> (P25), ZnO, AgVO<sub>3</sub>/C<sub>3</sub>N<sub>4</sub> respectively. This concludes that Photocatalysts/SiO<sub>2</sub> behave similarly in mechanism of their precursor photocatalysis, producing similar active species. This concludes that supporting silica plays no role in the process of providing active species.
- From the selected silica as MCM-48(s), KIT-6, FDU-12(S), MCM-41(S) and in part SBA-15 are good support for CAT-25 in photocatalysis and show high performance, while supporting on SBA-12 and SBA-16 shows less photocatalytic activity. These differences might be due to the mechanical mixing (preparation method) with milling. The homogeneous mixing of equivalent amount of single components is easier to be achieved with 45% loading. On other side structure is better retained.
- The preparation influences the performance of photocatalyst on interface of used silica material therefore this make difficult to estimate the effect of the support. Over all the mesoporous material mentioned efficient support.
- Attractive photocatalytic system and hierarchical structuring useful for noble metal material saving and improve of activity.
- Atomic efficiency and degradation is achieved on the expense of mineralization, the active species are similar, we see attendance from small to high degradation and low mineralization but FDU-12-L we see also high mineralization as same as degradation.
- Finally, the photocatalytic degradation activity is different with different supports. But a clear dependence on pore size, specific surface area and specific pore volume is difficult to derive. Obviously, the preparation procedure conditions like mixing, milling and post thermal treatment influence the catalytic behavior and overlap textural effects as size and pores shape of silica particle. The conversions observed with different mesoporous supports scatter by *ca.*20%.

## 5 Appendixes

### 5.1 Materials

All chemicals were of analytical grade and used without further purification: double distilled water, polyoxyethylene-polyoxypropylene co-block polymer (Pluronic<sup>®</sup> F68) ((C<sub>3</sub>H<sub>6</sub>O.C<sub>2</sub>H<sub>4</sub>O)<sub>x</sub> or EO<sub>80</sub>PO<sub>80</sub>EO<sub>80</sub>, average M=8350, Sigma-Aldrich, 96%), Poly(ethyleneglycol)-*block*-poly(propylene glycol)-*block*-poly(ethylene glycol) (Pluronic<sup>®</sup> P-123) average M<sub>n</sub> ~5,800, BASF), Poly(ethylene glycol)-*block*-poly(propylene glycol)-*block*-poly(ethylene glycol) (Pluronic<sup>®</sup> P-127) average M<sub>n</sub> ~11000, BASF), ibuprofen sodium salt (C<sub>13</sub>H<sub>17</sub>O<sub>2</sub>Na, Sigma-Aldrich, 98%), melamine (Fluka, 99%), sulfuric acid (Fisher Scientific, 95%), *tert*-butanol (C<sub>4</sub>H<sub>10</sub>O, Sigma-Aldrich, 99%), ethylenediaminetetraacetic acid (C<sub>10</sub>H<sub>16</sub>N<sub>2</sub>O<sub>8</sub>, Sigma-Aldrich, 99%), silver nitrate (Sigma-Aldrich, 99%), ammonium vanadate (VEB LaborchemieApolda, 98%), benzoquinone (Sigma-Aldrich, 98%), titania P25 Degussa Evonik, (80/20 Anatase / Rutile), zinc oxide (Sigma-Aldrich, 99.99%), cetyltrimethyl ammoniumbromide (CTAB), tetraethylammonium hydroxide (TEAOH), tetraethyl orthosilicate (TEOS, Sigma-Aldrich, 98%), Ethanol (CH<sub>3</sub>CH<sub>2</sub>OH, Merck, 99.9%), ammonium hydroxide (aqueous) (NH<sub>4</sub>OH, (Merck, 32 wt%), *n*-hexadecyltrimethyl-ammoniumbromide (CH<sub>3</sub>(CH<sub>2</sub>)<sub>15</sub>N(Br)(CH<sub>3</sub>)<sub>3</sub>, Sigma Aldrich, 95%), Brij<sup>®</sup>76 Polyoxyethylene (10) Stearyl Ether C<sub>18</sub>EO<sub>10</sub>, (Aldrich).

### 5.2 Synthesis of Photocatalysts

#### *Synthesis of Mesoporous Graphitic Carbon Nitride (mpg-C<sub>3</sub>N<sub>4</sub>)*

The mpg-C<sub>3</sub>N<sub>4</sub> was prepared according to the reported procedure,<sup>[91]</sup> however, using the amphiphilic block copolymer polyoxyethylene-polyoxypropylene (Pluronic F68) ((C<sub>3</sub>H<sub>6</sub>O.C<sub>2</sub>H<sub>4</sub>O)<sub>x</sub> or EO<sub>80</sub>PO<sub>80</sub>EO<sub>80</sub>, M=8350, Aldrich) as template. To 150 mL doubly distilled water, melamine (5 g) and template Pluronic F68) (1.5 g) was added at once and was refluxed under magnetic stirring for 1h. After cooling to room temperature with stirring, 3 mL of H<sub>2</sub>SO<sub>4</sub> solution (H<sub>2</sub>SO<sub>4</sub>:H<sub>2</sub>O=1:1) was added. A white precipitate was obtained, filtered off by a paper filter, and dried at 80°C overnight. The obtained white powder was thermally treated at 380 °C with a rate of 5 °C min<sup>-1</sup>, then to 600 °C by 1.5 °C min<sup>-1</sup> in a quartz tube under uniform flow of argon, and kept at this temperature for four hours. The obtained yellow sample is named mesoporous graphitic carbon nitride (mpg-C<sub>3</sub>N<sub>4</sub>).

### ***Synthesis of $\beta$ - Silver Vanadate ( $\beta$ -AgVO<sub>3</sub>)***

Nanorods of  $\beta$ -AgVO<sub>3</sub> were prepared by the precipitation as reported before with some modifications.<sup>[92]</sup> Typically AgNO<sub>3</sub> (8.5 mmol, 1.443 g) and NH<sub>4</sub>VO<sub>3</sub> (8.5 mmol, 0.994 g) were dissolved separately in 50mL deionized water. Both solutions were simultaneously added drop wise from separate funnels into a 250 mL round bottom flask containing 30 mL deionized water during 5 minutes, followed by stirring for 30 minutes. The formation of a bright yellow precipitate was noted. The yellow suspended solution was refluxed with vigorous stirring for 3 hours. A change in color from yellow to orange was noticed. The reaction mixture was aged for 14 hours followed by filtration with a F4 paper filter. The collected precipitate was washed with 50 mL deionized water and ethanol, respectively. Finally, the orange colored solid was dried at room temperature for 5 hours and then at 110°C for 12 hours. Then the material was calcined at 500°C for 3 hours. In the process of calcination,  $\beta$ -AgVO<sub>3</sub> melts at 476°C. After calcinations  $\beta$ -AgVO<sub>3</sub> was obtained as a solid block and powdered with mortar and pestle.

### ***Preparation of the $\beta$ -AgVO<sub>3</sub>/mpg-C<sub>3</sub>N<sub>4</sub> Core Shell Catalyst and Composites***

Suitable amounts of  $\beta$ -AgVO<sub>3</sub> and carbon nitride were physically mixed together and grounded by hand for fifteen minutes in a porcelain mortar with the help of a pestle. The fine powdered composite mixture was calcined at 300°C for 3 hours in a closed crucible. The material was stored in a vial and used for further photocatalytic testing. For testing,  $\beta$ -AgVO<sub>3</sub>/mpg-C<sub>3</sub>N<sub>4</sub> composites containing 5, 10, 20, 30, 40, 50 and 70% of  $\beta$ -AgVO<sub>3</sub>, were prepared.

#### ***5.2.1 Preparation of the Advanced Complex Inorganic Nanomaterials (ACIN) $\beta$ -AgVO<sub>3</sub>/mpg-C<sub>3</sub>N<sub>4</sub>/SiO<sub>2</sub> Composite***

Different amounts of  $\beta$ -AgVO<sub>3</sub>/mpg-C<sub>3</sub>N<sub>4</sub> Core Shell /Composite catalyst were mechanically mixed with mesoporous silica such as (KIT-6, MCM41, MCM48, SBA-n where n = 12, 15, 16 and FDU-12). Mechanically mixed mixture was grounded for fifteen minutes in a mortar with the help of a pestle. Resultant powder was heated at 300°C for 2h in air. In such a way different compositions of ACIN with 5, 10, 20, 30, 40, 50 and 70% of  $\beta$ -AgVO<sub>3</sub>/mpg-C<sub>3</sub>N<sub>4</sub> were prepared whereby also the vanadate content was changed.

## ***5.2.2 Preparation of Mesoporous Silica Materials***

### ***Synthesis of MCM-41-L***

Typically 2.95g of CTAB dissolved in 70ml ultra-pure water with stirring. Then 4.5 ml TEOS and 3.5ml aqueous solution of 70% TEAOH (0.866ml + 4.45ml Et-OH) were added drop wise to the mixture under stirring at room temperature for 3h. Then the remaining TEAOH solution was added drop wise to the milky solution. <sup>[93]</sup>The pH of the resultant gel was 11.45. The molar composition of the obtained synthesis gel was: TEAOH/Si = 0.30, CTAB/Si = 0.4, water/Si = 60. Stirring was continued for 13h. The reaction product was filtered off, washed with double distilled water and dried in an oven at 60°C overnight and calcined at 500°C for 6h under air.

### ***Synthesis of MCM-41-S***

The molar composition of the synthesis gel was 1 x TEOS x 1.64 NH<sub>4</sub>OH x 0.15 CTAB x 126 H<sub>2</sub>O. <sup>[94]</sup>Procedure: Typically, 2.4g of CTAB were dissolved in 120g of deionized water, Then were added the 8ml 30% aqueous solution of NH<sub>4</sub>OH and 10ml of TEOS under stirring during 30 min. The gel was stirred for 12h and the solid obtained was filtered off, washed consecutively 2-3 times with water and ethanol and calcined at 823k (550°C) for 5h.

### ***Synthesis of MCM-48-L***

MCM-48 was synthesized hydrothermally from a gel having the composition 1 TEOS x 0.65x CTABr x 0.25 NaOH x 62 H<sub>2</sub>O. N-hexadecyltrimethylammonium bromide and sodium hydroxide were dissolved in deionized water slowly under continuous stirring. <sup>[73]</sup>After 15 min of stirring, TEOS was added drop wise and the stirring was continued until the gel became homogeneous. The whole synthesis was done in a water bath at 50° C. The solution was stirred for about 1h, charged into bottle, and heated at 383 k for 11 days. The product was filtered, washed with water and calcined at 823 k for 6h. The material was synthesized under ambient pressure in polypropylene bottles.

### ***Synthesis of MCM-48-S***

2.6 g aliquot of N- hexadecyltrimethylammoniumbromide (6.6 m mol) was dissolved in 120 g of deionized water and 50 mL of technical ethanol (0.87 mol), and 12mL of aqueous ammonia

(32 0.20 mol) was added to the surfactant solution under stirring.<sup>[74]</sup> The solution was stirred for 10 min (450 rpm), and 3.4 g of TEOS (16 m mol) was added at one time. The molar composition of the gel was 1TEOS x 12.5NH<sub>3</sub>x 54 EtOH x 0.4template x 417 H<sub>2</sub>O. After being stirred for 10 h (sample 5) at room temperature, the resulting solid was recovered by filtration, washed with distilled water, and dried in air at ambient temperature. The template was removed by calcination at 823 K for 6 h.

### ***Synthesis of KIT-6***

Kit-6 mesoporous silica was synthesized in acidic condition using a mixture of Pluronic P123 (BASF) tri block copolymer (C<sub>3</sub>H<sub>6</sub>O.C<sub>2</sub>H<sub>4</sub>O)<sub>x</sub>(EO<sub>20</sub> PO<sub>70</sub> EO<sub>20</sub>) and butanol<sup>[95]</sup>. 6 g of P123 was dissolved in 220 g distilled water and 12 g of concentrated HCl (35%). After 6 h stirring at 35°C, 6g of butanol was added while stirring for a further 1h. 12.48 g of tetra ethylorthosilicate (TEOS, 98%, Aldrich) was added and stirred for 24h at same temperature. The solution was transferred to a Teflon lined stainless steel autoclave and treated hydrothermally at 120 °C, for 3 days. The product was filtered and washed with a mixture of (5mL HCl + 70mL Et-OH + 70mL distilled water) and dried in vacuum at 50 mbar for 5h. The resulting white powder was calcined at 550°C for 6h to remove the surfactant.

### ***Synthesis of SBA-15***

Ordered mesoporous silica SBA–15 powders were synthesized according to the well-known procedure.<sup>[96]</sup> Typically, 8 g of Pluronic® P123, Poly(ethylene glycol)-*block*-poly(propylene glycol)-*block*-poly(ethylene glycol), (C<sub>3</sub>H<sub>6</sub>O.C<sub>2</sub>H<sub>4</sub>O)<sub>x</sub> tri block copolymer was added to 260 mL of distilled water and 40 mL of concentrated hydrochloric acid (37 wt.%HCl). The mixture was stirred until the surfactant was dissolved. Then 17 mL of TEOS was added under stirring at 45°C. The reaction gel was stirred for 8 h at 45 °C and aged for another 16 h at 80 °C. The obtained gel with molar ratios of reaction components 1 SiO<sub>2</sub>: 0.017 P123: 5.85 HCl: 190 H<sub>2</sub>O was hydrothermally treated in a stainless steel Teflon–lined autoclave at 100 °C for 24 h. The obtained product was continuously washed with distilled water and dried at room temperature. The surfactant was removed by calcination at 550°C for 6 h in an air flow at a heating rate of 1 °C min<sup>-1</sup>.<sup>[97]</sup>

### ***Synthesis of SBA-16***

For synthesizing SBA-16, 2.0 g of Pluronic<sup>®</sup> F127 (poly-(oxyethylene)-poly (oxypropylene) block copolymer,  $(C_3H_6O.C_2H_4O)_x$ ) and 4.0 g of KCl were dissolved in 100 mL of distilled water and 20 mL of HCl (37%) in a beaker with stirring at 40 °C. 8.6 g of TEOS was added to the solution, stirring for 24 h until clear. The solution was transferred into a Teflon bottle and matured in an oven at 100 °C for 48-72 h. The white precipitate was filtered, washed with distilled water three times and dried at 40 °C. The as-prepared SBA-16/surfactant was calcined at 550 °C for 5 h to remove the surfactant. <sup>[98]</sup>

### ***Synthesis of SBA-12***

Typically at room temperature, 4.0 g of Brij<sup>®</sup> 76 ( $C_{58}H_{118}O_{21}$ , polyoxyethylene (10) stearyl ether) was dissolved in 20 g of water and 80 g of 2 M HCl solution with stirring. Then 8.80 g of TEOS was added to that homogeneous solution with stirring at room temperature for 20 h. The solid product was recovered, washed, and air-dried at room temperature. Yields are typically ~95% (based on silicon). <sup>[69, 70]</sup>

### ***Synthesis of FDU-12-S***

2 g of Pluronic<sup>®</sup> F127 poly-(oxyethylene) poly-(oxypropylene) block-copolymer- $(C_3H_6O.C_2H_4O)_x$  and 5.0 g of KCl (potassium chloride) were dissolved in 100 ml distilled water and 20 ml HCl (37%) in a beaker. The solution was stirred at 40°C (>1h). <sup>[99]</sup> 2.0 g of TMB (tri methylbenzene) was added to this clear solution drop wise, and stirred for 24h. Thereafter 8.3 g of TEOS were added to the solution and stirred for a further 24 h. The solution was matured in an oven at 100°C for 48-72h. The white precipitate was filtered off, washed with distilled water three times and dried at 40°C. The as-prepared surfactant containing FDU-12 was calcined at 550° C for 5h to remove the surfactant.

### ***Synthesis of FDU-12-L***

For the synthesis of FDU-12-L the same procedure was used as for FDU-12-S, but the hydrothermal treatment was done at 120°C instead of 100° C for 1 day. <sup>[104]</sup>

### 5.3 Characterization

**PXRD:** The XRD measurements were carried out on a powder X-ray diffractometer STADI-P (STOE) using monochromatic Ni-filtered  $\text{CuK}\alpha_1$  radiation ( $\lambda = 1.5406 \text{ \AA}$ ) for checking crystallinity and phase composition. A curved Ge (111) monochromator (40kV, 40mA, linear PSD) was used in the  $2\theta$  diffraction angle range of 5 to  $90^\circ$ , with a resolution (scan stepsize) of 0.02 and scan step time 180 sec.

**SAXS:** Small angle X-ray scattering measurements were carried out using a Kratky-type instrument (SAXSess, Anton Paar, Austria) operated at 40 kV and 50 mA in slit collimation using a two-dimensional CCD detector ( $T = -40^\circ\text{C}$ ). The 2D scattering pattern was converted into a one-dimensional scattering curve as a function of the magnitude of the scattering vector  $q = (4/\lambda)\sin(\theta/2)$  with SAXS Quant Software (Anton Paar). A Göbel mirror was used to convert the divergent polychromatic X-ray beam into a collimated line-shaped beam of Cu K radiation ( $\lambda = 0.154 \text{ nm}$ ). Slit collimation of the primary beam was applied in order to increase the flux and to improve the signal quality. The sample cell consisted of a metal body with two windows for the X-ray beam. The powdered samples were sealed between two layers of Scotch® tape. Scattering profiles of the mesoporous materials were obtained by subtraction of the detector current background and the scattering pattern of the Scotch® tape from the experimental scattering patterns. Correction of instrumental broadening effects (smearing) was carried out with SAXS Quant software using the slit length profile determined in a separate experiment.

**Nitrogen Ad-and Desorption:** The porosity, specific surface area, pore volumes and pore sizes were determined by  $\text{N}_2$ -adsorption/desorption isotherm measurements using an automated device “Sorptomatic” (Porotec, Thermo Scientific). Nitrogen adsorption isotherms were measured at  $-196^\circ\text{C}$ . Before adsorption measurements, the samples were degassed under vacuum for at least two hours at  $200^\circ\text{C}$ . The specific surface areas of the samples were calculated using the BET (Brunauer-Emmett-Teller) method using the relative pressure range of 0.05-0.35. The mesopore sizes and pore distributions and specific pores volumes were determined from the adsorption branch in the relative pressure range 0.3-0.99, using the BJH (Barrett-Joyner-Halenda) method.<sup>[100]</sup> Total pore volumes were calculated from the adsorbed amount of  $\text{N}_2$  at relative pressure of 0.995.

**UV/Vis Spectrometry:** Optical properties were measured and studied with UV/Vis diffuse reflectance spectra using a Cary 5000 spectrometer (Varian) equipped with a diffuse

reflectance accessory (praying mantis, Harrick) at room temperature. The spectra were collected in the spectral range of 200-800 nm, using BaSO<sub>4</sub> as reference material. The spectra were converted into the Schuster-Kubelka-Munk function F(R) using Tauc plot, where for direct band gap  $(h\nu\alpha)^2$  is plotted against the photon energy  $h\nu$ , where  $\nu$  is the photon frequency, and  $\alpha$  the absorbance at the considered frequency and  $h$  is the Planck's effective quantum.<sup>[101]</sup>

**TEM:** The morphology and size of the catalysts were characterized on a LIBRA 120 transmission electron microscope (TEM) operated at 120 kV, or with EM 902A, ZEISS, TEM with at 80 kV acceleration voltage. Samples were prepared using 400 mesh copper grids with a wholly carbon layer (PLANO GmbH) by sputtering with gold for 60s prior to measurement. (Written by EMZ center. But normally they haven't done it with these samples.

**SEM:** Samples were mounted on aluminum stubs with a sticky carbon tape, either uncoated or carbon coated (Lica SCD 500) and measured on a MERLIN VP COMPACT Field Emission SEM (Zeiss) with different detector types and settings (respective settings: see legend on the pictures). SEM is a comparatively simple method and does not require substantial sample preparation and long analysis times, but with the limitations of this low resolution.

**EDX:** Element composition and element distribution of samples were analyzed by a Bruker Quantax XFlash 6130 EDX detector with an energy resolution of 126 eV. (Respective settings: see legend on the pictures and graphs).

**FT-IR:** Vibrational spectra were recorded with the FT-IR spectrometer (Nicolet 380) with a Smart Orbit ATR device in the spectral range of 500-4000 cm<sup>-1</sup>. The powder samples were directly dispersed above the ATR device and spectra was recorded.

**Raman:** Raman spectrometer LabRAM HR 800 HoribaJobin YVON carrying Olympus BX41 microscope with changeable lenses was used for recording Raman spectra. Samples were excited with infrared laser (785 nm, 100 mW), or red laser (632.817 nm, 20 mW, polarized), or a blue laser (473 nm, 20 mW, air-cooled solid-state laser) is used. Powder sample was dispersed on a glass Tab and laser was focussed on single particles for recording Spectra.

**Mass Spectrometry:** ESI-TOF-MS measurements were performed using an electro spray ionization mass spectrometer coupled with a HPLC system 1200/ESI-TOF-MS 6210 (Agilent) to investigate qualitatively the formation of intermediates during photocatalytic treatment of the aqueous ibuprofen solution by using the molecular mass peak in positive and negative mode. An aqueous solution containing 10 vol. % of methanol (MeOH for HPLC,

gradient grade,  $\geq 99.8\%$ ) and 0.1 vol.-% formic acid HCOOH was used as mobile phase. The flow rate was 1.0 mL/min.

#### 5.4 Photocatalytic Testing and Analysis

The photocatalytic abatement and adsorption of non steroidal anti-inflammatory drug ibuprofen (IBP) was studied under batch conditions. Typically, the batch reactor (250 mL glass beaker) containing 250 mL of 10 ppm aqueous IBP solution and 10 mg of the catalyst, was placed into a closed aluminum box equipped with four UV/Vis solarium lamps (Phillips). The lamps positioned on the top had a total power of 60 W (4 lamps x 15 W, Phillips). These lamps mainly simulate the UV part of sun light besides of additional emission lines in the visible light range. The irradiation intensity of the experimental setup was *ca.* 3.2 mW/cm<sup>2</sup> in case of UV/Vis solarium lamps. For visible light irradiation, a white light lamp (Toshiba 16 W, LED cold white light lamp), normally used for illumination of offices (rooms) was used. The solution was stirred magnetically during the photocatalytic experiments. For quantitative analysis of the irradiated solution, aliquots were taken at certain time intervals using a syringe equipped with a 0.45  $\mu\text{m}$  PTFE filter. Adsorption experiments were carried out in the dark. The remaining IBP content in the samples was determined by the change of the intensity of IBP band at *ca.* 220 nm using a UV/Vis spectrometer (Varian, Cary Win UV). After particular intervals of time the amount of total organic carbon in taken aliquots was analyzed with Shimadzu TOC-L CSH/CSN device. The percentages of abatement of IBP after various intervals of UV/Vis irradiation were calculated using equation below:

$$\text{Abatement (\%)} = (A_0 - A_t) / A_0 \times 100 \quad (1)$$

Where  $A_0$  and  $A_t$  are the initial absorbance and the absorbance of the aromatic ring of ibuprofen at *ca.* 222nm after various time intervals of UV/Vis irradiation (t), respectively. According to the law of Lambert-Beer, the UV absorbance intensity is directly proportional to the concentrated of the measured substance. All data were obtained at room temperature.

### 6 Titanium dioxide (TiO<sub>2</sub>)

Titania Degussa P-25 is generally known as one the best photocatalysts due to its suitable phase composition as mixture of  $\sim 80\%$ Anatase and  $\sim 20\%$ Rutile, and is more active than pure Anatase<sup>[102]</sup>. In the present work, TiO<sub>2</sub>-SiO<sub>2</sub>,<sup>[103]</sup> nanoparticles supported photocatalysts were formed with the physically mixing, milling and calcinations, with same procedure as

discussed in experimental section for the development of appropriated 10, 20, 30, and 50% loading of TiO<sub>2</sub> on mesoporous silica.

## 6.1 Experimental: TiO<sub>2</sub>/SBA-12

The binary catalyst of titaniaP-25 supported on SBA-12 is studied with nitrogen sorption. Nitrogen adsorption isotherm confirms the nature of SBA-12 remains constant with the presence of micropores at very low relative pressure (Fig. 66). Type IV isotherm remains identical as SBA-12 in Figure 2. Isotherm starts with mesoporous followed by narrow steps of capillary condensation which shows similar pore size uniformity. A hysteresis loop of type H4 at  $p/p_0 \sim 0.5$  is noted. Although no much multilayer adsorption is noted above the knee, which remains

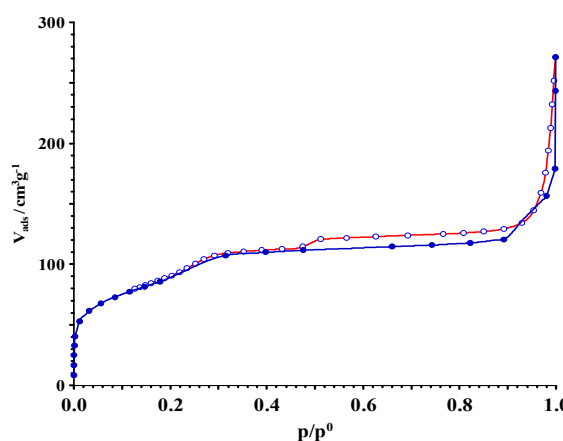


**Figure 66:** N<sub>2</sub> adsorption-desorption isotherm curve of the 20% TiO<sub>2</sub>/SBA-12.

uniform from relative pressure of 0.3 – 0.95, but due to large inter particle mesopores, increase

happens above relative pressure of 0.95. BET surface area is decreased with 20% loading of titaniaP-25 to 318 m<sup>2</sup>/g from 513 m<sup>2</sup>/g. Mesopore diameter is changed from ~3.81 nm to 2.38 nm, but total cumulative volume remains almost constant to 0.37 cm<sup>3</sup>/g.

Figure.68 shows the adsorption desorption isotherm of the 20% TiO<sub>2</sub> loaded silica. 20% TiO<sub>2</sub>/MCM-41-S shows surface area of 838 m<sup>2</sup>/g which is decreased from 1034 m<sup>2</sup>/g for the pure MCM, with cumulative volume of 1.16 cm<sup>3</sup>/g. Out of it mesoporous cumulative volume 0.88 was noted, with maximum diameter of 1.7 nm and mean diameter of 2.64nm. The pores remain same with and without TiO<sub>2</sub>. Microporous volume goes up-to 0.54 cm<sup>3</sup>/g from 0.40 cm<sup>3</sup>/g.

Nitrogen adsorption isotherm of 20% TiO<sub>2</sub>/SBA-16 shows a uniform and gradual uptake which represents broad distribution of mesopores. The irreversible adsorption isotherm is of type IV with specific surface area of 838 m<sup>2</sup>/g, gives hysteresis loop of most probably H2 type at  $p/p_0 \sim 0.45$ , instead of 0.5. Mesoporous pores diameter is reduced from ~3.47 nm to 1.7 nm. Total cumulative volume is increased from 0.389cm<sup>3</sup>/g to 1.16 cm<sup>3</sup>/g.

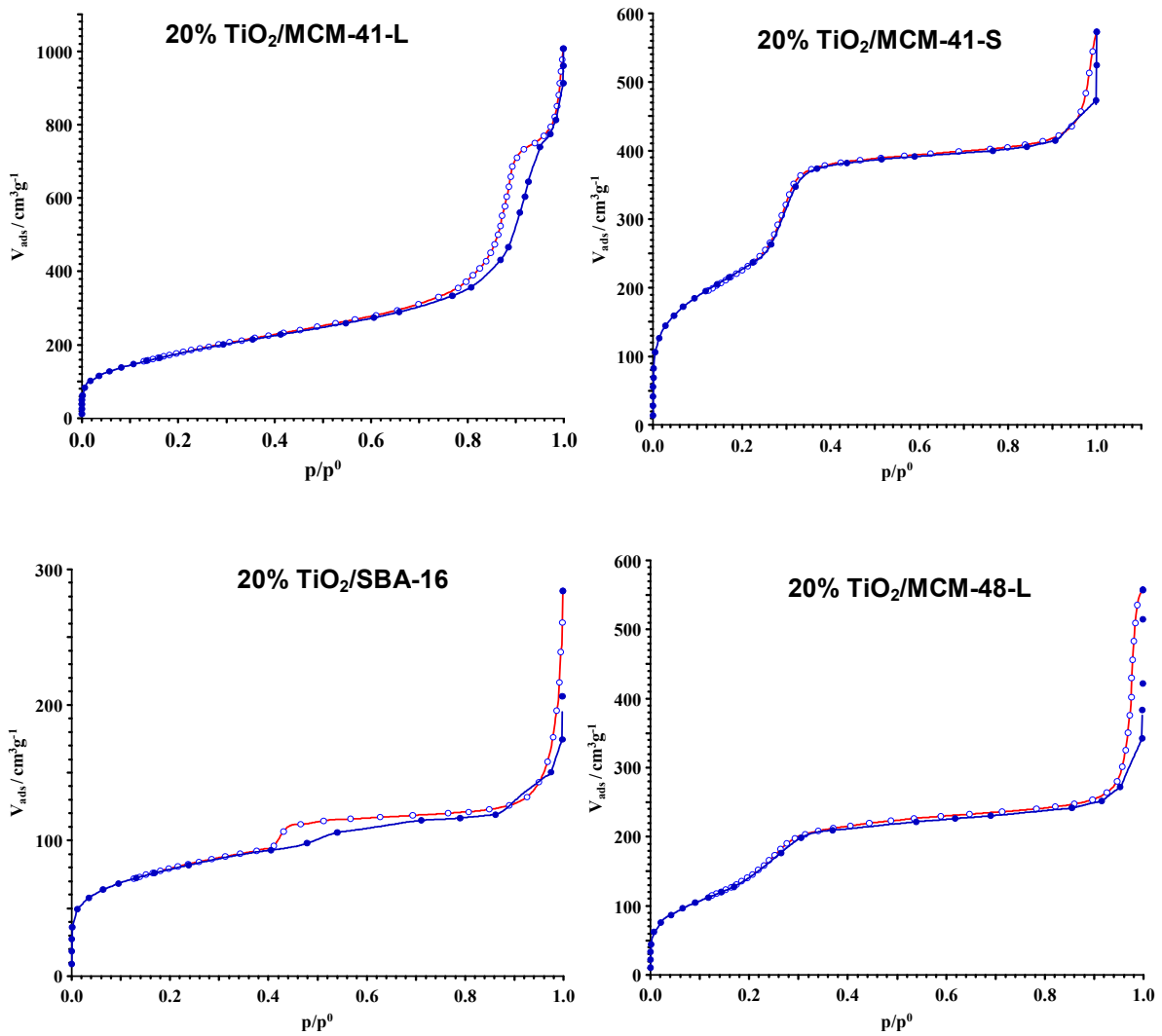


**Figure 67:** N<sub>2</sub> adsorption-desorption isotherm curve of the 20% TiO<sub>2</sub> over MCM-41-L, MCM-41-S, SBA-16 and MCM-48-L.

Nitrogen adsorption isotherm of MCM-48-L with 20% TiO<sub>2</sub> shows similarity of gradual uptake in the region up to 0.35 reflects high quality small mesoporous material. BJH calculations show uniform and narrow distribution of mesopores with maximum at  $\sim 1.7$  nm of  $0.90 \text{ cm}^3/\text{g}$  mesoporous cumulative volumes which are increased due to the addition of non poroustitania. Above  $p/p_0$  of 0.9 sudden increases in volume of adsorbed nitrogen indicates the presence of large mesopores. Surface area is highly decreased from  $1100 \text{ m}^2/\text{g}$  to  $508 \text{ m}^2/\text{g}$ . [104]

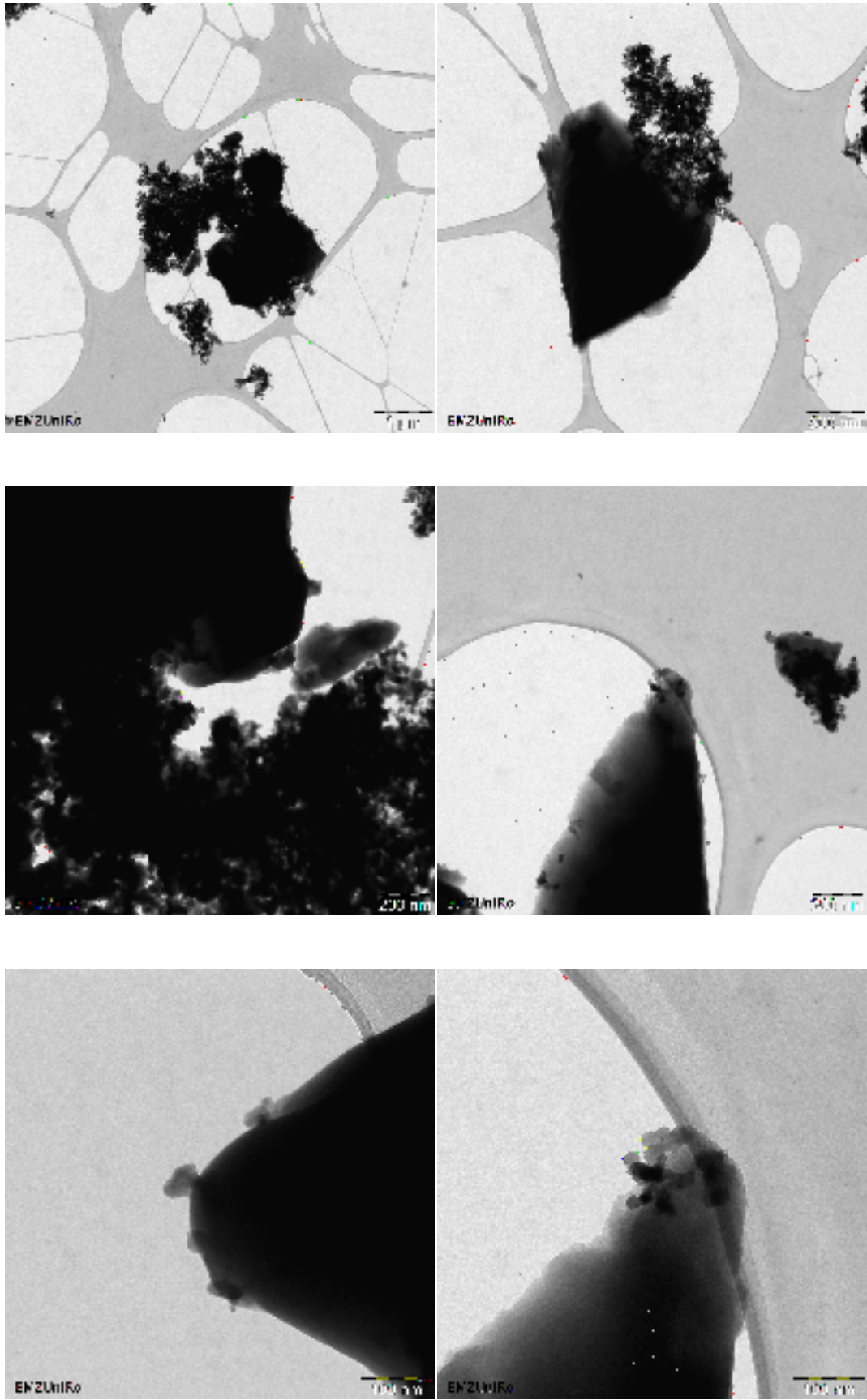


**Figure 68:** TEM images showing the morphology of  $\text{TiO}_2/\text{SBA-12}$ .

Unlike high dispersion of CAT-25 or CAT-30 over silica, TEM images of 20% TiO<sub>2</sub> and SBA-12 binary photocatalyst (Fig. 68) shows aggregates of titania P-25 near silica with anchoring on it. Dispersion is noted on the particles of silica which also confirms the little to no change in nitrogen adsorption isotherms as silica without TiO<sub>2</sub>.

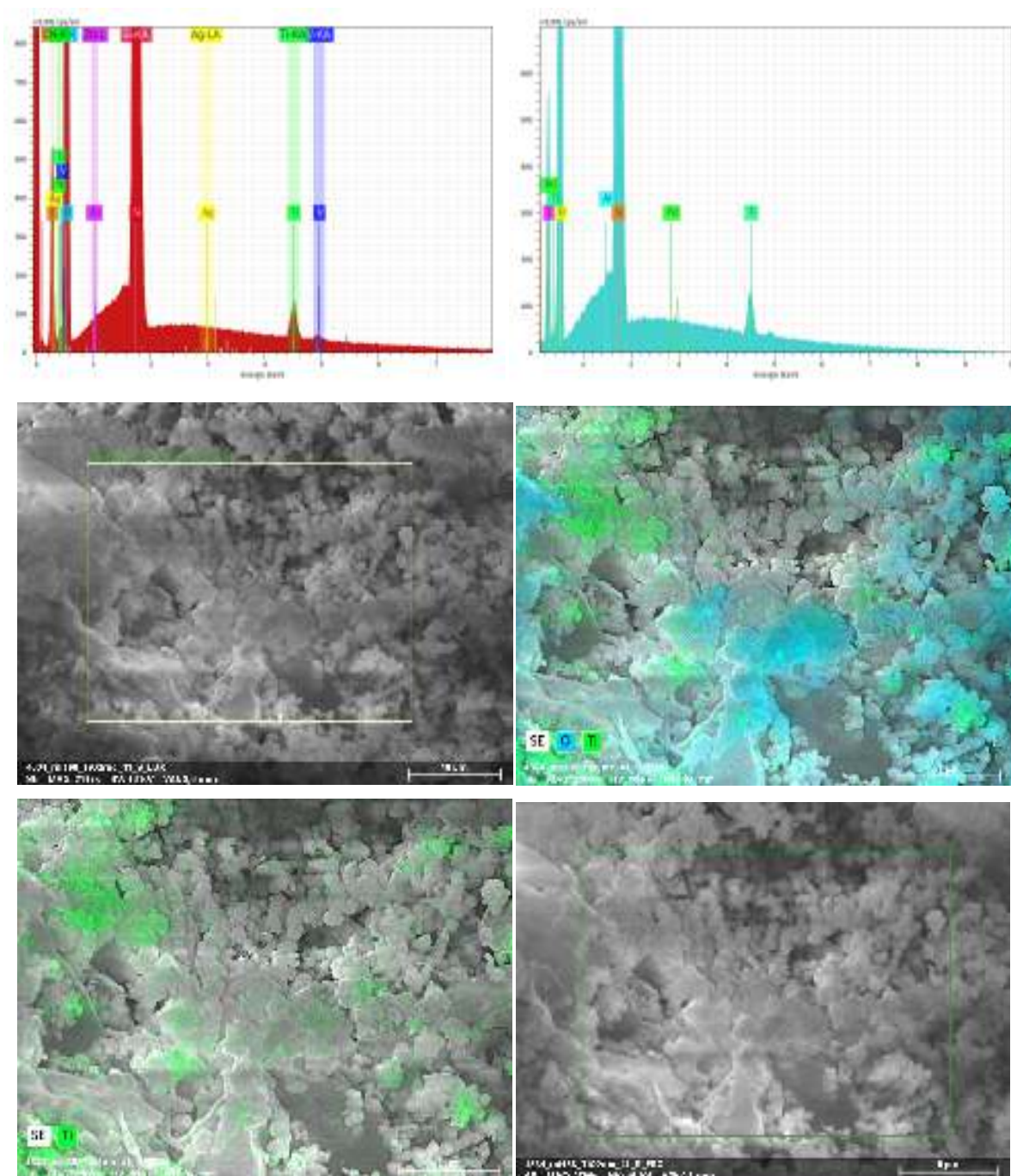


**Figure 69:** EDX spectrum, and elemental mapping showing the uniform distribution of the 20% TiO<sub>2</sub>/MCM-41-S. Elements Ti (●), O (●), Si (●)

**TiO<sub>2</sub> EDX:** The elemental analysis of the prepared 20% TiO<sub>2</sub>/Silica composites was studied with Energy dispersive X-ray spectra (EDX). The EDX spectra reveals the elements Ti, O, Si,

but meanwhile impurities less than 1 percent can also be found in Figure. 70. These impurities are due to the glassware and personal errors in specific sample. Elemental mapping doesn't show uniform distribution of all elements within sample, TiO<sub>2</sub> is dispersed in non uniform way above the silica. Where it is in line with TEM images showing that TiO<sub>2</sub> particles are self aggregated on big crystals of silica (Fig. 69).

## 6.2 Photocatalytic Activity of Titania P-25 / Mesoporous Silica Composite

The photocatalytic activity of the synthesized nanoparticles was evaluated by the photo degradation of Ibuprofen (as a model for pollutants in wastewater) under UV irradiation.

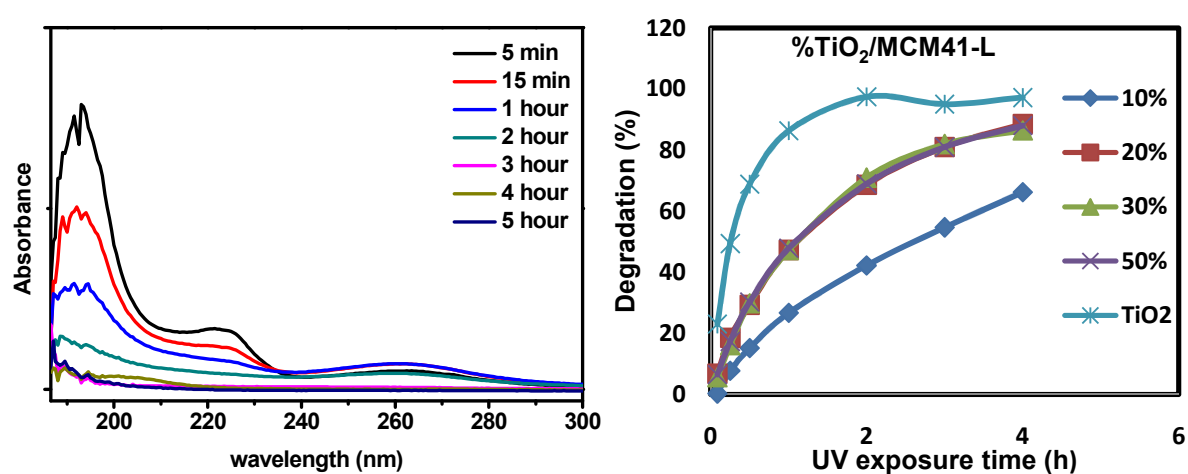


**Figure 70:** Photocatalytic degradation of IBP over TitaniaP-25 (a) and % TiO<sub>2</sub>/MCM-41 with different catalyst content (b). Condition: 250 ml batch reactor, 10 ppm IBP solution, 10 mg catalyst loading, cat /IBP = 4, 60 W UV/Vis Solarium lamp irradiation.

The intensity change in UV/Vis spectra of ibuprofen solutions after photocatalytic treatment under UV irradiation is shown in Figure.70 a-b. A decrease of the aromatic ring absorbance at 193.5 and 222 nm is observed due to the degradation or cleavage (opening) of the aromatic ring. At the same time, a new absorbance appears at *ca.* 260 nm. Its intensity increases and later decreases again with prolonged photo catalytic treatment. This band is assigned to the formation of reaction intermediates, likely phenyl radicals, which show a strong absorbance at *ca.* 250 nm. The phenyl radical can be formed by holes as is general accepted:  $RH + h^+ \rightarrow R\cdot + H$ . The photocatalytic performance of commercial titaniaP-25 Degussa (Evonik) starts immediately as shown by the abatement curve (Fig. 70a). A sharp decrease in the concentration of IBP is noted, within course of photocatalytic treatment. In half an hour almost *ca.* 50% of IBP is abated, while in one hour degradation reaches to ~ 86% while maximum degradation is achieved within 2 hours to 98% which remains constant to 4 hours.

In case of supported catalysts (Fig. 69b), 10% TiO<sub>2</sub>/MCM-41 which contains almost 90% of silica and out of 10% of titaniaP-25 shows almost ~27% photo catalytic activity in 1 hour, which is increasing to 66% abatement in 4 hours of photo catalytic treatment. Loading with 20%, 30% and 50% titaniaP-25 results in similar achievement of ~ 48% photo catalytic activity which is thoroughly increasing with reaction time to 88% within 4 hours.

**Atomic efficiency:** In Figure.71, the calculated atomic efficiency based on photocatalytic abatement after 4 hours, is presented. Calculations based on formula 3.1 shows that 10% loading is about 6.8 times effeceint, with respect to atomic % of TiO<sub>2</sub>P-25. Further increase of the loading percentage a gradual decrease of effeciency is noted, 20% loading shows the atomic effeciency of 4.5 times respectively. While loading to 30 and 50% results in 3 and 1.8effeciency ratio. But still the atomic efficiency of the resultant photocatalysts is higher than starting TiO<sub>2</sub>-P-25.

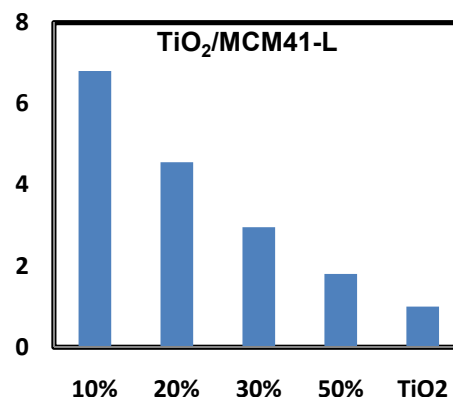


**Figure 71:** Atomic efficiency of % TiO<sub>2</sub> P-25/MCM-41 based on the TiO<sub>2</sub> content after 4h photo catalytic treatment.

**Summary:** A summary of the results obtained with different loaded of titania-P-25 on different types of silica are shown below (Fig. 71). Different supports behave differently. In case of MCM-4-S trend of photo catalytic abatement is 10% < 50% < 20% < 30% < TiO<sub>2</sub>-P-25. Surprisingly the photo catalytic activity observed with 50% loading is lesser than observed with 20 and 30%.loading.Titania supported on SBA-15 showed similar photo catalytic activity for 10% and 30% loading, showing the importance of the dispersion of titania for the final activity obviously it is higher with 10% loading.

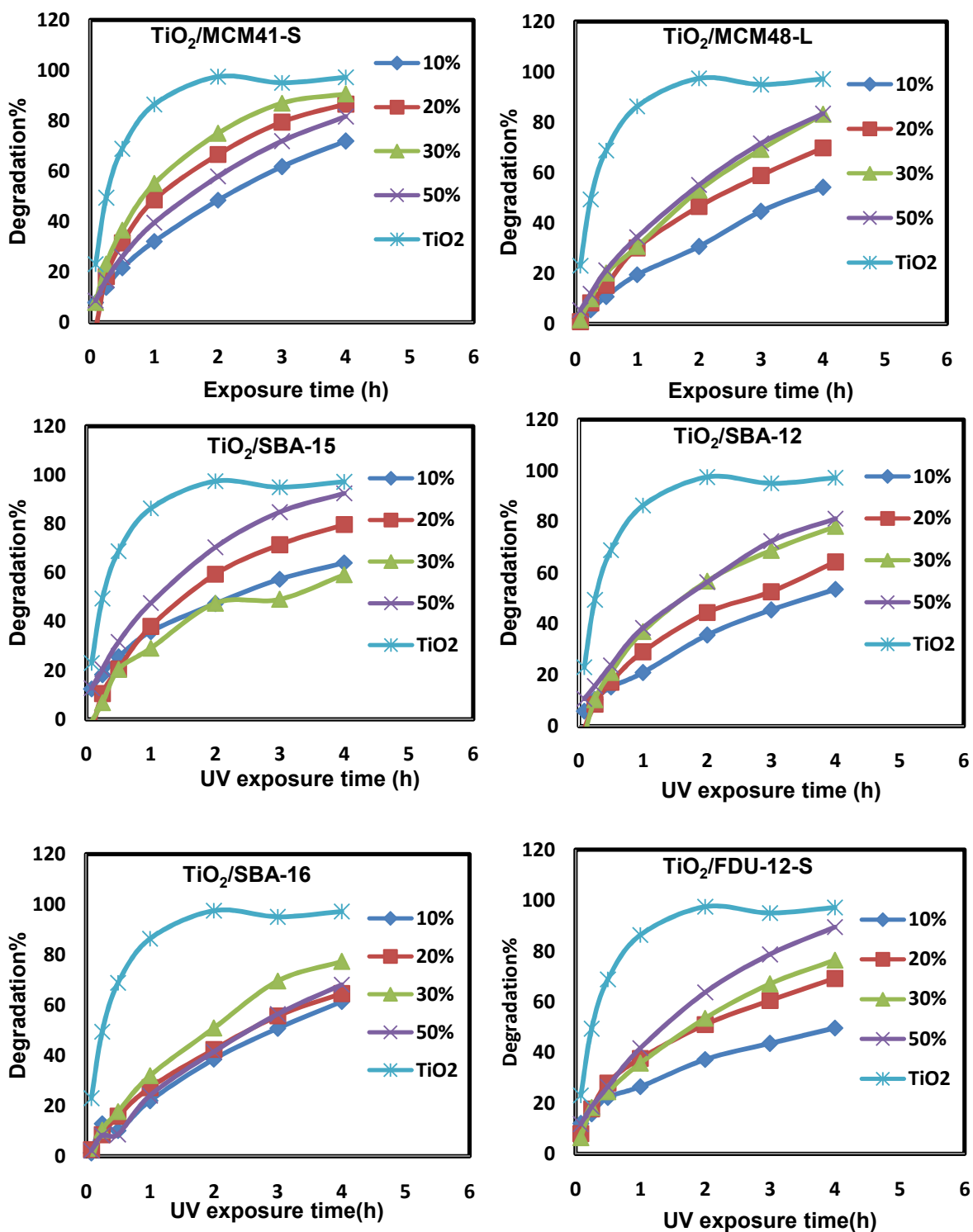


**Figure 72:** Photocatalytic degradation of IBP over titania P-25/Mesoporous silica with different catalyst content. Condition: 250 ml batch reactor, 10 ppm IBP solution, 10 mg catalyst loading, cat /IBP = 4, 60 W UV/Vis Solarium lamp irradiation.

The activity in terms of conversion shows the following trend with titania loading: 30% = 10% < 20% < 50% < TiO<sub>2</sub>-P-25. Whereas with SBA-16 the trend with loading is the following: 10% < 20% < 50% < 30% < TiO<sub>2</sub>-P-25. Supporting titania P-25 on MCM-48-L, SBA-12, and FDU-12-S resulted with a general trend of gradual increase in photo catalytic

activity with increase of titania P-25 loading as 10% < 20% < 30% < 50% < TiO<sub>2</sub>-P-25. Obviously, deviations in the order are caused by dispersion effects.

In case of 20% loaded titania P-25, an average value of the range of ~64 to 69 was noted for silica except high values for SBA-15 and MCM-41(S) of ~80 and ~86%. Same pattern for 30% loading was found except SBA-15 giving very low activity of ~59% which is considered as experimental error. Highest value of ~90% was found for MCM-41-S other silica gave value in the range of ~76 - ~83%. In case of 50% loading of titania P-25 on silica showed that SBA-15 shows highest value of ~97% while others are in range of ~82 – 89%. Lower value was noted for SBA-16 of ~68%. These findings showed that loading of titania P-25 with huge amount of deviations with loading percentage is highly sensitive to percent loading and physical mixing. Personal error plays a big role in deviations from a standard pattern.

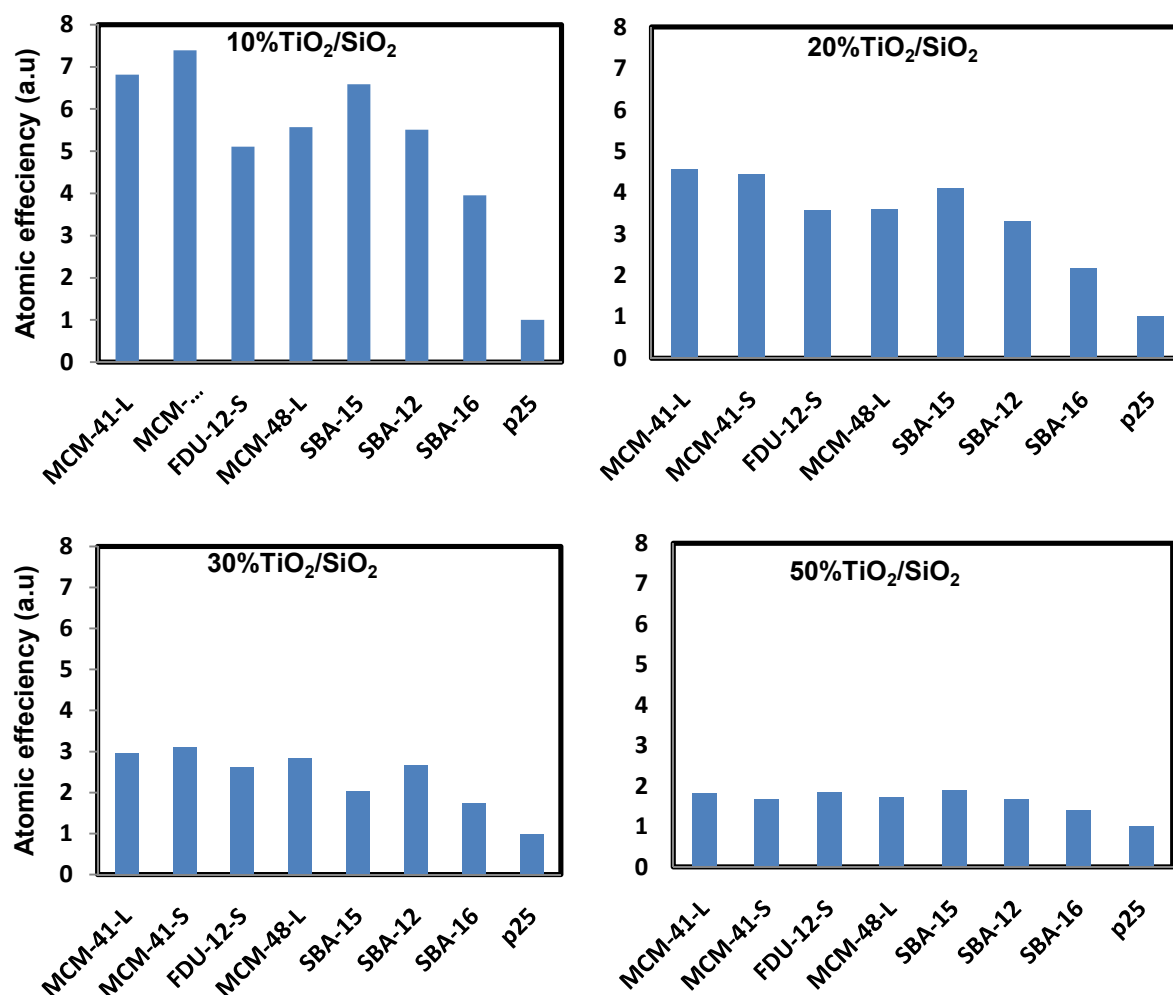


**Figure 73:** Improvement of the atomic efficiency of titania P-25/ Silica based on titania P-25 content after 4h photo catalytic treatment.

Calculations based on the formula 3.1 described in experimental section, atomic efficiency was found with quantity of titania P-25 and graphed as below (Fig. 73). Calculations were

carried out with data taken after 4 hours of photo catalytic treatment while for comparison also calculations were performed with data from one hour of photo catalytic treatment.

Highest efficiency of upto  $\sim 7.4$  was calculated for MCM-41 (S) with 10% loading of titania P-25. Similar behaviour of  $6.8$  was noted for MCM-41 (L) followed by SBA-15 with  $\sim 6.6$ . Other silicas showed atomic efficiency of  $\sim 5$  with respect to titania P-25. Same behaviour was noted with 20% loading of titania P-25 on silicas with atomic efficiency of  $\sim 4.1 - 4.5$  times with MCM-41 and SBA-15, while  $3.0$  to  $3.6$  times efficiency was noted for other silicas except SBA-16 showing activity of almost  $\sim 2.2$ .

Similarly with 30% loading of titania P-25 on silicas same pattern is retained with the calculation of  $\sim 3$  times with MCM-41 and SBA-15, than original P-25.  $\sim 2$  times efficiency is noted with other silicas while similarly lowest efficiency of  $1.7$  times for SBA-16. Trend in boosting of efficiency decreases with increase of the loading content, of titania P-25 to 50%. Although abatement of 50% titania P-25 loaded on silica is near to original titania P-25. But resultant atomic efficiency is reduced to almost lower than  $\sim 2$ .

**Active Species:** For understanding deeply the role of photocatalytic active species during the degradation of IBP over Titania P-25 and silica supported titania P-25. Different types of scavengers for holes/radical trapping during experiments were added. The impact of t-BuOH ( $\bullet\text{OH}$  scavenger), EDTA (holes scavenger) and 1,4-BQ ( $\text{O}_2^{\bullet-}$ ), added respectively on the abatement of IBP are shown in (Fig. 74).

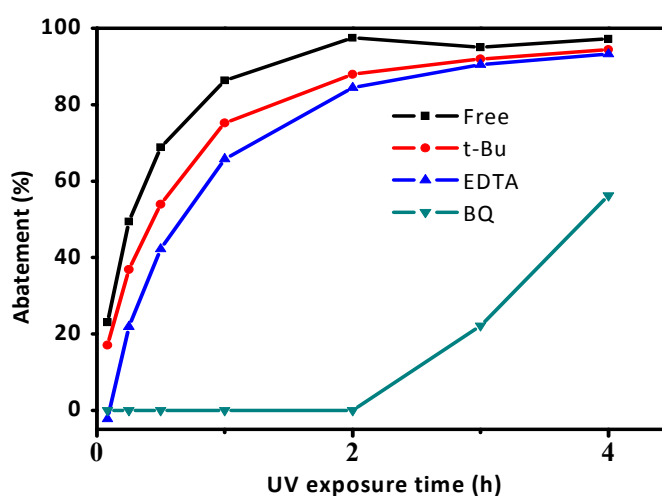


**Figure 74:** Impact of different scavengers on abatement of IBP over commercial  $\text{TiO}_2$  (P-25) under UV/Vis irradiation. Reaction conditions: T: room temperature, Co (IBP): 10 ppm, Vo (IBP): 250 mL, C (catalyst): 10 mg, scavengers: 1.46 mg EDTA, 0.1 mL t-BuOH, 2.704 mg-BQ.

The nature of the reactive species contributing to the abatement of IBP over commercial  $\text{TiO}_2$  (P-25) was studied with the addition of selective scavengers as shown in (Fig.75). The addition of the t-BuOH has low effect on lowering down the reaction rate which shows that  $\bullet\text{OH}$  radicals are not the major species playing role in the abatement. While addition of EDTA leads to more pronounced lowering in the rate of abatement in first 2 hours of the photocatalytic reaction. But still has no major effect which shows that hole( $\text{h}^+$ ) also contributes in low amount. Addition of 1,4-BQ leads to a markedly drop of the conversion until

2 hours, indicating that superoxide radicals  $O_2^{\bullet-}$  or hydroperoxyl  $^{\bullet}OOH$  radicals behaves as main active species for the abatement of ibuprofen in photocatalytic reaction of  $TiO_2$ P-25.

This indicates that superoxide radicals  $O_2^{\bullet-}$  or hydroperoxyl ( $^{\bullet}OOH$ ) radicals formed at the conduction band are important active species formed with commercial  $TiO_2$  (P-25) in the abatement of pollutants [105]. The addition of hole ( $h^+$ ) and  $^{\bullet}OH$  radical scavenger also reduces the photocatalytic abatement of IBP from originally ~98% (no scavenger) to ~80% within 2 hours of photocatalytic treatment. Because titania is very active we conclude that the low decrease is due to the large amount of formed holes and hydroxyl radicals.

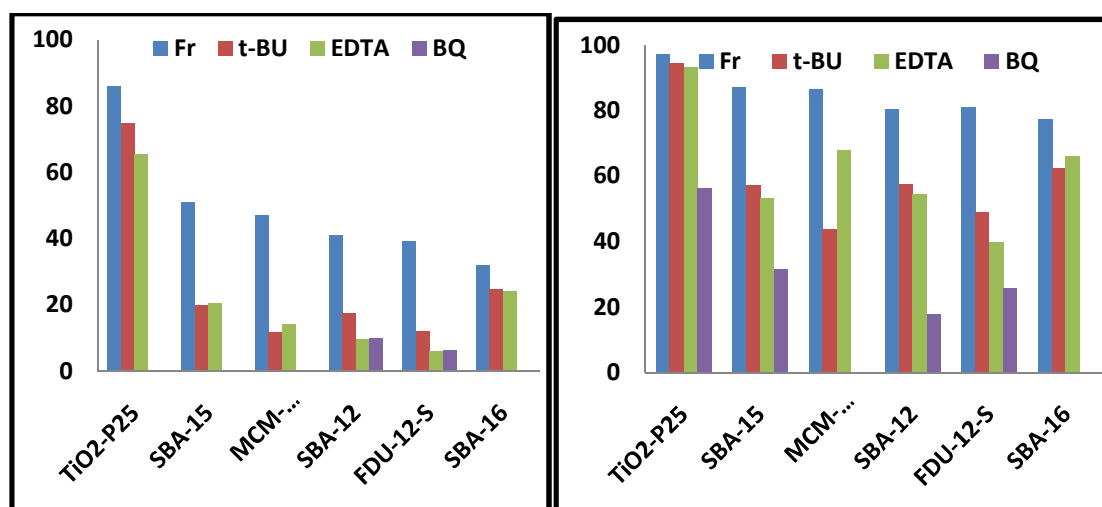


**Figure 75:** Impact of different scavengers on abatement of IBP over titania P-25 and silica supported titania P-25 under UV/Vis irradiation after 1 hour (a) and 4 hours (b). Reaction conditions: T: room temperature, Co (IBP): 10 ppm, Vo (IBP): 250 mL, C (catalyst): 10 mg, scavengers: 1.46 mg EDTA, 0.1 mL t-BuOH, 2.704 mg 1,4-BQ.

Results show that to the photocatalytic reaction of titaniaP-25, the addition of  $^{\bullet}OH$  radical scavenger influences the reaction rate up to 10% within one hour from originally 86% (no scavenger) to 75% indicating the strong contribution of  $^{\bullet}OH$  radicals, as shown in (Fig.75a), but within time duration of 4 hours the effect is not much pronounced showing only difference of 3% (originally 97% (no scavenger) to 93%) abatement (Fig 75b). But with supported reactions a strong influence of the scavenger was found which concludes that the required active species are quantitatively smaller due to 3.3 times low amount of titania, but still there is near 40% abatement to the original no scavenger.

Valence band holes were also found to involve directly in the photocatalytic decomposition of organics. EDTA as a hole scavenger resulted with retardation of reaction rate. With titaniaP-25 photocatalytic abatement of IBP decreased from 86% (without addition of EDTA) to 66% (addition of EDTA) for 1hrs of irradiation. With supported titaniaP-25 on different silica the retardation rate is almost similar as with OH radical scavenger as in SBA-15 and SBA-16.

While more effective retardation is found in SBA-12, FDU-12-S and less effective in case of MCM-41-L.

The order of affecting the rate for abatement of IBP over Rutile is as following:  $O_2^{\bullet-} > \bullet OH$ , no holes contribution. The photocatalytic abatement of IBP was nearly completely inhibited with the addition of  $O_2^{\bullet-}$  radical scavenger. Hydroperoxyl ( $\bullet OOH$ ) radicals or superoxide formed at the conduction band could be considered the primary active species formed with silica supported titania in the abatement of pollutants. Within one hour of abatement under irradiations almost zero abatement of IBP was found except SBA-12 and FDU-12. Within 4 hours of irradiations abatement of IBP can also be noted with TiO<sub>2</sub>P-25.

Silica only improves the dispersion of the catalyst with increased accessibility and photocatalytic reaction rate, but the mechanism involved in the abatement remains same.

**Mineralization:** Although increased photocatalytic abatement was noted for the composite formation of the TiO<sub>2</sub>/silica, but no mineralization was achieved during course of photocatalytic treatment within 4 hours of reaction time.

**In summary:**

- 1- Material (dispersion): Preformed well-crystallized TiO<sub>2</sub> particles (P-25, 20–30 nm in diameter) were directly embedded into mesoporous silica, with the formation of different percent of nano composite mixtures. The nanocomposites were prepared by mechano-chemically by mixing and milling of TiO<sub>2</sub> particles with mesoporous silica supports. This method ensured that the mesoporous silica was almost completely surrounded by TiO<sub>2</sub> particles mesoporous silica and vice versa.
- 2- Activity (degradation, mineralization): Photocatalytic experiments show that degradation is growing rapidly with increasing titania loading ratio. Mineralization does not grow in parallel but has completely decreased (e.g with 30%TiO<sub>2</sub>/MCM41 (L) degradation of 86% was achieved within 4 hours treatment while 25% of total organic carbons were mineralized).
- 3- Atomic efficiency: Highest atomic efficiency (~5-7) is calculated with low percent loading (10-20%) of TiO<sub>2</sub> P-25 on MCM-41-S and MCM-41-L followed by SBA-15. Almost ~ 3 times atomic efficiency is calculated for 30% loading of titania P-25 on silicas such as MCM-41 and SBA-15, than original P-25. Trend in boosting of atomic efficiency decreases to almost 2 with increase of the loading content of titania P-25 to 50%.

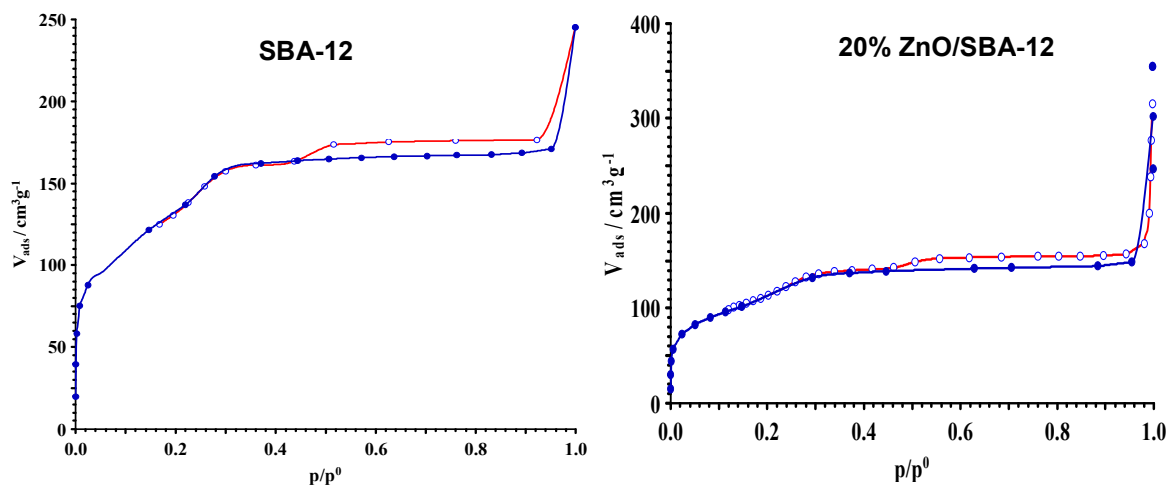
- 4- Improvement of the efficiency due to high dispersion of the photocatalyst on the mesoporous support. High dispersion and in part decoration of the mesoporous support with photocatalyst nanoparticles allow easy access to the catalyst surface and better usage of the photocatalyst surface (completely exposed to the solution) compared to agglomerated pure photocatalysts suspended in the reaction solution.
- 5- Active species: Generally EDTA as a hole ( $h^+$ ) scavenger profoundly affect the abatement of ibuprofen while t-butanol has little effect showing low amount of hydroxyl radicals ( $\bullet OH$ ) involved in photocatalytic reactions. Addition of scavenger benzoquinone for quenching superoxide  $O_2^{\bullet -}$  and hydroperoxide  $\bullet OOH$  radicals strongly stops the abatement of ibuprofen in the course of photo catalytic reaction.

## 7 Zinc oxide (ZnO)

In this chapter commercial ZnO was used for the photo catalytic treatment of ibuprofen, where binary supported catalysts were developed with mesoporous silica via wet impregnation <sup>[106]</sup> and dry physical mixing milling and calcinations. It was found that wet impregnation has highly low to no photo catalytic activity while physical mixing procedure resulted boosting of activity based on ZnO content.

### 7.1 Experimental: Composite-Type Inorganic Nanomaterials: 20% ZnO/SBA-12

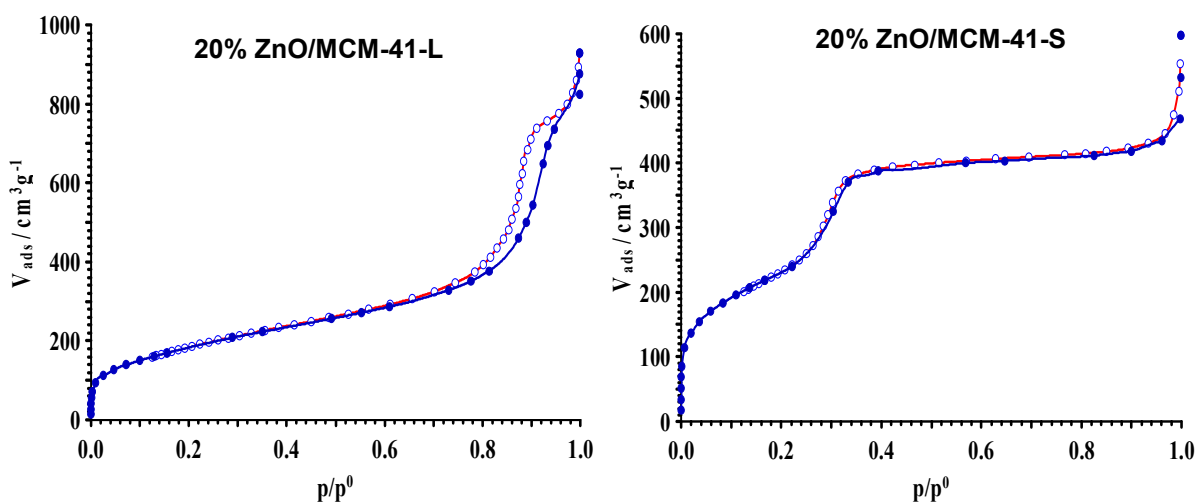
Composite of ZnO with mesoporous silica such as SBA-12 is discussed in detail for the nature of resultant photo catalyst. Nitrogen adsorption isotherm reveals same pattern as calculated for SBA-12 confirms presence of micropores at very low relative pressure (Fig.76a). Type of isotherm remains of type IV where adsorption occurs with narrow steps of capillary condensation resulting with pore size uniformity having hysteresis loop of H4 type at  $p/p^{\circ} \sim 0.5$ . Due to large inter particles mesopores, an increase of the nitrogen uptake above a relative pressure of 0.95 is observed. With addition of ZnO, the BET surface area is decreased resulting  $397 m^2/g$  (Fig.76b) . The mesopore size of  $\sim 3.81$  nm remains constant, but mesopore volume decreases and the textural inter particle volume increase as can be concluded from the course of the isotherms.



**Figure 76:** N<sub>2</sub> ad- and desorption isotherm curve of SBA-12 (a) and 20% ZnO/SBA-12 (b).

Summarizing the nitrogen sorption data of 20% ZnO over silica binary composite systems, we conclude (Fig. 77).

- No change in type of isotherm confirms the pores system remains similar as bare silica.
- Decrease in surface areas are noted in all systems means the addition of 20% ZnO while decrease of silica volume refers to decrease of pores.



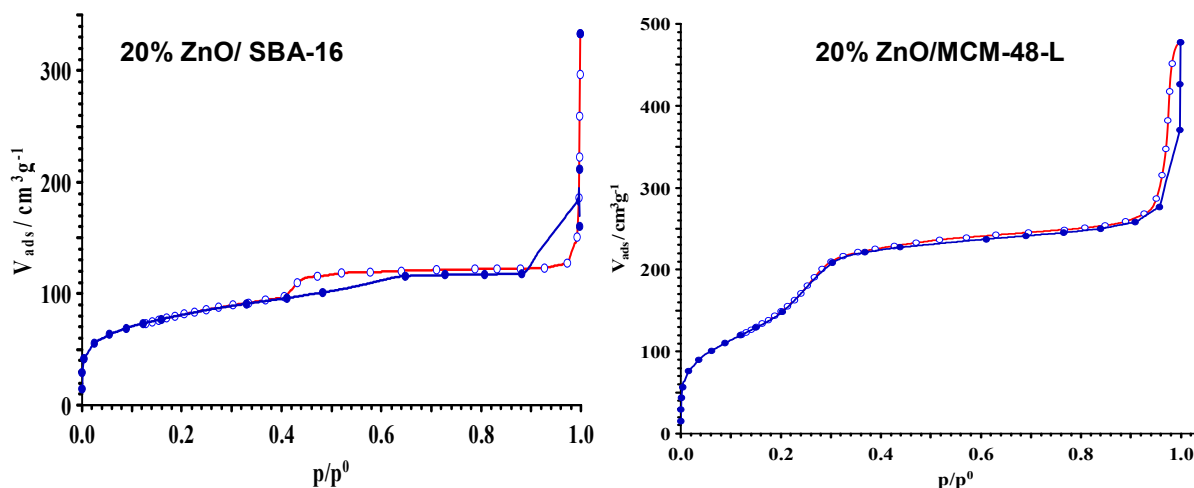


**Figure 77:** N<sub>2</sub> ad- and desorption isotherm curve of the 20% ZnO loading over MCM-41-L, MCM-41-S, SBA-16, and MCM-48-L.

The SEM images reveal the formation of agglomerated zinc oxide hexagonal crystallites of probably 100-200 nm in length, sometimes two or more rods are stacked together result in formation of large rods (Fig. 78). The average diameter of spheres is around 50–70 nm. It shows that ZnO particles are uniform in size and shape with homogeneous distribution

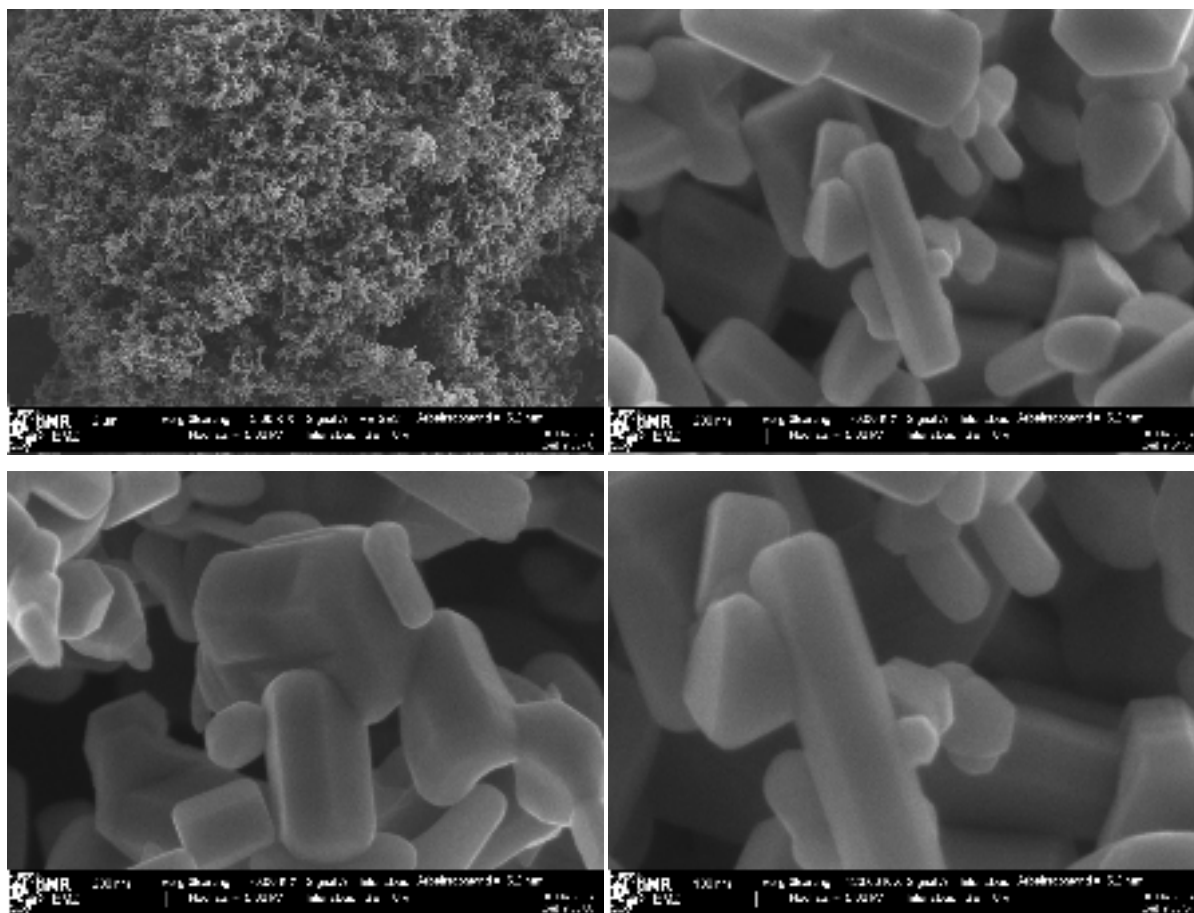


**Figure 78:** SEM images of commercial ZnO nanoparticles.

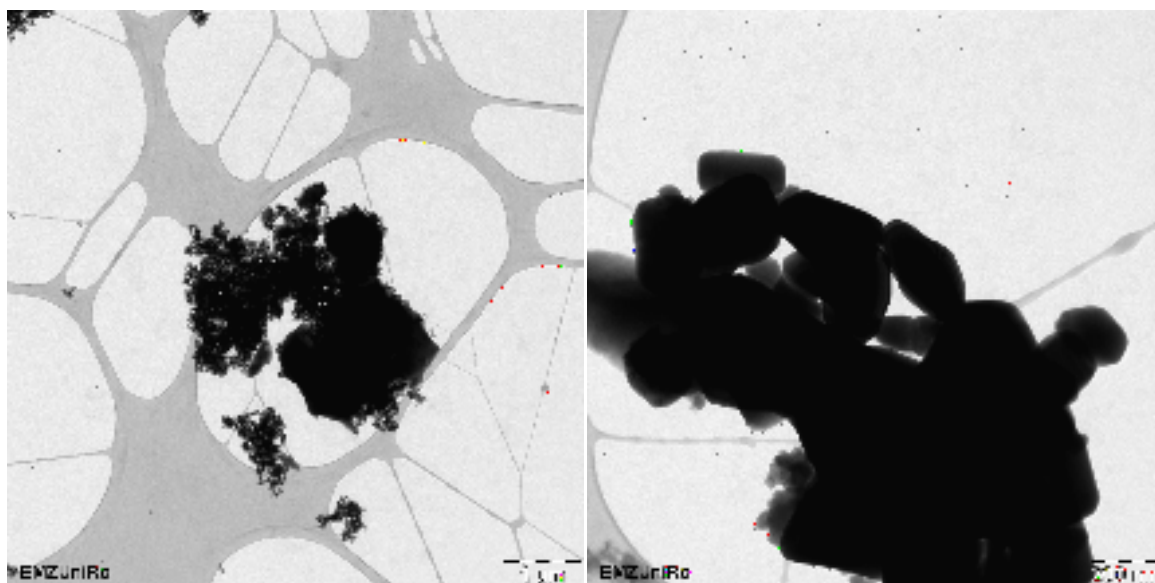
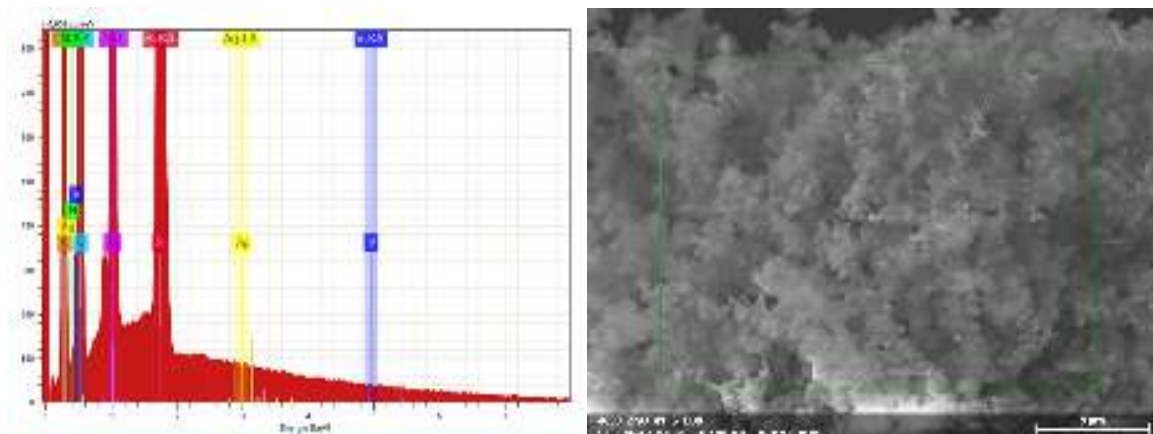


**Figure 79:** TEM images showing the morphology of ZnO/SBA-12.

In Figure.79, TEM images shows that ZnO are aggregated loosely with embedding SBA-12 particles. Also nanoparticles of each ZnO and SBA-12 dispersed unequally covering the upper body of the SBA- crystals resulting in dispersion of the ZnO materials. ZnOnanorods are combined in a special way of producing hierarchically secondary pores which may direct the flux of the pollutant solution during photo catalytic treatments.<sup>[107]</sup>

It is evidenced from the TEM images, that ZnO particles are aggregated which contribute to secondary meso- and macropore formation with relatively increase adsorption above  $p/p_0$  0.95.

**ZnO EDX:** Elemental mapping via SEM microscopy reveals a uniform distribution of elements above silica (Fig. 80). Although uniformity cannot be perceived in nanoscale as predicted from Zn mapping but still it is higher than Ti distribution shown in Appendix 2. Very low amount of impurity such as Ag, or V can be seen in spectra.



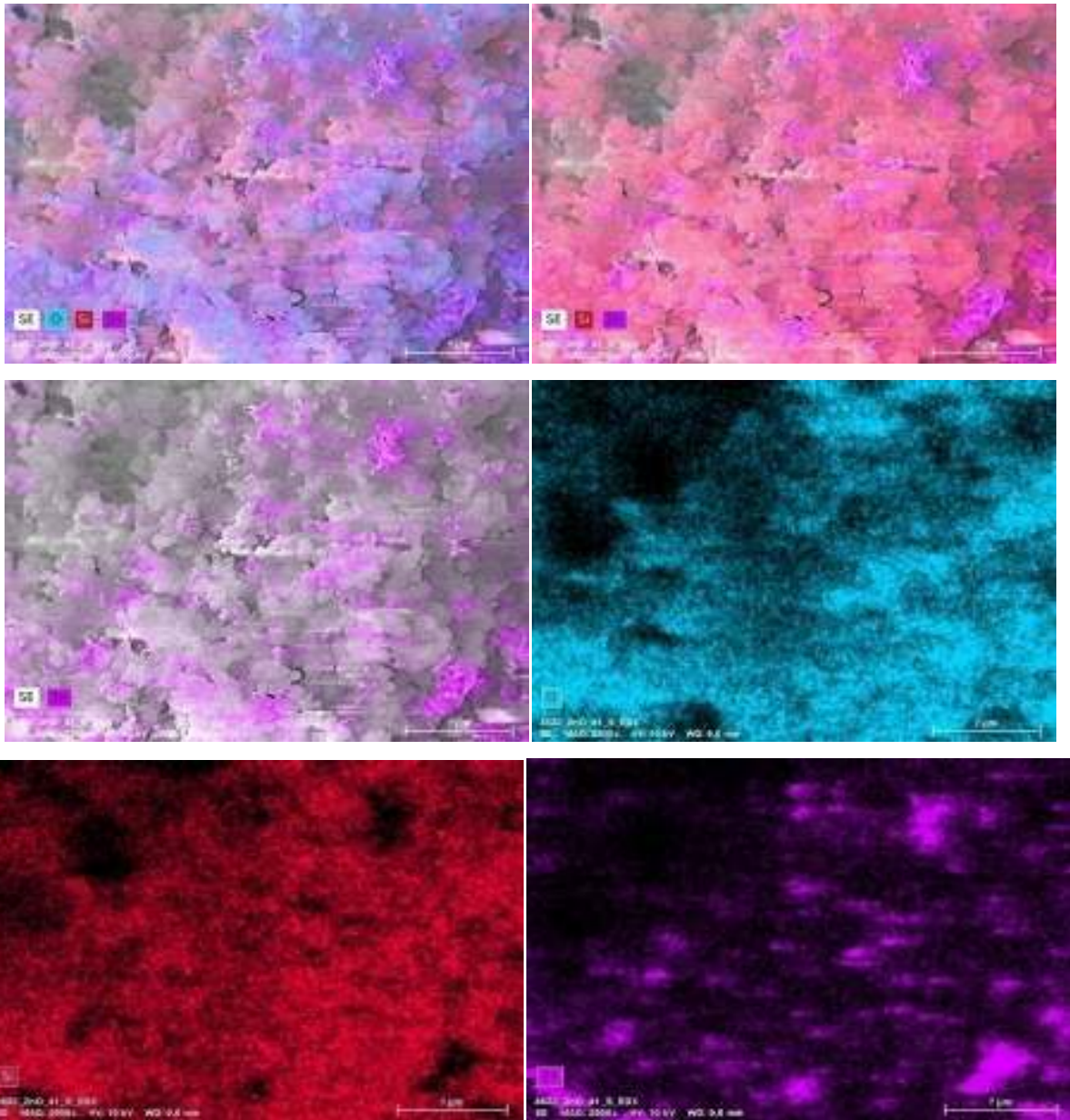


**Figure 80:** EDX elemental mapping of 20% ZnO/SiO<sub>2</sub> mixtures and single elements Zn ● Si ● O. ●

## 7.2 ZnO/SiO<sub>2</sub> Composite Photocatalytic Activity

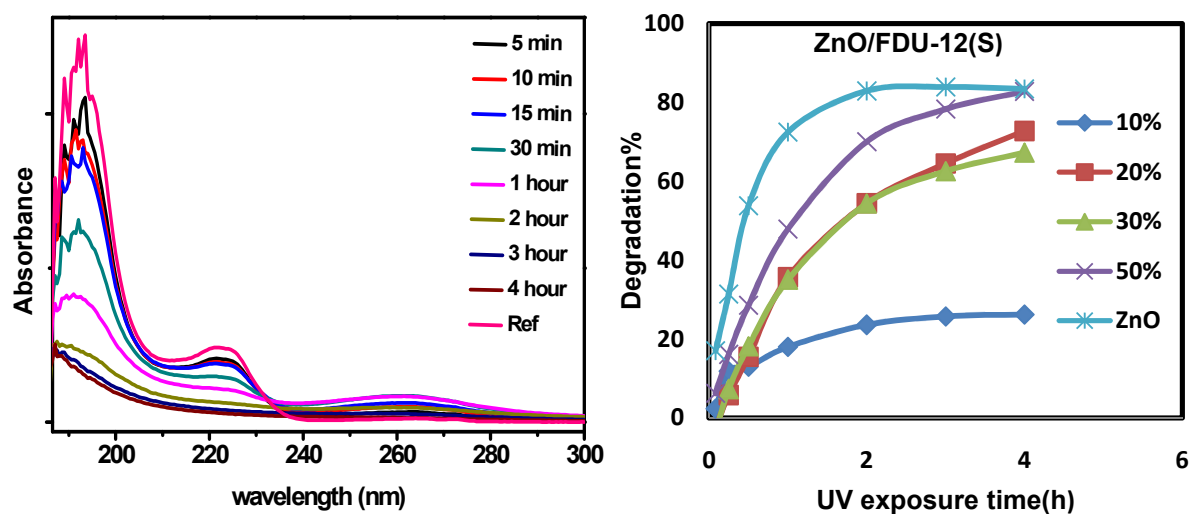


**Figure 81:** UV absorption spectra of photocatalytic degradation of IBP over ZnO within course of time (a), and % ZnO/FDU-12-S with different catalyst content (b). Condition: 250 ml batch reactor, 10 ppm IBP solution, 10 mg catalyst loading, cat /IBP = 4, 60 W UV/ Vis Solarium lamp irradiation.

Figure.82 shows the intensity change in UV/Vis spectra of ibuprofen solutions after photocatalytic treatment under UV irradiation. A decrease of the aromatic ring absorbance at 193.5 and 222 nm is observed due to the degradation or cleavage (opening) of the aromatic ring. At the same time, a new absorbance appears at *ca.* 260 nm. Photocatalysis starts immediately within treatment time as shown by the abatement curve (Fig. 81b). Almost *ca.* 45% of IBP is abated within half an hour of the treatment time, while in one hour degradation reaches to *ca.* 83% while maximum degradation is achieved within 2 hours to 90% which remains almost near to constant for 4 hours. (Fig. 81b) shows the impact of percent loading of ZnO/FDU-12-S supported catalysts. Beside 10% loading huge photocatalytic activity is noted on the onset of photocatalysis. Within one hour of reaction time 10% loading shows an average activity of 18% abatement while less increase in photocatalytic activity is noted after 4 hours (26%). An average of 70% photocatalytic activity is noted for 20 and 30% loading after 4 hours. An increase of ~85% is noted for 50% loading.

Photocatalytic activity was investigated of supported catalysts, such as 10, 20, 30 and 50% ZnO loaded over mesoporous silica. Large and small pore silica were used as supports. ZnO loaded on MCM-41 with large porous system shows high inset activity within 2 hours with respect to MCM-41 with small pores (Fig. 82). 42% abatement is noted within one hour for 20% ZnO loaded on MCM-41 large porous. With course of 4 hours ~ 71% abatement is noted. While sample with small porous MCM-41 have lower photocatalytic activity, instead gives only ~33% abatement within 1 hour and final abatement within 4 hours is only ~55%

which is almost  $\frac{3}{4}$  of large porous system. But if the ZnO loading is above 20%, no pronounced difference can be seen. Photocatalysis proceed in the same way and results in almost  $\sim 83\%$  abatement within 4 hours of treatment.

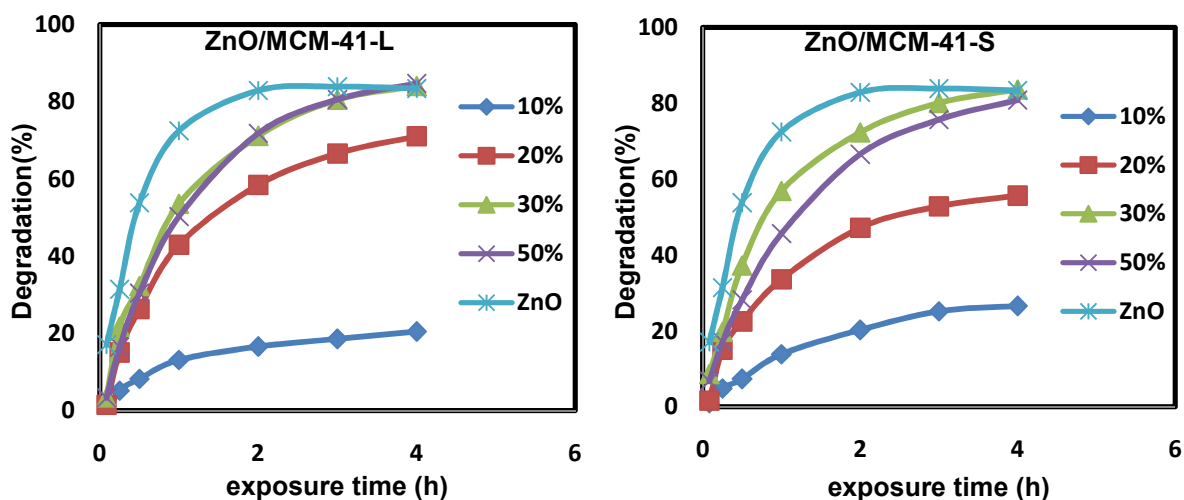


**Figure 82:** Photocatalytic degradation of IBP over % ZnO/MCM-41 large porous (a) and small porous (b). Condition: 250 ml batch reactor, 10 ppm IBP solution, 10 mg catalyst loading, cat /IBP = 4, 60 W UV/Vis Solarium lamp irradiation.

### Summary:

Summary of the resultant reactions with different load percent of ZnO on different types of silica is shown below (Fig. 83).

Different mesoporous silica supports behave differently. A general trend is noted with increase of photocatalytic activity within time with increasing ZnO percent loading within same silica. Huge photocatalytic activity is noted on the onset of photocatalysis. Within one hour of reaction time 10% loading shows an average activity of 13-18 % abatement while SBA-15 and SBA-12 shows highest activity of  $\sim 33$ . But this trend is not clear in case of 20% ZnO loading, where highest activity is noted with MCM-41 L and lowest with SBA-15. In case of 30% ZnO loading highest activity is noted for MCM both large and small porous systems reaching to 57% abatement of Ibuprofen. But increasing ZnO loading percentage to 50% results with maximum amount of abatement  $\sim 82-87\%$  with SBA-15, 12, 16 and FDU-12. While minimum amount of photocatalytic abatement (34%) is noted with MCM-48, but MCM-41 shows moderate photocatalytic activate of 50%.

After four hours of photocatalytic treatment mostly 10% loading shows an average activity of 20-40% abatement with maximum of SBA-15 and SBA-12. MCM-48 is highly low active

with 10% abatement. With increasing ZnO percent loading to 20% an average abatement is noted of 60-70%.

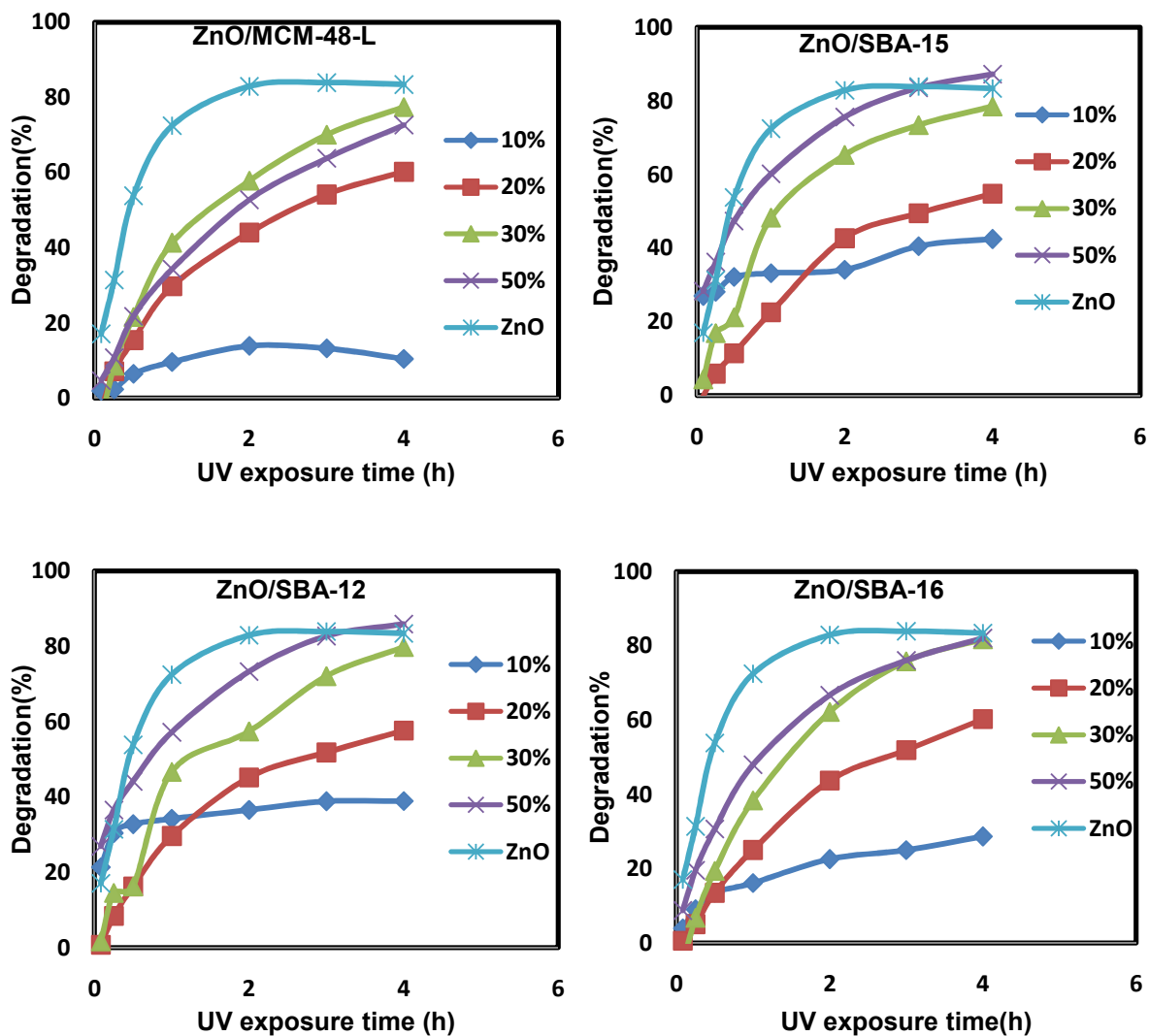


**Figure 83:** Photocatalytic degradation of IBP over ZnO / Mesoporous silica with different catalyst content. Condition: 250 ml batch reactor, 10 ppm IBP solution, 10 mg catalyst loading, cat /IBP = 4, 60 W UV/Vis Solarium lamp irradiation.

**Atomic efficiency:** Atomic efficiency calculated based on the quantity of ZnO is graphed as below (Fig. 84). Calculations were carried out with data taken after 4 hours of photocatalytic treatments.

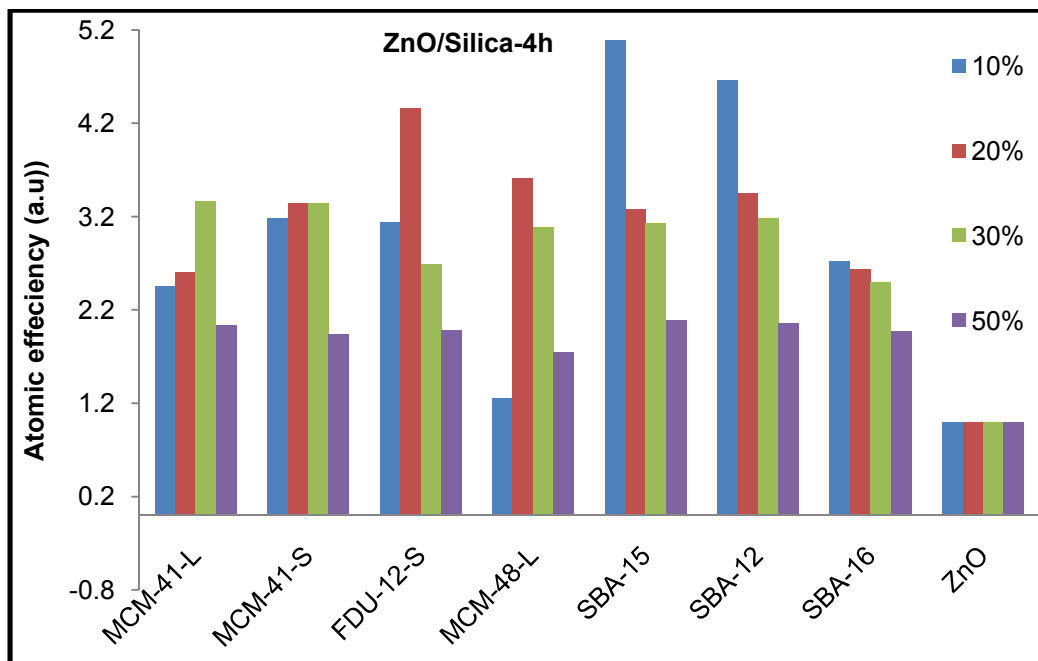


**Figure 84:** Improvement of the atomic efficiency of ZnO / Silica based on ZnO content after and 4h photocatalytic treatments.

Figure.84 shows the calculated efficiency after 4 hours of photocatalytic treatment. As described for 1 hour calculations, same pattern is noted for 10% ZnO/silica system where SBA-15 and SBA-12 shows highest atomic efficiency reaching ~ 5. Except the lowest activity of MCM-48-L (~1.2) others show activity ~2-3. 20% loading of ZnO/silicas with atomic efficiency of ~ 4.3 times with MCM-41 large pores and FDU-12-S of 4.4 times efficiency was noted. Nicely other also shows activity above ~3, unlike 1 hour treatment, which confirms increase of efficiency with time of photocatalytic treatment. Exceptional is SBA-16 showing activity of almost ~2.5. Same pattern was also found in titania P-25/silica system. Nicely similar pattern is noted for 30% ZnO/silica system as shown in figure with efficiency ~2.6- 3.3. SBA-16 showed the lowest activity. With 50% loading of ZnO/silica although pattern with different silica remain same but the boosting atomic efficiency is decreased to ~1.7-2.1.

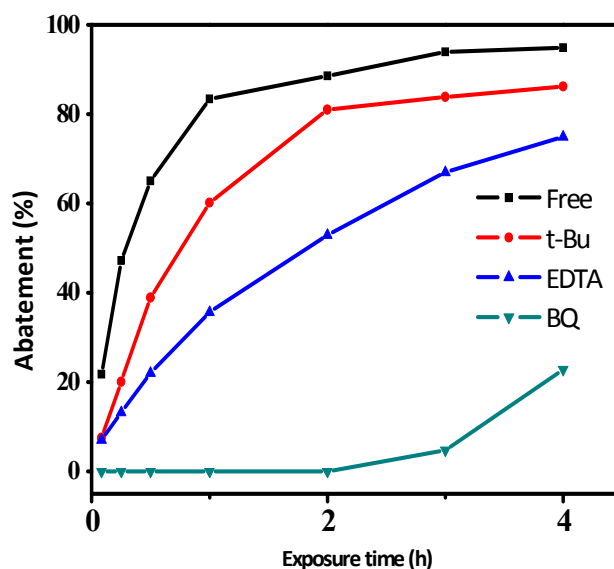
**Active Species:** The nature of the reactive species contributing to the abatement of IBP over commercial ZnO was studied with the addition of selective scavengers as shown below (Fig. 85). Pronounced effect of the hole-scavengers has been observed in the case of addition of EDTA as a hole scavenger which has retarded the degradation of the ibuprofen mostly in first 2 hours. Almost ~ 50% photocatalytic abatement is noted with EDTA while ~88% is noted without any scavenger. The addition of t-butanol retards the rate of reaction to

10% showing of ~ 80% photocatalytic activity. With the addition of scavenger benzoquinone for quenching superoxide  $O_2^{\bullet-}$  and hydroperoxide  $\bullet OOH$  radicals a strong retardation is observed with no activity up to 2 hours of photocatalytic treatment which is followed with increase of the abatement ~22% in 4 hours. These findings prove that all 3 types of active species are involved in the abatement of organic pollutants but major ones are holes and superoxide  $O_2^{\bullet-}$  or hydroperoxide  $\bullet OOH$  radicals.

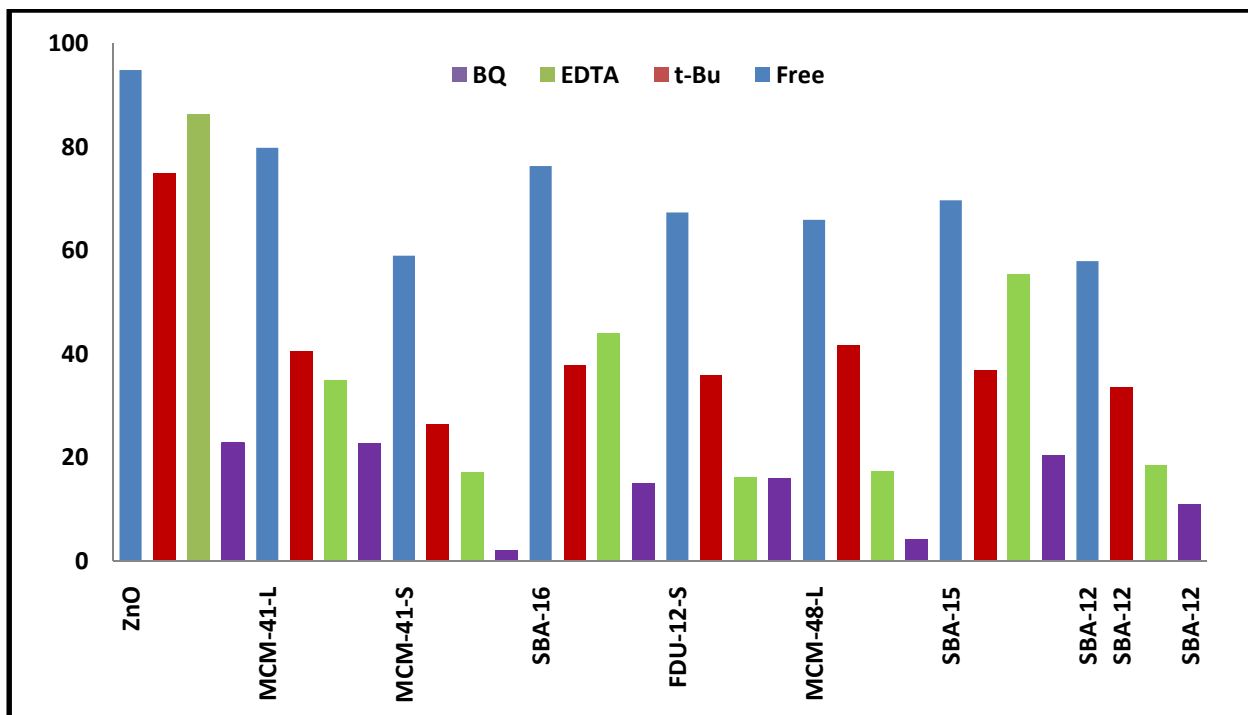
A strong retardation is observed with the addition of benzoquinone (Fig.86). This shows that both holes and superoxide  $O_2^{\bullet-}$  or hydroperoxide  $\bullet OOH$  radicals are the major active species in the photocatalytic decomposition of organics over ZnO.

Figure 86 shows the final abatement after 4 hours with the contribution of the different species derived from quenching experiments with different scavengers on silica supported ZnO. Analysis shows similar pattern of the effect of scavengers on different active species. Generally EDTA as a hole ( $h^+$ ) scavenger has a pronounce effect

on the abatement of ibuprofen which is in line with ZnO as shown in Figure 12, while t-butanol has little effect than EDTA, showing low amount of hydroxyl radicals ( $\bullet OH$ ) involved in photocatalytic reactions. Addition of scavenger benzoquinone for quenching superoxide  $O_2^{\bullet-}$  and hydroperoxide  $\bullet OOH$  radicals strongly inhibits the abatement of ibuprofen in the course of photocatalytic reaction. This proves that main species involved in photocatalytic reaction are same in ZnO/SiO<sub>2</sub> as for unsupported ZnO.



**Figure 85:** The impact of different scavengers on abatement of IBP over commercial ZnO under UV/Vis irradiation. Reaction conditions: T: room temperature, Co (IBP): 10 ppm, Vo (IBP): 250 mL, C (catalyst): 10 mg, scavengers: 1.46 mg EDTA, 0.1 mL t-BuOH, 2.704 mg 1, 4-BQ.



**Figure 86:** Impact of different scavengers on abatement of IBP over ZnO and silica supported zinc oxide under UV/Vis irradiation after 4 hours Reaction conditions: T: room temperature, Co (IBP): 10 ppm, Vo (IBP): 250 mL, C (catalyst): 10 mg, scavengers: 1.46 mg EDT A, 0.1 mL t-BuOH, 2.704 mg 1,4-BQ.

After 24 there's no effect of MCM-41(L), SBA-15 and SBA-16 different from molecular sieves has highest activity between 70-80% conversion and show low impact of EDTA addition then the others. Lowest activity MCM-41(S), MCM-48(L), FDU-12(S) and SBA-12 between 58-67% show high impact of EDTA addition (high decrease of IBP abatement).

- No clear correlation between the conversion, structure and porosity despite MCM-41(L), SBA-15 and SBA-16.
- Compare to ZnO the effect of Scavenger is increase with mesoporous silica composite even the abatement still high (20% less), the impact of butanol addition markedly lower than the other scavenger (that main large amount of hydroxyl radical present. Maybe the large amount EDTA and BQ molecules are adsorbed on the mesoporous support.

### Summary:

1-Material (dispersion): ZnO nanocrystals are embedded on mesoporous silica by thermal treatment. ZnO crystallites are dispersed as secondary phase in the extra framework of

mesoporous materials. Distribution of ZnO is higher than TiO<sub>2</sub>. High dispersion by mechanochemical preparation of ZnO/mesoporous silica composites.

2- Photocatalytic activity (degradation, mineralization): ZnO nanoclusters within intraparticle mesoporous silica show low degradation after short reaction time, while full conversion is noted within 4hs for ZnO loadings of 30% and higher. Though increased photocatalytic abatement was noted for the composite formation of the ZnO<sub>2</sub>/silica, but very lower mineralization was achieved during the course of photocatalytic treatment within 4 hours of reaction. E.g., 30% ZnO/MCM-41-S achieve 83.6% degradation while 20% mineralization of total organic carbon.

3- Photocatalytic testing under reliable conditions in the photocatalytic degradation of low concentrated ibuprofen in water (10mg, 10ppm). Artificial sunlight UV/Vis is used for irradiation at low power of only 60W.

4- Relative atomic efficiency: Low amount of atomic efficiency is noted with low loading with exceptions of SBA-15 and SBA-12 which show highest atomic efficiency. With high loading of ZnO/silica although pattern with different silica remain same but the boosting relative atomic efficiency is decreased. 30% ZnO/silica system have similar pattern efficiency of ~2.6- 3.3.

5- Active species: From scavenger experiments with ZnO loaded on Silica reveal in general similar pattern of the effect of scavengers on different active species. EDTA as holes (h<sup>+</sup>) scavenger has a pronounced effect in retarding the abatement of ibuprofen, while t-butanol has little effect than EDTA, which shows the low amount of hydroxyl radicals (•OH) involved in photocatalytic reactions. Addition of scavenger benzoquinone for quenching superoxide O<sub>2</sub><sup>•-</sup> and hydroperoxide •OOH radicals strongly inhibits the abatement of ibuprofen in the course of photocatalytic reaction. This proves that main species such as superoxide O<sub>2</sub><sup>•-</sup>, hydroperoxide •OOH radicals and hole (h<sup>+</sup>) involved in photocatalytic reaction are same in ZnO/SiO<sub>2</sub> as in unsupported ZnO.

6- MCM-41 small and large porous best supports for increase of atomic efficiency in photocatalytic degradation of ibuprofen over titania and zinc oxide/ mesoporous silica composite catalysts.

7- General results scatter, no clear dependency on porosity (pore size, specific surface area and pore volume) which indicates the additional impact of the mechano-chemical preparation procedure (milling) and of the particle shape and size of the supports and the achieved dispersion of the catalytic component in the mesoporous silica composite.

8- Silica support particles. Thereby the accessibility to reactant molecules and mass transfer is the improvement of the atomic efficiency is related with the increase of the dispersion of the catalytic component in the composite. It is in part decorated on the support materials or form nanocluster located in between the improved. (Improved flux in the inter particle nano and macro pores by directed motion in lamellar streams is proposed.

## Final Conclusion

- 1- Efficiency increase due to the dispersion effect of catalyst supported silica.
- 2- No direct relation and clear impact of pore system and the activity scatter.
- 3- Preparation procedure obviously effect strongly catalytic performance.
- 4- It's hard to prepare homogeneous mixture of catalytic components with support.
- 5- High efficiency is obtained with highest dispersion with low content of active components. For example with 10% loading of catalyst on most of mesoporous molecular sieves supports has achieved photocatalysis of half of pure catalyst or 30% ACINs.

**Table 4:** Percent degradation and mineralization of IBP over TiO<sub>2</sub>/ silica after 1h and 4h photocatalytic treatment time

<i>TiO<sub>2</sub>/Silica</i>	<i>Degradation loading (%)after 1 hours</i>				<i>mineralization</i>
	<i>10%</i>	<i>20%</i>	<i>30%</i>	<i>50%</i>	<i>30%loading</i>
MCM-41-S	32.07	48.61	55.01	39.54	13.52
MCM-41-L	26.74	47.34	47.25	47.92	12.47
MCM-48-L	19.53	30.18	30.73	34.42	-----
SBA-15	35.88	38.05	29.08	47.61	11.98
SBA-12	20.92	29.12	37.01	38.5	4.82
SBA-16	22.01	27.25	32.05	24.12	4.82
FDU-12-S	26.56	37.72	35.76	41.79	9.49

<i>TiO<sub>2</sub>/Silica</i>	<b>Degradation loading (%)after 4 hours</b>				<b>mineralization</b>
	<b>10%</b>	<b>20%</b>	<b>30%</b>	<b>50%</b>	<b>30%loading</b>
MCM-41-S	71.91	86.59	90.58	81.65	44.06
MCM-41-L	66.24	88.60	86.48	88.03	29.05
MCM-48	54.20	69.92	83.49	83.49	-----
SBA-15	64.08	79.76	59.20	97.23	11.98
SBA-12	53.56	64.29	78.17	81.22	4.82
SBA-16	61.44	64.64	77.32	68.15	11.83
FDU-12-S	49.68	69.23	76.50	89.51	9.49

**Table 5:** Percent degradation and mineralization of IBP over ZnO/ silica after 1h and 4h photocatalytic treatment time

<i>ZnO/Silica</i>	<b>Degradation loading (%)after 1 hours</b>				<b>mineralization</b>
	<b>10%</b>	<b>20%</b>	<b>30%</b>	<b>50%</b>	<b>30%loading</b>
ZnO				72.50	-----
MCM-41-L	13	43	54	50	9.25
MCM-41-S	14	34	57	46	11.35
MCM-48-L	10	30	41	34	4.42
SBA-15	33	23	48	87	-----
SBA-12	34	30	47	86	12.13
SBA-16	16	25	38	82	-----
FDU-12(S)	18	36	35	83	-----
<i>ZnO/Silica</i>	<b>Degradation loading (%)after 4 hours</b>				<b>mineralization</b>
	<b>10%</b>	<b>20%</b>	<b>30%</b>	<b>50%</b>	<b>30%loading</b>
ZnO				83.45	35.17
MCM-41-L	20	71	84	85	26.86
MCM-41-S	27	56	84	81	20.31
MCM-48-L	10	60	77	73	8.9
SBA-15	42	55	78	87	-----
SBA-12	39	58	80	86	8.81
SBA-16	29	60	82	82	10.25
FDU-12(S)	26	73	67	83	-----

**Table 6:** Percent degradation and mineralization of IBP over CAT25/ silica after 6h and 8h photocatalytic treatment time

<i>1-CAT25/KIT-6</i>	<i>Deg %at 6h</i>	<i>Deg% at 8h</i>	<i>Min% at 6h</i>	<i>Min% at 8h</i>	<i>%catalyst loading</i>
	11.75	15.24	-----	-----	10
	26.61	37.69	7.297	5.89	20
	42.67	49.68			30
	50.47	59.83			45
	54.96	63.96			60
<i>2-CAT25/MCM41-L</i>	12.62	16.39			10
	25.36	33.29			20
	43.64	47.65			30
	46.37	58.21			45
	57.28	67.52			60
<i>3-CAT25/MCM41-S</i>	18.02	25.74	8.67	17.32	10
	28.82	35.54			20
	34.12	47.58			30
	49.67	62.81			45
	61.61	69.29			60
<i>4-CAT25/FDU-12-L</i>	12.90	18.13	9.08	18.89	10
	24.37	34.94	21.64	33.96	20
	35.42	47.19	32.92	44.57	30
	46.36	58.01	43.29	55.81	45
	57.52	67.11	55.64	65.57	60
<i>5-CAT25/FDU-12-S</i>	11.01	23.34	1.52	9.094	10
	19.26	26.85			20
	32.86	59.93			30
	41.53	62.58			45
	47.62	59.69			60

**Table 7:** Percent degradation and mineralization of IBP over CAT25/ silica after 6h and 8h photocatalytic treatment time

1-CAT30/KIT-6	<i>Deg% at 6h</i>	<i>Deg% at 8h</i>	<i>Min% at 6h</i>	<i>Min% at 8h</i>	<i>%loading</i>
	14.93	22.44	17.14	19.69	10
	25.84	40.25	29.74	43.51	20
	32.54	45.34	34.65	50.65	30
	44.5	58.71	49.20	62.23	45
	46.42	58.86	51.04	62.77	60
2-CAT30/MCM41-L	4.45	5.22	7.12	9.77	10
	14.14	23.54	15.18	24.88	20
	22.25	35.46	22.62	39.80	30
	46.59	64.41	49.89	62.01	45
	55.28	64.01	56.086	65.76	60
3-CAT30/MCM41 S	20.78	20.48			10
	26.29	34.74	12.94	16.71	20
	35.84	47.09	24.13	32.06	30
	35.43	47.51	25.62	37.69	45
	41.94	54.01	47.81	60.39	60
4-CAT30/FDU-12-L	6.259	9.087	4.64	9.82	10
	14.029	21.79	14.96	25.686	20
	27.70	39.95	10.92	15.27	30
	43.07	59.76	28.68	39.00	45
	45.17	62.76	30.8	39.49	60
5- CAT30/FDU-12-S	5.536	8.34			10
	11.31	22.31			20
	20.71	33.86	16	28.62	30
	26.31	39.42			45
	39.45	54.40			60

## List of Figures

Figure 1: Band gaps and band edge positions of some semiconductor photocatalysts on a potentialscale (V) versus the normal hydrogen electrode (NHE) at pH= 0.....	10
Figure 2: Solid state structure of $\alpha$ -AgVO <sub>3</sub> and $\beta$ -AgVO <sub>3</sub> .....	14
Figure 3: Types of adsorption isotherms according to IUPAC classification .....	16
Figure 4: The four main types of hysteresis loops according to IUPAC classification. ....	16
Figure 5: Formation pathway of hexagonal structured mesoporous silica MCM-41. ....	17
Figure 6: Pore models of mesostructures with different symmetries of (A) Hexagonal, (SBA-15), (B) 3Dgyroidal cubic pores structured,(MCM-48), (C) Cubic, (SBA-1 and6), (D) Cubic, 3D cage-likestructure of pores, (SBA-16), (E) Cubic, (FDU-2) (F) Centered cubic closed-packing (fcc) mesostructure, (KIT-5).....	18
Figure 7: A schematic representation of SBA-15, synthesized at 80 °C (a) and 140 °C (b), respectively. ....	19
Figure 8: 3D structure of SBA-12' .....	20
Figure 9: KIT-6 with interpenetrating mesoporous channels in the template (a) [111] projection of the mesostructure (b). ....	20
Figure 10: 3D structure of FDU-12 (left) and SBA-16 (right). ....	22
Figure 11: Supported Catalyst composite mixture, Core-Shell, hierarchical structured photocatalysts green defines the active component; blue defines nonporous or porous support, while other colors show in part contribution to the photocatalytic process. ....	23
Figure 12: Nitrogen adsorption (assigned lines) and desorption (plain lines) isotherms of prepared $\beta$ -AgVO <sub>3</sub> , mpg-C <sub>3</sub> N <sub>4</sub> , and the corresponding $\beta$ -AgVO <sub>3</sub> /mpg-C <sub>3</sub> N <sub>4</sub> composite and "Core-Shell" material. ....	25
Figure 13: TEM images of $\beta$ -AgVO <sub>3</sub> (a,b) and mpg-C <sub>3</sub> N <sub>4</sub> after calcination at 500°C (c,d). ....	26
Figure 14: TEM images of 20% $\beta$ -AgVO <sub>3</sub> /mpg-C <sub>3</sub> N <sub>4</sub> (a-b). ....	27
Figure 15: N <sub>2</sub> adsorption-desorption isotherm curve (a) and pore size distributions (b) of the .....	28
Figure 16: N <sub>2</sub> adsorption-desorption isotherm curve (a) and pore size distributions (b) of the MCM-41-L. ....	28
Figure 17: SEM images showing the morphology of MCM-41-L (Large porous). ....	29
Figure 18: SEM images showing the morphology of MCM-41-S (small porous). ....	30
Figure 19: SAXS patterns of MCM-41-L (large pore), as-synthesized and calcined at 550°C (a), and MCM-41-S (small pore) (b). ....	30
Figure 20: N <sub>2</sub> adsorption-desorption isotherms (a) pore size distributions (b) of the MCM-48-S (obtained after 10h hydrothermal treatment and calcined). ....	31
Figure 21: N <sub>2</sub> adsorption-desorption isotherms (a) and pore size distributions (b) of the MCM-48-L (obtained after 11days of hydrothermal treatment and calcined). ....	32
Figure 22: SEM images showing the morphology of MCM-48-S. ....	33
Figure 23: SEM images showing the morphology of MCM-48-L. ....	33
Figure 25: N <sub>2</sub> adsorption-desorption isotherm curve (a) and pore size distributions (b) of the KIT-6. ....	34
Figure 24: SAXS patterns of MCM-48-L and MCM-48-S .....	34
Figure 26: SAXS patterns of KIT-6. ....	35

Figure 27: SEM images showing the morphology of KIT-6.....	36
Figure 28: N <sub>2</sub> adsorption-desorption isotherm and pore size distribution of the SBA-15. ....	37
Figure 29 : SAXS patterns of the SBA-15.....	37
Figure 30: SEM images showing the morphology of SBA-15.....	38
Figure 31: N <sub>2</sub> adsorption-desorption isotherm curve (a) and pore size distributions (b) of the SBA-16. .....	39
Figure 32: SAXS patterns of the SBA-16.....	39
Figure 33: SEM images showing the morphology of SBA-16. The big bulky-like particles are composed of agglomerated small nanoparticle (bottom right).....	40
Figure 34: N <sub>2</sub> adsorption-desorption isotherm curve (a) and pore size distributions (b) of the SBA-12 calcined. ....	41
Figure 35: SAXS patterns of the calcined SBA-12. ....	41
Figure 36: SEM images showing the morphology of SBA-12. Primary SBA-12 particle (top) consist of agglomerated submicron-sized particles (bottom).....	42
Figure 37: TEM images of the secondary agglomerated sub- $\mu$ m-sized nanoparticles forming the spherical $\mu$ m-sized primary particles of SBA-12.....	43
Figure 38: N <sub>2</sub> ad-desorption isotherm curve and pore size distributions of the FDU-12-S.....	43
Figure 39: N <sub>2</sub> adsorption-desorption isotherm curve and pore size distributions of the FDU-12-L. ....	44
Figure 40: Small angle XRD patterns of the calcined FDU-S and FDU-12-L.....	44
Figure41: SEM images showing the morphology of FDU-12-S.....	45
Figure 42:SEM images showing the morphology of FDU-12-L. ....	46
Figure 43: TEM images showing the uniform sized and ordered arranged mesopores of FDU-12-L.	47
Figure 44: N <sub>2</sub> adsorption-desorption isotherm curve of the 20% CAT-25/MCM-41-L and 20% CAT- 25/MCM-41-S.....	49
Figure 45: TEM images showing the morphology of 20% CAT-25/MCM-41-S.....	50
Figure 46: EDX spectrum, and elemental mapping showing the uniform distribution of the 20% CAT- 25/MCM-41-S. Elements Ag , V , O , Si , N , C .....	52
Figure 47: UV/Vis spectra of photocatalytic treated Aqueous IBP solution in dependence of time, over $\beta$ -AgVO <sub>3</sub> /mpg-C <sub>3</sub> N <sub>4</sub> Core Shell photocatalyst using a) UV/Vis, b) Visible light; (10 mg/L catalyst, 250 mL of 10 ppm IBP. Solution, Irradiation: 60W UV/Vis light or 16. ....	54
Figure 48: Relative abatement of IBP during the course of photocatalytic treatment under UV/Vis (left) and visible light (right) irradiation over a) $\beta$ -AgVO <sub>3</sub> , b) mpg-C <sub>3</sub> N <sub>4</sub> , and $\beta$ -AgVO <sub>3</sub> /mpg-C <sub>3</sub> N <sub>4</sub> composites containing c) 5% d) 10% e) 20% f) 30% g) 40% h) 50% i) 70% of silver vanadate and 20% $\beta$ -AgVO <sub>3</sub> /mpg-C <sub>3</sub> N <sub>4</sub> (j) prepared with co-precipitation. ....	55
Figure 49 Relative abatement of IBP during the course of photocatalytic treatment under UV/Vis irradiation over a) % CAT-30/MCM-41-L (Left, up) and % CAT-30/MCM- 41-S (left down). Final degradation of IBP after 8 hours of photocatalytic treatment over a) % CAT-30/MCM- 41-L (right, up) and % CAT-30/MCM- 41-S (right down). ....	58
Figure 50: Calculated relative atomic efficiencies compared to the starting CAT-30 composite of (a) % CAT-30/MCM-41-L and (b) % CAT-30/MCM- 41-S in the photocatalytic treatment of IBP after 8 hours, under UV/Vis irradiation.....	60

Figure 51: Mineralization of IBP over % CAT-30/MCM-41-L and % CAT-30/MCM-41-S composites after photocatalytic treatment (8 h)using UV/Vis irradiations.....	61
Figure 52: Photocatalytic degradation of IBP over CAT-30/KIT-6 (a) UV/Vis and (b) Visible light irradiation. With different percentage of catalyst loaded on mesoporous silica KIT-6 and final degradation of IBP over CAT-30/KIT-6 composite with different catalyst co content after 8h under UV/Vis (c), under visible light irradiation after 22 hours (d).....	62
Figure 53: Calculated relative atomic efficiency of CAT-30/KIT-6 in the photocatalytic treatment of IBP after 8 hours, under UV/vis irradiation. ....	63
Figure 54: Mineralization of IBP over CAT-30/KIT-6 photocatalyst) under UV/Vis b) under visible light irradiations (Cat. 10 mg/L, 250 mL of 10 ppm IBP). ....	64
Figure 55: Photocatalytic degradation of IBP over % CAT-30/FDU-12-L with different photocatalyst loading (a). Final degradation of IBP over % CAT-30/FDU-12-L composite with different catalyst content after 8h (b). ....	65
Figure 56: (a) Improvement of the atomic efficiency of % CAT-30/FDU-12-L composite independence of $\beta$ -AgVO <sub>3</sub> /mpg-C <sub>3</sub> N <sub>4</sub> content after 8h photocatalytic treatment, (b) mineralization of IBP over CAT-30/FDU-12-L composite after photocatalytic treatment.....	66
Figure 57: Photocatalytic degradation of IBP over CAT30/FDU-12-S with different catalyst content(a),Final degradation of IBP over % CAT-30/FDU-12-L composite with different catalyst content after 8h (b). ....	67
Figure 58: Atomic efficiency of IBP over % CAT-30/ FDU-12-S composite with different catalyst content after 8h (a). mineralization of IBP over 30% CAT-30/FDU-12-S composite after photocatalytic treatment(b). ....	68
Figure 59: Photocatalytic degradation of IBP over % CAT-25/KIT-6 with different catalyst content (a). Final degradation of IBP over % CAT-25/KIT-6 composite with different catalyst content after 8h (b) Condition: 250 ml batch reactor, 10 ppm IBP solution, 10 mg catalyst loading, cat /IBP = 4, 60 W UV/Vis Solarium lamp irradiation. ....	69
Figure 60: (a) mineralization of IBP over % CAT-25/KIT-6 composite after photocatalytic treatment. (b) Improvement of the atomic efficiency of % CAT-25/KIT-6 composite independence of AgVO <sub>3</sub> /C <sub>3</sub> N <sub>4</sub> content after 8 hours of photocatalytic treatment.....	70
Figure 61: Influence of the type of mesoporous materials and of the catalyst CAT-25 content(25% $\beta$ -AgVO <sub>3</sub> / mpg-C <sub>3</sub> N <sub>4</sub> )on the course of photocatalytic degradation of IBP over CAT-25/Mesoporous silica under UV/Vis and Visible light(bottom right): 250 ml batch reactor,10 ppm IBP solution, 10 mg catalyst loading, Cat /IBP = 4, 60 W UV/Vis Solarium lamp irradiationor16 W Visible LED room light (last). ....	72
Figure 62: Photocatalytic degradation of IBP over 20%, 30%, 45% and 60% loading of CAT-25/Mesoporous silica (reaction volume: 250 mL reaction time: 8h, IBP concentration: 10 mg/L, catalyst loading 10 mg). ....	74
Figure 63: Improvement of the atomic efficiency of CAT-25/Silica composite independence of AgVO <sub>3</sub> /C <sub>3</sub> N <sub>4</sub> content after 8h photocatalytic treatment (reaction volume: 250mL reaction time: 8h, IBP concentration: 10mg/L, catalyst loading 10 mg). ....	76

Figure 64: mineralization of IBP over 30% CAT-25/Silica composite after photocatalytic treatment with UV/Vis irradiation (reaction volume: 250 mL reaction time: 8h, IBP concentration: 10 mg/L, catalyst loading 10 mg). .....	76
Figure 65: Impact of different scavengers on abatement of IBP over CAT-25 under UV/Vis irradiation. Reaction conditions: room temperature, Co (IBP): 10 ppm, Vo (IBP): 250 mL, C (catalyst): 10 mg, scavengers: 1.46 mg EDTA, 0.1 mL t-BuOH, 2.704 mg 1,4-BQ. ....	77
Figure 66: N <sub>2</sub> adsorption-desorption isotherm curve of the 20% TiO <sub>2</sub> /SBA-12. ....	90
Figure 67: N <sub>2</sub> adsorption-desorption isotherm curve of the 20% TiO <sub>2</sub> over MCM-41-L, MCM-41-S, SBA-16 and MCM-48-L.....	91
Figure 68: TEM images showing the morphology of TiO <sub>2</sub> /SBA-12. ....	92
Figure 69: EDX spectrum, and elemental mapping showing the uniform distribution of the 20% TiO <sub>2</sub> /MCM-41-S. Elements Ti , O , Si .....	93
Figure 70: Photocatalytic degradation of IBP over TitaniaP-25 (a) and % TiO <sub>2</sub> /MCM-41 with different catalyst content (b). Condition: 250 ml batch reactor, 10 ppm IBP solution, 10 mg catalyst loading, cat /IBP = 4, 60 W UV/Vis Solarium lamp irradiation. ....	94
Figure 71: Atomic efficiency of % TiO <sub>2</sub> P-25/MCM-41 based on the TiO <sub>2</sub> content after 4h photo catalytic treatment. ....	95
Figure 72: Photocatalytic degradation of IBP over Titania P-25 / Mesoporous silicas with different catalyst content. Condition: 250 ml batch reactor, 10 ppm IBP solution, 10 mg catalyst loading, cat /IBP = 4, 60 W UV/Vis Solarium lamp irradiation. ....	96
Figure 73: Improvement of the atomic efficiency of Titania P-25/ Silica based on titania P-25 content after 4h photo catalytic treatment.....	97
Figure 74: Impact of different scavengers on abatement of IBP over commercial TiO <sub>2</sub> (P-25) under UV/Vis irradiation. Reaction conditions: T: room temperature, Co (IBP): 10 ppm, Vo (IBP): 250 mL, C (catalyst): 10 mg, scavengers: 1.46 mg EDTA, 0.1 mL t-BuOH, 2.704 mg-BQ. ....	98
Figure 75: Impact of different scavengers on abatement of IBP over Titania P-25 and silica supported titania P-25 under UV/Vis irradiation after 1 hour (a) and 4 hours (b). Reaction conditions: T: room temperature, Co (IBP): 10 ppm, Vo (IBP): 250 mL, C (catalyst): 10 mg, scavengers: 1.46 mg EDTA, 0.1 mL t-BuOH, 2.704 mg 1,4-BQ. ....	99
Figure 76: N <sub>2</sub> ad- and desorption isotherm curve of SBA-12 (a) and 20% ZnO/SBA-12 (b). ....	102
Figure 77: N <sub>2</sub> ad- and desorption isotherm curve of the 20% ZnO loading over MCM-41-L, MCM-41-S, , SBA-16, and MCM-48-L. ....	103
Figure 78: SEM images of commercial ZnO nanoparticles. ....	103
Figure 79: TEM images showing the morphology of ZnO/SBA-12.....	104
Figure 80: EDX elemental mapping of 20% ZnO/SiO <sub>2</sub> mixtures and single elements Zn , Si , O. ....	105
Figure 81: UV absorption spectra of photocatalytic degradation of IBP over ZnO within course of time (a), and % ZnO/FDU-12-S with different catalyst content (b). Condition: 250 ml batch reactor, 10 ppm IBP solution, 10 mg catalyst loading, cat /IBP = 4, 60 W UV/Vis Solarium lamp irradiation.....	106

Figure 82: Photocatalytic degradation of IBP over % ZnO/MCM-41 large porous (a) and small porous (b). Condition: 250 ml batch reactor, 10 ppm IBP solution, 10 mg catalyst loading, cat /IBP = 4, 60 W UV/Vis Solarium lamp irradiation.....	107
Figure 83: Photocatalytic degradation of IBP over ZnO / Mesoporous silica with different catalyst content. Condition: 250 ml batch reactor, 10 ppm IBP solution, 10 mg catalyst loading, cat /IBP = 4, 60 W UV/Vis Solarium lamp irradiation.....	108
Figure 84: Improvement of the atomic efficiency of ZnO / Silicas based on ZnO content after and 4h photocatalytic treatments.....	109
Figure 85 : The impact of different scavengers on abatement of IBP over commercial ZnO under UV/Vis irradiation. Reaction conditions: T: room temperature, Co (IBP): 10 ppm, Vo (IBP): 250 mL, C (catalyst): 10 mg, scavengers: 1.46 mg EDTA, 0.1 mL t-BuOH, 2.704 mg 1,4-BQ.....	<b>Error! Bookmark not defined.</b>
Figure 86: Impact of different scavengers on abatement of IBP over ZnO and silica supported zinc oxide under UV/Vis irradiation after 4 hours Reaction conditions: T: room temperature, Co (IBP): 10 ppm, Vo (IBP): 250 mL, C (catalyst): 10 mg, scavengers: 1.46 mg EDT A, 0.1 mL t-BuOH, 2.704 mg 1,4-BQ.....	111

## List of Tables

Table 1:Summary of the Prepared Silica; Used templates, BET Surface area(m <sup>2</sup> /g),Average Pore Diameter BJH (nm), Desorption Cumulative Volume of Pores BJH (Vp) (cm <sup>3</sup> /g).....	47
Table 2:Relative decrease in order, effect of the addition scavengers on the photocatalytic abatementof IBP (%) over photocatalysts CAT-25 or 30/SiO <sub>2</sub> .with different silica supports after 8hours. ....	78
Table 3: Order of the influence of the addition of scavenger sensitive to holes, hydroxyl radicals and and superoxide radical anions (or hydroperoxide radicals HOO•) on the abatement of ibuprofen over different photocatalysts (Scavenger reduce the abatement). ....	79
Table 4:Percent degradation and mineralization of IBP over TiO <sub>2</sub> / silica after 1h and 4h photocatalytic treatment time.....	113
Table 5:Percent degradation and mineralization of IBP over ZnO/ silica after 1h and 4h photocatalytic treatment time.....	114
Table 6:Percent degradation and mineralization of IBP over CAT25/ silica after 6h and 8h photocatalytic treatment time. ....	115
Table 7:Percent degradation and mineralization of IBP over CAT25/ silica after 6h and 8h photocatalytic treatment time. ....	116

## List of Schemes

Scheme 1: Photocatalytic reaction mechanism.....	9
Scheme 2 : Formation of (1) side chain products and (2) deep oxidation products, (3) aromatic ring opening of phenol and (4) decarboxylation as intermediate during the photocatalytic degradation of ibuprofen.....	11
Scheme 3 : Reaction Pathway for synthesis of carbon nitride C <sub>3</sub> N <sub>4</sub> . ....	13

## 8 References

---

- [1] Rife, R., Thomas, T. W., Norberg, D. W., Fournier, R. L., Rinker, F. G., Bonomo, M. S. *Environ. Prog.*, **1989**, *8*, 167-173.
- [2] a) Pojasek, R. B., *Toxic and Hazardous Waste Disposal*, Ann Arbor Science: Ann Arbor, MI., **1979**, Vols. I-IV. (b) Kim, B. J., Gee, C. S., Bandy, J.T., Huang, C. S. *J. Water Pollute. Science: Control Fed.*, **1991**, *63*, 501-509.
- [3] Ternes, T. A. *Trends Anal. Chem.*, **2001**, *20*, 419-434.
- [4] De Renzo, D. J. *Biodegradation Techniques for Industrial Organic Wastes*, Noyes DataCorporation: *Park Ridge, NJ.*, **1980**, 358.
- [5] Hoffmann, M. R., Martin, S. T., Choi, W., Bahnemann, D. W. *Chem. Rev.*, **1995**, *95*, 69-96
- [6] Poole, A. J. *Water. Res.*, **2004**, *38*, 3458-3464.
- [7] Guo, Y., Yang, L., Cheng, X., Wang, X. *J. Environ. Anal. Toxicol.*, **2012**, *2*, 1-6.
- [8] Staehelin J., Hoigne J. *Environ. Sci. Technol.*, **1982**, *16*, 676-681.
- [9] Bahnemann, D. In: Boule P, editor. *Handbook of environmental photochemistry*. Springer Verlag, **1999**, 285.
- [10] Robert, D., Malato, S. *Sci. Total Environ.*, **2002**, *291*, 85-97.
- [11] Mills, A., Hunte, S. L. *J. photchem. Photobiol; A: Chem.*, **1997**, *108*, 1-35.
- [12] Hashimoto, K., Irie, H., Fujishima, A. *Jpn. J. Appl. Phys.*, **2005**, *44*, 8269-8285.
- [13] He, W., Zhao, H., Jia, H., Yin, J. J., Zheng, Z. *Mater. Res. Bull.*, **2014**, *53*, 246-250.
- [14] Westerhoff, P., Yoon, Y., Snyder, S., Wert E. *Environ. Sci. Tech.*, **2005**, *39*, 6649-6663.
- [15] Martin, D. J., Qiu, K., Shevlin, S. A., Handoko, A. D., Chen, X., Guo, Z.; Tang, J. *Angew. Chem. Int. Ed.*, **2014**, *53*, 9240-9245.
- [16] O'Shea, K.E., *J. Phys. Chem. Lett.*, **2012**, *3*, 2112-2113.

- 
- [17] Anpo, M., Ichihashi, Y., Takeuchi, M., Yamashita, H. *Res. Chem. Intermed.*, **1998**, *24*, 143-149. b) Liu, G., Zhao, Y., Sun, C., Li, F., Lu, G. Q., Cheng, H.-M. *Angew. Chem.*, **2008**, *120*, 4592-4596.
- [18] Adriana, Z., *Recent Patents Eng.*, **2008**, *2*, 157-164
- [19] Hara, M., Hitoki, G., Takata, T., Kondo, J. N., Kobayashi, H., Domen, K. *Catal. Today*, **2003**, *78*, 555-560.
- [20] Wang, Y. J., He, Y. M., Li, T. T., Cai, J., Luo, M., Zhao, L. H. *Catal. Commun.*, **2012**, *18*, 161-164.
- [21] Li, T. T., Wang, Y. J., He, Y. M., Cai, J., Luo, M.; Zhao, L. H. *Mater. Lett.*, **2012**, *74*, 170-172.
- [22] Bi, Y. P.; Ouyang, S. X., Umezawa, N., Cao, J. Y., Ye, J. H. *J. Am. Chem. Soc.*, **2011**, *113*, 6490-6492.
- [23] Shang, M., Wang, W. Z., Zhou, L., Sun, S. M., Yin, W. Z. *J. Hazard. Mater.*, **2009**, *172*, 338-344.
- [24] Bai, X., Zong, R., Li, C., Liu, D., Liu, Y., Zhu, Y. *Appl. Cat. B: Env.*, **2014**, *147*, 82- 91.
- [25] Zhu, T., Song, Y., Ji, H.; Xu, Y., Song, Y., Xia, J., Yin, S., Li, Y., Xu, H., Zhang, Q., Li, H. *Chem. Eng. J.*, **2015**, *271*, 96-105.
- [26] Kumar, S., Surendar, T., Baruah, A., Shanker, V. *J. Mater. Chem. A.*, **2013**, *1*, 5333.
- [27] Xua, H., Yana, J., Xua, Y., Song, Y., Li, H., Xia, J., Huang, J., Wan, H. *Appl. Cat. B: Env.*, **2013**, *129*, 182-193.
- [28] Li, T.; Zhao, L., He, Y., Cai, J., Luo, M., Lin, *Appl. Catal. B: Env.*, **2013**, *129*, 255-263.
- [29] He, Y., Cai, J., Zhang, L., Wang, X., Lin, H., Teng, B., Zhao, L., Weng, W., Wan, H., Fan, M. *Ind. Eng. Chem. Res.*, **2014**, *53*, 5905-5915.
- [30] Shen, K., Gondal, M. A., Siddique, R. G., Shi, S., Wang, S., Sun, J., Xu, Cn. *J. Catal.*, **2014**, *35*, 78-84.
- [31] Zhao, W., Guo, Y., Wang, S., He, H., Sun, C., Yang, S. *Appl. Cat. B: Env.*, **2015**, *165*, 335-343.
- [32] Chen, Y., Huang, W., He, D., Situ, Y., Huang, H. *ACS Appl. Mater. Interfaces*, **2014**, *6*, 14405-14414.
- [33] a) Djouadi, D., Chelouche, A., Aksas, A., Sebais, M. *Physics Procedia*, **2009**, *2*, 701-705. b) Ismail, L. F., Emara, M. M., El-Moselhy, M. M., Maziad, N. A., Hussein, O. K. *Spectrochim. Acta. A: Mol. Biomol. Spectrosc.*, **2014**, *131*, 158-68. c) Neslihan, A.,

- 
- Bunyamin, K., Tuncer, E. A., Niyazi, B. *J. Appl. Poly. Sci.*, **2010**, *116*, 165–171. d) Shams, G., Godini, H., Darvishi R., Soltani, C., Noorimotlagh, Z. *Yafteh*, **2015**, *16*, 34-43.
- e) Egerton, T. A. *Catal.*, **2013**, *3*, 338-362. f) Gao, X., Wachs, I. E. *Catal. Today*, **1999**, 233-254. g) Ko, E. I., Chen, J.P., Weissman, J.G. *J. Catal.*, **1987**, *105*, 511. h) Cauqui, M.A., Calvino, J. J., Cifredo, G., Esquivias, L., Rodriguez-Izquierdo, J. M. *J. Non-cryst. Solids*, **1992**, *147*, 758-763.
- [34] Pelaez, M., Nolan, N. T., Pillai, S. C., Seery, M. K., Falaras, P., Kontos, A.G., Dunlop, P. S. M., Hamilton, J. W. J., Byrne, J. A., O'Shea, K., Entezari, M. H., Dionysiou, D. D. *App. Catal. B: Environ.*, **2012**, *125*, 331-349.
- [35] a) Liu, Z., Tabora, J., Davis, R. J. *J. Catal.*, **1994**, *149*, 117. b) Miller, J. B., Johnston, S.T., Ko, E. I. *J. Catal.*, **1994**, *150*, 311. c) Itoh, M., Hattori, H., Tanabe, K. *J. Catal.*, **1974**, *35*, 225. d) Nakabayashi, H. *Bull. Chem. Soc. Jpn.*, **1992**, *65*, 914. e) Contescu, C., Popa, V. T., Miller, J. B., Ko, E. I., Schwarz, J. A. *Chem. Eng. J.*, **1996**, *64*, 265. f) Molnar, A., Bartok, M., Schneider, M., Baiker, A. *Catal. Lett.*, **1997**, *43*, 123.
- [36] a) Dagan, G., Sampath, S., Lev, O. *Chem. Mater.*, **1995**, *7*, 446. b) Matthews, R. W. *J. Catal.*, **1988**, *113*, 549. c) Inoue, H., Matsuyama, T., Liu, B., Sakata, T.; Mori, H., Yoneyama, H. *Chem. Lett.*, **1994**, 653. d) Fu, X., Clark, L. A., Yang, Q., Anderson, M. A. *Environ. Sci. Technol.*, **1996**, *30*, 647.
- [37] a) Livraghi, S., Czoska, A. M., Paganini, M. C., Gimello, E. *J. Solid State Chem.*, **2009**, *182*, 160-164. b) Zhou, X., Peng, F., Wang, H.; Yu, H., Yang, J. *Mater. Res. Bull.*, **2011**, *46*, 840-844. c) Zhang, D., Zeng, F. *Appl. Surf. Sci.*, **2010**, *257*, 867-871. d) Devi, L. G., Kumar, S. G. *Appl. Surf. Sci.*, **2012**, *261*, 137-146. e) Devi, L. G., Rajashekhar, K. E. *J. Mol. Catal. A.*, **2011**, *334*, 65-76.
- [38] a) Zhang, J., Zhang, M., Sun, R. Q., Wang, X. *Angew. Chem. Int. Ed.*, **2012**, *51*, 10145-10149. b) Wang, Y., Wang, X. C., Antonietti, M. *Angew. Chem. Int. Ed.*, **2012**, *51*, 68-89. c) Wang, Y. J., Shi, R., Lin, J., Zhu, Y. F. *Energy Environ. Sci.*, **2011**, *4*, 2922-2929.
- [39] Ribeiro, A. R., Nunes, O. C., Pereira, M. F. R., Silva, A. M. T. *Environ. Int.*, **2015**, *75*, 33-51.
- [40] Augugliaro, V., Litter, M., Palmisano, L., Soria, J. *J. Photochem. Photobiol. C: Photochem. Rev.*, **2006**, *7*, 127-144 .

- 
- [41] Andreozzi, R. *Catal. Today* **1999**, *53*, 51-59. b) Litter, M. *Appl. Catal. B: Environ.*, **1999**, *23*, 89-114.
- [42] Herrmann, J.-M. *Catal. Today*, **1999**, *53*, 15-129.
- [43] a) Hirakawa, T., Yawata, K., Nosaka, Y. *Appl. Catal. A: Gen.*, **2007**, *325*, 105-111. b) Xu, H., Ouyang, S., Liu, L., Reunchan, P., Umezawa, N., Ye, J. *J. Mater. Chem. A.*, **2014**, *2*, 12642. c) Bai, S., Jiang, J., Zhang, Q., Xiong, Y. *Chem. Soc. Rev.*, **2015**, *44*, 2893–2939. d) Pan, J., Liu, G., Lu, G. Q. M., Cheng, H.-M. *Angew. Chem.*, **2011**, *50*, 2133–2137. e) Grabowska, E., Reszczyńska, J., Zaleska, A. *Water Res.*, **2012**, *46*, 5453–5471.
- [44] a) Zangeneh, H., Zinatizadeh, A., Habibi, M., Akia, M., Isa, M. H. *J. Ind. Eng. Chem.* **2015**, *26*, 1–36. b) A. N. Ökte, M. S. Resat, Y. Inel, *Tox. Environ. Chem.*, **2001**, *79*, 171–178. c) M. Buchalska, M. Kobielski, A. Matuszek, M. Pacia, S. Wojtyła, W. Macyk, *ACS Catal.*, **2015**, *5*, 7424–7431.
- [45] a) Fujishima, A., Zhang, X., Tryk, D. A. *Surf. Sci. Rep.* **2008**, *63*, 515-582. b) Ohtani, B. *Catalysts*, **2013**, *3*, 942-953.
- [46] Wu, W., Jiang, C., Roy, V. A. L. *Nanoscale*, **2015**, *7*, 38–58.
- [47] Choina, J., Kosslick, H., Fischer, C., Flechsig, G.-U., Frunza, L., Schulz, A. *Appl. Catal. B: Environ.*, **2013**, *129*, 589-598.
- [48] Hollmann, D., Karnahl, M., Tschierlei, S., Kailasam, K., Schneider, M., Radnik, J., Grabow, K., Bentrup, U., Junge, H., Beller, M., Lochbrunner, S., Thomas, A., Bruckner, A. *Chem. Mater.*, **2014**, *26*, 1727-1733.
- [49] Zheng, Y., Lin, L., Wang, B., Wang, X. *Angew. Chem. Int. Ed.*, **2015**, *54*, 12868-12884.
- [50] Wang, X., Blechert, S., Antonietti, M. *ACS Catal.*, **2012**, *2*, 1596-1606.
- [51] Yan, H. *Chem. Comm.*, **2012**, *48*, 3430-3432.
- [52] Yuan, X., Zhou, C., Jin, Y., Jing, Q. *J. Colloid Interf. Sci.*, **2016**, *468*, 211-219.
- [53] Gibot, P., Schnell, F., Spitzer, D. *Micropor. Mesopor. Mater.*, **2016**, *219*, 42-47.
- [54] Liang, S., Zhou, J., Pan, A., Li, Y., Chen, T., Tian, Z., Din, H. *Materials Letters*, **2012**, *74*, 176-179.
- [55] Cheng, F., Chen, J. *J. Mater. Chem.*, **2011**, *21*, 9841-9848.

- 
- [56] Huang, C-M.; Cheng, K-W., Pan, G-T., Chang, W-S., Yang, T. C.-K. *Chemical Eng. Sci.*, **2010**, *65*, 148-152. b) Mao, C., Wu, X., Zhu, J-J. *J. Nanosci. Nanotechnol.*, **2008**, *8*, 1-5.
- [57] Li, G., Chao, K., Ye, C., Peng, H. *Mater. Lett.*, **2008**, *62*, 735-738.
- [58] McCusker, L., Liebau, F., Engelhardt, G., Nomenclature of structural and compositional characteristics of ordered microporous and mesoporous materials with inorganic hosts (IUPAC Recommendations 2001). *Pure Applied Chemistry*, **2009**, *73* (2), 381-394.
- [59] Sing, K.S.W., Everett, D.H., Haul, R.A.W., Moscou, L., Pierotti, R.A., Rouquerol, J.; Siemieniewska, T. *Pure & Appl. Chem.* **1985**, *57*, 603-619.
- [60] AlOthman, A.Z., *Materials*, **2012**, *5*, 2874-2902.
- [61] a) Wan, Y., Zhao, D. *Chem. Rev.*, **2007**, *107*, 7. b) Lu, A. H., Schüth, F. *Adv. Mater.*, **2006**, *18*, 1793. c) Tiemann, M. *Chem. Mater*, **2008**, *20*, 961. d) Tüysüz, H., Salabas, E. L., Weidenthaler, C., Schüth, F. *J. Am. Chem. Soc.*, **2008**, *130*, 280.
- [62] a) Selvam, P., Bhatia, S. K., Sonwane, C. G., *Ind. Eng. Chem. Res.*, **2001**, *40*, 3237. b) Galarneau, A., Cambon, H., Di Renzo, F., Fajula, F. *Langmuir*, **2001**, *17*, 8328. c) Groen, J. C.; Peffer, L. A. A., Ramirez, J. P. *Microporous Mesoporous Mater.*, **2003**, *60*, 1. d) Kruk, M.; Jaroniec, M.; Ko, C. H.; Ryoo, R. *Chem. Mater.*, **2000**, *12*, 1961. e) Albouy, P. A.; Ayral, A. *Chem. Mater.*, **2002**, *14*, 3391.
- [63] Yu, T.; Zhang, H., Yan, X. W., Chen, Z. X.; Zou, X. D.; Oleynikov, P., Zhao, D. Y. *J. Phys. Chem. B.*, **2006**, *110*, 21467.
- [64] Kruk, M., Jaroniec, M. *Langmuir*, **1999**, *15*, 5279-5284.
- [65] Mohamed S. AbdelSalam, M.S., Betiha, M.A., Shaban, S.A., Elsabagh, A.M., AbdEl-Aal, R.M., El-kady, F.Y., *Eg. J. Petro.*, **2015**, *24*, 49-57
- [66] Valange, S., Palacio, R., Charmot, A., Barrault, J., Louati, A., Gabelica, Z. *J. Mol. Catal., A: Chem.*, **2009**, *305*, 24-33.
- [67] Brodie-Linder, N., Dosseh, G., Alba-Simonesco, C., Audonnet, F., Imperor-Clerc, M. *Mater. Chem. Phys.*, **2008**, *108*, 73-81.
- [68] a) Anderson, M. W., Ohsuna, T., Sakamoto, Y., Liu, Z., Carlsson, A., Terasaki, O. *Chem. Commun.*, **2004**, 907-916. b) Che, S., Lund, K., Tatsumi, T., Iijima, S., Joo, S. H., Ryoo, R., Terasaki, O. *Angew. Chem., Int. Ed.*, **2003**, *42*, 2182-2185.

- 
- [69] Sakamoto, Y., Díaz, I., Terasaki, O., Zhao, D., Pérez-Pariente, J., Kim, J. M.; Stucky, G. D. *J. Phys. Chem. B.*, **2002**, *106*, 3118–3123.
- [70] Zhao, D., Huo, Q., Feng, J., Chmelka, B. F., Stucky, G. D. *J. Am. Chem. Soc.*, **1998**, *120*, 6024-6036.
- [71] Guillet-Nicolas, R., Ahmad, R., Cychosz, K. A., Kleitz, F., Thommes, M. *New J. Chem.*, **2016**, *40*, 4351-4360.
- [72] Almar, L., Torrell, M., Morata, A., Yedra, L., Estradé, S., Peiró, F., Andreu, T., Tarancón, A. *Ceram- Eng. Sci. Proc.*, **2015**, *35*, 111-116.
- [73] Alfredsson, V., Anderson, M. W. *Chem. Mater*, **1996**, *8*, 1141–1146.
- [74] Schumacher, K., Ravikovitch, P. I., Chesne, A. D., Neimark, A. V., Unger, K. K. *Langmuir*, **2000**, *16*, 4648-4654.
- [75] Yu, T., Zhang, H., Yan, X., Chen, Z., Zou, X., Oleynikov, P., Zhao, D. *J. Phys. Chem. B.*, **2006**, *110*, 21467-72.
- [76] Carta, D., Bullita, S., Casula, M. F., Casu, A., Falqui, A., Corrias, A. *ChemPlusChem*, **2013**, *78*, 364-374.
- [77] Huang, L., Yan, X., Kruk M., *Langmuir*, **2010**, *26*, 14871-14878.
- [78] a) Nikola Z. Knezevic., J-Olivier Durand. *Nanoscale*, **2015**, *7*, 2199. b) Sandra. S, Karina.N, Marlon.G, Jeann.L, Diana. A. *Microporous and Mesoporous Materials*, **2013**, *180*, 284–292.
- [79] Kuld, S., Thorhauge, M., Falsig, H., Elkjaer, C. F., Helveg, S., Chorkendorff, I., Sehested, J. *Science*, **2016**, *352*, 969-974.
- [80] Kruk, M., Jaroniec, M. *Langmuir*, **1999**, *15*, 5279-5284.
- [81] Huo, Q. S., Margolese, D. I., Stucky, G. D. *Chem. Mater*, **1996**, *8*, 1147-1157.
- [82] Soni, K., Rana, B. S., Sinha, A. K., Bhaumik, A., Nandi, M., Kumar, M., Dhar, G. M. *Appl. Catal. B: Environ.*, **2009**, *90*, 55–63. b) Hussain, M., Akhter, P., Fino, D., Russo, N. *J. Environ. Chem. Eng.*, **2013**, *1*, 164–174.
- [83] Soncheva, T., Issa, G., Nieto, J. M. L., Blasco, T., Concepcion, P., Dimitrov, M., Atanasova, G., Kovachev, D. *Microporous Mesoporous Mater*, **2013**, *180*, 156–161.
- [84] Van der Voort, P., Benjelloun, M., Vansant, E. F. *J. Phys. Chem. B.*, **2002**, *106*, 9027-9032.
- [85] Kim, T.-W, Ryoo, R., Kruk, M., Gierszal, K. P., Jaroniec, M., Kamiya, S., Terasaki, O. *J. Phys. Chem. B.*, **2004**, *108*, 11480-11489.

- 
- [86] Ravikovitch, P. I., Neimark, A. V. *Langmuir*, **2002**, 18, 1550-1560.
- [87] Sakamoto, Y., Diaz, I., Terasaki, O., Zhao, D. Y., Perez-Pariente, J., Kim, J. M., Stucky, G. D. *J. Phys. Chem. B.*, **2002**, 106, 3118-3123.
- [88] Wang, W.H., Xie, S. H., Zhou, W. Z., Sayari, A. *Chem. Mater.*, **2004**, 16, 1756-1762.
- [89] Zhu, Z., Chang, Z., Kevan, L. *J. Phys. Chem. B.*, **1999**, 103, 2680-2688.
- [90] a) Serpone, N., Texier, I., Emeline, A.V., Pichat, P., Hidaka, H., Zhao, J. *J. Photochem. Photobiol.: A.*, **2000**, 136, 145-155. b) Minero, C., Mariella, G., Maurino, V., Pelizzetti, E. *Langmuir*, **2000**, 16, 2632-2641. c) Minero, C., Mariella, G., Maurino, V., Vione, D., Pelizzetti, E. *Langmuir*, **2000**, 16, 8964-8972.
- [91] Yan, H. *J. Chem. Commun.*, **2012**, 48, 3430-3432.
- [92] Huang, C.M., Cheng, K.W., Pan, G.T., Chang, W.S., Yang, T. C. K. *Chem. Eng. Sci.*, **2010**, 65, 148-152.
- [93] Elias, V. R., Crivello, M. E., Herrero, E. R., Casuscelli, S. G., Eimer, G. A. *J. Non-cryst. Solids*, **2009**, 355, 1269-1273.
- [94] Jyothi, D., Deshpande, P. A., Venugopal, B. R., Chandrasekaran, S., Madras, G. *J. chemi sci.*, **2012**, 124, 385-393.
- [95] Zamani, C., Illa, X., Abdollahzadeh-Ghom, S., Morante, JR., Rodríguez, A. R. *Nanoscale Res Lett.*, **2009**, 4, 1303-1308.
- [96] Zhao, D.; Feng, J., Huo, Q., Melosh, N., Fredrickson, G. H., Chmelka, B. F., Stucky, G. *D. Science*, **1998**, 279, 548-552.
- [97] Mazaj, M., Stevens, W. J. J., Logar, N. Z., Ristić, A., Tušar, N. N., Arčon, I., Daneu, N., Meynen, V., Cool, P., Vansant, E. F., Kaučič, V. *Microporous Mesoporous Mater.*, **2009**, 117, 458-465.
- [98] Andrade, G.F., Soares, D.C.F., Santos, R.G., Sousa, E.M.B., *Microporous Mesoporous Mater.*, **2013**, 168, 102-110.
- [99] Fan, J., Yu, C., Gao, F., Lei, J., Tian, B., Wang, L., Luo, Q., Tu, B., Zhou, W., Zhao, D. *Angew. Chem. Int. Ed.*, **2003**, 42, 3146-3150.
- [100] Wang, W., Qi, R., Shan, W., Wang, X., Jia, Q., Zhao, J., Zhang, C., Ru, H. *Microporous Mesoporous Mater.*, **2014**, 194, 167-173.
- [101] a) A.B. Murphy, *Sol. Energ. Mater. Sol. Cells.*, **2007**, 91, 1326-1337. b) A.B. Murphy, *Appl. Optics*, **2007**, 46, 3133-3143. c) B.M. Weckhuysen, R.A. Schoonheydt, *Catal. Today*, **1999**, 49, 441-451.

- 
- [102] Ohno, T., Sarukawa, K., Tokieda, K., Matsumura, M. *J. Catal.*, **2001**, *203*, 82-86.
- [103] Zaccariello, G., Moretti, E., Storaro, L., Riello, P., Canton, P., Gombac, V., Montini, T., Rodriguez-Castellone, E., Benedetti, A. *J. Jpn. Petrol. Inst.*, **2016**, *59*, 165-173
- [104] Zaccariello, G., Moretti, E., Storaro, V., Riello, P., Canton, P., Gombac, V., Montini, T., Rodriguez-Castellone, E., Benedetti, A. *RSC Adv.*, **2014**, *4*, 37826-37837.
- [105] Ishibashi, K-I., Fujishima, A., Watanabe, T., Hashimoto, K., *Electrochem. Comm.*, **2000**, *2*, 207-210.
- [106] Lihitkar, P.B., Violet, S., Shirolkar, M., Singh, J., Srivastava, O.N., Naik, R.H., Kulkarni, S.K. *Mater. Chem. Phys.*, **2012**, *133*, 850-856.
- [107] Pouretedal, H.R., Ahmadi, M. *Iranian J. Catal.*, **2013**, *3*, 149-155.